KfK 5099
EUR 14795 EN
Oktober 1992

Nuclear Fusion Project Annual Report of the Association KfK/EURATOM

October 1991 – September 1992

Projekt Kernfusion

Kernforschungszentrum Karlsruhe

KfK 5099
EUR 14795 EN
Oktober 1992

Nuclear Fusion Project Annual Report of the Association KfK/EURATOM

October 1991 - September 1992

compiled by
G. Kast

Kernforschungszentrum Karlsruhe

Kernforschungszentrum Karlsruhe GmbH
Postfach 3640, 7500 Karlsruhe 1

ISSN 0303-4003

Preface

The Nuclear Research Centre Karlsruhe (KfK) contributes to the European Fusion Programme in developping the technologies needed to build the International Thermonuclear Experimental Reactor (ITER) and to design commercial fusion reactors. It thus complements the plasma physics and plasma engineering work of IPP Garching and KFA Jülich, respectively.

The historical basis of the present fusion activity are various nuclear technology projects and accelerator development. Whereas the nuclear projects gave the background for the present fusion related materials programme, blanket - fuel cycle - and safety activities, the earlier accelerator work gave origin to the present disciplines of superconductivity and rf-heating.

Technologies developed for the Next European Torus (NET) are now made available to ITER. During the ten years of existence of the KfK fusion project several major test facilities have been built which constitute a considerable potential to test components and systems relevant for ITER in a technical scale. In particular the model coil test facility TOSKA, the in-vessel-handling demonstration facility EDITH, the tritium laboratory TLK and the test arrangement for first wall components FIWATKA shall be named.

One of the major missions of ITER will be the qualification of first wall and fuel cycle components, in particular the breeding blankets. Within a European Community wide cooperation KfK elaborates breeding blanket designs for a Demonstration Reactor (DEMO) and conducts the basic r+d to qualify these concepts for further development and implementation into ITER as a test section. Associated to the blanket activities is a programme to develop and qualify structural materials with sufficient lifetimes and reasonable activation properties. The work conducted in this frame necessitates extensive reactor and accelerator irradiations and consequent hot cell examinations. Reactor irradiations are performed out of site, whereas two cyclotrons combined as Dual Beam Facility provide a unique tool for simulation of irradiation effects and for activation measurements.

The safety related part of the fusion project contributes to the component studies (blankets, superconducting magnets) and investigates the risk of severe accidents of fusion installations in nuclear operation.

The present yearly report of the KfK fusion project compiles the work under contract with the Commission of the European Community. References given on the responsible staff and on available reports may serve to provide the interested reader with more information on our programme.

J.E. Vetter

Contents Page

Report on the Technology Programme for NET

Nuclear Engineering / Basic Blanket

Plasma Facing Components

Introduction:

In the period to which this report refers KfK has continued to contribute to the already established tasks and in addition increased its share in taking up work on the new tasks related to CFC materials (PPM 0) and CFC-metal joints (PSM 4.4). The rather modest commitment to structural materials investigations has essentially remained the same.

Without anticipating the reporting by the task-leaders it may be allowed to stress a few highlights.

The machine for multiaxial isothermal fatigue tests as sketched in the previous report is near completion. An improved cooling is being installed for the thermal fatigue testing device (PSM 3.9).

An analysis has been made on stress distributions in a bonded ceramic-metal specimens and geometric means to reduce the peak stresses are under consideration (PSM 4.4).

Three different high emissivity coatings on the basis of Al_2O_3-TiO_2 have been selected for fatigue and thermal shock tests, and the respective 316 L tube specimens will be tested in the same devices as used for PSM 3.9 (PSM 8.1+2).

A characterization program accounting for the complex anisotropic behaviour of CFC and the wide range of operating temperatures has been set up, pretests on available machinery have been started with monolithic graphite as long as the CFC specimens have not been supplied yet (PPM 0.3).

The investigations on SiC have concentrated on post-irradiation measurement of thermal conductivity and fracture strength. For these properties the neutron dose thresholds were found to be different (PPM 1.2).

The influence of irradiation on fracture strength of insulator materials has comprehensively been investigated, and an understanding of microstructural evolution was achieved. Similarly the mechanism for thermal conductivity deterioration could be clarified for the high temperature region (PPM 4.1).

Means for continuously measuring dielectric properties between 70 and 400 K have been established, and a detection limit for tan δ down to 3×10^{-6} could be attained. On the basis of the steep decrease with temperature engineering design work for cryogenically cooled windows has carried on (PPM 4.2).

The facility for thermomechanical tests of FW mock-ups is nearing completion. The NET specimen TS1 has been received and is being adapted. A wishable further instrumentation at the tile attachment seems not be possible (PDT 1.4).

In the modified plasma-spray facility the screening tests with divertor bulk materials have been completed. From these pure W and liquid phase sintered metals have to be ruled out as heat sink materials (PDT 2.1).

PSM 3 Low Cycle Fatigue of 316 and Welds

Subtask 9: Tubular Uniaxial and Multiaxial Isothermal and Thermal Fatigue on 316L

The loading of the First Wall (FW) of a fusion reactor causes cyclic temperature gradients. This leads together with thermal expansion to cyclic stresses and fatigue. To reliably design the FW it is necessary to estimate the lifetime under this loading. But yet, it is not clear if experimentally determined isothermal fatigue data can be used to predict the lifetime of the FW under cyclic thermal and multiaxial loading. Neumann [1] observed remarkably shorter times to fracture on tubes loaded similar to the FW than on uniaxial isothermally loaded LCF-specimens with a commercial 316L steel. In this program the influence of multiaxial and thermocyclic loading is investigated on 316L SPH steel to obtain the results necessary for a reliable design. The program is splitted up into 3 parts [2]: 1.) Thermocyclic fatigue of tubes, 2.) isothermal multiaxial fatigue of tubes, 3.) isothermal uniaxial fatigue of tubes and solid specimens.

As mentioned in the last annual report a modification of the experimental setup for thermocyclic tests was necessary to obtain better cooling conditions. This modification is finished [3]. Fig. 1 shows a comparison between the old and the new setup. The history of the temperature at the inner and outer side of the tube Fig. 2 shows clearly that boiling of the cooling water is suppressed, now. A series of experiments has been started.

To perform isothermal uniaxial fatigue tests under similar stress conditions as in thermocyclic tests, an experimental setup was developed to load tubes under tension and external /internal pressure (Fig. 3) [4]. First tests were performed satisfactory. Since this part was shift to stage II of the technology task further tests were shift to beginning 1993.

For comparison isothermal tests under uniaxial loading were performed, too. Fatigue tests on tubes and solid specimens in water and in air show lifetimes as presented in Fig. 4. The crack initiation and crack propagation was visualized by a replica technigue. Fig. 5 shows clearly, that there is an influence of demineralized water on the crack initiation, contrary to prior investigations in [5]. The hardening of the specimens under cyclic load (Fig. 6) leads to different ranges of stress for tubes and solid material. This may be caused by the smaller grain size of the tubes compared to the solid material (Fig. 7).

Literature:

[1] J. Neumann:
Unpublished Report of KfK, 1990.

[2] B. Schinke, B. Windelband:
Unpublished Report of KfK, 1991.

[3] A. Zeller:
Modifikation und Erprobung eines Versuchsstandes zur thermozyklischen Ermüdung von Rohren aus dem austenitischen Stahl 1.4909. Studienarbeit am Inst. f. Zuverlässigkeit und Schadenskunde, Universität Karlsruhe 2/1992.

[4] B. Windelband, B. Schinke, D. Munz:
Cyclic deformation and crack initiation in tubes under multiaxial loading, to presented on 3rd Int. Conf. on low cycle fatigue and elasto-plastic behaviour of materials, September 7.-11., 1992, Berlin.

[5] J. Neumann:
Untersuchungen zur thermozyklischen Ermüdung von Rohren aus dem Stahl 1.4436, Bericht des KfK 4669, Kernforschungszentrum Karlsruhe, 1989

Staff:

W. Hartlieb
B. Schinke
B. Windelband
A. Zeller

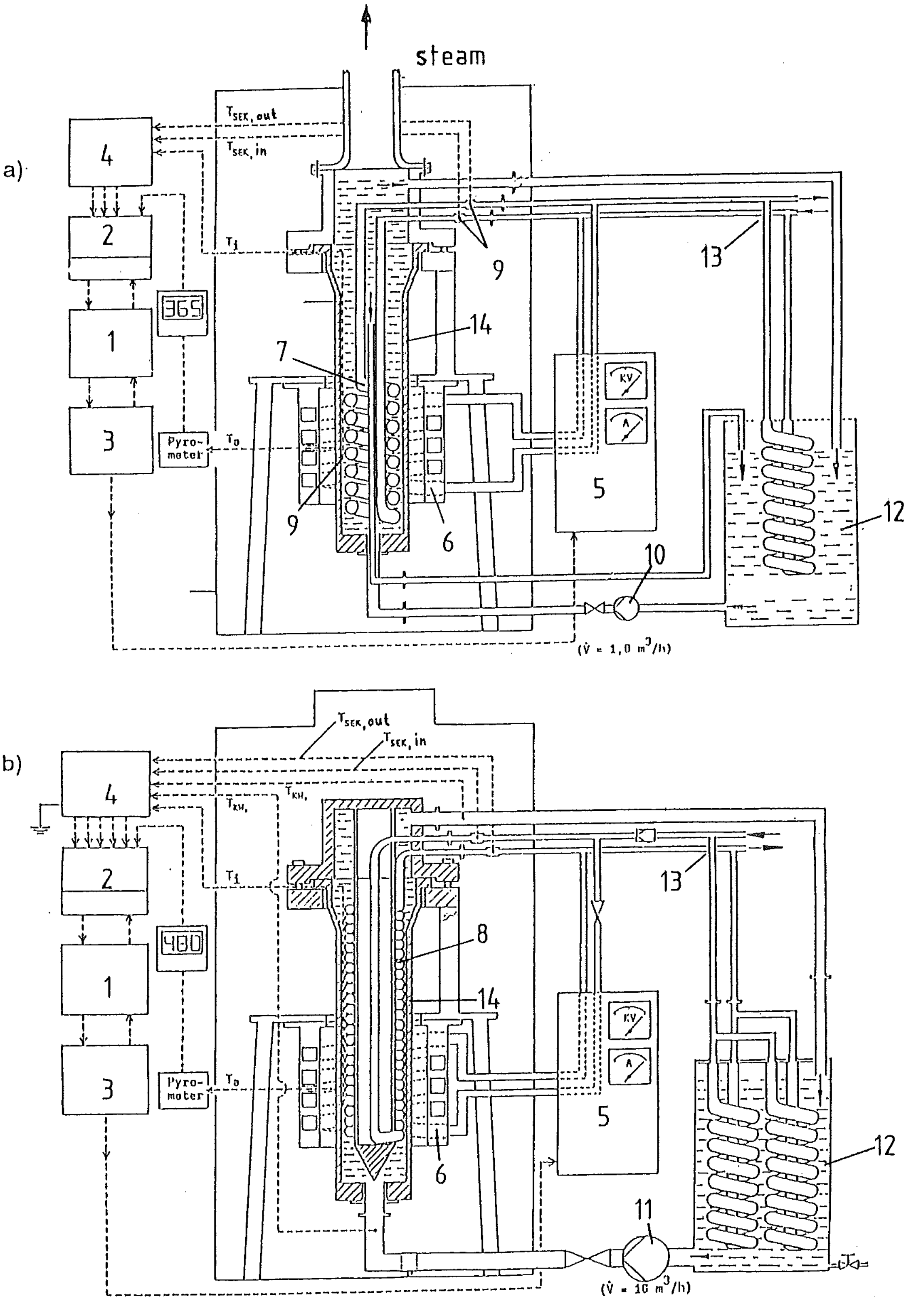

Fig. 1: Comparison between old [1] and modified [3] experimental setup for testing tubes under thermal fatigue

1 computer
2 data-logger
3 set-point generator
4 filter
5 HF-generator
6 heating coil
7 cooling coil (old)
8 cooling coil (new)
9 thermocouples
10 primary-cooling-circuit pump (old)
11 primary-cooling-circuit pump (new)
12 primary-cooling-circuit pump (fully demineralized water)
13 secondary cooling circuit
14 specimen

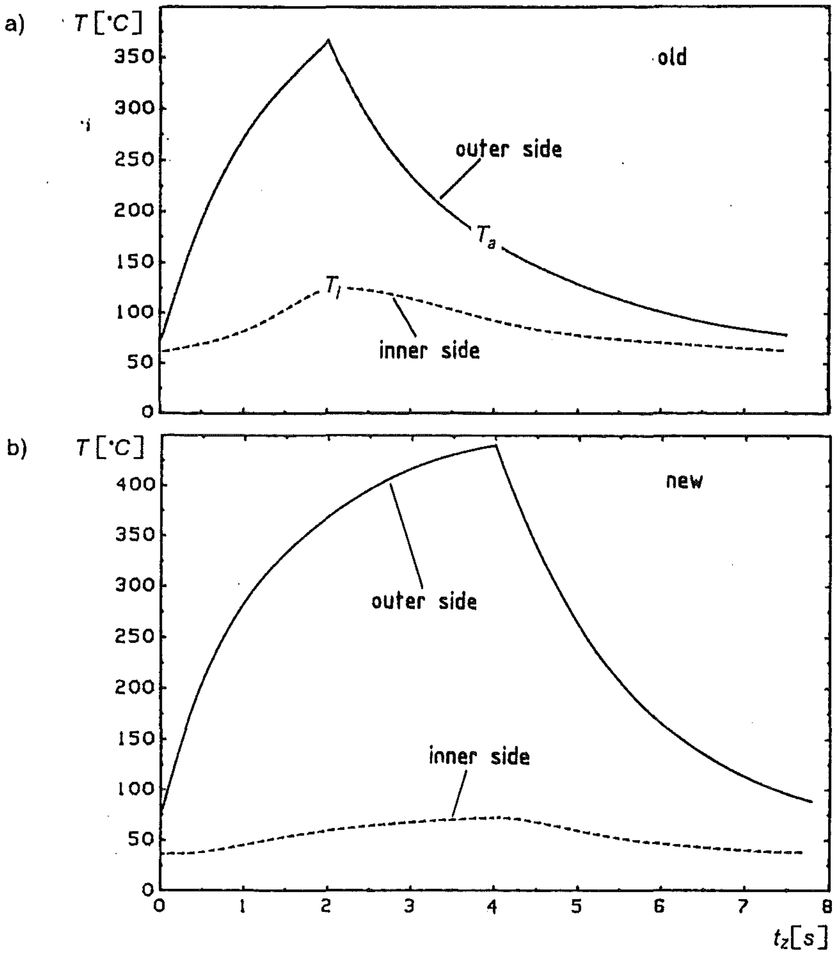

Fig. 2: Comparison between old [1] and modified [3] temperature histories during a cycle of heating and cooling of the tube

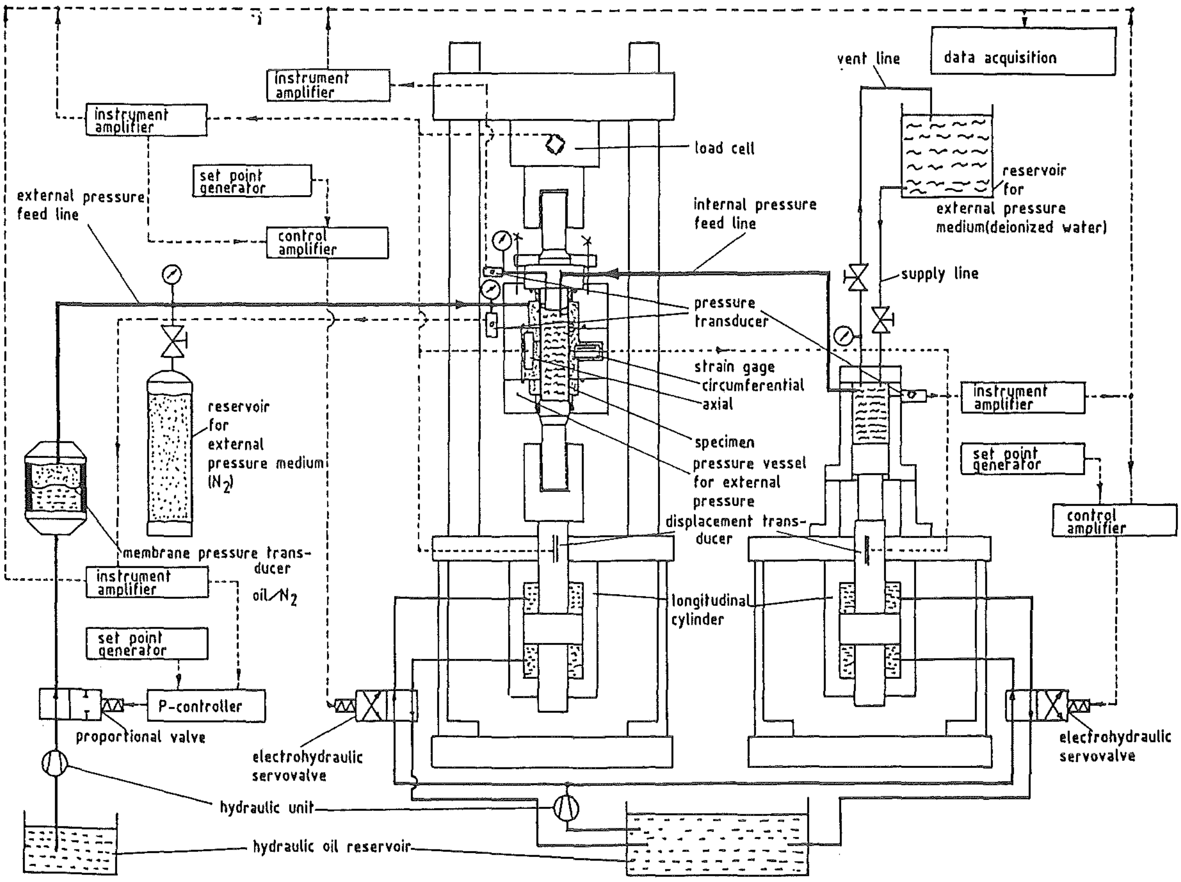

Fig. 3: a) Schematic layout of an experimental setup to fatigue tubes under push/pull and external/internal pressure at room temperature

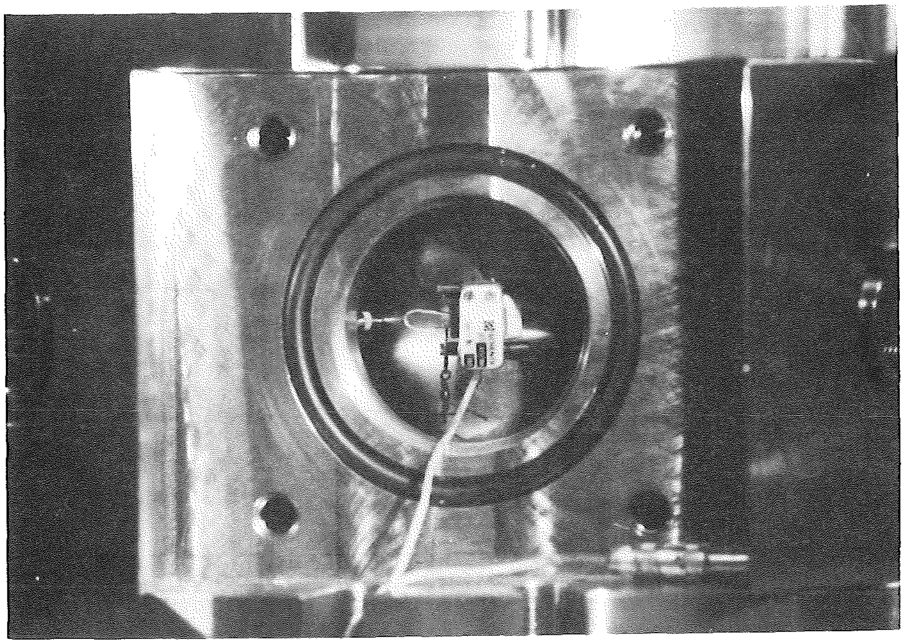

b) Photography of the pressure vessel with specimen and extensometer

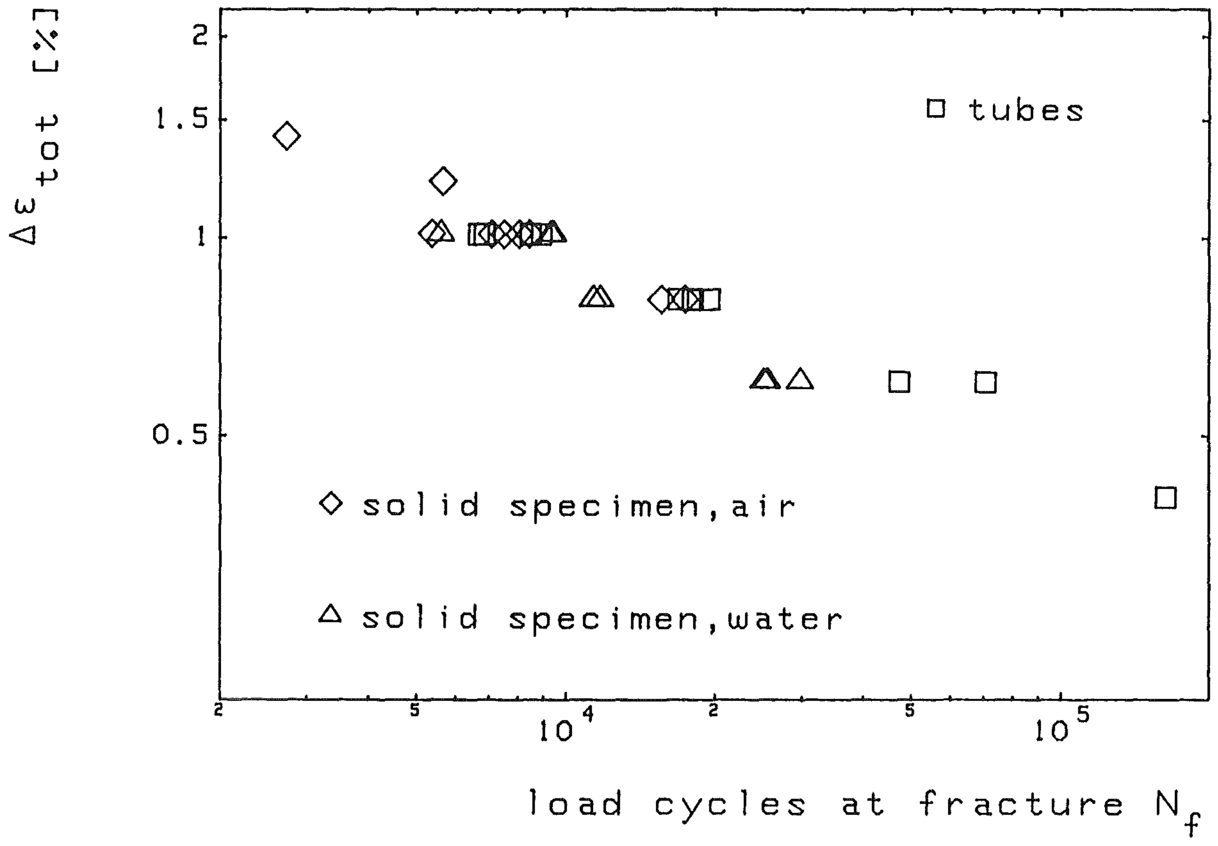

Fig. 4: Lifetime of uniaxial isothermal tests on tubes and solid specimens made of 316 L SPH

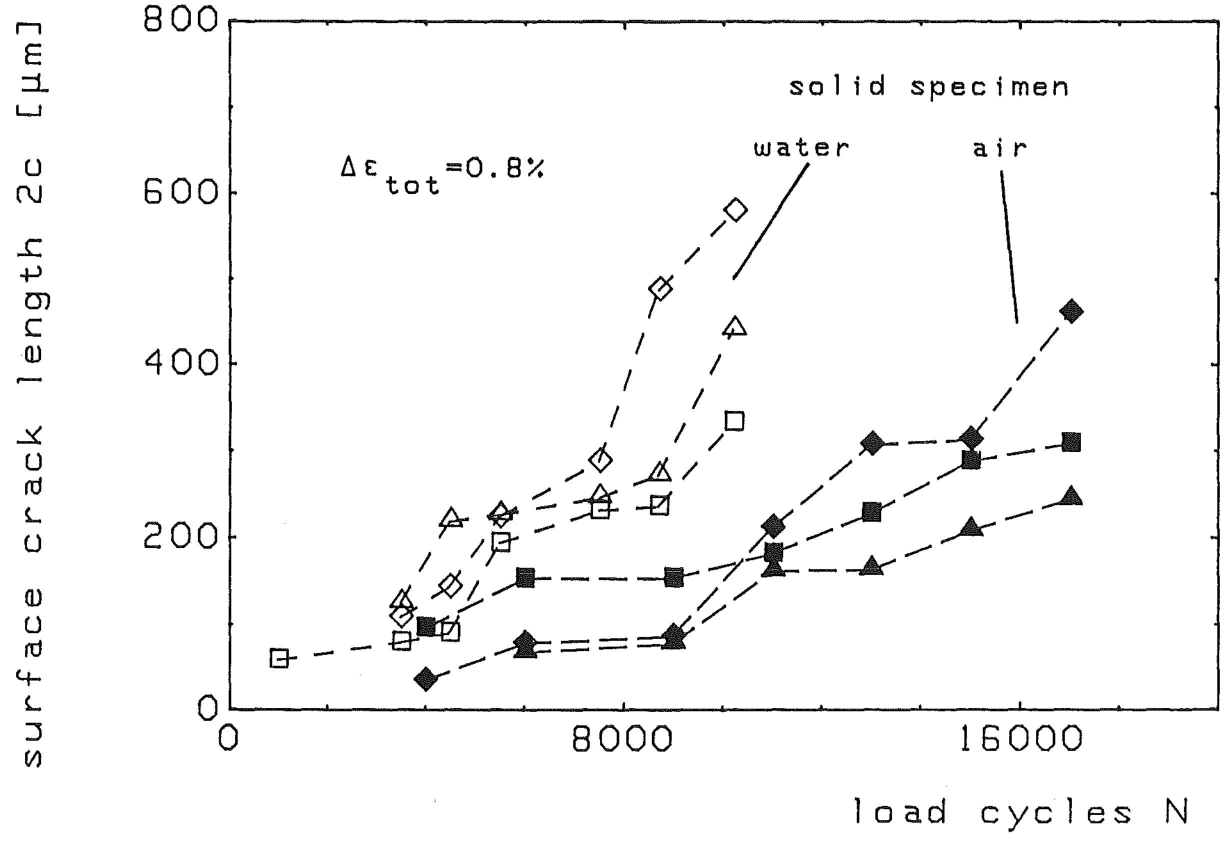

Fig. 5: Comparison of the crack size of individual cracks measured on the surface of solid specimens in air and in water

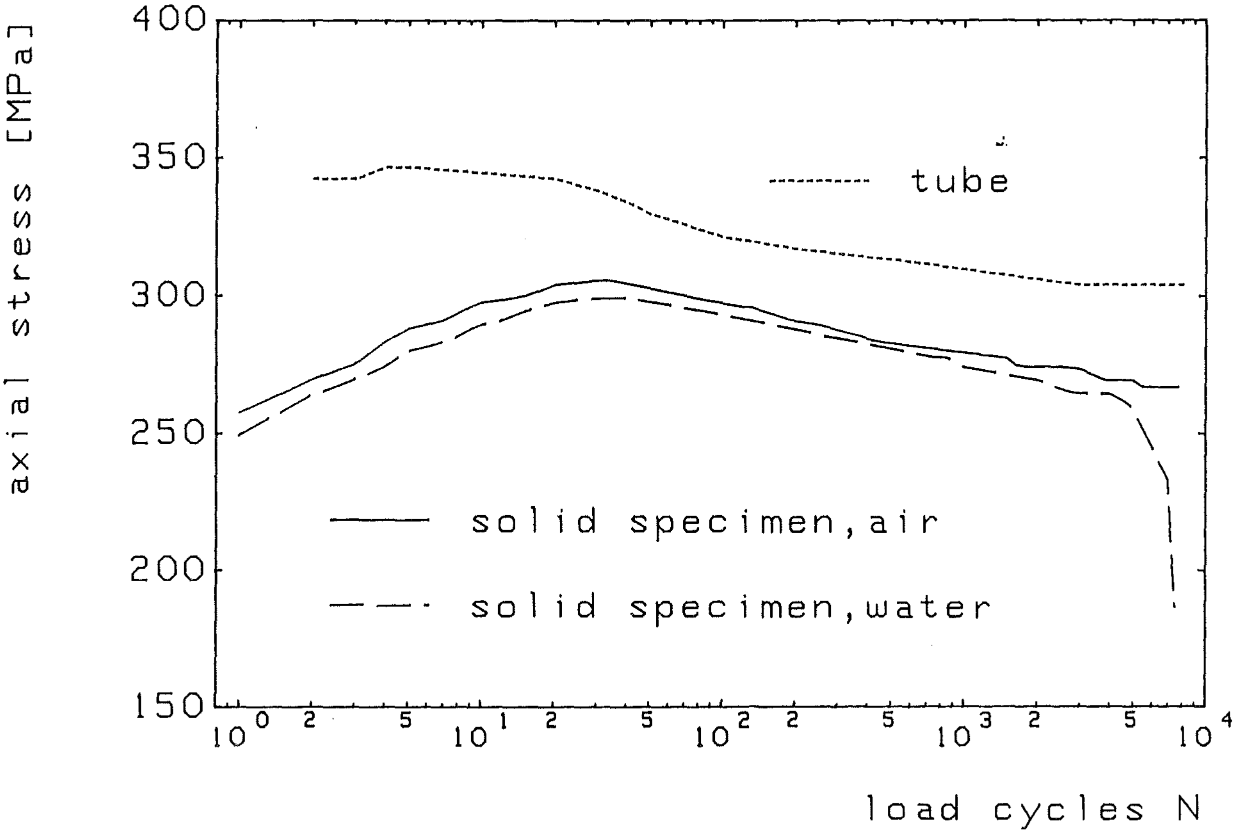

Fig. 6: Comparison of the cyclic hardening of tubes and solid specimens

Fig. 7: Microsections of the investigated 316L SPH material for

a) tubes and

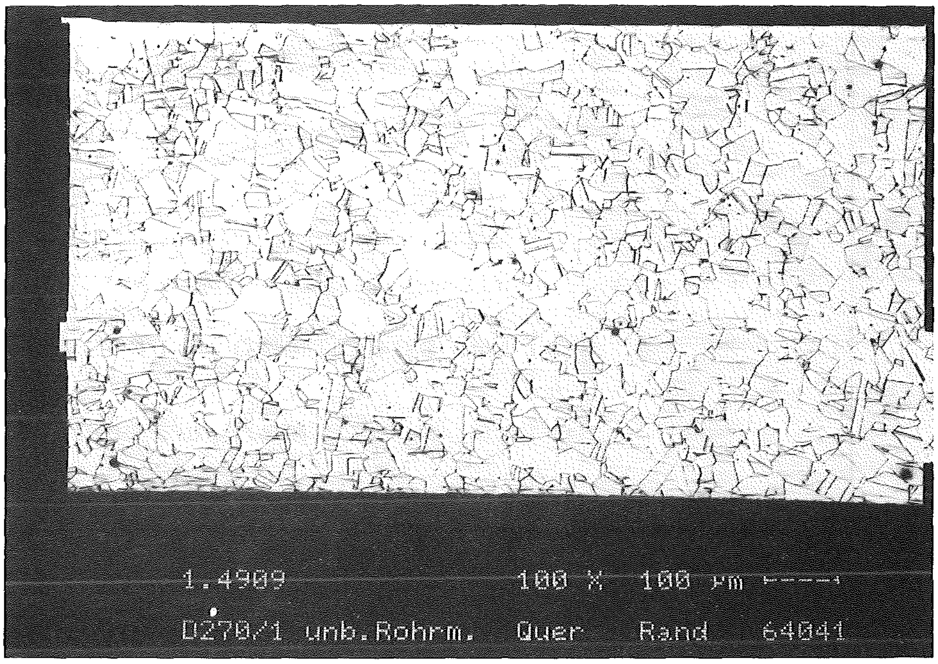

b) plates (solid specimen)

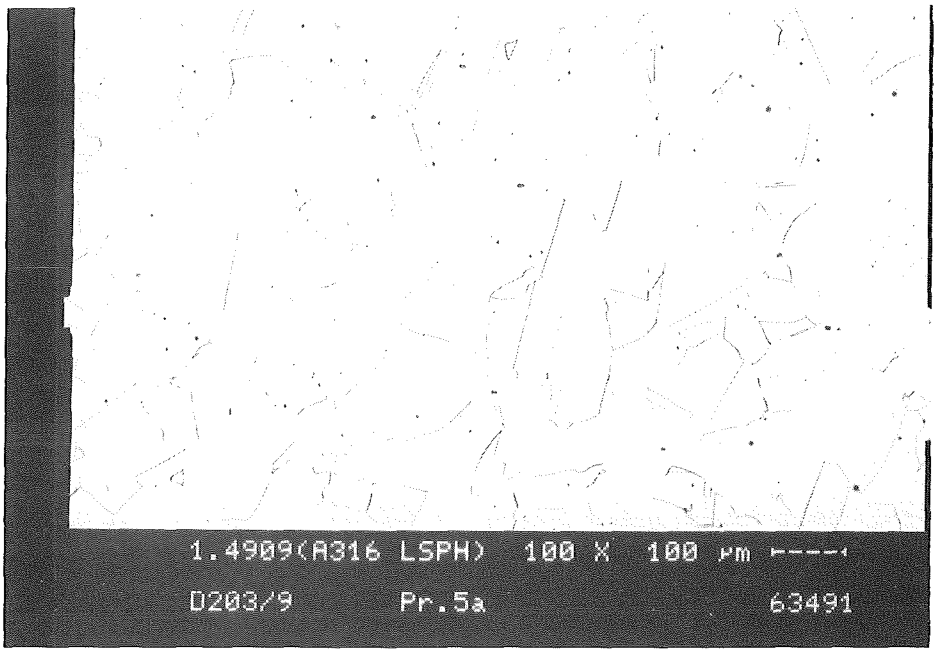

PSM 8 High Emissivity Coatings on 316L

Subtask 1: Development of High Emissivity Coatings on 316L

The objective of this investigation is to develop and examine oxide coatings for the first wall of a fusion device with radiatively cooled protective tiles.

Three promising plasma spray coating types on the basis of Al_2O_3-TiO_2 that were chosen for further comparative tests in the frame of the European fusion technology program have been produced by subcontractors on several different geometrical forms of specimens suitable for thermal fatigue, bending tests and thermal shock tests to be performed under PSM 8.2 and 8.3. The coated specimens were handed to the investigators in KfK and ECN. For the thermal shock test specimens the total normal emissivity was measured at PTB Braunschweig. The values of ε are in the range between 0.85 for APS Al_2O_3-40%TiO_2 and 0.91 for VPS Al_2O_3-13%TiO_2 coatings.

Staff:

A. Skokan

Subtask 2: Fatigue Behaviour of High Emissivity Coatings

To improve the emissivity of the metallic part of the First Wall (FW) a coating will be used. The loading of the FW causes cyclic temperature gradients, cyclic stresses and fatigue. Therefore the coating will be loaded cyclicly, too. The objective of this subtask is to examine different coatings under cyclic thermal and thermally induced mechanical loading similar to FW-conditiones. For this tests tubes made of steel 316L SPH were coated by different laboratories and tested with an experimental set up described in [1].

In the last year tubes with coatings made of CrO_2 (galvanic), Al_2O_3 / 13 % TiO_2 (VPS) with and without an NiCrAlY interlayer, Al_2O_3 / 40 % TiO_2, Cr_2O_3 (VPS) and TiC were tested [2]. The coatings were produced by JRC Ispra, KfK-IMF II Karlsruhe and ECN Petten. The geometry of the specimens is shown in (Fig. 1). The coated specimens can be seen in Fig. 2.

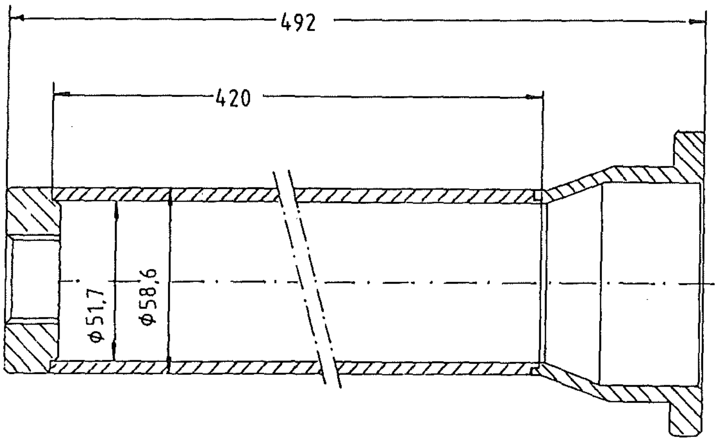

Fig. 1: Specimen made of AISI 316L SPH coated from the outer side

The tubes were heated from the outside cyclicly between 100 °C and 450 °C. On the inner side they were cooled by flowing water to a nearly constant temperature of 50 °C. In specified intervalls the coating was investigated with a microscope and the inner metallic side of the tube was inspected with an introscop. In all cases cracks initiated on the inner side of the tube and propagated through the wall until failure. A damage of the coatings were not observable. At the end of the tests all specimens were cut to investigate microsections of the coatings (Fig. 3). There was no remarkable difference observable between virgin and loaded coatings.

Staff:

F. Haffelder
W. Hartlieb
B. Schinke
B. Windelband
A. Zeller

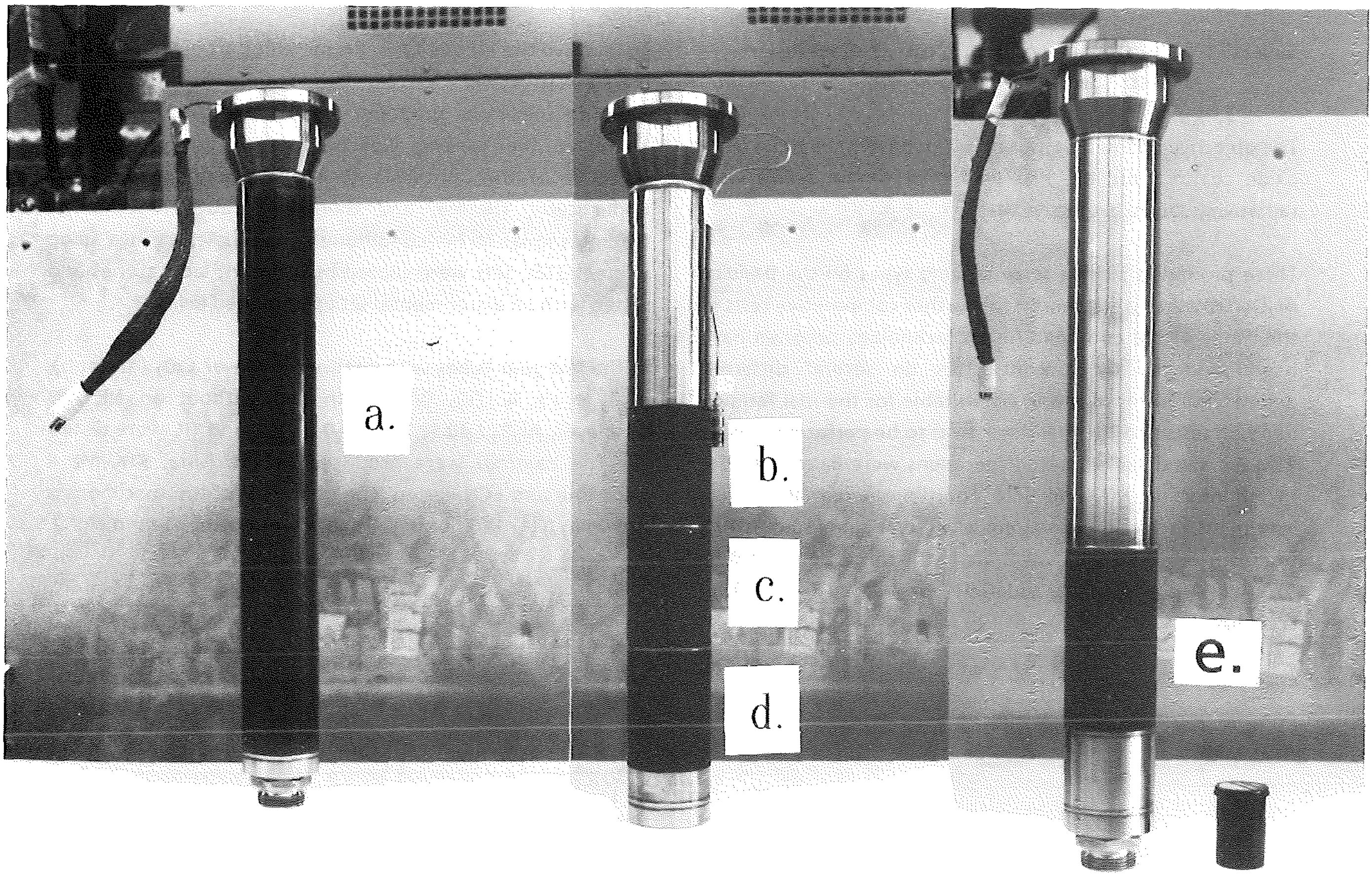

Fig. 2: Coated specimens:
a.) CrO_2 galvanic, b.) Al_2O_3/13 % TiO_2 without
c.) with interlayerd. d.) Al_2O_3/40 % TiO_2,
e.) Cr_2O_3 (VPS)

Literature:

[1] A. Zeller:
Modifikation und Erprobung eines Versuchsstandes zur thermozyklischen Ermüdung von Rohren aus dem austenitischen Stahl 1.4909. Studienarbeit am Inst. f. Zuverlässigkeit und Schadenskunde, Universität Karlsruhe 2/1992.

[2] F. Haffelder, B. Windelband, B. Schinke: Unveröffentlichter Bericht für das NET-Team, IMF II/IZSM, Kernforschungszentrum Karlsruhe 1992.

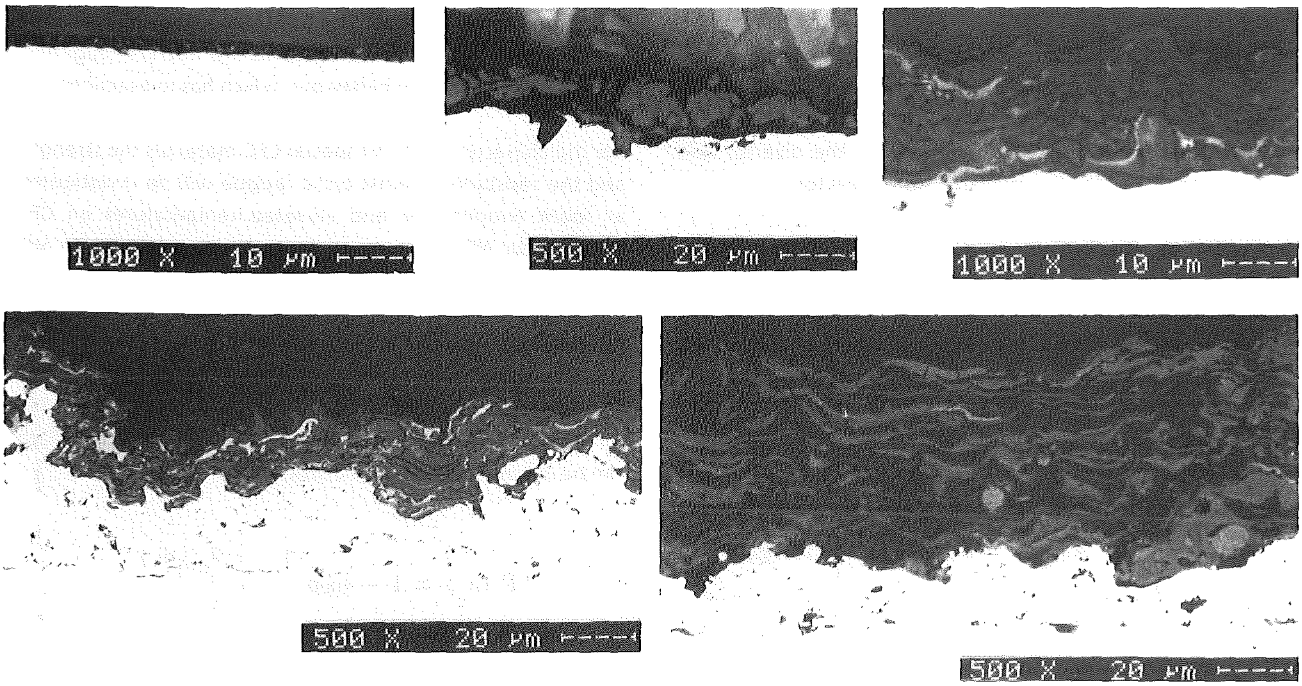

Fig. 3: Microsection of the coatings specified in Fig. 2

PPM 0 Development and Characterization of Graphites and CFCs including Neutron Irradiation Effects

Subtask 3: Development and Characterization of High Conductivity CFC Materials

CFC-materials are candidate materials for the divertor and protecting tiles of the first wall of a fusion reactor.

In order to establish an appropriate data base for the selection of these materials mechanical properties will be investigated. An overview of such material datas is given in Table 1 compiled from R + D reports and KfK measurements

Material producer	Type	Bending strength MPa	Young's modulus GPa
V 1325 Ringsdorff	mono-lithic fine grain	**84 ± 12**	**14.4 ± 0.4**
5890 Carbone Lorraine	mono-lithic fine grain	47	17
A 21 Carbone Lorraine	2-direct. laminate	∥ 133, ⊥ 13	∥ 26, ⊥ 4.8
CF 222 Schunk	2-direct. laminate	∥ 150-200	∥ 70-90
A 05 Carbone Lorraine	"2,5"-direct felt	**∥ 89 ± 13** ⊥ 19	**17 ± 2**
CX 2002 U Toyo Tanso	"2,5"-direct. felt	∥ 45 ⊥ 17	∥ 9
S 148-09 S. E. Propulsion	3-direct. texture	∥ 123 ⊥ 52	∥ 27
N112 S.E. Propulsion	3-direct texture	**∥ 85 ± 7**	**∥ 27 ± 1.5**
FMI 3333 FMI Composites	4-direct. texture	**∥ 79 ± 15**	**∥ 35 ± 7** **⊥ 10.7 ± 1**
S 75 S. E. Propulsion	4-direct. texture	∥ 120 ⊥ 23	∥ 27

Table 1: Mechanical strength of graphite and CFC materials

(It means the direction of strongest fibre reinforcement, the direction ⊥ transverse to that). The fat figures are KfK results; the Youngs's modulus was mostly determined from resonance frequency measurements on rod-shaped samples.

The table shows that one cannot expect much higher fracture strength of CFC materials compared to monolithic graphite of high strength, especially with regard to the comparable transverse strength needed in CFC for fusion reactor application. The exceptionally high strength, particularly in the laminates, are quasi-unidirectional and, moreover, a comparatively high E level (like in CF222) is unfavourable with regard to development of thermal stresses. So the properties of the CFC materials with 3-directional texture seem to offer an optimum compromise. The advantage of these materials over high-strength graphite concerns the fracture toughness and may be the fatigue behaviour, which has to examined.

For the characterization of special CFC-materials the strength and the resistance against cyclic fatigue will be investigated at room temperature and elevated temperatures on CFC delivered by NET. First experiments were performed on SEP N112 and for comparison on FMI 3333.

Mechanical behaviour at room temperature

The first results on bending strength are reported for SEP N112 (Fig. 1) and FMI 3333 (Fig. 2). The bending strength data can be described by Weibull distributions

$$F\ (\sigma_c) = 1 - \exp\left[-\left(\frac{\sigma_c}{\sigma_0}\right)^m\right]$$

where F denotes the cumulative density function and m, σ0 are the Weibull parameters. The material parameters are included in the figures.

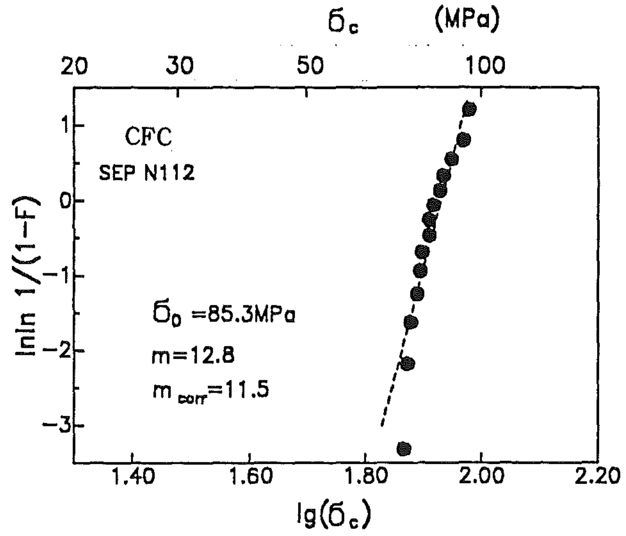

Fig. 1: Bending strength for SEP N112 in Weibull representation

A comparison shows the superiority of SEP N112 because of its low scatter (characterized by the significantly higher Weibull modulus m).

Microstructural investigation with a scanning electron microscope

Corresponding to the deviating mechanical properties the fracture surfaces of SEP N112 (see Fig. 3 and Fig. 4) respectively FMI 3333 (see Fig. 5 and Fig. 6) also show different microstructures.

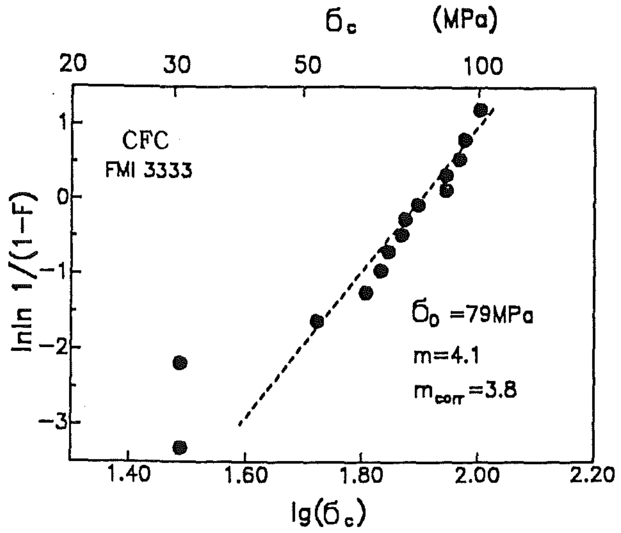

Fig. 2: Bending strength for FMI 3333 in Weibull representation

The SEP material shows a smooth fracture surface with fiber-bundle-pullout of the multidirectional arranged fibers. At higher magnification almost no significant single-fiber-pullout is perceptible but it is possible to discern the different layers of CVI processed matrix.

In contrast to this FMI 3333 sample shows fiber-bundles of very large diameters of about 1000µm. Parallel to the load-direction extensive single-Silament pullout is visible, while the fiber-bundle perpendicular to the load-direction is scarcely delaminated.

Mechanical behaviour at high temperature

To investigate the bending strength at high temperature a high temperature - high vacuum testing device was developed. It is used for the investigation of the strength and cyclic fatigue behaviour of CFC-materials at high temperature and in controlled environment.

The facility (see Fig. 7) consists of a servohydraulic testing machine, which is equipped with a vacuum chamber and a tungsten radiation furnace. The furnace allows testing temperatures up to 2000 °C under vacuum conditions of $p \leq 5 \cdot 10^{-6}$ mbar. It contains a 4-Point-Bending-Fixture with a 20 mm/40 mm span, by which it is possible to measure the specimen deflection with three sticks. The controll of the machine and the data aquistion will be performed with ascomputer.

Staff:

F. Ansorge
W. Dienst
T. Fett
B. Schinke
H. Schneider
G. Thun
H. Zimmermann

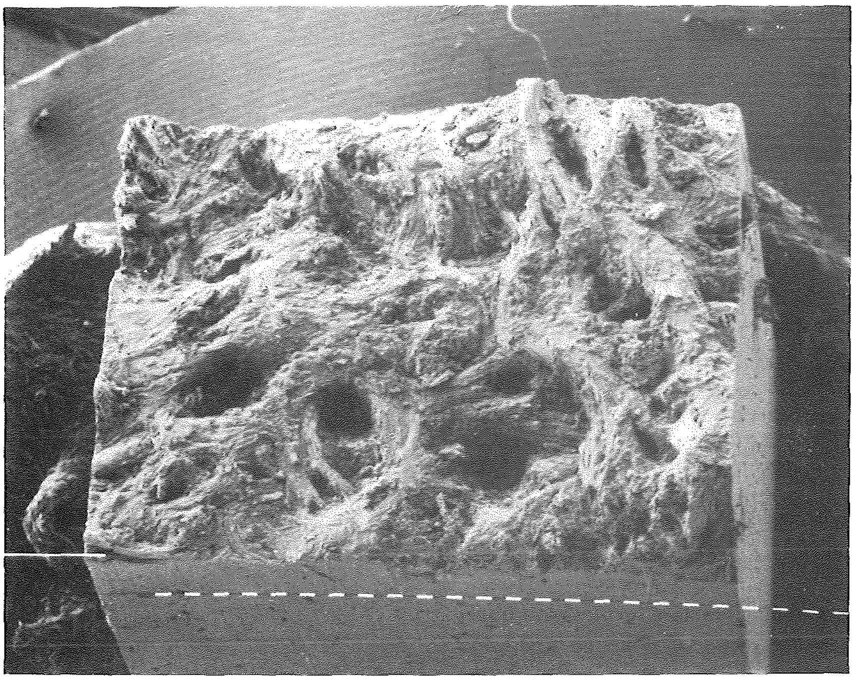

Fig. 3: SEM-photograph of Sample SEP N112 magnification 20 x

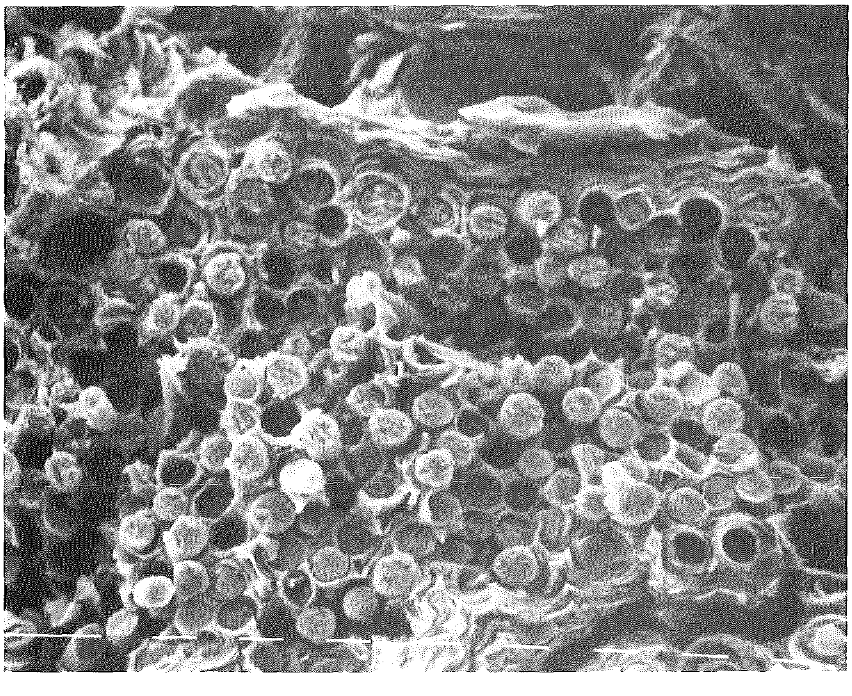

Fig. 4: SEM-photograph of Sample SEP N112 magnification 640 x

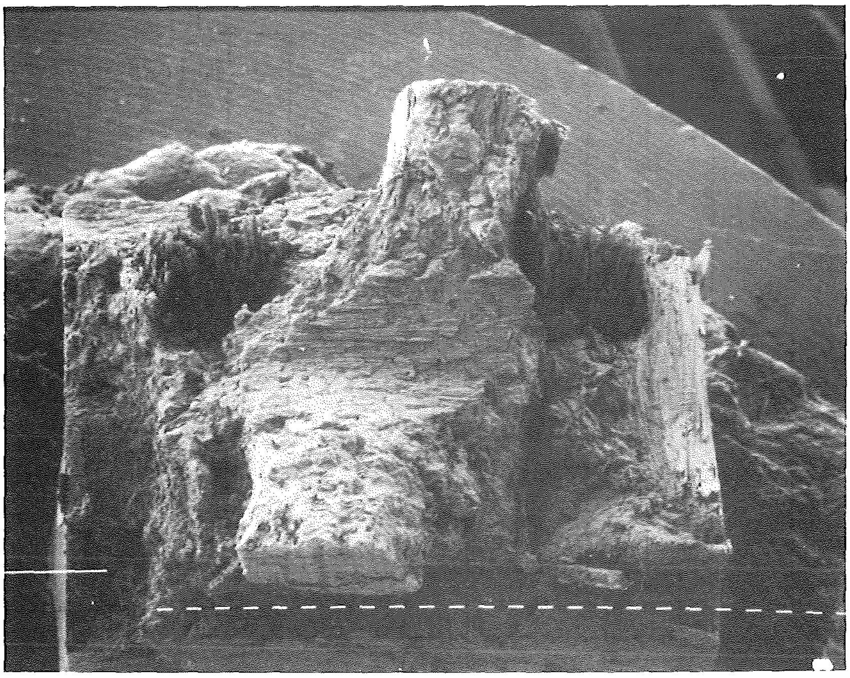

Fig. 5: SEM-photograph of sample FMI 3333 magnification 20 x

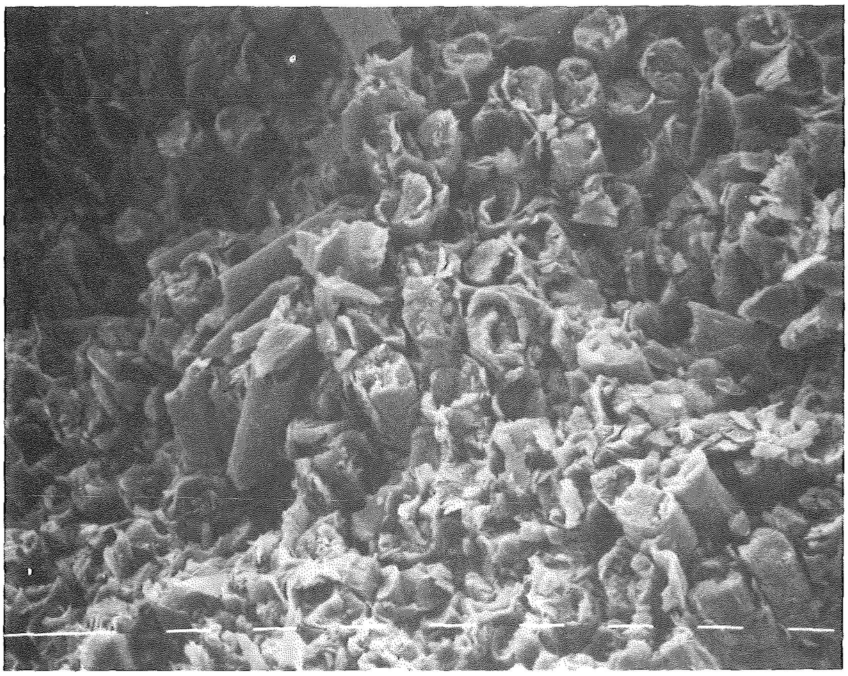

Fig. 6: SEM-photograph of sample FMI 3333 magnification 640 x

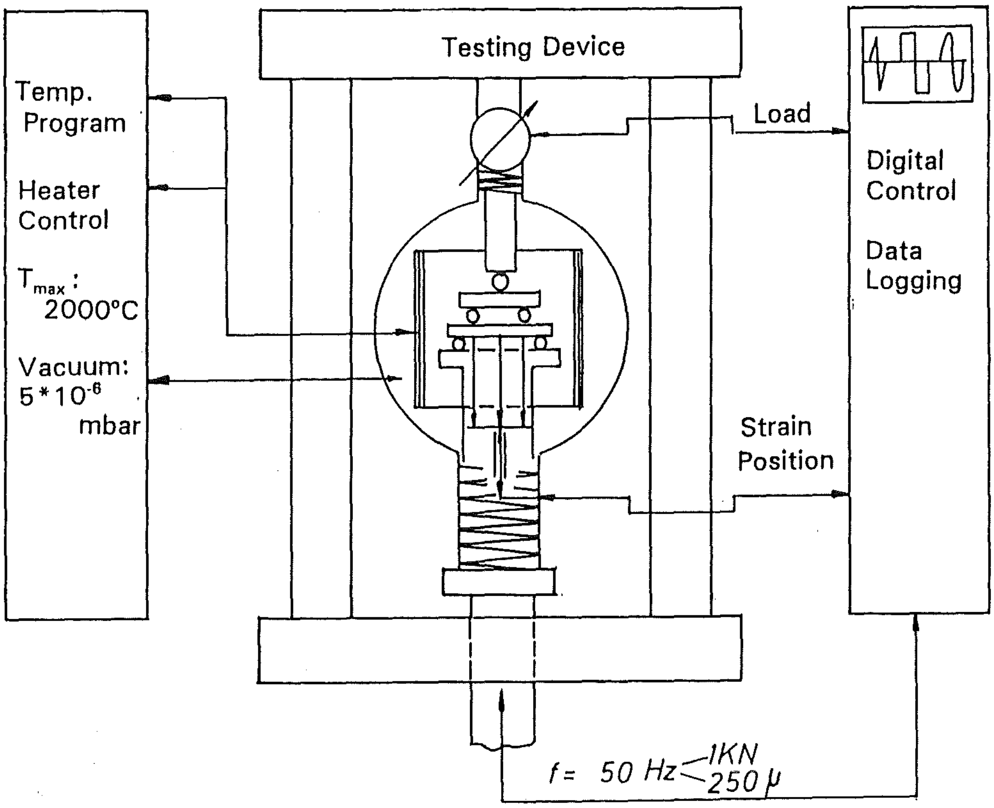

Fig. 7: Schematic scetch of the testing device

PPM 3 Off-Normal High Heat Loads

Subtask 2: Simulation of Off-normal Plasma Material Interactions

Theoretical work for the above task was started recently. The aim is to quantify the vapor shield effect in plasma target interaction and to predict erosion rates of divertor materials for ITER typical plasma disruptions. For simulation the Karlsruhe Target Code KATACO /1/ is used. This is a 1D plasma hydrodynamic code, including beam energy deposition and multigroup radiation transport.

To test and demonstrate the possibilities of KATACO first calculations were performed for a 10 keV proton beam with a power density of 5 MW / cm^2 and a pulse duration of 100 µs impinging perpendicular on an Al target /2/. Magnetic forces at the divertor were neglected and melt front propagation was not considered.

The first results show that vapor shielding is substantially due to radiation back into the cavity. Fig. 1 gives the energy partitioning of the incoming beam energy. About 80 % of the incoming power is radiated back into the cavity during a quasi steady state being established within 20 µs. Material erosion was found to be in the few micron range. The results support the preliminary experimental results obtained with plasma devices in view of a rather effective vapor shield and a rather low material erosion.

For the near future a more accurate and more realistic numerical simulation will be done. The underlying physical models (e.g. with respect to inclusion of magnetic forces and melting front propagation), the basic data libraries (e.g. opacities for carbon, berllyium and tungsten) and the computation tools (inclusion of line radiation transport and 2D hydrodynamics) will be improved.

Literature:

[1] B. Goel, W. Höbel, K. Küfner:
The Karlsruhe Target Code System KATACO, to be published

[2] W. Höbel, B. Goel, M. Küchle, H. Würz:
Numerical Simulation of Vapor Shielding and Range Shortening for Ions Impinging on a Divertor during Plasma Disruptions, 10th Int. Conference on Plasma Surface Interactions Monterey California, March 30 - April 3, 1992, to be published in the Journal of Nuclear Materials

Staff:

B. Goel
W. Hoebel
G. Piazza
H. Würz

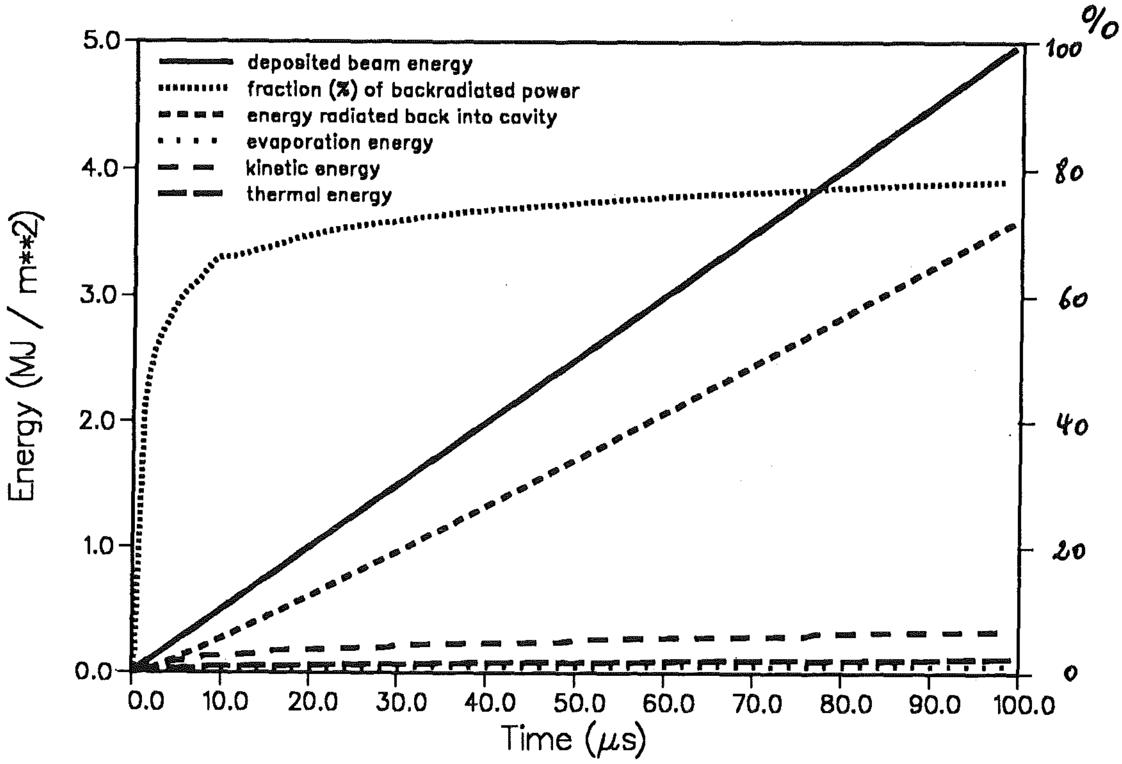

Fig. 1: Energy Partitioning: The energy partitioning is given for a 10 keV proton beam with 5 MW/cm^2 power density. The pulse duration is 100 µs.

PPM 4 Material Characterization and Irradiation Effects in Ceramic Insulators

Subtask 2: Pre-Irradiation Properties of Ceramics at Cryogenic Temperatures

The KfK work on ceramic insulators for fusion applications concentrates on the selection and characterization of suitable materials for windows in Electron Cyclotron systems. The results of the terminated subtask on pre- and post-irradiation properties above 300K proved for the materials under study (Al_2O_3, $MgAl_2O_4$, AlN) that the combination of low dielectric absorption of millimeter wave power and high resistance to thermal crack formation is not sufficient to allow conventionally cooled windows (starting off from room temperature) for transmission of 1 MW/CW power at 145 GHz.

Subtask 2 continues to build up a reliable data base which will guide the outlay of a cryogenically cooled window suitable to high power levels in absence of irradiation and to give first indications on tolerable neutron fluence levels. Even though the mechanical properties, in particular the fracture strength, have shown deterioration in previous high temperature irradiations only at fluence levels of 10^{25} - 10^{26} n/m^2 ($E > 0.1$ MeV) and above, which is at least two orders of magnitude more than the critical levels for dielectric and thermophysical properties, this relation has to be confirmed for low temperature irradiations. Therefore an additional experiment was performed in the HFR at Petten which is considerably lower than the range of enhanced point defect recovery due to interstitial movement above about 0.2 T_m (in K). The maximum neutron fluence was 2×10^{25} n/m^2 ($E > 0.1$ MeV) which is around the threshold of considerable strength decrease of ceramic materials at higher irradiation temperatures. The irradiation capsule contained bending test samples of sapphire, three different qualities of polycrystalline Al_2O_3, Al_2O_3 - 10 % ZrO_2, $MgAl_2O_4$, AlN and SiC (for comparison), mostly 26 samples each. Pellet samples of some materials were included to enable or facilitate measurements of the elastic modules, and perhaps of the thermal shock resistance.

For the most critical parameters, i. e. dielectric loss tangent (tan δ) and thermal conductivity (λ), strong efforts had to be devoted to the experimental installations to make relevant data accessible down to 70 K, and even to 20 K in selected cases. Measurements of dielectric loss at 145 GHz are being performed with a Fabry-Pérot resonator placed in a gas flow cryostat. The system produces a quasi-continuous dielectric data set over the full temperature range of 70 - 300 K. When in routine operation it is fed with liquid nitrogen. With a liquid helium supply, it could be demonstrated that also the range of 30 - 70 K could be covered.

At temperatures below ~150 K, tan δ levels of 10^{-5} have to be quantified. The statistical uncertainties could be reduced under this level. But for different specimens of nominally identical grades, systematic deviations in the observed loss curves appeared, which made the data in the very low temperature range ambiguous. Measurements series under different experimental conditions were started, sapphire was chosen as a reference material. A critical parameter turned out to be the number of half-wavelengths (N_λ) of the millimeter waves contained in the specimen. Extreme cases appeared when the specimen thickness is such that N_λ is integer on the one side and half-integer on the other (Fig. 1a). A critical review of the data evaluation formalisms gave the indication that by omitting one correction factor, the so-called loading factor, virtually fully consistant data sets could be achieved. (Fig. 1b). The basic justification, however, for this procedure is still missing.

Fig. 1: The dielectric loss of sapphire (ordinary ray) at 145 GHz determined in specimens of different thickness (expressed in number of half-wavelengths N_λ)

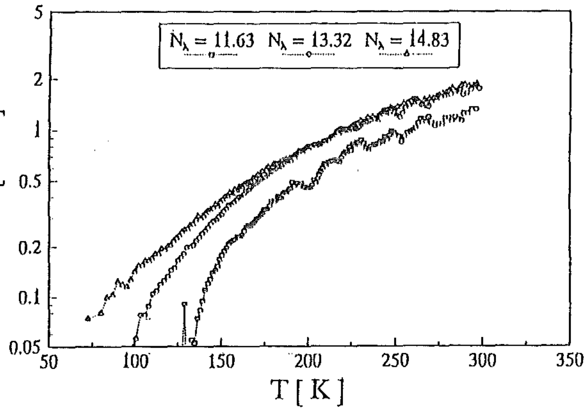

a) evaluation with the loading factor correction

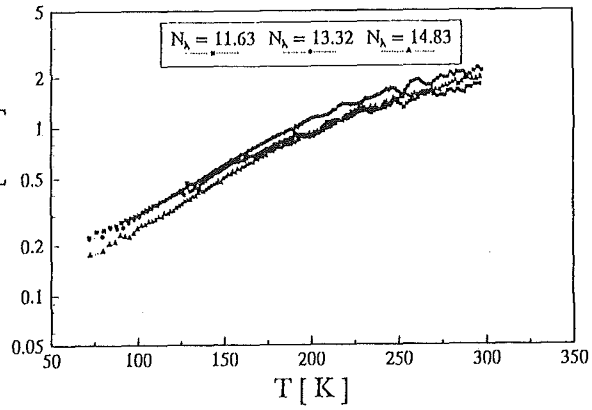

b) evaluation without the loading factor corrrection.

As a major consequence of this alternative empirical data treatment, any indications for tan δ decreasing with decreasing temperature by a law steeper than T^2 disappear in the range of 70 - 300 K. Further experimental evidence was looked for in single crystal (s.c.) quartz which ranks among the lowest loss materials. Indeed meaningless negative loss numbers which resulted from the standard data treatment, were shifted back into the positive sector by the empirical treatment (Fig. 2). Among the polycrystalline grades, special attention was given to a high purity grade (CERATEN 99.99 %) for which good mechanical strength data could be verified together with dielectric loss data corresponding to sapphire, even at temperatures down to 70 K.

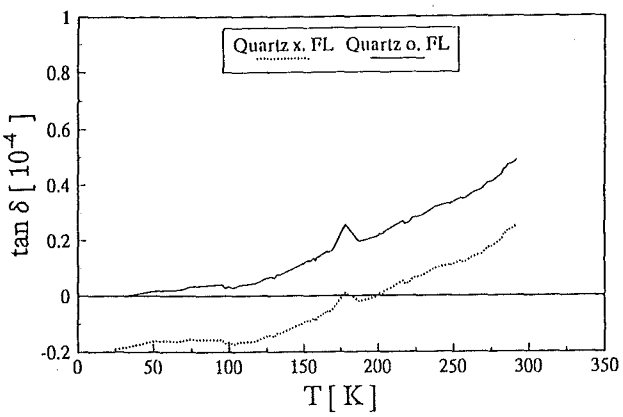

Fig. 2: The dielectric loss of s.c. quartz (ordinary ray) at 145 GHz determined having the loading factor correction omitted (solid line) and included (broken line).

In addition, alternative window materials were looked for in the group of homopolar ceramics. High resistivity silicon, which shows attractive low loss levels at 300 K, was found to be limited by extrinsic conductivity, which did not allow further reduction in loss when cooling down to 70 K. In addition, the extrinsic conductivity and the loss could also be enhanced under purely ionizing irradiation (such as X-rays).

Available sizes reduced the choice of diamond qualities to CVD grades. Two grades from different sources were acquired which have so far shown rather millimeter wave reflection then transmission, presumably, because of admixtures with graphite-like phases.

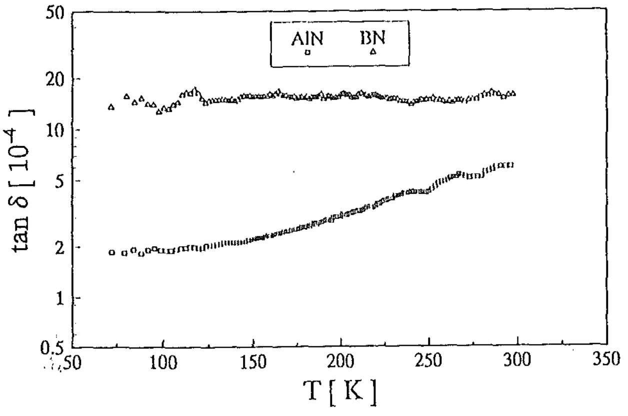

Fig. 3: The dielectric loss of a pyrolytic BN grade and a high thermal conductivity AlN grade (loading factor omitted)

The low temperature behaviour of nitride ceramics was exemplified for the selected grade of AlN and BN. While in BN, the loss and also the permittivity was virtually constant between 70 - 300 K; in AlN, tan δ was reduced upon cooling but a saturation level was reached at about 100K in the selected grade. This level is of the order of $2\text{x}10^{-4}$ for this grade compared to $(1 - 2)\text{x}10^{-5}$ for sapphire at 77 K.

The cryogenic equipment for measuring the thermal diffusivity by the Laser-Flash technique has been installed and tested down to 70 K and its extension down to 40 K is expected. The signal processing of the detected heat pulses is under optimization. The conversion of the thermal diffusivity data into thermal conductivity data requires the parameter sets of specific heat and thermal expansion. While the specific heat data had been measured and reported last year, the determination of the thermal expansion has now been brought to routine operation. The resulting data (Fig. 4) are of primary relevance for modelling the stress profiles in EC wave windows under thermal loads.

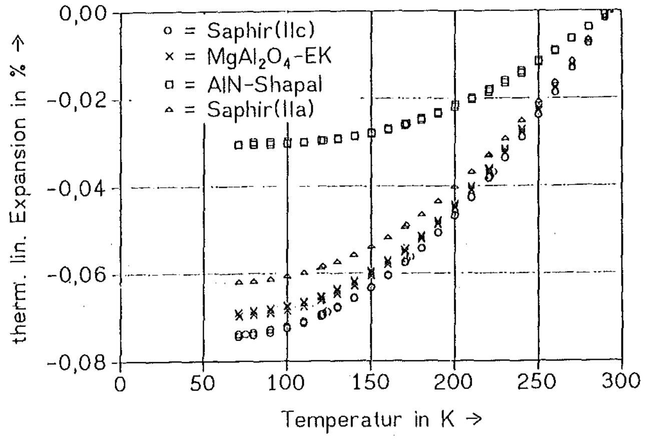

Fig. 4: Thermal expansion of sapphire, s.c. $MgAl_2O_4$ and p.c. AlN (SHAPAL).

The parametrization of low temperature thermal conductivity has been developed and tested for literature data on NaCl, AlN, Al_2O_3, and diamond with the following equation:

$$\lambda^{-1}(T) = \frac{1}{A\,c_p}\exp(-\theta/\alpha T) + C\cdot T + DT^n,$$

where the first term stands for the intrinsic phonon contribution, the second for the influence of point defects and the third for dislocations. Except for the relative weights C and D, all other parameters are characteristic constants for each material, especially: θ = Debye temperature, c_p = specific heat capacity and $n \approx -2$. The relevant parameters for sapphire have been used to extrapolate the room temperature measurements for the available grades to give first approximative thermal conductivity curves at cryogenic temperatures.

Staff:

St. Burghartz
J. Bürkin
W. Dienst
R. Heidinger
E. Katona
G. Link
S. Nazarè
B. Schulz
P. Severloh

Literature:

R. Heidinger, A. Kumlin
The impact of extrinsic conductivity on the mm wave dielectric loss in high resistivity silicon, 16th Int. Conf. on IR + MM Waves, Aug. 26 - 30, 1991, Lausanne (CH), SPIE Vol. 1576, 450 - 1

R. Heidinger, A. Kumlin, A. Ibarra, J. Molla
Increased dielectric loss in high resistivity silicon under X-ray irradiation. 16th Int. Conf. on IR - MM waves, Aug. 26 - 30, 1991 Lausanne (CH), SPIE Vol. 1576, 452 - 3

A. Ibarra, J. Molla, R. Heidinger, G. Link
The temperature function of the anisotropic permittivity of sapphire. 16th Int. Conf. on IR + MM waves, Aug. 26 - 30, 1991, Lausanne (CH), SPIE Vol. 1576, 446 - 7

A. Ibarra, R. Heidinger, J. Molla
New potentials for high mechanical strength grades of polycrystalline aluminum for EC waves windows, 5th Int. Conf. on Fusion Reactor Materials, Nov. 17 - 21, 1991, Clearwater(USA); to appear in J. Nucl. Mat.

G. P. Pells, R. Heidinger, A. Ibarra-Sachez, H. Ohno, S. J. Zinkle
An intercomparison of techniques for measuring dielectric permitivity and loss over a wide frequency range.
5th Int. Conf. in Fusion Reactor Materials, Nov. 17 - 21, 1991, Clearwater (USA); to appear in J. Nucl. Mat.

PDT 1 First Wall Mock-up and Tests

Subtask 4: Thermomechanical Tests on Specimens Protected by Mechanically Attached Carbon-Based Tiles

A test program FIWATKA is planned at KfK for testing first wall (FW) sections in order to:

1. observe the integral behaviour of different FW concepts including protection tiles.
2. provide an experimental basis to improve confidence in the prediction of thermal fatigue life by:
   a) validation of computational methods for
      - thermo-mechanical analysis
      - crack initiation by cyclic plastic-deformations
      - fatigue crack propagation in complicated geometries

   b) lifetime determination including
      - observation during life
      - study of failure modes for prototype FW sections under representative thermomechanical conditions.

The test specimens will be tested under mechanical boundary conditions and thermal loads close to those of a fusion device expect for internal heat sources in the specimens irradiation and for disruption forces.

The specimen will be positioned in a vacuum chamber; it will be actively cooled with water and will be heated by thermal radiation in a cyclic manner.

A resistance heater made of a graphite plate at temperatures up to 2200 °C in vacuum will serve as a heat source. It will radiate heat for a few minutes onto the surfaces of two specimens placed on both sides of the heater plate in a distance of two or three centimeters. The heater power will be turned down periodically for one or two minutes with the result that the temperature profile and the corresponding stress and strain profiles in the specimen change also periodically and cause thermal fatigue.

The start-up operation of the test facility was successfully completed by running at steady state a heat flux of $100^{W}/cm^2$ to each side of the heater for more than can hour; this corresponds to a total power of 375 kW; the heater reached a surface temperature of 2075 °C for the water cooled dummy-specimens without protection tiles that were used (receiving surfaces at low temperature and blackened).

A detailed characterization of the test conditions was started by mapping the heat flux distribution as received in the plane of the specimen surface; a movable heat flux sensor provides a high resolution in the x- and y- directions. The NET specimen TS1 which served before for temperature and strain measurements at JRC Ispra was modified in the header portions and will receive additional thermocouples to measure temperature at the tile attachment studs and of cooling water at inlet and outlet. It then will serve as structural background for experiments with radiatively and conductively cooled protection tiles, as they become available together with their attachment pieces.

Two problems have been investigated within the computational part of the task, namely

1. the effect of a local non-uniformity in the heat flux transmitted to the specimen which might arise from geometrical inhomogenities of the heat source arrangement and
2. studies on mock-ups with modified geometry.

A non-uniformity of the heater power transmitted to the test sample by 5 % locally is reflected in the induced thermal stress and strain fields. The good news, is, firstly, that smoothening, occurs (the stress field is effected by only 3 %) and, secondly, that locations, where the severest stress levels are expected are not altered.

Very often a key problem in code verification is, within the experimental part, the measurability of relevant quantities at representative points with sufficient accuracy.

For the assessment of models of structural elements valuable experimental information would include local stresses, local elastic and, preferably, inelastic strains and finally, detected damage and failure. Stresses cannot be measured directly; on-line measurability of strains with strain gauges is limited to specimen surfaces with low or zero heat fluxes, since otherwise the presence of strain gauges would locally disturb the temperature field and, as a consequence, the strain field to be measured.

Therefore, experiments aiming at such code assessment should be performed with specimens designed to not only have a sufficiently complex geometry but also develop sufficient plastic strain in low heat flux positions. Screening calculations have been performed to specify two adequate geometries for code assessment experiments.

Staff:

E. Diegele
E. Eggert
G. Hofmann
B. Schinke
G. Schweinfurther

PDT 2 Divertor Mock-up and Tests

Subtask 1: Pretests of Bonded Divertor Samples

The testing program on the thermomechanical behavior of candidate divertor and high heat flux components materials involves:

1. Screening tests with bulk materials up to 10^3 cycles
   - a on 31 carbon based materials
   - b on 14 copper and refractory alloys
2. Extended tests with selected materials up to 10^4 cycles
   - a on carbon fiber composites (Aerolor 05)
   - b on copper and copper alloys
   - c on molybdenum and tungsten alloys
3. Tests with bonded samples.

In these tests disc-shaped samples 5 cm in diameter and 0.8 cm thick are exposed to heat pulses of typically Q_O = 15 MW/m^2 absorbed heat flux and t_H = 1 - 2.7 s pulse duration, depending on the desired temperature level. A modified plasma spray facility (PSA) producing an Ar-10% He flame is used as heat source and pulse control device.

During the reporting period emphasis was placed on various types of bonded samples, in which candidate divertor surface materials are brazed onto typical structural materials by use of high temperature braze fillers. In some cases a thin intermediate layer is introduced to bridge the different thermal expansion coefficients of the main materials to be bonded.

In Table 1 are listed the selected material combinations and the individual layer thicknesses, forming a total sample thickness of 8 mm in all cases. Generally four samples of each group have been fabricated and 75 % of the delivered samples have been tested so far. As can be seen the seven material combinations involve basically felt type carbon fiber composites (CFC), A05 and N112, and highly oriented pyrolitic graphite (HOPG) as plasma facing materials. As structural materials the molybdenum alloy, TZM, and the dispersion hardened copper alloy, Glidcop Al25, are chosen. The braze filler is CuTi and TiCuSil with nominal melting ranges of 830 - 850 °C and 1050 - 1080 °C, respectively.

Heating times were chosen with regard to achieving adequate peak temperatures at the braze, tl.e supposedly weakest part of the sample. Since the failure mechanism and threshold were unknown, the following test strategy was adopted: Cycling started out at temperature amplitudes well below the melting point of the braze (corresponding to heating times of 1 - 1.6 s) and then the heating times were successively increased at increments of 0.1 - 0.2 s every 1000 cycles, resulting in temperature increments of about 25 - 50 K. Once the braze temperature approached the melting temperature to within about 100 K, the strategy was changed: part of those samples were continued at fixed heating times, just accumulating cycles, whereas others were operated at further increased heating times until melting temperatures were reached or even exceeded. For samples P39 with the Glidcop as substrate the decisive temperature was the weakening temperature of the copper alloy ($\simeq$ 600 °C) rather than the melting point of the braze.

Sample Name	Surface (4 mm)	Braze 1 (0.2 mm)	Inter-layer (1mm)	Braze 2 (0.2 mm)	Heat Sink (bal-ance)
P37-*	A05	CuTi	-	-	TZM
P38-*	A05	TiCu-Sil	-	-	TZM
P39-*	A05	TiCu-Sil	TZM	TiCu-Sil	Glidcop Al225
P40-*	N112	CuTi	-	-	TZM
P41-*	N112	TiCu-Sil	-	-	TZM
P42-*	HOPG	TiCu-Sil	-	-	TZM
P43-*	HOPG	TiCu-Sil	A05	TiCu-Sil	TZM

Table 1: Brazed samples material combinations

Figure 1 shows, as an example, the history of the best estimate temperature amplitudes at the braze. Plotted are mean values and standard deviations pertaining to coherent cycle sequences. In this case the braze temperature oscillated between 100 and $\simeq$ 750 °C in the beginning and then increased gradually to between 125 and $\simeq$ 1000 °C as the heating time was extended. There is a substantial scatter in

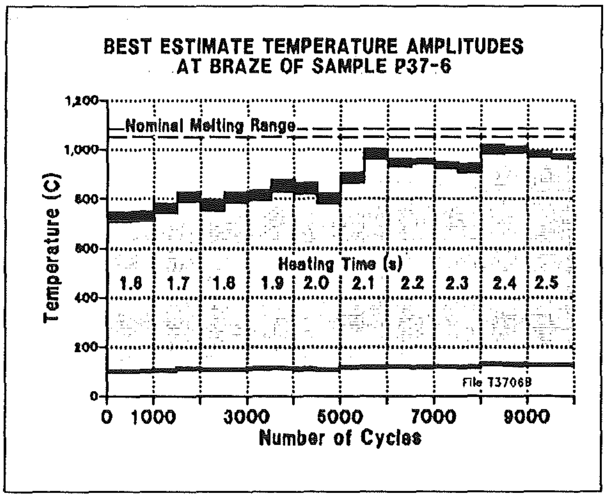

Fig. 1: Best Estimate Temperature History at Braze of Sample P37-6.
The braze temperature oscillated within the shaded area. The black ranges at top and bottom of the shaded area represent the standard deviations of the extreme values.

the upper mean values, caused mainly by noncontrollable wear of the plasma gun.

Table 2 gives a summary of heating times, accumulated cycles, peak temperatures, and calculated peak stresses obtained for each individual sample. Tests and post test examination are still in progress and a first summary will be published in [1]. Preliminary results can be stated as follows:

Sample Name	Heating Time (s)	Accu-mulated Cycles	Peak Temper-ature (°C) Braze1/2	Peak Stress Ampli tudes (MPa)
P37-6	1.6-2.5	10003	1000/-	432
P37-11	1.6-2.7	10004	1020/-	435
P37-12	1.6-2.5	10004	1030/-	432
P38-2	1.4-2.0	5009	890/-	419
P38-3	1.4-1.8	3009	920/-	408
P38-4	1.4-2.0	5010	910/-	419
P39-1	1.0-1.3	10000	660/620	603
P39-2	1.0-1.9	10000	800/760	750
P40-2	1.6-2.5	10003	910/-	474
P40-3	1.6-2.7	10004	970/-	485
P40-4	1.6-2.5	10003	910/-	474
P41-1	1.4-2.0	7010	810/-	443
P41-2	1.4-2.5	7010	860/-	474
P41-4	1.4-1.8	3009	810/-	378
P42-2	1.2-1.5	10000	680/-	380
P42-3	1.2-2.7	10000	980/-	520
P43-4	1.2-1.5	10000	710/680	416
P43-5	1.2-2.7	10000	910/880	542

Table 2: Brazed samples test conditions

- All samples (except sample P39-2) survived the tests without mechanical failure and without significant change in the thermal response.

- The thermal contact between the plasma facing material and the substrate remained intact, despite the fact that the nominal braze melting temperature (which might not be identical with the solidus temperature of the actual braze alloy) had temporally and locally been reached or exceeded in several cases.

- The brazing technique applied by Plansee, i.e., burning cone-like craters into the carbon fiber composite, and the choice of the braze materials, have proved to give a resistive bonding, at least in this laboratory type fabrication route with, presumably, a relatively high refuse rate.

- The CFC materials A05 and N112 don't show any evidence of cycle damage at peak temperatures up to 1200 °C. This is in agreement with results of the bulk material tests [2]. Both materials are equivalent in terms of their thermal response, in particular with view to conductivity.

- First destructive examination indicate formation of voids at the roots of the braze filler cones, once melting is reached. In regions of no melting, transverse cracks through the cones and recristallization of the braze filler had been found, but no substantial braze filler migration.

- Finite element stress analyses indicate that the stress component in and perpendicular to the braze layer is generally small (a few MPa) and compressive. For the P39 samples with the Glidcop Al25 substrate, however, this stress component is tensile (0 to ≃ 10 MPa) tending to cause separation.

- Peak equivalent stress amplitudes (v. Mises) in the TZM substrate (elastic analysis) range between 380 and 540 MPa. This is beyond the yield strength but less than twice the yield strength. Hence, progressive plastic deformation due to ratcheting or shake-down is not expected and has not been observed in the tests. (Measured deflections range between -10 and +20 µm, where positive values mean a bulging towards the heated side.)

- Peak equivalent stresses in the Glidcop Al25 is calculated to be far in excess of the yield limit. Thus an elastic-plastic analysis is needed here. A long crack in the substrate and progressive plastic deformation have been observed at sample P39-2 with the long heat pulses.

Literature:

[1] K. Kleefeldt, K. Schramm, C. Strobl:
Thermomechanical Cycle Tests on Bonded Divertor Materials in a Plasma Spray Facility, to be published at the 17th Symposium on Fusion Technology, Rome 14-18 September 1992

[2] K. Kleefeldt, K. Schramm, C. Strobl:
Unpublished Report of KfK.

Staff:

G. Class
K. Kleefeldt
K. Schramm
C. Strobl

Superconducting Magnets

Introduction:

The confinement of plasma in ITER/NET relies on a superconducting magnet system consisting of 16 D-shaped toroidal field coils, a central solenoid to drive the plasma current and a set of poloidal field coils for plasma stabilization. KfK is together with the NET team and other associated European laboratories involved in the development of these magnet systems. It develops technical conductors up to industrial production feasibility. Components of these conductors, subsize conductor assemblies and test coils are examined for their performances. Materials to be used in coil construction are qualified for their application under cycling load. Cryogenic loops and components are developed to establish stable forced flow conditions to cool the magnets. An important task consists of upgrading the existing large magnet test facility TOSKA to test model coils made out of different industrially manufactured conductors.

The safety of superconducting magnets is analyzed by code development and by experimental studies of effects, potentially initiating a sequence of events leading to an accident.

MCON Full-Size 40 kA Conductor

Subtask 3: I_c Characterization and FBI Upgrade

The aim of the sub-task is the critical current characterization of Nb_3Sn strands and subcables under the effects of field and external strain in the high field test facility FBI. The task is funded in the 1989-91 program. It is still continued caused by difficulties in the strand fabrication combined with delay in delivery.

For the high field test facility FBI a new 14 T magnet was ordered. The design and the preparations for fabrication are running at Oxford Instruments, England. The existing 12.5 T magnet had a malfunction which led to a burn out at the joint to the outer most pancake. The magnet was repaired by KfK rewinding the damaged layers and a new joint was made. The magnet was tested and reached its field and ramp rates. Thus the FBI facility is ready for testing.

A LHe transfer line is designed and will be ordered in July 1992.

The delivery of the ENEA sample being still open, the CEA sample will be expected in July 1992.

Staff:

H. Kiesel
W. Specking

MTOS TOSKA Upgrading for Model Coil Testing

Subtask 1: Preparation of the TOSKA Facility for the Test of the NET/ITER Model Coil

The aim of the task is the upgrading of the TOSKA facility for testing ITER model coils. An intermediate step is the testing of the LCT coil at 1.8 K up to 11 T field level in the task MBAC. Useful basis component developments and testing methods which can be transferred later on to ITER model coils and test procedures are running in the Polo project (previous tasks M4, M8 and MTOR).

A highlight was the installation and the starting of the commissioning phase of the new 2 kW refrigerator. Other activities were the conclusion of a specification and requirement for the TOSKA facility in joint collaboration with the NET team. The development of components for the TOSKA upgrade facility runs presently in the Polo project (e.g. current leads) and the task MBAC (e.g. helium pumps).

1. The New 2 kW Refrigerator

The installation of three important components namely the coldbox, the valve box and the 10 000 ℓ liquid helium storage dewar were already concluded at the end of the last reporting period. As the last large component the three sets of screw compressors were installed in the sound-proof cage (Fig. 1.1). Also two He buffer vessels of 80 m^3 volume each were installed. They are switched in a suitable way between the suction and the discharge side of the compressor sets to be able to store the required pure gas for starting and even for storage of gas of a cold experiment.

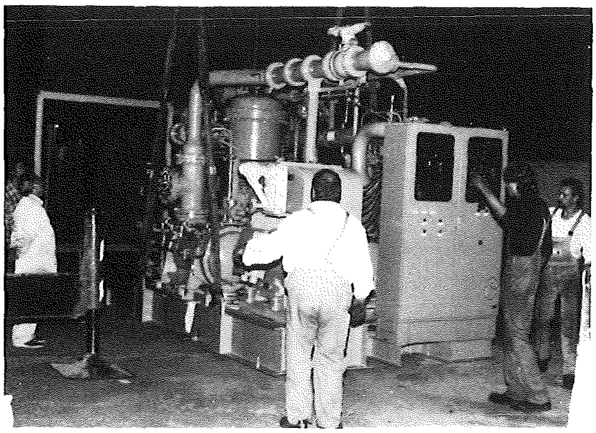

Fig. 1.1: A compressor set during lifting in the sound-proof cage

The plant is completely controlled and monitored by the high performance industrial process controll system SIEMENS TELEPERM M. The structure and main components of the system are shown in Fig. 1.2. All required functions such as automatic control, remote manual control, safety actions, data storage, and data handling are realized with this system, except some hard wired safety functions on compressors and turbines. There is also the possibility to link with the test facilities via the remote bus system (CS). The three automation systems (AS) in conjunction with the bus system are capable of performing all functions required to control the whole process. Two independent operator communication and monitoring systems (OS) offer acces to all components and data of the plant. An information system (IS) enables handling of the acquired data in several ways, e.g. to create central leading functions. The engineering system (ES) allows to configure the automation systems on-line and to generate self documentation.

Since delivery of the cold boxes in beginning August 1991 eight months af assembly and checks were necessary to have the first cool down in the end of March 1992. The uninsulated cold boxes are tested at low temperature to an overall tightness of better than 10^{-7} mbar l/sec. After insulation work an repeated cool down, first tests concerning both the pure liquefaction capacity of 9 g/s without LN_2 precooling and the "Basic capacity" (refrigeration capacity: 700 W at 3.3 K, 400 W at 4.4 K, 1000 W at 70 K; liquefaction rate: 4 g/s at 4.4 K; electric power consumption of the compressors 840 kW) showed preliminary results. Performance tests with highly accurate, calibrated instrumentation are presently under progress.

2. Specification and requirements for the TOSKA facility

The design of possible arrangement of model coils fabricated from different conductor types allowed a more detailed check of the requirements for testing the model coils in the TOSKA facility [1].

Test program: Besides the exploration of the magnet characteristic with its electrical, mechanical and thermohydraulic properties the testing with simulation of typical feedbacks of the plasma and the nuclear process (plasma ramp up, plasma disruption, divertor sweeping, nuclear heating) was emphazised in the test program.

Cryogenic power: For the estimation of the heat load a flow sheet for the supply system of the model coils was designed (Fig. 2.1). The supercritical helium mass flow is circulated by a pump across a heat exchanger immersed in a liquid helium bath and therefore completely decoupled from the refrigerator helium flow. Also a test pancake supplied by the old Linde refrigerator can be operated at a 1.8 K according to the same principle described before. Pump development and tests are described in task MBAC.

The different heat loads coming from the different components of the facility are summarized and balanced against the available refrigeraton capacity in Tab. 2.1 for steady state operation mode. Besides this also the cooldown, warmup and system disturbances by quench have to be controlled. During cooldown/warmup an energy of E = 11 GJ (10 GJ between 300 K to 80 K and 0.07 GJ between 80 K to 5 K) is removed/added in a controlled manner within temperature difference less than 30 K keeping the thermal stresses within their limits. For the cooldown operation the refrigerator is equipped with a LN_2 heat exchanger for getting sufficient cooldown power to cooldown the coil stack in about 150 h. Quenchs of coil sections can be handled with cold gas storage and the recovery system. For larger accidents a stepping of relief valves and burst discs protect the system. A cold line with valve box connecting the new 2 kW refrigerator with the TOSKA facility was odered. The design of the line is being discussed with the manufacturer.

Current leads and superconducting bus bars: A carefully developed current lead is indispensible for the successfull operation of the facility. They consume with their warm gas flow (Tab 2.1) a considerable part of the cooling power.

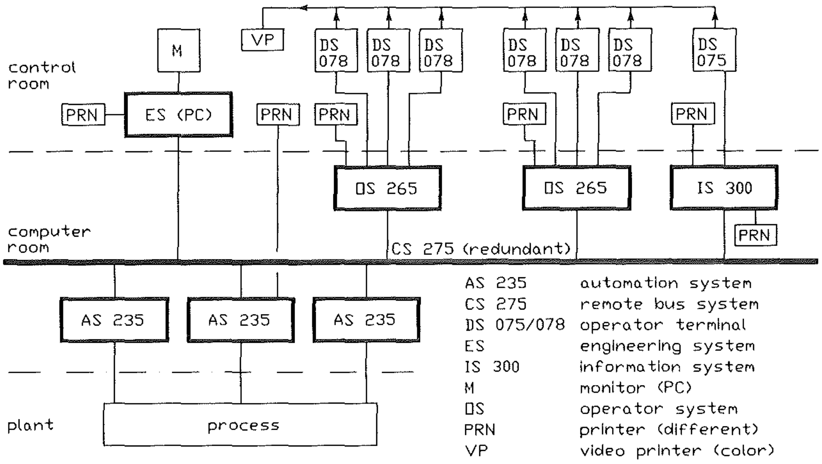

PROCESS CONTROL SYSTEM (SIEMENS TELEPERM M)

Fig. 1.2: The diagram of the process control system

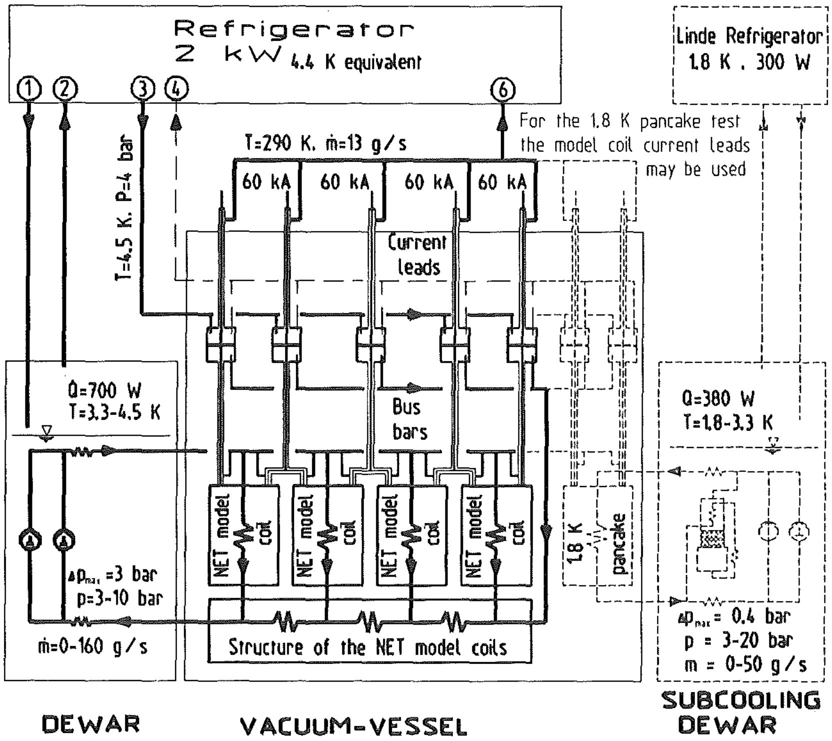

Fig. 2.1: Flow diagram of the cryogenic system for the test of ITER model coils in TOSKA

Winding		
Mass flow rate	[g/s]	140
Operating pressure	[bar]	6
Pressure drop (5 g/s / channel)	[W]	0.2
Pumping power	[W]	50
Heat load sc-joints at coils	[W]	198
Case and support structure		
Heat input	[W]	50
Mass flow rate		> 10
(in series with winding)	[W]	
Current leads (5 pieces)		
Nominal current	[kA]	60
Warm gas flow rate (3 x 60, 2 x 0 kA)	[g/s]	13
Cold flow through superconducting buses	[g/s]	20
Heat load sc-bus joints	[W]	40
Facility		
Heat load in dewar, valves etc.	[W]	200
Radiation and conduction to coils	[W]	47
Total refrigeration capacity at 4.5 K		
Available with 13 g/s warm flow	[W]	850
Needed	[W]	535
Available margin	[W]	300

Table 2.1: Cryogenic heat load of the TOSKA facility

The operational requirement are summarized in Tab. 2.2. The current lead developed within the Polo project (see 3.) is a intermediate step in this development. Calculations for extending the 30 kA Polo current lead were performed and showed that the same heat exchanger can be used at 60 kA if the length is adapted and warm end is equipped with a heat exchanger for more effective cooling [2]. The current have to be fed into the model coil stack from the current lead across a superconducting bus. An extensive parameter study about the superconducting bus was performed to investigate the boundary conditions and requirements [3]. The volume in which the buses run has field levels from 6 T to 2 T. Therefore NbTi can be used. The contact resistance at the bus joint has to be kept below 10^{-9} Ω to obtain sufficient margin to the current sharing temperature. The analysis leads to the following results. A high cross section of copper leads to safe operation in the case of loss of flow but the bus cannot stay superconducting during a dump or transient test conditions of the coil. The investigation showed that optimization between losses and the loss of flow is necessary and depend on the specified test conditions. The AC losses have to be very similar to coil conductor taking into account that NbTi material is used.

Power supply system: A switching system similar to those of the Polo project was elaborated by the NET team using a combined operation of the 30 kA and 50 kA power supply. A third power supply is used for sweeping a steady state current for simulating nuclear heating. All other transient tests will be performed by discharges of coil sections. The circuit is being discussed with experts to find the best way for realization and reliable operation.

Design Current	60 kA
Design Voltage	20 kV
Overload current for 2 sec	70 kA
Cooling flow at design current	≈ 3.3 g/s
Cooling flow at zero current	≈ 1.7 g/s

Table 2. 2: Operational requirements for the current leads

Instrumentation, control and data acquisition: Different sensor types and their signal conditioning were specified. 84 sensors require an isolation to ± 20 kV and 397 sensors to ground. A total of 513 channels will be needed. The cooldown/warm up will be performed computer controlled. The quench detection system has to be interact with triggering of the data acquisition system and control function with the cryogenic supply system. Presently it is being investigated to use for the programmed logic controllers and the signal conditioning the same digital bus to avoid a doubling of sensors.

Assembly of the model coil in TOSKA: The space limitations in the vacuum vessel require the lifting of the whole coil stack in the vacuum vessel. Therefore the installation of a second crane bridge with a lifting capacity of 70 t is necessary for getting a total lifting capacity of 120 t included a suitable lifting gear. Other solution e.g. a truck crane needs an opening of the building roof which is more expensive for mutiple lifting procedures.

TOSKA organisation and operation: The contruction of the model coil has to be performed in tight contact with KfK to assure that all coil interfaces fit to the specifications of the TOSKA facility.

3. The Polo project

The Polo project was started in the previous task M4 to develop the technology for poloidal field coils of tokamaks. It should be demonstrated in task M8 later on MTOR (outer poloidal field coil for TORE SUPRA) that the developed technology is suitable for application. The conductor is the first long length conductor produced with a fusion conductor like stainless steel jacket. Most of the components developed can be immediately used or they are an intermediate step in the development for the ITER model coils like insulators, feedthroughs, current leads, instrumentation cables etc. because the nominal voltage of the Polo coil and the model coils are nearly the same. The testing technique used for the Polo model coil to generate transient fields changes is intended to be applied also for the ITER model coils. Therefore the project can now be considered as a precursor of the model coils developing most of the components which are independent from the Nb_3Sn technology.

3.1 Conductor stability

The stability model elaborated shows good agreement with measurement performed on the Polo conductor (Fig. 3.1). The model assumes that for short disturbances (some ms) in the supercritical helium the heat transfer take place by diffusion. The stability limit can be calculated for different shapes of magnetic field pulses by the solution of the one dimensional heat diffusion equation with boundary conditions.

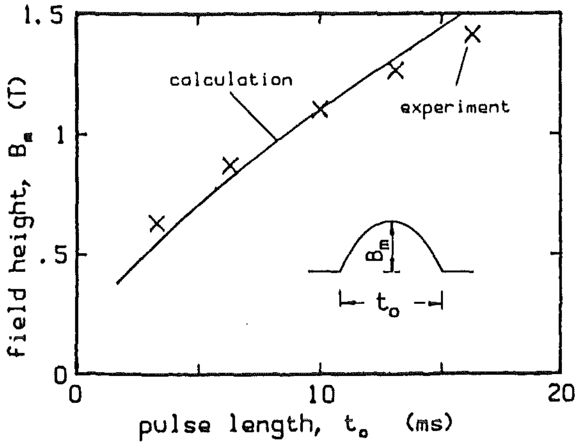

Fig. 3.1: Comparison of the measured and calculated stability limit according to the stability model for a sine like field pulse (stability experiment Polo conductor).

Fig. 3.2 shows a calculation for a sine like magnetic field pulse. The temperature profile caused by the heat dissipation of the magnet field pulse was calculated for a field pulse below and above the stability limit. The exceeding of the current sharing temperature generates additional Joule heat which is shown also in Fig. 3.2 for quench (q) and recovery (r). The dotted temperature profile was calculated without Joule heat for comparison.

The measured pressure increase in the stability experiment of the Polo conductor showed good agreement with the calculated pressure increase with a computer code developed by the Moscow Power Engineering Institute. Therefore the computer code was adapted to the Polo conductor in the coil and the pressure increase in the middle of a pancake was calculated with the quench propagation velocity as parameter (Fig. 3.3).

3.2 The fabrication of the Polo model

Since about one year the fabrication of the Polo model is running by GEC-Alsthom in Belfort, France. The winding facility (Fig. 3.4) was suitable with some additional equipment to wind the Polo conductor with the stainless steel jacket in double pancakes. Suitable tools were constructed and tested to bend the transition (Fig. 3.5) between the upper and the lower pancake at the inner most turn and in the connection area (Fig. 3.6). Further bends of 300 mm radius are necessary to bring the conductor together in the joint boxes (Fig. 3.7). The conductor was bent within the tolerances needed

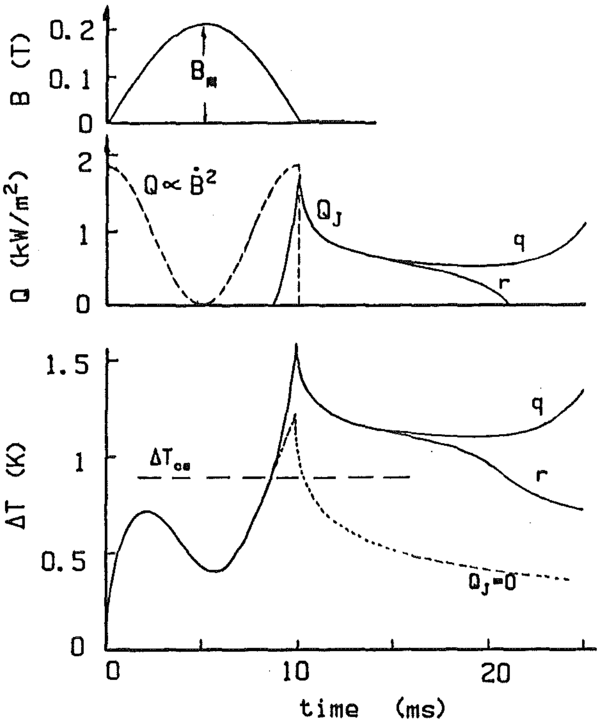

Fig. 3.2: Magnetic field pulse, losses Q, Joule heat Qj and temperature profile for a cosine square like disturbance of slight different energy
q: quench of the superconductor
r: recovery of the supercoductor

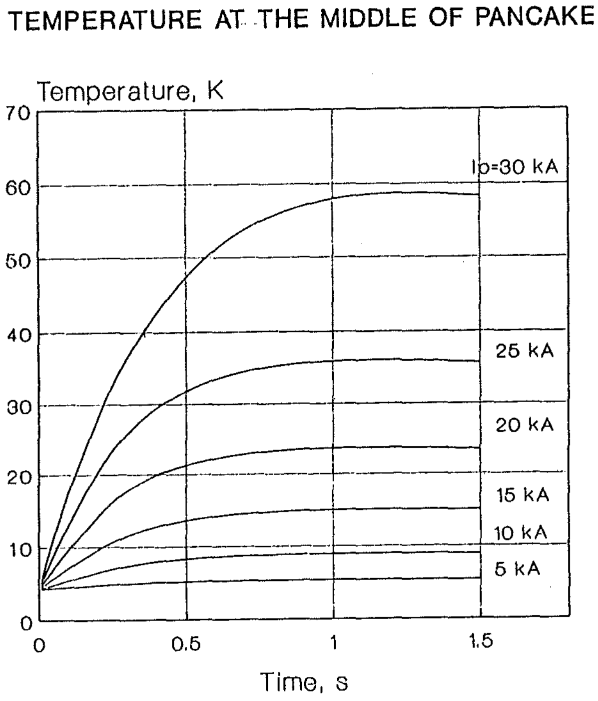

Fig. 3.3: Pressure increase after a quench at different currents in the middle of a double pancake of the Polo coil. The calculation was performed with a computer code of the Moscow Power Engineering Institute.

without problems. Each pancake was leak tested after winding and after the performance of the bend. Electrical and geometrical measurements were performed to assure the quality of the insulation system and the geometrical shape. For the manufacturing of the joints the jacket was dismantled. The subcables were opened to bring out the secondary cooling channel (two phase helium) (Fig. 3.8). Each subcable of one pancake were soldered in an overlapping joint with the subcable of the other pancake. Joints and subcables were fixed in grooves of a fiberglass reinforced epoxy cylinder. Three subcables were soldered in an overlapping joint in the center joint of the coil so that both halfs of the coil can be operated independently with full current. The joints were instrumented by voltage taps and temperature sensors and enclosed in a cylindrical stainless steel box. The feeding for the cooling circuits are insulated against the helium supply system at ground potential across axial insulation breaks (fiberglass reinforced epoxy). The instrumentation wires are brought out by a leak tight multipin feedthrough (Fig. 3.9). The winding was carefully enclosed by covering plates, was set in the mould and fastened with wedges. The area of the joint boxes (Fig. 3.9) was filled by a mixture of glasfiber fabrice and sand. Fig. 3.10 shows the coil in the mould before filling the connection area. All joint boxes were leak tested. After a pressure test at 25 bar the whole coil was again leak tested. After a repairment of one at the insulation breaks the coil was tight. The final preparations for impregnation are running.

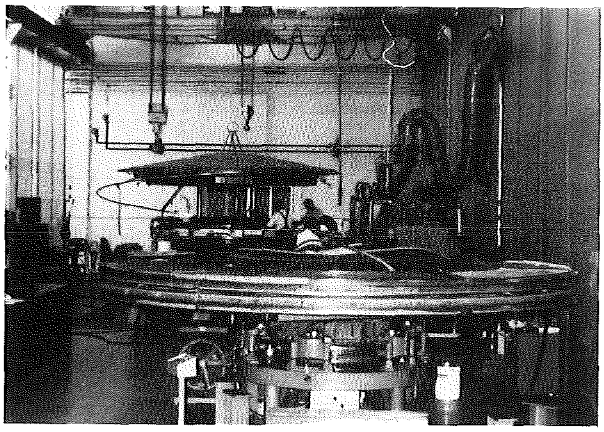

Fig. 3.4: Winding facility for the Polo model coil. In front the brake table with the Polo conductor reel. In background the winding table with reserve reel for winding the upper pancake (GEC Alsthom, Belfort).

3.2 Special developments and investigations for high voltage components

Seven high voltage multiwire instrumentation cables with a vacuum tight feedthrough connector at the vacuum vessel wall were assembled, tested and delivered to GEC-Alsthom for connecting them to instrumentation feedthroughs at the joint boxes. An axial insulation break for outlet of the warm helium gas was designed, constructed and successfully tested at a helium pressure of 0.1 - 1 MPa up to 23 kV (Fig. 3.14). The breakthrough voltage at 0.1 MPa was measured at 35 kV AC.

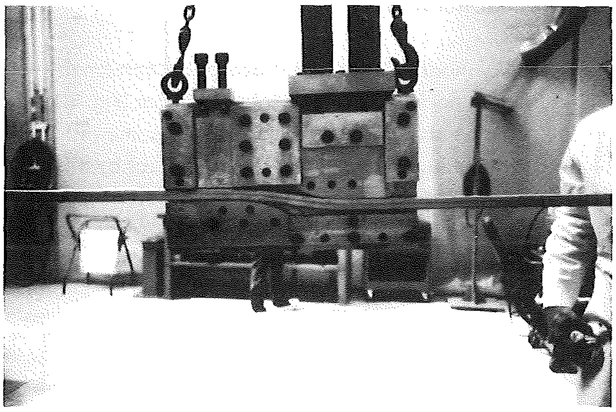

Fig. 3.5: Bending tool for bending the transition from the lower to the upper pancake (GEC Alsthom, Belfort).

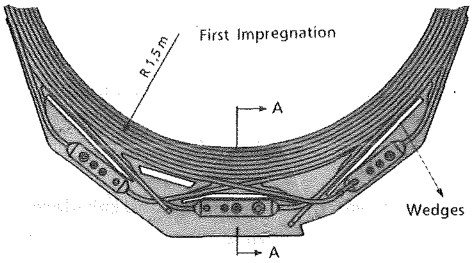

Fig. 3.6: The connection area of the Polo coil (GEC Alsthom, Belfort).

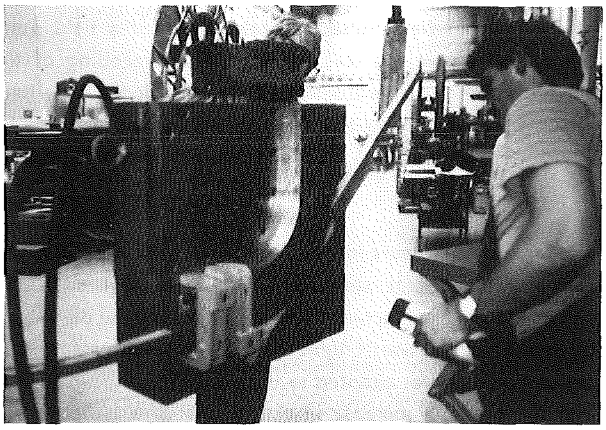

Fig. 3.7: Bending tool for making the r = 300 mm bendings in the connection area (GEC Alsthom, Beflort)

An important basis for the design of high voltage components which have to operated in vacuum is the Paschen law. It describes the breakthrough voltage in a homogenious field as function of gas density ρ times distance of the electrodes d. The density of a gas depends from pressure as well as from temperature. Thus two parameters can have an influence on the breakthrough voltage during the operation of a superconducting magnet in its cryogenic environment. For completion of the data basis the breakthrough voltage

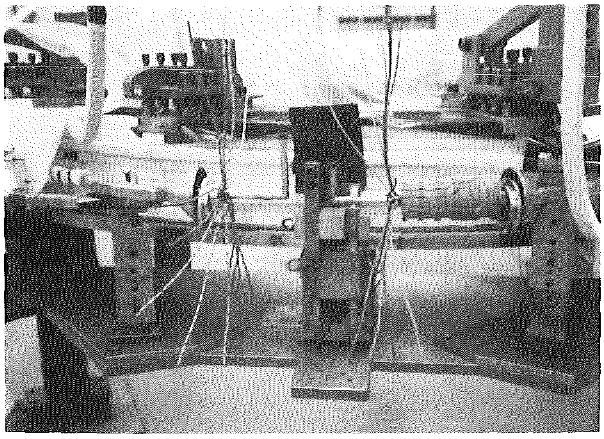

Fig. 3.8: Polo conductor cable ends prepared for making the joints (GEC Alsthom, Belfort)

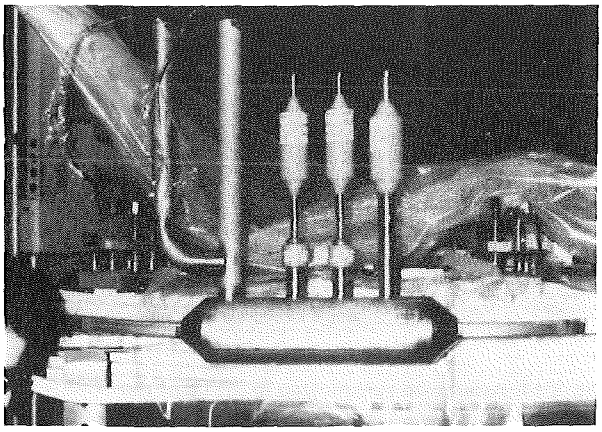

Fig. 3.9: Complete joint box with insulators in the helium supply tubes and two feedthroughs of instrumentation wires (GEC Alsthom, Belfort)

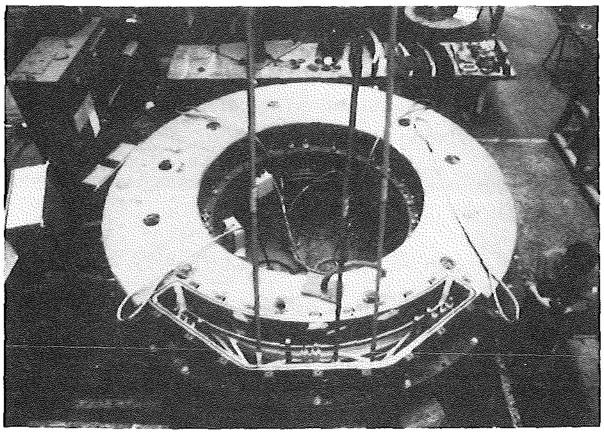

Fig. 3.10: The Polo in the mould for impregnation (GEC Alsthom, Belfort)

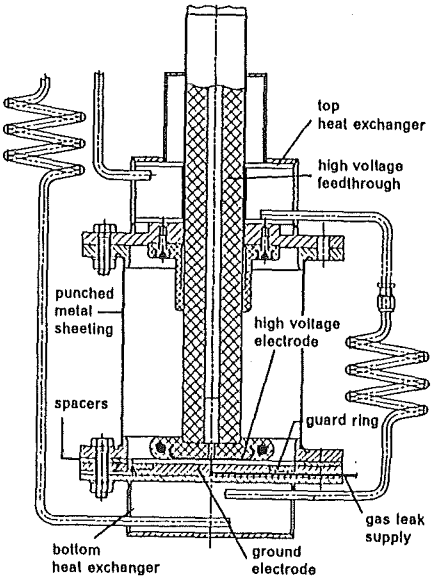

Fig. 3.11: Apparatus for the meausurement of Paschen curve at 300 K to 4 K

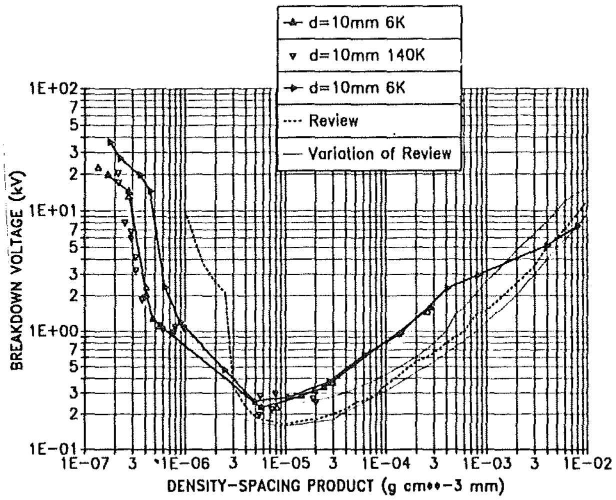

Fig. 3.12: Measured Paschen curve at cryogenic temperatures in comparison with values summaizred from the literature (dotted line)

was measured for helium gas in a homogenious field in the frame of two master thesises (Fig. 3.11) [3]. The results are presented as the breakthrough voltage versus the product density times electrode distance and compared with a review from the literature (Fig. 3.12).

The measured breakthrough voltage of the Paschen minimum was higher compared to the reviewed values. This effect was more visible at the room temperature measurements. The measurements were performed at same conditions under which superconducting magnet were operated. Therefore gaseous residual gases at 300 K or frozen gas at the electrode surface increase the breakthrough voltage in the Paschen minimum. In the center of the lower electrode a helium leak of 10^{-2} mbar l/s was brought in through a 0.1 mm bore. The influence of the leak on the breakthrough voltage in the Paschen minimum was visible but within the measuring accuracy. This fact has no importance because the leak rate required for the operation of a cryogenic facility has to be power of tens lower ($< 10^{-6}$ mbar l/s). There are no differences in the breakthrough voltage at 300 K and 4 K at the Paschen minimum what has taken into account for design of insulation systems at cryogenic temperatures operated in vacuum.

3.3 Completion of the TOSKA facility for testing of the Polo model coil

The support structure for testing the Polo model coil in TOSKA was completed and adjusted. The structure and the piping was checked to reduce possible loops for eddy currents as much as possible. The fabrication of the heat exchangers for the current leads (Fig. 3.13) (1 prototype, 1 spare, 3 for the Polo coil) and the leak and pressure test at 1 MPa are concluded. One of the heat exchangers has special instrumentation to check calculation code for the design of a 60 kA current lead for the model coil test. Two current leads will be shorted by a superconducting bus fabricated by GEC-Alsthom, Belfort, France and tested. The sc bus is a Polo conductor with the indentical terminals like the Polo model coil. Bus and current lead are being assembled for the test (Fig. 3.14).

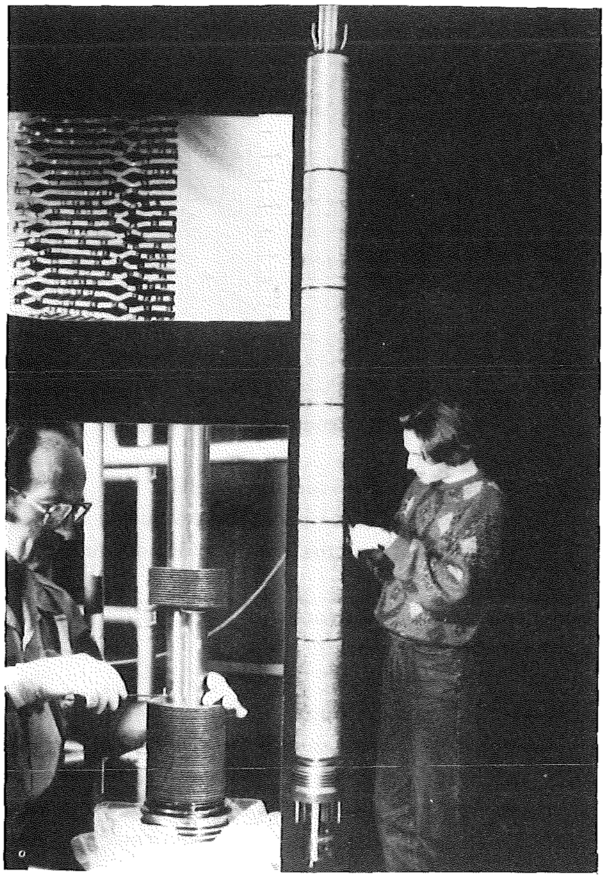

Fig. 3.13: The conductor with heat exchanger of the Polo current lead.
Left bottom: Stacking of the cooling fins on the copper rod.
Left top: Cut of a test brazing of the cooling fins on the copper rod.

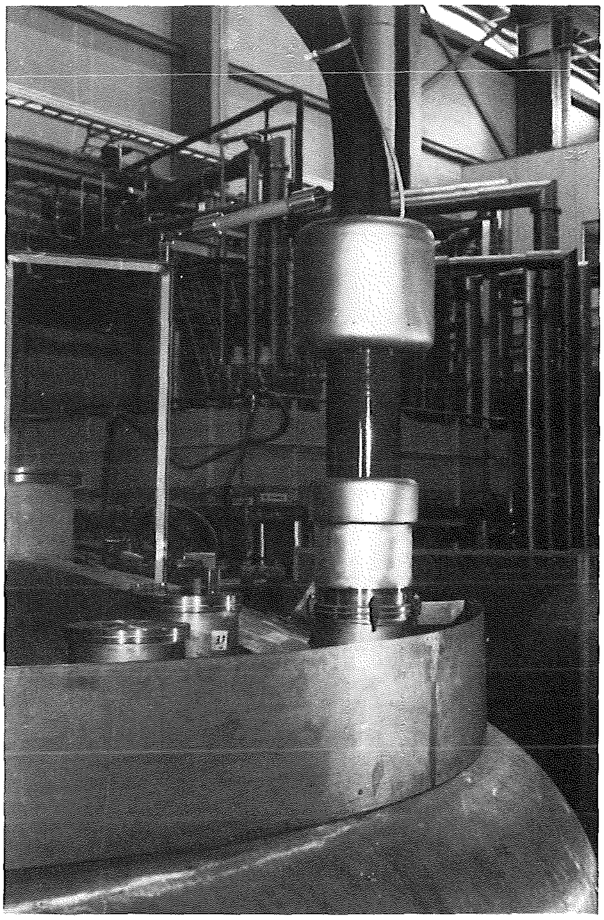

Fig. 3.14: Assembled current lead in the lid of the TOSKA vacuum vessel. Above the high voltage electrode the axial insulation break for the out coming warm helium gas can be seen.

At this test also the cryogenic circuit will be taken in operation. It had to be changed from the operation of a pool cooled lead at the cold end to a forced flow cooled lead.

The transient data acquisition at high voltage (23 kV) was tested and taken in operation. The patch panel for sensors at high voltage is being under construction.

Literature:

[1] M.L. Brown, H. Katheder, N. Mitchell, D. Robinson, R. Heller, W. Herz, L. Siewerdt, M. Süßer, F. Spath, A. Ulbricht, F. Wüchner, G. Zahn
Specification of the TOSKA-Upgrade Facility for Testing the ITER Model Coils
Document No. NIP/02239/X/A NET Team, Garching

[2] G. Friesinger, R. Heller, H. Katheder, G. Zahn
Numerical Study for a 50 kA Current Lead for the NET Model Coil Test in TOSKA-Upgrade
KfK Karlsruhe, KfK 4947, Oktober 1991

[3] R. Heller
Numerical Study of a 50 kA Superconducting Bus for

the NET/ITER Model Coil Test in TOSKA-Upgrade
KfK Karlsruhe, KfK 5008, März 1992

[4] F. Spath, R. Heil, J. Lesser, H. Schimmer, J. Weber, A. Gray, U. Wagner
A 2 kW Refrigerator for SC Magnet Tests Down to 3.3 K
Proc. ICEC 14 Kiev, Ukrainia, 8 - 12 June 1992

[5] M. Irmisch, R. Badent, A. Hinderer, M. Jaarah, J. Olbrisch, A. Ulbricht, V. Zwecker
Breakdown Characteristics of Helium Gas at Cryogenic Temperatures and Low Pressures with Respect to a Local Helium Leak
Proc. XVth. Int. Symp. on Discharges and Electrical Insulation in Vacuum, Darmstadt, Germany, 1992

Staff:

H. Barthel
A. Baumgärtner
H. Bayer
F. Becker
P. Duelli
S. Förster
G. Friesinger
A. Götz
P. Gruber
A. Grünhagen
W. Heep
R. Heil
R. Heller
W. Herz
H. Irmisch
H. Kapulla
R. Kaufmann
P. Klingenstein
B. Kneifel
W. Lehmann
W. Maurer
G. Nöther
A. Nyilas
U. Padligur
C. Rieger
K. Rietzschel
L. Schappals
L. Siewerdt
C. Schmidt
K. Schweikert
F. Spath (for 1.)
E. Specht
A. Speier
H.-J. Spiegel
F. Süpfle
F. Süß
M. Süßer
E. Ternig
A. Ulbricht (for 3.)
D. Uhlich
D. Weigert
F. Wüchner
G. Würz
G. Zahn (for 2.)
H.P. Zinecker
V. Zwecker

MBAC High Field Operation of NBTI at 1.8 K

Subtask 1: He II Forced Flow Cooling: 1.8 K Tests of EC LCT Coil plus Development of Circulation Pumps

The 1.8 K cooling technique is indispensible, if technically applicable superconducting materials shall obtain their highest field levels. Therefore the task was started with a program part for the development of components included in such a cooling circuit and is continued with the operation of a large forced flow cooled fusion magnet, the Euratom LCT coil. The last experiment is an intermediate step in the sequence for upgrading the TOSKA facility for ITER model coil test (Task MTOS).

1. The 1.8 K Test of the Euratom LCT Coil

The 1.8 K line between the 1.8 K control cryostat (B 1000) and the TOSKA vacuum vessel was installed. A design for the current leads and a short superconducting busbar were performed [1]. The currents leads are the same ones developed in the Polo project. Fig. 1 shows the calculated temperature profile for the loss of flow with and without fast discharge.

The reinforcement structure of the LCT coil passed the leak test at the factory and was delivered to KfK mid May 1992. The Euratom LCT coil was prepared for mounting of the reinforcement. That means a part of the sensors at the coil had to be removed, other sensors had to be changed and some new sensors had to be mounted now because the assembled reinforcement structure prevent the access later on. Also two plates of the case for the fixture of lifting had to be exchanged. A lateral support was mounted to allow later on the test of a Wendelstein VII X demonstration coil in the background field of the LCT coil.

The reinforcement structure of the LCT coil was assembled (Fig. 2). The headers for the in- and outlets of the cooling circuits of the belts have still to be mounted. The belts will pretensioned by heating up to a temperature of 50° C and fixing the tension by bolts with counteracting threads. Finite element calculation showed that pretensioning cannot reduce the shear stresses in the winding effectively. Pretensioning of the belts reduces the backlash.

2. The Test of Circulating Pumps with Superfluid Helium

The required pumps for the circulation of the He II have been developed, and available pumps were modified for this application and tested in the TOSKA facility. Three different types were chosen in order to find out the most suitable device for large scale application and to have redundancy during the LCT coil test.

Description of the Test Loop:

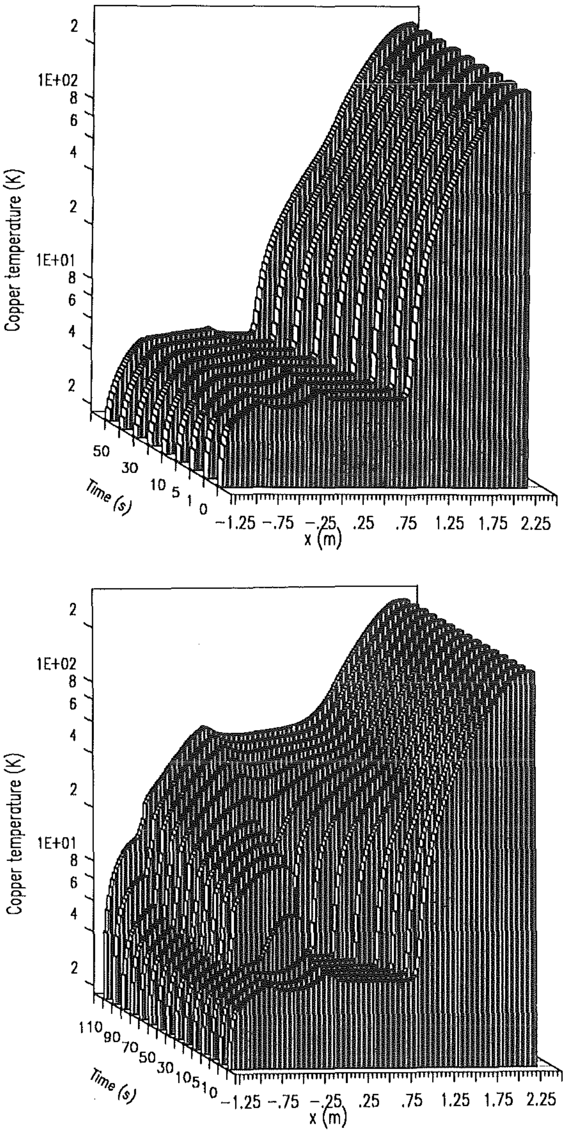

Fig. 1: Temperature profile of the superconducting bus (x = 1.25 to 0 m) and the current lead (x = 0 - 2.25 m) for 23 kA with and without fast discharge in the case of loss of flow. The temperature profiles are calculated with the time as parameter.

For the test of the pumps, a 1000 l He II control dewar with all the installations for the LCT coil test was used including the control and diagnostic systems. The control dewar was connected to the existing He II refrigerator with a cooling capacity of 380 W at a temperature of 1.8 K as shown in the simplified flow diagram Fig. 3. The pressure drop of the coil, transfer lines, and valves has been simulated by means of the control valve (CV). The heat load of these components was simulated by the heater (H). Each pump could be operated separately by opening or closing the corresponding valves.

Centrifugal pump:

A centrifugal immersion pump, developed for a low loss liquid helium transfer system, was adapted for our application, with an expected mass flow rate of 50 g/s and pressure head of 400 mbar. The centrifugal pump consists of an axial inlet stator, a covered rotor (∅ = 36 mm), and a radial/axial guide wheel. An exact axial position is achieved by active magnetic bearing. An exact radial position of the rotor is achieved by passive magnetic bearings at both ends of

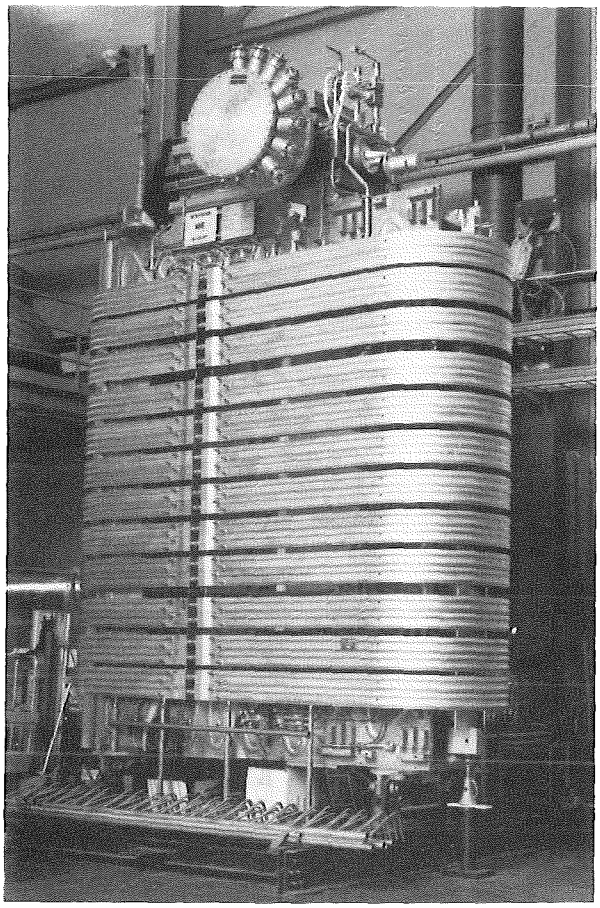

Fig. 2: Euratom LCT coil with its reinforced structure

the rotor shaft. The rotor is driven by a superconducting self-synchronous motor at liquid helium temperature. The rotational speed, and in consequence the mass flow rate and/or pressure head, can be adjusted continuously with the electronic control device of the motor. In order to withstand the maximum pressure of 20 bar within the closed forced flow cooling system the pump is installed in a small vessel (Ø = 130 mm, height = 270 mm).

The centrifugal pump was operated in the closed secondary loop as shown in Fig. 3 with a system pressure between 2.5 and 8 bar at an inlet temperature of 1.8 K and a rotation speed from 100 s^{-1} to 210 s^{-1}.

Fig. 4 shows the pressure drop versus flow rate characteristic. The He II operational data (◇) prove to be in good agreement with the data obtained from previous tests with liquid He at 4.2 K, done at the Walther-Meissner-Institut (full lines).

Advantages of this pump are the continuous flow, small dimensions without a motor at room temperature, and the maintenance-free design. The flat pump characteristics can be compensated by means of a controller which keeps the flow rate constant by adjusting the rotational speed to the pressure drop in the cooling system. For the next test the electronic control device of the motor will be equipped with such a hardware controller.

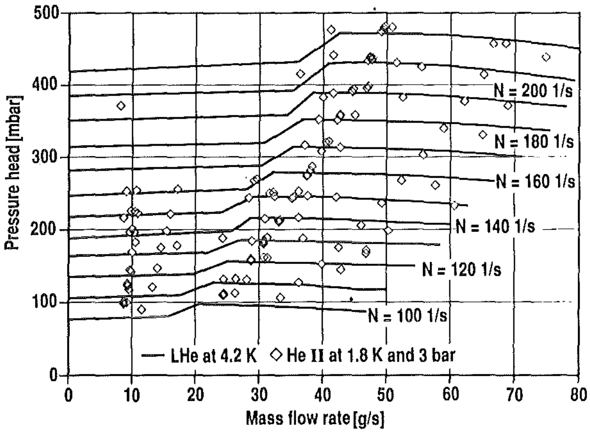

Fig. 4: Characteristic of the centrifugal pump

Piston pump:

A piston pump similar to that used during the test of the LCT coil in TOSKA was also tested. Good experience with this type of pump led only to an adjustment of the mass flow rate by a reduction of the piston stroke and to an increase of the case thickness for a maximum system pressure of 20 bar.

The pump is a three cylinder, vertically arranged single acting, piston pump driven with a speed controlled motor at room temperature. For continuous flow, the three cylinders are used in parallel and the pistons are actuated successively with 120° phase difference.

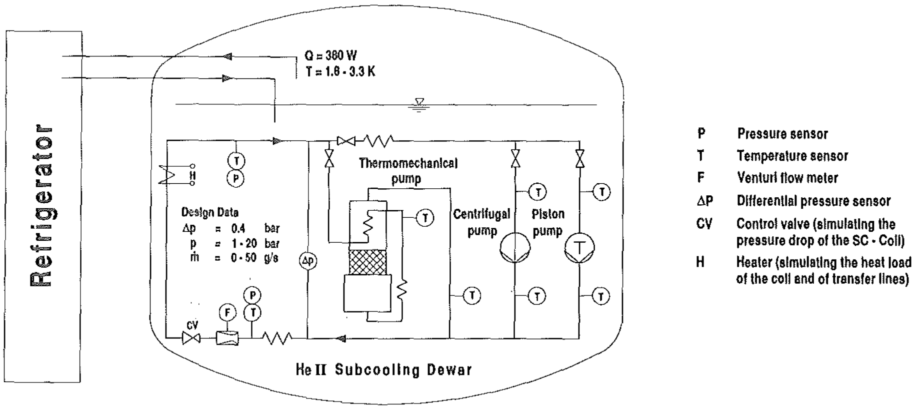

Fig. 3: Flow diagram of the test loop

The piston pump was tested under the same conditions as the centrifugal pump, but up to a pressure head of 2.2 bar as shown in Fig. 5. A stable operation of this pump was possible up to a speed of 160 min^{-1}. At higher frequencies the helium flow and pressure head were unstable as shown in Fig. 5 at a speed of 180 min^{-1}. Tests under He I conditions clarified that these results are not caused by the special He II conditions.

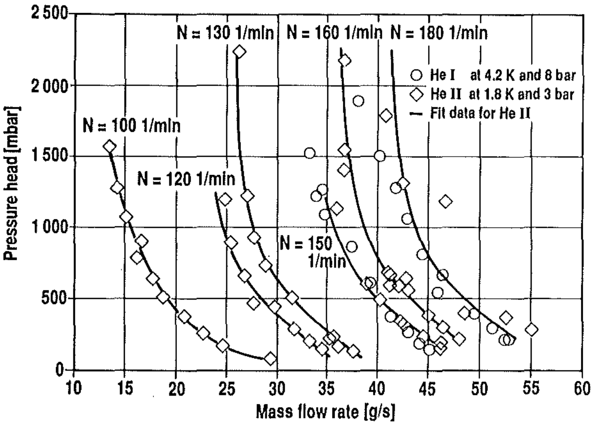

Fig. 5: Characteristic of the piston pump

After the test the pump was dismantled and it was found that the teflon sealing of the gravity type suction valves have been partly destroyed. However, the piston pump could be operated under He II conditions and a satisfying operation of this pump is expected with a new sealing.

The advantage of this pump is a pressure head up to 3 bar and a flow rate which is nearly independent of the pressure drop in the system, as shown in Fig. 5 above 1000 mbar pressure head. Below this value, the leaking outlet valve caused a different characteristic. A stable flow rate can be achieved even in case of a changing pressure drop, caused by a short normal conducting zone in a superconducting coil.

Thermomechanical Pump (TMP):

The thermomechanical (fountain effect) pump (Fig. 6) is operated in a so-called self-driven mode. This means that He II mass flow is driven by the heat which is to be extracted from the loop. In our case this load is simulated by the heater (H). A second heater is mounted within the pump (behind the filter).

There was no difference in mass flow rate whether the power was applied to (H) or to the internal heater. It increased with heater power up to 70 W. Higher powers cause a small decrease in the flow rate. The saturation in the flow rate was found to be caused by the limited cross sectional area of the porous plugs. There was also an appreciable flow rate at zero heater power. This indicates that there was about 10 W of parasitic heat load to the loop.

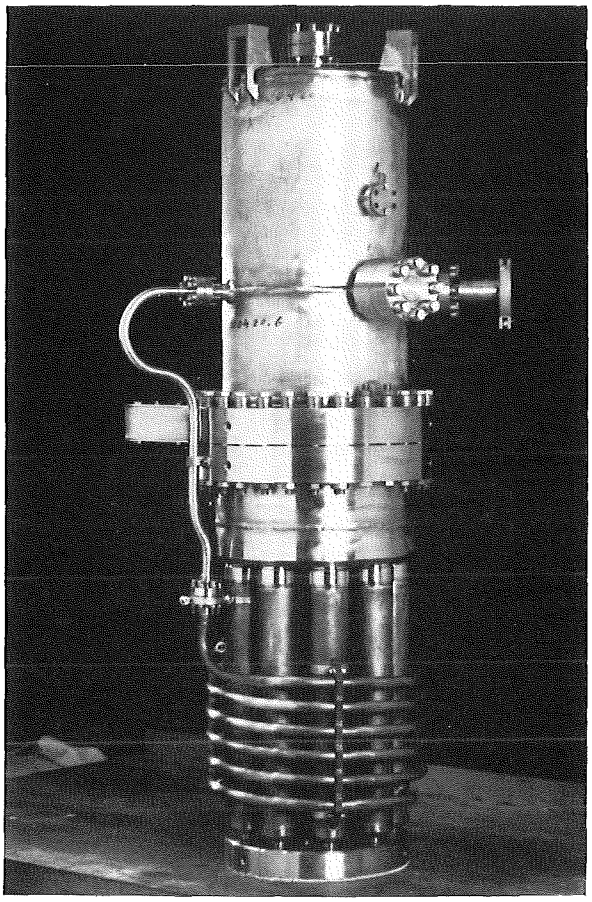

Fig. 6: The thermomechanical pump

The next series of tests was done with constant heater power applied to (H) and with variation of the flow impedance by stepwise closing of the valve (CV). In Fig. 7 the pressure head measured at the outlet of the pump is plotted versus the mass flow rate. The results are compared with calculations for ideal pumps. The agreement is judged as fairly good.

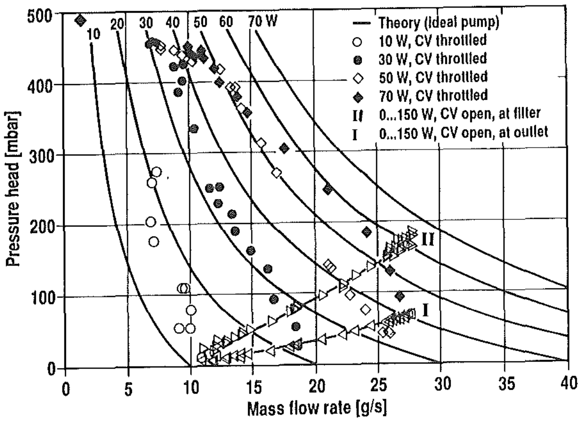

Fig. 7: Characteristic of the thermomechanical pump

Summarizing the results, the TMP yields a peak mass flow rate of 28 g/s. It can be operated with pressure heads of up to 450 mbar, a value close to the calculated thermomechanical effect.

Conclusions:

Each of the three pumps proved to be able to circulate the expected mass flow of forced flow He-II through the cooling system of the LCT coil. The decision, which is the most suitable and the most reliable device for this application, still depends on long term operational behaviour. This will take place during the test of the EURATOM LCT coil under He II conditions in TOSKA. The piston and the centrifugal pumps have been operated under He I conditions too and the same characteristic in pressure head versus mass flow rate was found for both conditions as shown in Fig. 4 and 5.

Literature:

[1] G. Friesinger, R. Heller, L. Schappals, G. Zahn
Current Lead and Bus Bar System for the 1.8 K Test of the Euratom LCT-Coil
KfK Karlsruhe, KfK 4958, Nov. 1991

[2] G. Zahn, A. Hofmann, H. Bayer, H. Berndt, R. Doll, W. Herz, M. Süßer, E. Turnwald
Test of Three Different Pumps for circulating He I and He II
Proc. ICEC 14, Kiev, Ukraine, 8-12 June 1992

Staff:

H. Barthel
H. Bayer
F. Becker
G. Friesinger
A. Götz
A. Grünhagen
A. Hofmann (for 2.)
W. Herz
M. Irmisch
H. Kapulla
B. Kneifel
W. Lehmann
W. Maurer
C. Rieger
K. Rietzschel
L. Schappals
L. Siewerdt
F. Spath
J. Spiegel
F. Süß
M. Süßer
A. Ulbricht
D. Uhlich
T. Völkel
B. Vogeley
G. Zahn (for 1. and 2.)

Vacuum and Fuel Cycle

Introduction:

KfK contributes essentially to NET-Fuel Cycle development by its acticities in the areas of plasma vacuum pumping and plasma exhaust gas purification. The Tritium Laboratory (TLK) will provide the means to verify the concepts developed for a fusion-relevant tritium-atmosphere. For the testing of large prototypical vacuum components preparations are under way to provide the necessary infrastructure.

In the following a few highlights have been extracted from the reports on the tasks and study contracts given below.

Graphite dust, a major concern in long-term vacuum components performance of a fusion device, will not pose a problem in the burn-mode, but possibly in the dwell-mode. Particle entrainment in case of sudden pressure vise is currently being investigated (TPV 1.1).

Measurements of pumping speed on specimens which have survived frequent regeneration cycles have shown that NET-specifications can easily be attained both by charcoal and zeolite sorbents. The emphasis is now more on thin, low tritium inventory cryosorption layers (TPV 2.1).

The performance of a large cryopanel has been tested in a simulated cryopump configuration with NET-typical gas mixtures. No poisoning could be observed, even in a two-stage operation mode when the sorption panel is loaded not only by He but also by the surplus of hydrogen and those impurities that cannot condense on the LN-cooled baffle (TPV 2.2).

TPV 1 Mechanical Vacuum Components

Subtask 1: Dust Transport Experiments

1. Objective

In the ITER design, besides the normal operation conditions different accident scenarios (e.g. damage of windows or cooling water tubes) are defined. In these instationary modes the pressure in the reactor rises from the current operational pressure to atmospheric pressure within a few seconds. This comprises a big risk that dusts previously deposited in the exhaust duct are whirled up and entrained through the valves into the pumps.

Such accidental conditions are simulated in the model test facility SPARTA by means of an orifice in front of a fast acting solenoid valve. Dust of a known size distribution is applied to a substrate in the tube. The influence of different pressure rises (different accident scenarios) on dust resuspension is investigated in relation to the total quantity of dust applied. Dusts of three different particle size distributions are used.

2. The Model Test Facility SPARTA

The test stand is shown schematically in Fig. 1. The facility has been designed by Lieberknecht [1] on the basis of similarity rules for dust transport in a continuum, and of special effects in rarefied gases. This model that resembles NET- I with respect to fluid dynamics was built in a 1:15 scale.

The model facility consists of an equalizing tank in front of the pumps, a test section, a dust dosing system and a gas inlet vessel (see Fig. 1).

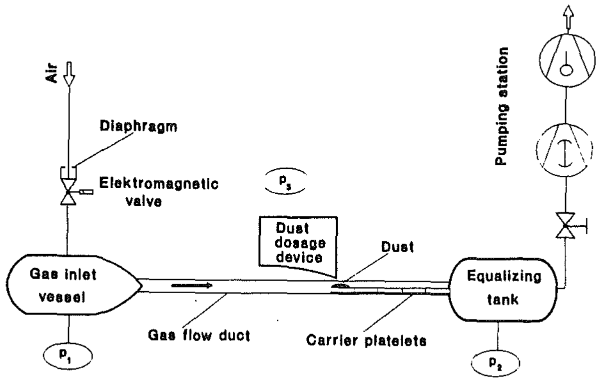

Fig. 1: Schematic diagram of test facility SPARTA

In the gas inlet vessel the fed gas is allowed to expand relatively homogeneously. In the connected intake duct (D = 0.1 m; L = 3 m) an undisturbed flow is developing. At the transition of the intake duct the dust dosing device is placed. Behind the dust entrance the test section begins, consisting of a horizontal glass tube followed by a stainless steel tube (D = 0.1 m; L = 1 m). The bottom of this test section is covered by a probe which supports 13 glass carrier platelets. Under vacuum the dust is dosed unto the first carrier platelet.

A sudden pressure rise in the previously evacuated device ($p=10^{-3}$ mbar) is attained by the opening of the solenoid valve with an opening time of 100 ms. Different pressure rise times are obtained by orifices of different apertures. The pressure rises are recorded by means of a membrane manometer with a resolution time of 25 ms.

3. Dusts Used

Fromentin (3) showed, that the physical behaviour of big and small particles is different. Whereas the small particles (< 100 µm) are whirled up and follow to a large extent the air flow, big particles slip alongside the tube wall.

In our own investigations fine and coarse dusts are used with different size distributions. "Dust 1" is an ultrafine graphite powder from the company Edelgraphit. "Dust 2" is supplied by the company Sigri as a by-product from the machining of graphite electrodes. "Dust 3" is a pure electrode graphite powder of the company Richard Anton. All dusts contain 99.5 % carbon.

The median values of the volume distribution "$d_{50,3}$" the average Sauter diameters "d_{sv}", and the shape factors ψ_{vs} of these dusts are specified as follows:

	d_{sv} [µm]	$d_{50,3}$ [µm]	ψ_{vs} [-]
Dust 1	0.75	5.12	0.54
Dust 2	14.9	87.06	0.25
Dust 3	461.6	893.64	0.67

4. Experiment Implementation

Glass carrier platelets which have previously been weighed are placed on the probe. The probe is then carefully introduced in the test section, and the device is closed tight with a CF-flange. The facility is evacuated, and at a pressure of 10^{-3} mbar dust dosage begins. Then the pump is switched off and the device is cautiously permitted to ambient pressure in order to take out the first carrier platelet once more, and weigh the quantity of dust dosed unto it.

The probe with the carrier platelets is then rearranged and the facility is cautiously re-evacuated. At 10^{-3} mbar the pump stand is switched off again and the pressure rise is realized by opening of the solenoid valve. Afterwards the probe is disassembled, and the quantity of dust deposited on each carrier platelet is determined.

The next test campaign can be started, e.g. with another pressure rise time which implies another orifice aperture.

5. Measurement Methods

For the determination of the deposited dust quantities a balance R 200 D of the company Sartorius with an accuracy of ± 50 µg is available. A microscope of the company Leitz is being used for tracing particles on the carrier platelets. Thus the maximum particle entrainment can be detected on the test section.

6. Evaluation

The total dust quantity dosed (m) and the residual dust quantity (m_{d1}) on the first carrier as well as the total dust quantity deposited (m_d) on the platelets 2.....13 are determined by weight analysis. Therefrom the resuspended dust quantity (m_r) can be calculated:

$$m_r = m - m_{d1} \qquad (1)$$

m_{d1}: dust quantity remaining on the first carrier platelet after pressure rise.

The resuspension ratio (Ω) is formed by the quotient of dust resuspended (m_r) and the total dust quantity dosed (m):

$$\Omega = \frac{m_r}{m} \qquad (2)$$

Note: The term resuspension is used rather than suspension because in reality the first deposition of particles (starting condition) is already preceded by a suspension process.

7. Results

7.1 Dust Resuspension Ratio

The resuspended dust quantity (m_r) in relation to the total dust quantity (m), i.e. the resuspension ratio Ω is shown in Fig. 2...4 as a function of the pressure rise.

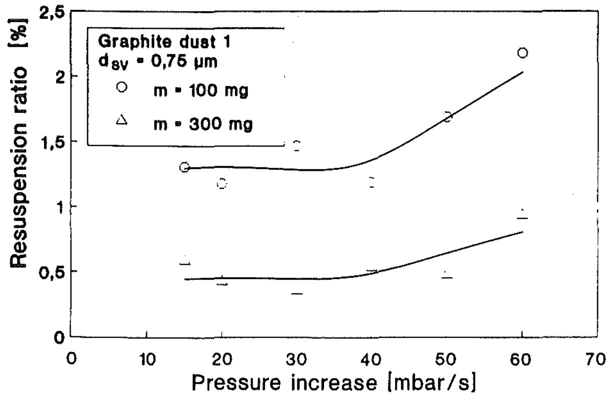

Fig. 2: Dust 1 resuspension during pressure rise

According to Fig. 2 low resuspension of "Dust 1" is occurring below 40 mbar/s pressure increase. Only above this value adhesion forces can be overcome by the forces resulting from gas flow. Under the microscope one can determine that "Dust 1" on the initial carrier platelet 1 does not only exist in form of single particles, but also as small or big agglomerates which are only whirled up by higher pressure rise rates. This is the reason for the bend in resuspension curves at about 40 mbar/s.

From Fig. 3 it is obvious that resuspension of "Dust 2" rises almost continuously with increasing pressure rise rates and that the difference between total amounts of 100 and 300 mg is insignificant. Some increase in the slope of the curves can be seen above 30 mbar/s pressure increase rate. Microscopy shows that "Dust 2" was initially deposited as a heap of single particles (no agglomerates).

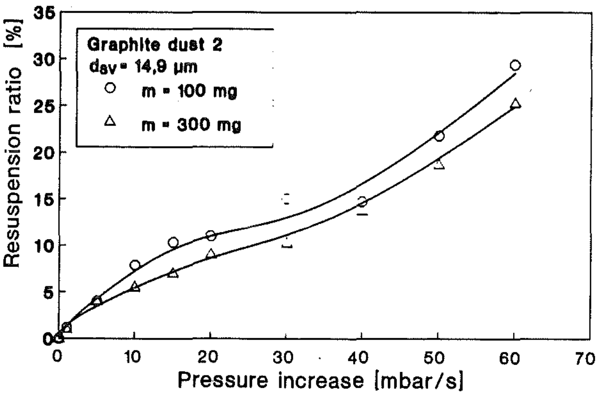

Fig. 3: Dust 2 resuspension during pressure rise.

Resuspension of "Dust 3" first doesn't exhibit a great increase but above 40 mbar/s the rise is significant (see Fig. 4). Before the pressure is changed the dust exists in form of single particles. The quantities applied (100 and 300 mg respectively) have virtually no influence on the resuspension ratios.

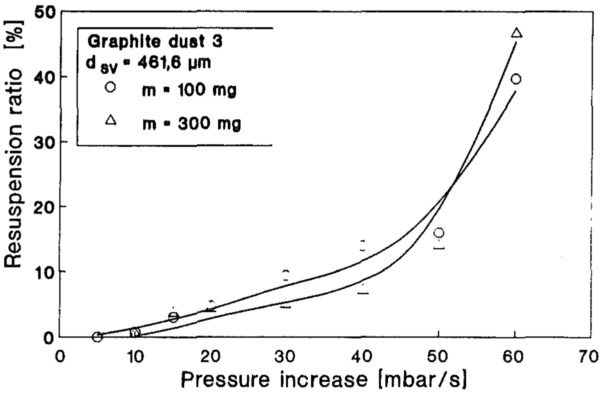

Fig. 4: Dust 3 resuspension during pressure rise

From size distribution of "Dust 3" one can infer that it contains a much small fraction of fine particles. The first slight increase of resuspension is related to this fraction.

7.2 Entrainment of suspended dust particles

"Dust 1" and "Dust 2" are whirled up by all pressure rises investigated. One fraction of dust deposits on tube walls and carrier platelets, and another fraction is transported beyond the test section into the equalizing vessel. On the carrier platelets when carrying out experiments with these dusts one could determine by microscopy homogeneous dust deposits throughout the test sections.

In contrast to dusts "1" and "2" a maximum transport length can clearly be determined on the carrier in the case of "Dust 3". This length increases linearly with pressure rise rate.

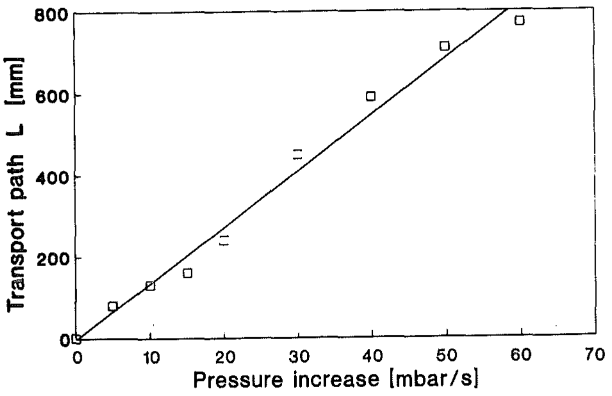

Fig. 5: Transport of dust 3 during pressure rise

8. Prospects

Investigations up to now into the simulation of accidental conditions with the model facility yield a better understanding of the physical phenomena of dust resuspension. It is demonstrated that pressure pulses are responsible for the whirl-up of dust. For the transfer of the results on ITER conditions pressure shock waves have to be taken into account in further experiments, if necessary with a modified model test facility (SPARTA).

Literature:

[1] Lieberknecht, M.:
Unpublished Report of KfK, October 1989

[2] Fromentin, A.:
Particle Resuspension from a Multi-Layer Deposit by Turbulent Flow; PSI-Bericht Nr. 38, September 1989

Subtask 2: Dust on Elastomer Seals

1. Introduction

Dusts arising during fusion reactor operation can be entrained through the exhaust ducts into the valves in front of the pumps. There they can impede the functioning of valve seals.

The dust compatibility of elastomer seals is experimentally studied at the model test facility SPARTA. With this facility flow conditions like the ones in the exhaust duct between torus and manifold of ITER can be simulated. Dusts being anticipated as typical for a tokamak with graphite liners can be dosed in.

2. Test Valves in the SPARTA Test Facility

Three pneumatically actuated bellows gate valves ND 100 of the company VAT were built in the model facility. The arrangement of valves can be seen in Fig. 6. The first valve (V1) is between the test section and the equalizing tank, the second valve (V2) is at the top of the equalizing tank closed off from atmosphere by a blind flange and in a similar way valve V3 at the bottom of the tank.

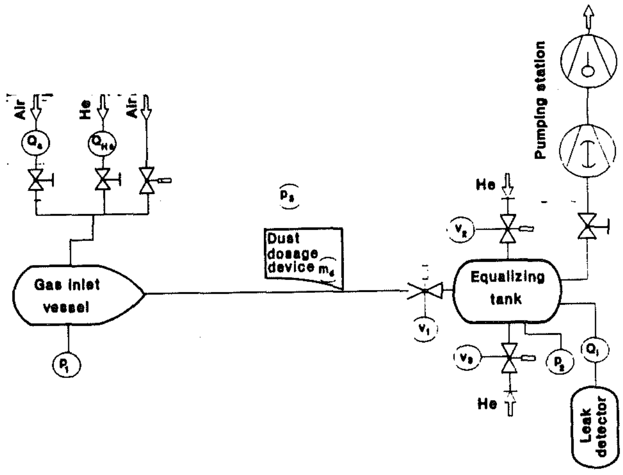

Fig. 6: Locations of the test valves V1, V2 and V3 at the SPARTA model facility

The double valve disks are sealed on both sides with vulcanized elastomer O-rings. Three materials are under investigation:

VITON
BUNA-N
EPDM.

3. Test Procedure

Series of test campaigns with an increasing number of valve opening and closing cycles are carried out with a semi-permanent air flow of 1 mbar·l/s at $p = 2 \cdot 10^{-2}$ mbar going through the device while graphite dust grade "1", (conf. TPV 1-1 reporting) is continuously dosed in at a rate of 0.02 mg/s.

After each test campaign, i.e. after 100, 200, 500, 1000, 2000 and 5000 cycles - as described in detail in the Experiment Definition Document - leakage through the valves in closed condition is determined as a measure for the evaluation of valve behaviour over extended periods of routine operation.

In addition, at the end of each test campaign, sudden venting is simulated with a pressure rise at a rate of 450 mbar/s and its influence on valve tightness is determined by a further leak test followed by valve disassembly and optical inspections as described below.

Before the next test campaign a virgin state of the facility is re-established by careful cleaning of all inner surfaces and, if necessary, replacement of impaired seals.

The whole test procedure is repeated both with another grade of dust (grade "2") and another one of the seal materials enumerated above.

4. Methods and Evaluation

Leak detection is carried out after pump-down and closure of all valves. The leak rate through the valves is determined with helium leak detectors.

Optical inspection of valve interiors is carried out after removal of valve discs with their elastomer seals. Since direct observation of dust on the seal surfaces is not possible samples are taken by means of sticking tape and mounted on base boards for microscopy and photographic documentation. For image analysis a LEITZ-analyzer is available elsewhere. With this method only fractions of the seal surface can be examined, and it is assumed that this is transferable to the total of the surface.

5. First Results and Prospects

The leak rate of double disc valves V1, V2 and V3 with VITON seals was found to be below 10^{-6} mbar·l/s for all cycle numbers and dust grades "1" and "2". For the single valve discs on the dust-exposed side leak-rates increased to $7.3 \cdot 10^{-5}$ mbar·l/s. No correlation could be found yet between leak rate and cycle number or dust size distribution. The increase in leak rates seemed to be of a particle rather random nature.

Results on seal surfaces coverage with dust are not available yet.

The valves with the other seal materials, BUNA-N and EPDM are still under investigation.

Staff:

W. Höhn
I. Özdemir
D. Perinic
R. Rinderspacher

TPV 2 Cryogenic Vacuum Components

This task is aimed at developing and optimizing cryogenic vacuum pumping of plasma exhaust containing helium. To develop cryosorption panels a variety of eligible material combinations for helium cryosorption have been tested on a reduced scale. The best suited technical solutions will be optimized on the technical scale under simulated ITER operating conditions. As a result of these investigations design data and requirements will be obtained with respect to the operation of the cryopumps to be used in the plasma exhaust pumping system of a fusion machine.

Subtask 1: Sorbent Pre-Selection

1. Development of Coating Technique

The development of a coating technique for cryosorption panels has been continued. In addition, a new task was adopted: For the reduction of the tritium inventory in the plasma exhaust pumping system, the sorption capacity of the sorbent layer for tritium is to be reduced to the largest possible extent with the specific helium pumping speed remaining on a high level. This task can be solved among others by using thin sorbent layers.

From the result of the cryopumping experiments at the TITAN test facility using panel No. 3 (sorbent, Degusorb AS 16/450, activated carbon pellets of 1.6 mm in diameter) under three stage operating conditions with a gas mixture similar to that of the ITER reactor, a reduction factor of about 150 was determined with the duration of the ITER pumping cycle assumed to be 80 min. Thus, a reduction of the thickness of the sorbent layer from 1.6 mm to about 10 µm would be theoretically permissible.

Industrial companies producing these thicknesses were contacted to find out, whether the techniques used there could be applied for the fabrication of cryopanels. Two industrial techniques are suited for this purpose: Varnishing of sheet metal and coating of abrasive paper. The application of the spraying technology of the varnishing industry for the panel fabrication seems to be possible. The applicability of the abrasive paper coating technique is being tested at the moment.

In addition to these investigations of the coating technology, studies are carried out with a view to optimize the preparation of the panel surfaces for the coating with inorganic cements. This work is aimed at obtaining an optimum adhesion of the sorbent layer to the metal surfaces. The following methods are compared and optimized: Grinding with emery, sandblasting, blasting with glass beads and turning.

At KfK, small specimen plates of 50 mm in diameter are coated using the spraying method. For the thermal cycling tests and the cryosorption tests with helium, specimens with an activated carbon grain size of 0.02, 0.1 and 0.5 mm, respectively and an inorganic bonding of Thermoguß 2000 were prepared.

Within the framework of an order, a LHe panel (d = 890 mm) produced by L'Air Liquide was coated at KfK using a spraying technique for the generation of thick sorbent layers. For this purpose, the activated carbon (Degusorb C-25) was applied to the panel surface by means of the Thermoguß 2000 bonding material. This LHe panel is part of the cryopump used for exhausting the LHCD (Lower Hybride Current Drive) antenna of the JET tokamak in Great Britain.

To determine the sorption properties under tritium loading conditions, specimens produced at KfK (d = 100 mm) are being tested at TSTA, Los Alamos at the moment.

2. Molecular Sieve Optimization

Within the framework of the development of a cryosorption pump for the ITER experimental reactor, the helium pumping speeds and sorption capacities of various adsorbents are investigated. The results obtained with activated carbon panels were very satisfactory. Now, various types of molecular sieves shall be examined with a view to find an optimum adsorbent in terms of the helium pumping speed and the reactivation behavior. A low reactivation temperature is required for the case of water entering the pumping system and inhibiting the activity of the molecular sieve.

Molecular sieves are inorganic materials which are chemically inert and, hence, cannot react catalytically with oxygen or radiolytically with tritium in contrast to the activated carbons. The adsorption properties of the molecular sieves are based on their exactly defined pore structures which allow the separation of molecules of different sizes (geometrical selectivity) as well as on the large intracrystalline surface area of their cavity structure. As a result of the polarity of the inner surface, the intensity of which is described by the modulus of

$$m = SiO_2 / Al_2O_3,$$

polar and polarizable molecules are adsorbed preferably (polar selectivity). Due to their hydrophilic character, however, polar molecular sieves do not meet our requirement of a minimum reactivation temperature. For our test programme we therefore selected molecular sieves with the lowest possible polarity expressed by high modulus values: The molecular sieves to be tested are represented in Table 1.

Molecular sieve	Pore size [A]	Modulus m
ZSM -5	5	1000
ZSM -5	5	100
Zeolite -Y	7.5	70
Zeolite -Y	7.5	25

Table 1: Various types of molecular sieves to be tested

Assuming that the pumping speeds of pure gases on molecular sieves can be derived qualitatively from their cryosorption properties, adsorption isotherms are evaluated for the selection of optimum molecular sieve types in terms of the properties mentioned above. These isotherms represent the amount of adsorbed gas as a function of its partial pressure. They are recorded by the OMNISORP test facility of the Omicron Technology Corporation. The standard conception of this facility allows the dynamic measurement of nitrogen adsorption isotherm at LN_2 temperature (77,3 K). The adsorption behavior of nitrogen at LN_2 temperature may be transferred qualitatively to the adsorption behavior of helium at LHe temperature. The most important difference between both adsorptives is found to exist in the kinetic diameter as is evident from the Table 2. In contrast to the critical diameter, the kinetic diameter is obtained from viscosity measurements and, thus, takes into account the diffusion properties of the molecules investigated.

Adsorptive	Critical diameter [nm]	Kinetic diameter [nm]
N_2	0.3	0.38
He	0.2	0.255

Table 2: Critical and kinetic diameter of nitrogen and helium

To justify the assumptions made above and to investigate the temperature dependence of the adsorption properties of both adsorptives, some helium adsorption isotherms are recorded at LHe temperature and compared with the respective nitrogen isotherms.

The basic advantage of this test conduct consists in the fact that the pure adsorption properties of the adsorbents investigated can be tested in a reproducible manner by measuring the adsorption isotherms using adsorbent powders. Furthermore, isotherm measurements particularly with nitrogen are quicker and cheaper than the helium pumping speed measurements.

Reactivation temperature	ZSM -5, 5 A		Zeolite -Y, 7.5 A	
	m = 100	m = 1000	m = 25	m = 70
100 °C	X	X	X	X
200 °C	X	X	X	X
300 °C	X	X	X	X
Reference isotherm 400 °C	X	X	X	X

Table 3: Test matrix : Measurement of nitrogen isotherms at 77.3 K

The test matrix for the measurement of the nitrogen adsorption isotherms is represented in Table 3.

Except for the reference specimen which is reactived at 400 °C, all specimens are saturated with water and subjected to subsequent heating at various temperatures. This is done to simulate water entering the pumping system and to investigate the poisoning effect of the molecular sieve specimens resulting from the humidity contained in the pores.

Finally, the helium pumping speed of the optimum molecular sieve type is determined quantitatively at the HELENE test facility. For this, the adsorbent must be bonded to a metal plate in the form of granulates.

Substask 2: Sorbent Pumping Speed

1. Introduction

The TITAN experiments are carried out to investigate the cryopumping of the plasma exhaust generated in a Tokamak during the burn mode with cryosorption panels of technical scale. All plasma exhaust constituents, except for helium, can undergo cryocondensation on the cooled surfaces.

Helium pressure of 10^{-6} mbar can be achieved by cryocondensation at 0.3 K. This is not acceptable economically. The helium gas is therefore subjected to cryosorption on a panel which takes place at a higher temperature already. The panel consists of a metal plate with the sorbent layer being fixed on to the plate by an inorganic cement.

The experiments described in the following sections were carried our using thick-layer panels with a thickness of the sorbent layer of > 1 mm.

2. Test conduct

2.1 Cooling

Prior to cooling, the TITAN facility has room temperature and the pressure amounts to 10^{-7} mbar.

Cooling is divided into two phases. At first, the pool of the first baffle is filled with liquid nitrogen.

After three days, the second baffle and the panel have been cooled down to about 150 K by means of thermal radiation. Then, the pool of the panel is filled with liquid helium. The filling of the pool of second baffle may either consist of liquid nitrogen or of liquid helium. By means of cooling, the pressure of the facility is reduced to below 10^{-9} mbar.

2.2 Pumping

In the pumping tests, the pumping properties of the panel-baffle-recipient system are determined. Pumping is characterized by the pumping speed.

During the pumping tests, the parameters of dosage rate [mbarl/s], pressure [mbar] and temperature [K] are measured and recorded.

The pumping speed [l/s] is determined by means of the constant pressure method. It is obtained from the dosage rate/pressure ratio.

2.3 Regeneration

Upon the completion of the pumping operation, the sorbent layer is regenerated. For this purpose, the electrical heater at the bottom of the helium pool is activated. When the heating system is switched on, the refrigerant still contained in the pools of the baffles and of the panel is evaporated. Then, the heating is adjusted such that the temperature of the sorbent layer is increased to 90 K. At this temperature, desorption of the pumping gas takes place.

For the pumping of the exhaust gas, a turbomolecular pump is applied.

2. Heating

The cryosorption panels of ITER cryopumps have to be reactivated at elevated temperatures from time to time.

At the TITAN facility, heating is carried out for a period of 2 hours at 150 °C. During heating, the pressure of the facility is kept at about 10^{-5} mbar by means of the turbomolecular pump installed. After heating, it takes one day for the facility to cool down to room temperature. The cooling to room temperature results in a pressure drop to 10^{-7} mbar.

3. Simulation of ITER conditions at TITAN

3.1 ITER Specific Pumping Speed

During the ITER burn mode, a gas flow of 4,7 mol/h is pumped by each cryopump with the pressure at the pump inlet being

$$p = 1.9 \times 10^{-4} \text{ mbar}.$$

This pump inlet pressure was taken from the concept of an ITER cryosorption pump [1]. It corresponds to a flow rate of

$$Q_{ITER} = 28.75 \text{ mbarl/s}.$$

As a result of the flow rate and the pumping inlet pressure, a pumping speed of

$$S_{ITER} = 150\,000 \text{ l/s}$$

is obtained. For a panel surface area of 8 m^2, the specific pumping speed then amounts to

$$S_{ITER}, \text{spec.} = 1.9 \text{ l/(s cm}^2\text{)}.$$

3.2 Gas Dosage

For the pumping tests at the TITAN facility, the gases helium, hydrogen (protium), deuterium and the gas mixture M 3 which is similar to that generated in ITER are applied.

The ITER similar gas mixture M 3 consist of:

helium	:	3.98 vol.%
protium	:	1.67 vol.%
deuterium	:	93.90 vol.%
and impurities	:	0.49 vol.%

3.3 Gas Flow Rates

The ITER similar gas flow rates metered into the TITAN facility Q_{TITAN} are determined from the ITER gas flow rates Q_{ITER} by the ratio of the sorption surface of the ITER pump A_{ITER} to the sorption surface of the TITAN pump A_{TITAN}

$$A_{ITER}/A_{TITAN} = Q_{ITER}/Q_{TITAN}$$

$A_{ITER} = 8 \times 10^4$ cm2

$A_{TITAN} = 1186$ cm2

The ITER similar gas flow rates then amount to:

Q_{M3} (total) = 0.426 mbarl/s

Q_{He} = 0.0148 mbarl/s

Q_{H2} = 0.00463 mbarl/s (protium)

and Q_{D2} = 0.396 mbarl/s.

The minimum possible dosage rate of the TITAN facility, however, is 0.01688 mbarl/s which means that the dosage of the ITER similar helium and hydrogen (protium) flow rates cannot be carried out.

4. Tests Using the Molecular Sieve Panel No. 15

Panel No. 15 consists of a copper plate onto which the bonding agent and the sorbent are sprayed by means of a compressed gas. THERMOGUß 2000 is applied as the bonding agent. A molecular sieve produced by the MERCK company (Type: 0.5 nm, Art. 5703) serves as the sorbent.

Using panel No. 15 pumping tests were run with two and three pumping stages, respectively. Under three-stage operating conditions, the first pumping stage consists of the first baffle which is kept at the LN-temperature. There cryocondensation of the impurities takes place. The second pumping stage is the second baffle which is kept at liquid helium temperature. Here, cryocondensation of the hydrogen isotopes is to take place. In the third pumping stage, the panel, only helium is to be pumped.

Under two-stage operating conditions, the pools of both baffles are filled with liquid nitrogen. In this case, hydrogen isotopes are pumped together with the helium on the panel. This process is referred to as copumping. In the pumping tests under two-stage operating conditions, copumping proved to be working.

For further tests, one baffle was removed to increase the conductance. The higher conductance is supposed to result in an increased pumping speed. The copumping tests with one baffle only are referred to as "real" two-stage pumping.

4.1 Test Results: Panel No. 15

A survey of the test results obtained with panel No. 15 is given in Tab. 4.

	p_{min}/p_{max} [mbar]	S_{min}/S_{max} [l/(scm²)]	T_{min}/T_{max} [K]	Test no.
3-stage pumping	8.0×10^{-5} 1.0×10^{-4}	4.45 3.56	5.0 5.0	52
2-stage pumping	2.0×10^{-4} 2.7×10^{-4}	1.71 1.27	5.8 6.6	55
Real 2-stage pumping	1.5×10^{-4} 2.0×10^{-4}	2.30 1.70	6.7 7.6	62

Table 5: Results of pumping tests with gas mixture M3 and a flow rate of 0.422 mbarl/s

	pmin/pmax [mbar]	Smin/Smax [l/(s cm2)]	Tmin/Tmax [K]	Test no.
3-stage pumping	3.6×10^{-5} 2.9×10^{-4}	0.40 0.25	5.0 5.0	50
2-stage pumping	6.0×10^{-5} 6.0×10^{-5}	0.24 0.24	5.4 6.4	53
Real 2-stage pumping	8.0×10^{-5} 8.0×10^{-5}	0.18 0.18	6.2 6.2	63
ITER requirement	6.3×10^{-6}	1.9	-	-

Table 6: Results of pumping tests with helium and a flow rate of 0.01688 mbarl/s

The pumping tests using the molecular sieve panel No. 15 focussed above all on the investigation of three-stage pumping, two-stage pumping and real two-stage pumping.

In Tab. 5, the test results for the mixture M 3 are listed as a function of the pumping stages. The minimum and maximum values measured for the pressure, pumping speed and panel temperature during three dosage phases of 30 min each are indicated. An ITER similar gas flow of 0,422 mbarl/s was metered into the system.

The most important requirement to be met during plasma exhaust pumping refers to helium pumping. In an additional test series, the helium pumping characteristics were investigated as a function of the number of pumping stages. The minimum and maximum values measured for the pressure, pumping speed and panel temperature during two dosage phases of 30 min. each are indicated. The minimum possible gas flow of 0,01688 mbarl/s was metered into the system. The results are represented in Tab. 6.

It is obvious from Tabs. 5 and 6 that the panel temperature is increased under two-stage operating conditions as expected. The removal of one baffle, however, was not expected to lead to a further increase in the panel temperature. This may be attributed to the increased intensity of the thermal radiation of the second baffle which is blackened ($\varepsilon > 0,9$).

Compared to the three-stage pumping, higher panel temperatures and, hence, higher pumping pressures and smaller pumping speeds are obtained under two-stage operating conditions as is evident in Tab. 5. During two-stage pumping operation, the removal of one baffle results in a decreased pressure of the recipient and an increased pumping speed of the gas mixture M 3 due to the higher baffle conductance.

During helium pumping as represented in Tab. 6, the increase in the panel temperature measured under two-stage operating conditions is below that of M3 pumping, as the amount of gas metered into the system is much smaller. But here as well the temperature increase in the panel caused an increased pressure in the recipient. Thus, the pumping speed is decreased which is a function of the pumping pressure.

In contrast to the pumping of M3, which contains 93.9 vol.% hydrogen isotopes, the removal of a baffle does not have any positive effect on the pumping speed. The helium pumping speed is reduced instead.

The pressure increase observed during helium pumping due to the increased panel temperature resulting from the removal of a baffle may probably be attributed to the steeper increase in the helium sorption pressure curve versus the temperature compared to the hydrogen vapor pressure curve. This means that the increase in the helium partial pressure measured in the recipient with increasing temperature exceeds that of the hydrogen partial pressure. With an

Test No.	50	51	52	53	54	55	56	57	58	59	60	61	62	63
Pumping stages	3	3	3	2	2	2	3	3	3	2	2	2 ④	2 ⑤	2 ⑤
Kind of gas	He	Mixture1	Mixture3	He	Mixture1	Mixture3	He	D_2	H_2	D_2	H_2	Mixture1	Mixture3	He
Min/Max dosage rate [mbar l/s]	0.017 0.084	0.4221 0.4221	0.4221 0.4221	0.01688 0.0844	0.4221 0.4221	0.406 0.406	0.1688 0.1688	0.01688 16.88	0.01688 0.1688	0.01688 0.1688	0.01688 0.1688	0.1688 0.6753	0.405 0.405	0.01688 0.0844
Min/Max pumping pressure [mbar]	$3.6x10^{-5}$ 3.8x10	$1.2x10^{-4}$ $2.9x10^{-4}$	$8.0x10^{-5}$ $1.0x10^{-4}$	$6.0x10^{-5}$ $6.0x10^{-4}$	$3.3x10^{-4}$ $3.5x10^{-4}$	$2.0x10^{-4}$ $4.0x10^{-4}$	$1x10^{-3}$ $>10^{-2}$	$1.26x10^{-6}$ $7.91x10^{-6}$	$3.24x10^{-6}$ $2.9x10^{-5}$	$4.7x10^{-6}$ $4.2x10^{-5}$	$3.3x10^{-6}$ $6.4x10^{-5}$	$7.1x10^{-5}$ $6.9x10^{-4}$	$1.0x10^{-5}$ $2.2x10^{-4}$	$8.0x10^{-5}$ $7.0x10^{-4}$
Min/Max pumping speed [l/s]	468.47 221.78	3607.81 1055.54	5277.7 4222.16	281.08 142.32	1280.88 1209.72	2030.43 1015.22	168.41 ③	13401.8 10674	5206.54 5811.4	3558 4032.4	5028.64 2656.64	2372 972.52	4151 1779	213.48 11.86
Min/Max pumping speed ① [l/(s cm^2)]	0.395 0.187	3.042 0.89	4.45 3.56	0.237 0.120	1.08 1.02	1.712 0.856	0.142 ③	11.3 9.0	4.39 4.90	3.0 3.4	4.24 2.24	2.0 0.82	3.5 1.5	0.18 0.01
Min/Max pumping speed ② [l/(s cm^2)]	0.215 0.102	1.653 0.484	2.42 1.93	0.129 0.060	0.59 0.55	0.930 0.465	0.077 ③	6.14 4.89	2.38 2.67	1.63 1.85	2.30 1.20	1.09 0.45	1.9 0.8	0.10 0.05
Quantity of dosed gas [mbar l]	668.58	2279.25	2279.25	516.95	2279.25	2842.9	2836.4	334.29	972.48	668.58	668.58	5348.64	3646.8	972.29
Pressure before test start [mbar]	$8x10^{-9}$	$3.5x10^{-9}$	$3.1x10^{-9}$	$6x10^{-9}$	$3x10^{-9}$	$1.6x10^{-9}$	$1.0x10^{-8}$	$1.0x10^{-9}$	$1.0x10^{-9}$	$1.0x10^{-9}$	$1.0x10^{-9}$	$1.0x10^{-9}$	$3.0x10^{-9}$	$6x10^{-8}$
Pressure after test end [mbar]	$2.6x10^{-6}$	$8.0x10^{-6}$	$1.0x10^{-7}$	$2.0x10^{-7}$	$1.4x10^{-5}$	$2x10^{-7}$	$1.0x10^{-4}$	$6.5x10^{-9}$	$1.2x10^{-5}$	$1.0x10^{-7}$	$4.0x10^{-5}$	$6.0x10^{-6}$	$3.5x10^{-7}$	$1x10^{-7}$
Min/Max panel centre temperature during dosage [K]	5.0 5.0	5.0 5.0	5.0 5.0	5.35 6.8	7.5 8.2	5.8 6.7	5.0 7.4	4.7 4.7	5.1 5.2	5.3 5.4	5.1 5.6	6.0 9.0	6.7 7.8	6.2 8.1

Table 4: Results of pumping tests with molecular sieve panel No. 15

Mixture 1 Volume percent 0.113 Ar, 0.112 CO_2, 0.225 CO, 0.194 N_2, 0.236 O_2, 1.44 CH_4, 5.02 He, remainder H_2
Mixture 3 Mass percent 0.108 Ar, 0.111 CO_2, 0.225 CO, 0.214 O_2, 1.44 CH_4, 4.00 He, 1.1 He, remainder D_2
① Related to panel surface = 1186 cm^2
② Related to baffle surface = 2182 cm^2
③ Evaluation is not possible. Pressure rises continously. Dosage stopped when pressure has attained 10^{-2} mbar
④ Intermediate baffle is not cooled
⑤ Only one baffle installed

increasing partial pressure the pumping pressure is increased as well.

5. Tests Using Panel No. 12

Panel No. 12 is an activated carbon panel, which like panel No. 15 has been manufactured by means of the spraying technique. Again, THERMOGUß 2000 and copper were used as the cement and the plate material, respectively. The sorbent is Type SC II, average grain size 1 mm.

Up to now, panel No. 12 has been tested under real two-stage operating conditions. Tests under three-stage operating conditions are planned to be carried out.

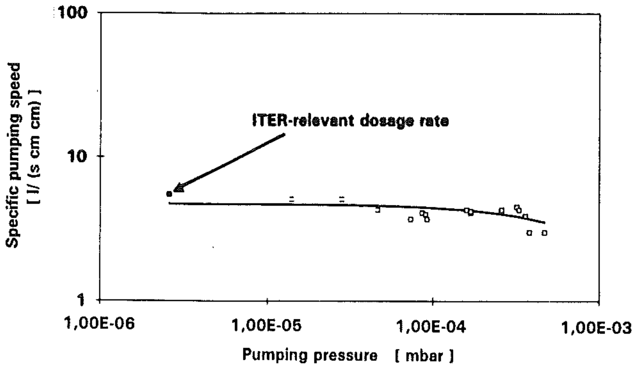

Fig. 1: Panel no. 12, spec. helium pumping speed

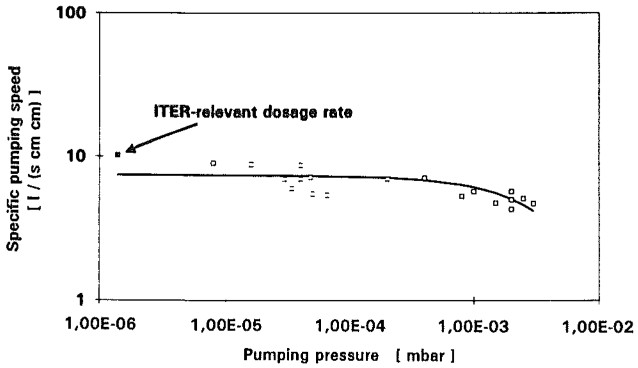

Fig. 2: Panel no. 12, spec. protium pumping speed

5.1 Test Result: Panel No. 12

A survey of the test results obtained with panel No. 12 is given in Tab. 7.

The pumping speed curves for helium, hydrogen (protium), deuterium and mixture M3 are represented in Figs. 1 through 4. The points entered in Fig. 1 through 4 result from the dosage rates applied in the experiments.

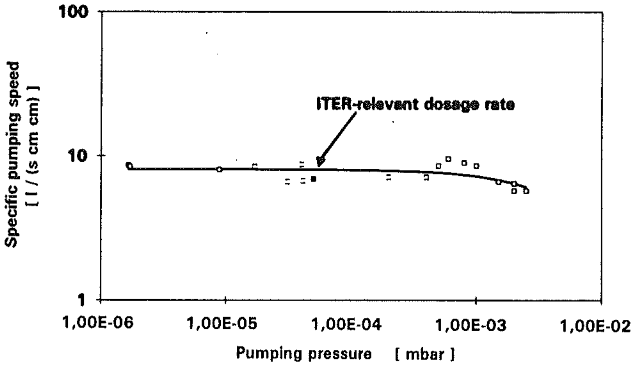

Fig. 3: Panel no. 12, spec. deuterium pumping speed

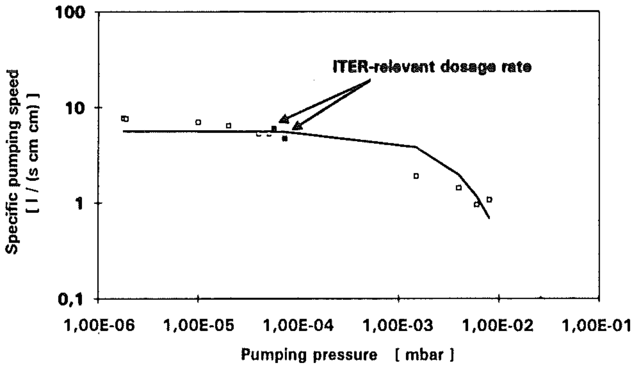

Fig. 4: Panel no. 12, spec. gasmixture 3 pumping speed

The pumping speed curves are determined from these points by exponential regression.

The range of the ITER requirements is indicated by the hatched areas.

Fig. 1: The He pumping speed amounts to about 4 l/(s cm^2) in the range of 10^{-6} mbar to 10^{-3} mbar.

Fig. 2: In the range of 10^{-6} mbar to 10^{-3} mbar, the H2 pumping speed is about 6 l/(s cm^2). At the minimum possible dosage rate of ~ 0.017 mbarl/s, the pumping speed is at 10 l/(scm^2). It is expected that the ITER requirements are even better complied with for the ITER similar dosage rate of 0.0046 mbarl/s, as the pressure of the recipient is decreased due to the reduced dosage rate.

Fig. 3: The D_2 pumping speed amounts to about 8 l/(s cm^2) in the range of 10^{-6} mbar to 10^{-2} mbar. For the ITER similar dosage rate of 0.396 mbarl/s, the pumping speed is at 7 l/(scm^2).

Fig. 4: In the pressure interval of 10^{-6} mbar to 10^{-4} mbar, the M 3 pumping speed amounts to about 6 l/(s cm^2). For

Test No.	64	65	66	67	68	69	70	71
Pumping stages	2 ⑤	2 ⑤	2 ⑤	2 ⑤	2 ⑤	2 ⑤	2 ⑤	2 ⑤
Kind of gas	He	He	He	H_2	H_2	D_2	D_2	Mixture3
Min/Max dosage rate [mbar l/s]	0.422 0.844	0.422 2.533	0.01688 0.4052	0.414 16.88	0.01688 0.414	0.414 16.88	0.01688 0.414	0.01688 10.13
Min/Max pumping pressure [mbar]	$9x10^{-5}$ $2.4x10^{-4}$	$8.6x10^{-5}$ $>10^{-2}$	$2.6x10^{-6}$ $9.2x10^{-5}$	$4.0x10^{-5}$ $3.0x10^{-3}$	$1.4x10^{-6}$ $6.5x10^{-5}$	$4.0x10^{-5}$ $2.5x10^{-3}$	$1.7x10^{-6}$ $5.0x10^{-5}$	$1.8x10^{-6}$ $8.0x10^{-3}$
Min/Max pumping speed [l/s]	4744 3558	4862.6 ③	6523 4388.2	10318.2 5574.2	12097.2 6404.4	10318.2 6760.2	9962.4 8183.4	9132.2 1304.6
Min/Max pumping speed ① [l/(s cm2)]	4.0 3.0	4.1 ③	5.5 3.7	8.7 4.7	10.2 5.4	8.7 5.7	8.4 6.9	7.7 1.1
Min/Max pumping speed ② [l/(s cm2)]	2.17 1.60	2.2 ③	3.0 2.0	4.7 2.6	5.5 2.9	4.7 3.1	4.6 3.8	4.19 0.58
Quantity of dosed gas [mbar l]	1772.75	5105.2	1124.4	85713.0	1147.5	36630.5	1147.3	13847.6
Pressure before test start [mbar]	$1.0x10^{-8}$	$1.0x10^{-8}$	$4.0x10^{-9}$	$2.0x10^{-9}$	$6.0x10^{-9}$	$2.0x10^{-9}$	$1.5x10^{-9}$	$1.5x10^{-9}$
Pressure after test end [mbar]	$>10^{-2}$	$2.0x10^{-2}$	$9.0x10^{-8}$	$1.0x10^{-5}$	$3.5x10^{-6}$	$2.0x10^{-6}$	$1.5x10^{-7}$	$1.0x10^{-6}$
Min/Max panel centre temperature during dosage [K]	5.6 7.0	5.7 10.0	5.3 5.1	5.5 9.0	5.5 5.5	5.6 9.1	5.4 5.4	5.2 10.0

Table 7: Results of pumping tests with activated charcoal panel No. 12

Mixture 1 Volume percent 0.113 Ar, 0.112 CO_2, 0.225 CO, 0.194 N_2, 0.236 O_2, 1.44 CH_4, 5.02 He, remainder H_2
Mixture 3 Mass percent 0.108 Ar, 0.111 CO_2, 0.225 CO, 0.214 O_2, 1.44 CH_4, 4.00 He, 1.1 He, remainder D_2
① Related to panel surface = 1186 cm^2
② Related to baffle surface = 2182 cm^2
③ Evaluation is not possible. Pressure rises continously. Dosage stopped when pressure has attained 10^{-2} mbar
④ Intermediate baffle is not cooled
⑤ Only one baffle installed

the ITER similar dosage rate of 0.426 mbarl/s the pumping speed varies from 4 to 6 l/(scm^2).

Literature:

[1] L.S. Gurevich et al., Conceptual Design Description of a Pumping System based on Cryosorption Pumps with Solid Sorbents. August, 1990. ITER-IL-FC-5.1-0-2.

[2] D. Leger et al., "ITER FUEL CYCLE", ITER Documentation Series, No. 31, International Atomic Energy Agency, Vienna, 1991, Table III-7

[3] D. Leger et al., "ITER FUEL CYCLE", ITER Documentation Series, No. 31, International Atomic Energy Agency, Vienna, 1991, Table III-11.

Subtask 3: Endurance Testing of Cryosorption Panels

A cryosorption pump shall be procured for testing panel segments (d = 200 mm - 250 mm) in the typical ITER-geometry and under simulated ITER operating conditions. This facility is intended to investigate the suitability of sorption panels produced at KfK under continous operating conditions.

The conceptual design study for the LOTTE test facility was ordered from an industrial company. The first part of these activities consisted in carrying out a design study. As a result of this study, the basic design criteria of the LOTTE facility were defined.

LHe is supplied from three 450 l transport dewars. The cryogenic liquids are led to the test facility via a main transfer line. This line has the advantage that the refrigerating capacity of the helium gas can be used for the cooling of the transfer lines. Hence, this technique contributes to the reduction of the LHe amount required for operation. To ensure a continous LHe supply over several days, the three LHe containers are selected automatically one after the other.

The test facility consists of two subassemblies. The vacuum chamber with its components required (LN shield, LHe shield, panel) is separated functionally from the service module including the LHe auxiliary tank and the valves needed for process control. The vacuum chamber is designed for a pressure of 10 bar. The panel is surrounded by a LHe and a LN shield. A pumping station and a gas dosage system are connected with the vacuum chamber.

Pressure measurement is carried out by means of capacitance diaphragm type manometers which up to $p = 10^{-5}$ mbar allow measurements which are independent of the type of gas used. In addition, cold-cathode (Penning) and hot-cathode ionization type pressure gauges (Bayard Albert) are applied for the low pressure range of $p < 10^{-3}$ mbar.

The temperature is measured using resistance transducers (Rh Fe and Pt 100 sensors).

The components required for the test are linked up by means of a process control system. The data of the pressure, temperature and flow rate measuring points are stored by a ystem for the acquisition of measured data.

Subtask 5: Backing Pumps

After the procurement and fabrication of all components, the assembly of the test circuit was started. The completion of some parts was delayed due to manufacturing problems and material defects. Both PNEUROP measuring domes were designed as pressure vessels (12 bar) and inspected for acceptance by the TÜV (Technical Control Board) with a test overpressure of p = 15.6 bar. In addition to mechanical construction electrotechnical assembly was started and brought to a conclusion.

A system for the acquisition of measured data including the user-specific software was developed and connected with the experiment. Upon the completion of the current leak test and subsequent evacuation of the test circuit to a pressure of $p \approx 10^{-5}$ mbar, test operation will be started.

TEST MATRIX FORTE (DRAFT)
Gas Flow Range 0,05 - 3000 mbarl/s
To be measured: pump performance

Gas	Outlet pressure	
	600 mbar	1200 mbar
N_2	X	X
He	X	X
H_2	X	X
D_2	X	X
Ar	X	X
Simulated ITER gas mixture	X	X

The test matrix is valid for the individual tests of the fore-pumps of 1300, 600, 60 and 6 m^3/h and for the series combinations: 1300 + 600, 1300 + 600 + 60 and 1300 + 600 + 60 + 6 m^3/h.

For the experiments at the FORTE test facility, a test matrix was created for tests with five individual gases, one gas mixture similar to that of the ITER reactor and two back-pressure stages of 600 and 1200 mbar.

Subtask 8: Preparations for the Testing of Prototype Components for Vacuum Systems

Staff:

D. Burghardt
A. Edinger
H. Haas
J. Hanauer
W. Höhn
S. Horn
H. Illbruck
B. Kammerer
D. Kausch
U. Kirchhof
H. Knauß
H. Lukitsch
A. Mack
D. Perinic
W. Reeb
D. Stern
J. Weinhold
D. Zimmerlin

To demonstrate the efficiency of the prototype components of the plasma exhaust pumping system, they have to be tested under simulated normal and off normal ITER operating conditions. The following components should be tested on a 1:1 scale:

- primary particle separator
- gate valves ND 1500, ND 1000
- cryocompound pump 100 000 l/s
- advanced cryopump concept
- turbomolecular pump 18 000 l/s
- dust filter for forepumps
- mechanical forepump train 1300 + 600 + 60 m^3/h
- cryogenic forepump cascade

The prototype components should be tested under representative normal and off normal operating conditions to demonstrate their adequacy for ITER and provide engineering specifications for series components. It is proposed to include in the testing programme:

- Demonstration of suitability for normal operation:
  - vacuum characteristics measurements
  - cycling operation
  - dust impact
  - magnetic field impact

- Demonstration of suitability for off normal operation:
  - sudden pressure rise
  - loss of power and pressurized air
  - plasma disruptions and earthquake simulation

- Demonstration of remote handling end-effector suitability for large flanges.

The work with regard to the planning of the VENUS test facility was continued. Possibilities for the installation of the facility together with the infrastructure required have been studied.

In cooperation with an industrial company, possible systems of the LHe and LN supply were investigated. LHe supply from an existing LHe liquefaction system was found to be the cheapest solution. This liquefaction system is located in an adjacent building. The supply of the VENUS facility takes place via a LHe pipeline.

The test parameters for the simulation of reactor operation without tritium have been compiled in a preliminary test programme.

TEP 1 Cryosorption

Subtask 2: Molekular Sieves

Recently a study on the adsorption of deuterium on type 3A, 5A, and mordenite and on the adsorption of hydrogen, deuterium and helium on active carbon was carried out. Within the frame of tritium technology activities at Kfk these experiments are of interest to the development of cryosorption pumps, fuel clean-up process steps and techniques for the recovery of tritium from a blanket.

The composition of the elementary cell of completely hydrated type A zeolite in the K form (type 3A) and in the Ca form (type 5A) is

$K_{12}[(AlO_2)12(SiO_2)_{12}]$ 27 H_2O

$Ca_6[(AlO_2)12(SiO_2)_{12}]$ 30 H_2O.

To achieve a high degree of dryness these type A zeolites were heated to at least 450 °C. The pore diameter of the larger cavity of zeolite 5A varies between 0.42 - 0.44 nm. The kinetic diameter of deuterium, i.e. r_{D2} = 0.295 nm, is therefore considerably smaller. The pore diameter of zeolite 3A, on the other hand, has been reported to be 0.31 - 0.32 nm at room temperature with a tendency to decrease at lower temperatures (about 0.29 nm at 77 K). Thus a poorer adsorption of the above mentioned gases is expected.

Mordenites are zeolites of high density with very high silica content (SiO_2/Al_2O_3 = 10). To remove the adsorbed water the mordenite was heated to at least 350 °C. The large channels of the unit cell of mordenite are accesible through a twelve-membered oxygen window of approx. elliptical shape. The free cross section of the channels is characterized by a major axis of 0.695 and a minor axis of 0.581 nm. The pore diameter of mordenite is therefore much larger than that of the adsorbent under investigation.

The deuterium adsorption results as compiled in Table 1 were obtained at temperatures in the range -25 to -200 °C and at pressures between 0.1 and 1000 mbar employing zeolite 3A, 5A, and mordenite. The highest deuterium adsorptions were

Temp. °C	Zeo-lite	Equilibrium Pressure [mbar]								
		1000	500	100	50	10	5	1	0.5	0.1
-200	3A	13.0	10.0	3.6	2.5					
	5A	200.0	195.0	170.0	155.0	125.0	110.0	95.0	55.0	35.0
	mord.	140.0	130.0	115.0	10.05	80.0	68.0	42.0	32.0	12.0
-175	3A	12.0	8.5	2.6	1.5					
	5A	155.0	147.0	113.0	100.0	42.0	32.0	13.5	9.0	
	mord.	105.0	87.0	55.0	44.0	23.0	16.0			
-150	3A	11.0	6.3	1.6	0.9					
	5A	100.0	80.0	38.0	23.5					
	mord.	54.0	40.0	18.5	12.5					
-125	3A	7.5	4.0	1.0	0.55					
	5A	45.0	28.0	7.0	5.0					
	mord.	21.0	13.5	4.4	2.5					
-100	3A	4.3	2.1	0.5	0.3					
	5A	17.0	9.5	2.0	0.9					
	mord.	7.3	4.4	1.1	0.62					
-75	3A	2.4	0.9	0.23	0.15					
	5A	7.0	4.0	0.8	0.36					
	mord.	2.4	1.4	0.36	0.18					
-50	3A	1.0	0.4	0.11	0.08					
	5A	4.6	2.0	0.40	0.17					
	mord.	1.0	0.6	0.15	0.07					
-25	3A	0.7	0.24	0.06	0.04					
	5A	2.6	1.3	0.18	0.07					
	mord.	0.1								

Table 1: Deuterium sorption on different zeolites [cm^3/g]

Temp. °C	Gas	Equilibrium Pressure [mbar]								
		1000	500	100	50	10	5	1	0.5	0.1
-200	H_2	298.0	266.0	205.0	185.0	130.0	108.0	62.0	53.0	14.5
	D_2	305.0	295.0	238.0	207.0	137.0	110.0	63.0	48.0	24.0
	He	8.0	4.0							
-175	H_2	172.0	150.0	94.0	72.0	32.0	24.0			
	D_2	190.0	160.0	98.0	76.0	36.0	23.0			
	He									
-150	H_2	100.0	73.0	29.0	18.5	5.6				
	D_2	100.0	79.0	35.0	22.0	6.2				
	He									
-125	H_2	46.0	29.0	8.2	4.3	0.75				
	D_2	45.0	32.0	10.9	6.4	1.65				
	He									
-100	H_2	17.2	11.5	2.65	1.7					
	D_2	18.5	11.2	2.58	1.2					
	He									

Table 2: Sorption of hydrogen, deuterium and helium on active charcoal

observed - under all examined conditions - for zeolite 5A. Mordenite adsorbed about 30 % less deuterium than zeolite 5A at the very low temperatures and much less than that as the adsorption temperature was raised. It is interesting to compare the adsorption of deuterium on mordenite, zeolite 3A, and 5A. While at high temperatures a temperature decrement of 25 °C is accompanied by a substantial adsorption increase in all molecular sieves, at the lower temperatures the same temperature increment will only increase significantly the adsorption on zeolite 5A and mordenite. For instance, at an equilibrium pressure of 1000 mbar increases the adsorption of deuterium on zeolite 5A and a temperature decrease from -175 to -200°C, while that on zeolite 3A increases only from 12 to 13 cm³/g. This is in line with the diminishing pore size diameter of zeolite 3A with decreasing temperatures. The data in Table 1 suggest that this effect becomes important already at about -150 °C.

To evaluate active charcoal as an adsorber, experiments on the adsorption of hydrogen, deuterium, and helium were performed under conditions similar to those employed for the zeolites. The results of these runs have been compiled in Table 2. They indicate that at high pressures and low temperatures the adsorption of hydrogen on active charcoal is substantially higher than that on any of the examined zeolites. At low equilibrium pressures, i.e. < 1 mbar, the situation is reversed, i.e. at a given temperature more molecular hydrogen is adsorbed on zeolite 5A than on active charcoal. This observation is of importance to technological applications.

Staff:

E.Noppel
R.-D.Penzhorn

TEP 2 Permeation and Catalytic Cracking

former: Plasma Exhaust Processing: Alternative Options

Subtask 1: Permeator Studies

Main objective of the PETRA facility is a long-term endurance test of a commercial palladium/silver permeator placed in a outer containment of achieve tritium compatibility. In addition, the PETRA facility will a) contribute to the development of in-line infrared process analytics of gases such as methane, carbon dioxide, and carbon monoxide in a tritium environment, b) yield information on the performance of auxiliary equipment over extended periods of time and c) increase knowledge on the use of ZrCo for tritium handling.

Two newly developed double containment bellows pumps (Siemens, KWU) will be employed in the PETRA experiment: one for the circulation of gases and the other as a forepump to a Normetex scroll pump. This tritium compatible, oil-free two stage double containment bellows compressor, has heads in series, which are hermetically sealed in an UHV-tight stainless steel housing. The mechanical power from the motor is transmitted to the compressor via a magnetic clutch. Optimal pumping speed can be selected with an electronic speed control. With a prototype of this pump a series of tests were carried out to study its performance with the gases used in the PETRA experiment. As apparent from the data in Table 1 the compression ratios of H_2, He and N_2 achieved with the double containment pump show only a slight dependance from the discharge pressure and the type of pumped gas. This is due to the operation principle of the pump, i.e. intermittent compression/depression via a two valve sytem. When the double containment pump was used as forepump to a 150 m³/h scroll pump in closed loop operation at an exhaust pressure of approx. 1000 mbar, the vacuum achieved with hydrogen and helium was found to be better than 5×10^{-3} mbar.

Table 1: Compression ratios of several gases attained with the double containment bellows pump (operated at 50 Hz) at zero flow as a function of the discharge pressure p_v

p_v [mbar]	k_{H2}	k_{He}	k_{N2}
1000	11.49	12.79	13.95
600	10.71	n.d.	14.42
300	10.00	n.d.	13.45

n.d. = not determined

The pumping characteristics of scroll pumps with nominal pumping speeds of 15 and 18 m³/h (for nitrogen), of similar characterisitics to the one employed in the PETRA experiment, were also examined employing either pure gases or their mixtures. Both scroll pumps were supplied by Normetex, Pont Audemer, France. Scroll pumps use nutating bellows to seal the motion of the compression chamber. The gas compression involves a thin-walled cylinder, which describes an involute. The pump cavity, which is of sickle form, is enclosed between two clock spring spirals, one fixed to the pump base and the second displaced from it by a vector whose magnitude is the pitch of the spiral. The clearance between the spirals, which do not touch each other, is of the order of 0.1 mm. The gas inlet is placed at the outside and the gas outlet a the inside of the spiral.

From plots of the pumping throughputs of nitrogen vs. the suction pressure at a constant exhaust pressure of approx. 1000 mbar with scroll pumps having nominal pumping speeds of 15 and 18 m³/h it was observed that these pumps pump nitrogen better than anticipated from the nominal values given for this gas by the manufacturer. Fig. 1 shows throughput/suction pressure curves of gases relevant to the PETRA experiment obtained with the 18 m³/h pump. Similar but not identical results were obtained with other scroll pumps. For instance, a comparison between the 18 and the 60 m³/h pumps reveals that whereas with former the maximum pumping speed for nitrogen and argon is attained at suction pressures in the range 8 - 20, the maximum with the latter is attained in the range 10 - 80 mbar. The efficiency to pump N_2, Ar, H_2, D_2, and He of the 60 m³/h was found to be at all times higher than that of the 18 m³/h pump.

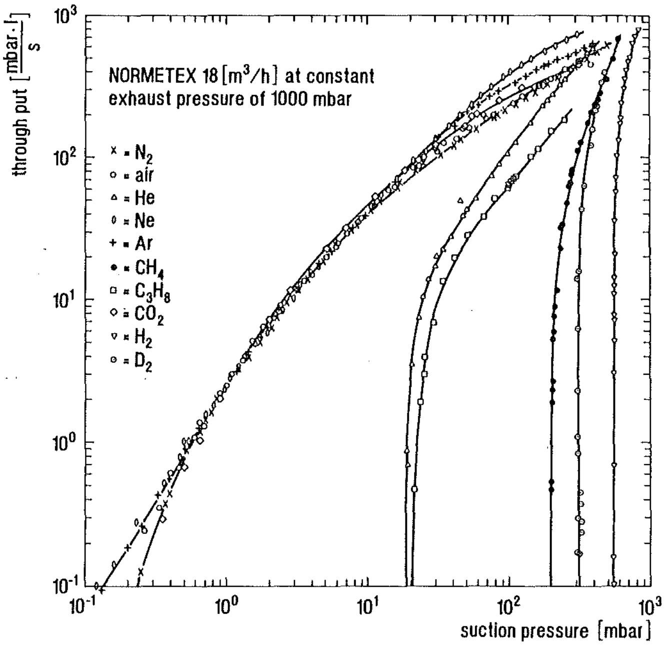

Fig. 1: Pumping throughput of the Normetex 18 m³/h scroll pump as a function of the suction pressure for various gases at constant exhaust pressure of 1000 mbar. The filter from the pump was removed.

Typical results for the throughput of hydrogen and helium with the 18 m³/h scroll pump as a function of the suction pressure at various constant exhaust presssures are given in

Figs. 2 and 3. It is seen that max. throughput is achieved at exhaust pressures lower than 500 and 200 mbar when pumping He and H_2, respectively.

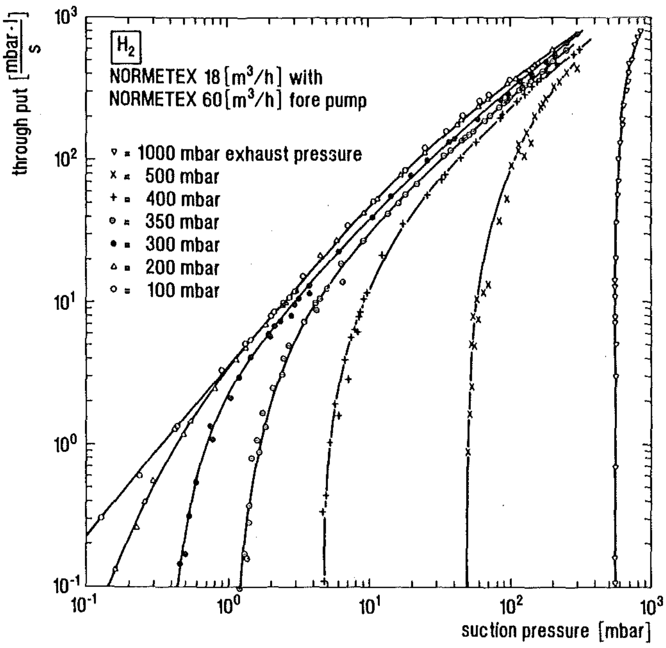

Fig. 2: Hydrogen throughput of a 18 m³/h scroll pump as a function of suction pressure at several constant exhaust pressures

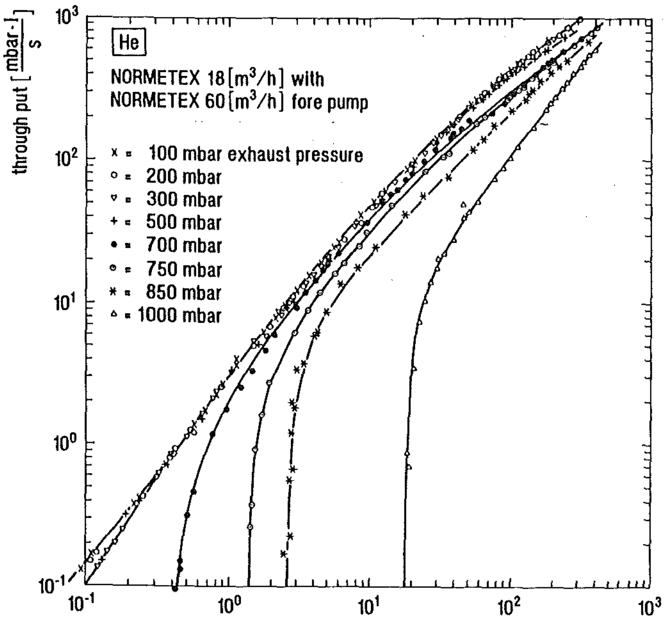

Fig. 3: Helium throughput of a 18 m³/h scroll pump as a function of suction pressure at several constant exhaust pressures

The vacua achievable when H_2, D_2, CH_4, or He are pumped at various exhaust pressures with the 15 or the 18 m³/h scroll pumps have been compared in Fig. 4. From the data it is apparent that at backing pressures below 150 mbar the ultimate vacua ($< 3 \times 10^{-2}$ mbar) become independent of the type of gas pumped. Vacua achievable when pumping H_2, D_2, He, and N_2 at a constant exhaust pressure of 1000 mbar are summarized in Table 2.

Table 2: Vacua achievable with a small scroll pump operated at an exhaust pressure of 1000 mbar

pump [m³/h]	H_2 [mbar]	D_2 [mbar]	CH_4 [mbar]	He [mbar]	N_2 [mbar]
18	550	310	210	90	0.2

Because of the irregular geometry inside of the pump, the dynamic conditions and the fact that the flow regime may vary with the type of gas a quantification of the pumping performance is difficult. From vacuum technology considerations it can be calculated that the conductances for hydrogen isotopes, helium and methane are significantly higher than for N_2. While this calculation strongly suggests that backstreaming is mainly responsible for the gas type dependant pumping efficiency of scroll pumps, backstreaming alone cannot explain the observed effects. A simple backleakage calculation is an oversimplication that does not take into account all the aspects responsible for the observed effects, such as for instance a change in flow regime.

To investigate the effect of filters incorporated by the manufacturer into the pumps to protect the spiral zone from aerosols, the pumping efficiency for nitrogen and helium of a 18 m³/h scroll pump with and without filters was compared, using two different suction ports at a constant exhaust pressure of 1000 mbar (see Fig. 5). The results indicate, that the effect of the filter (pore dimension 0.063 mm) is small compared to that of the suction port. It is concluded that the pumping efficiency is governed by the clearance between the spirals.

The obtained data demonstrate that the selected pumps and pump combinations satisfy the requirements of the PETRA experiment.

Staff:

U. Berndt
M.Glugla
E. Kirste
R.-D.Penzhorn

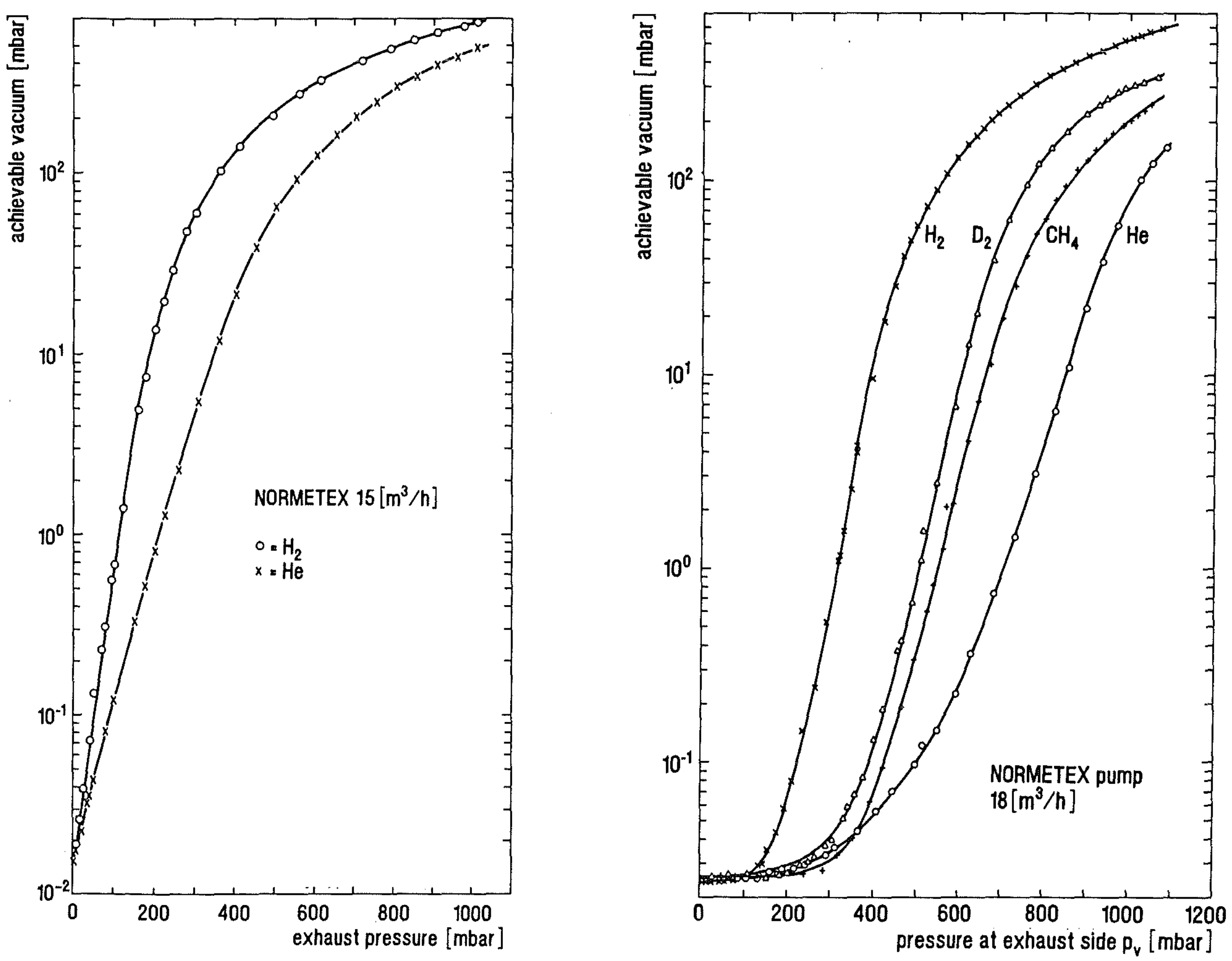

Fig. 4: Vacua achievable with a) the 15 and b) the 18 m³/h scroll pump at various exhaust pressures employing the gases to be used in the PETRA experiment

Subtask 2: Catalytic Crack Process

A catalytic process combined with selective permeation of hydrogen isotopes to recover tritium from fusion reactor exhaust gases during all operational phases was developed at IRCh of KfK during the last few years. The process is based on extensive experimental work including tests of technical scale and integral laboratory tests with up to 50 % tritium. The process shall now be demonstrated on a 1/8th NET scale with DT and tritiated impurities at the Tritium Laboratory Karlsruhe (TLK) with a facility called CAPRICE (Catalytic Purification Experiment).

The contract to design, manufacture, assemble and commission CAPRICE within a period of only 21 months was awarded to the National Nuclear Cooperation (NNC), Great Britain in March 1991. In October 1991 the engineering of the primary system described in a detailed design concept document was frozen. Engineering effort was then focussed on control and instrumentation, software development (sequence and interlocks) and in the preparation of all Job Enquiry Specifications for the complete secondary containment including inert gas atmosphere control and tritium retention systems. Finally the plant layout was assessed and also frozen. Manufacturing was started in December 1991 in accordance with the original schedule. The actual time table of CAPRICE shows, that the facility will be delivered to site by the end of 1992.

An outline flow diagramm of CAPRICE is shown in Fig. 6. The torus mock-up in the upper region of the figure comprises buffer vessels and an isotope exchange reactor for the continous synthesis of highly tritiated methane. Impurities are separated from the main DT stream with the primary loop permeator and corresponding pumps to be seen in the center of the figure. Impurity processing is carried out in the secondary loop, which esssentially comprises a catalytic methane cracker, a water gas shift catalyst bed and an additional permeator (lower right part of the figure). Liquid tritiated water will be processed with carbon monoxide as a carrier gas via the water gas shift reactor shown on the lower left. The off-gas will be sent through the primary and secondary loop in a once-through mode. Detritiated gases are sent to waste.

The layout of CAPRICE is shown in Fig. 7. The experiment is housed in a row of four gloveboxes, each with 1.5 m in length, equipped with ductwork on the roofs for atmosphere

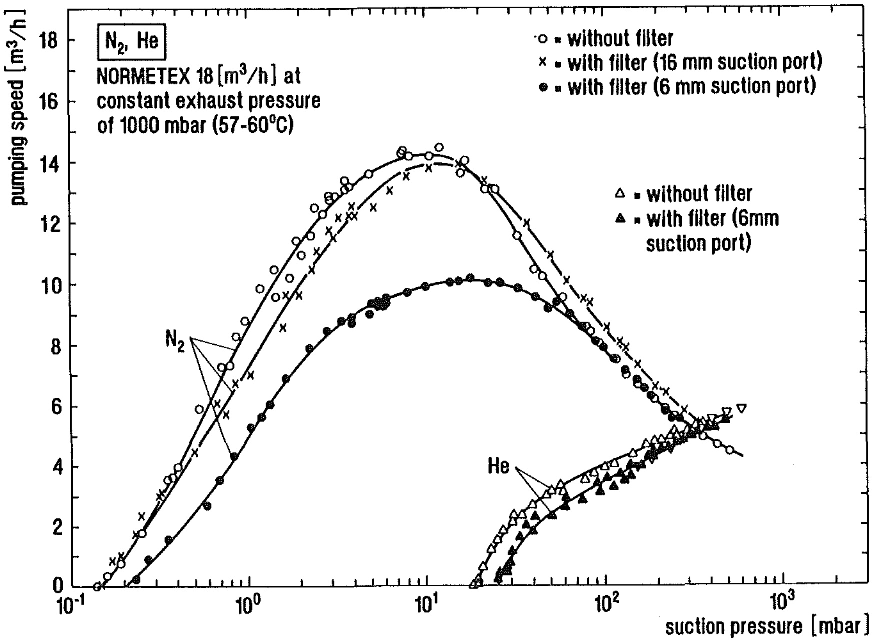

Fig. 5: Effect of filters and suction port size on the pumping speed of a 18 m³/h scroll pump when pumping nitrogen or helium at a constant exhaust pressure of 1000 mbar

cooling. The 150 m³/h Normetex pump to evacuate the primary permeator is located in a separate containment. Detritiation systems and tritium monitors for the secondary containment are shown on the right side of the figure, while operator console and electric and electronic cubicles are seen in the upper left part.

The work carried out by NNC was supported by the TLK and the IRCh staff. While at TLK the work concentrated on design, engineering and layout of infrastructure services for the CAPRICE experiment including tritium supply, return and a hard wired safety system, the IRCh was mainly in charge of i.) overall project management, ii.) the set up of the gas chromatograph, iii.) writing a safety report for licensing, iv.)

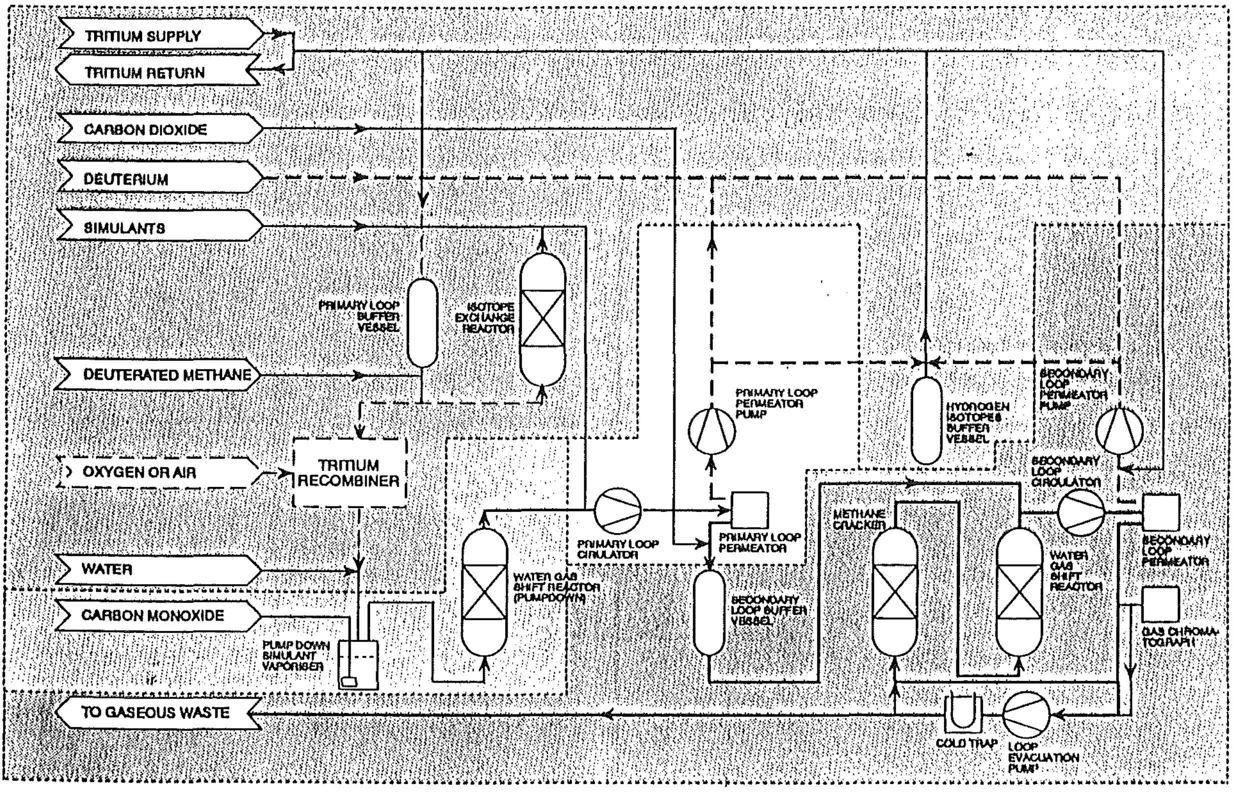

Fig. 6: Outline flow diagram of CAPRICE

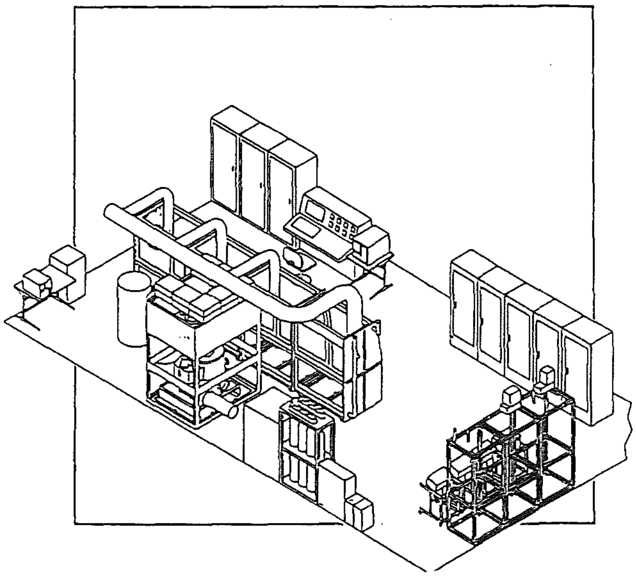

Fig. 7: Layout of CAPRICE

the conceptual design and construction of a semitechnical plant for the synthesis of deuterated methane v.) the experiments and mathematical modelling of a two hydrogen isotope permeation through Pd/Ag membranes and vi.) experimental tests on the heterogenously catalyzed CH_4/D_2 isotope exchange reaction to substantiate the design of the CAPRICE reactor for the continuous synthesis of tritiated methane.

Within the experimental program of CAPRICE the beginning of the tritium experiments is scheduled for the first half of 1993.

Staff:

M. Glugla
R.D. Penzhorn

TEP 3 Tritium Storage and Transportation

Subtask 1: Getter Storage Beds - Zr Alloys

A new facility has been constructed to evaluate the performance of the ZrCo getter beds supplied by Culham Laboratories under conditions that simulate those of the PETRA experiment. The ZrCo beds will be used not only for ttitium storage, but also to bring the experiment into the safety condition in case of abnormal occurences. Test parameters will be a) the reaction rate of ZrCo with hydrogen as a function of the bed cooling, the influence of impurities, the heat evolution during gettering, and b) the rate of release rate from the ZrCo hydride as a function of heating rate.

Employing a suitably modified experimental apparatus (thin sample layer of less than 0.5 mm thickness placed over a large thermostatized area) the reaction rate of molecular hydrogen with ZrCo powder was measured under quasi isothermal conditions. The activation energy for the reaction was found to be [10.7 kJ/mol]. At hydrogen pressures in the region 25 - 200 mbar the kinetics of hydrogen sorption can be described by a first order reaction. At higher pressures a nucleation and two dimensional growth mechanism becomes rate determining. The final evaluation of the experimental results is in progress.

Performance of technical getter beds

Performance tests were carried out with four identical large tritium storage vessels containing equimolar amounts of either U or ZrCo. The getter beds were constructed i) to characterize the properties of the ZrCo/hydrogen system under technical conditions, ii) to compare the tritium gettering properties of ZrCo with those of U, and iii) for the handling of tritium in the PETRA experiment at the Tritium Laboratory Karlsruhe.

The storage vessels, constructed using ultrahigh vacuum standards, were manufactured by Culham Laboratories according to a design from JET. The secondary vessel of the bed is sealed on one end to a flange, which also provides structural support to the hydride bed itself and to the inlet as well outlet feedthroughs. The hydride bed is of thick-walled all-welded construction to minimize tritium losses. The design allows for a pressure of 40 bar at 600 °C. The main bed body houses an axially placed finned/heater cooler assembly and two tubular filters supported from one end cap. The other end cap is fitted externally to a spacer that centralizes the bed inside the secondary container. An extension tube, which is positioned between the bed body and its supporting flange acts as a heat transfer barrier between the hot bed and the secondary container flange. Heating of the beds is accomplished in the finned heater/cooler assembly with two independent and therefore redundant electrical resistance heating elements. On the outside of the stainless steel heater body a number of circular nickel fins are brazed to assure uniform and rapid heat transfer from the heater to the intermetallic alloy hydride. The storage vessels were supplied without heating shields.

The performance of one of the storage beds upon heating to 200 °C is shown in Fig. 1. It is seen that the outer vessel temperature rises slowly up to 40 °C over a period of 400 min, when the outer vessel is continuously pumped out. The previously evacuated vessel is closed during the heating period, the vacuum deteriorates from $3 \cdot 10^{-6}$ to $1.6 \cdot 10^{-5}$ mbar; the temperature of the outer vessel, however, remains essentially unchanged. Heating the tritium storage vessel axially up to 350 °C, which is the temperature required to attain approx. 1 bar pressure with ZrCo, causes the maximum temperature of the outer vessel to reach 75 °C, provided the outer vessel is continuously evacuated (see Fig. 2). When this experiment is repeated while keeping the previously evacuated vessel closed, the isolation vacuum breakdown, i.e. reaches $2.5\ 10^{-1}$ mbar, and the temperature of the outer vessel escalates to 115 °C.

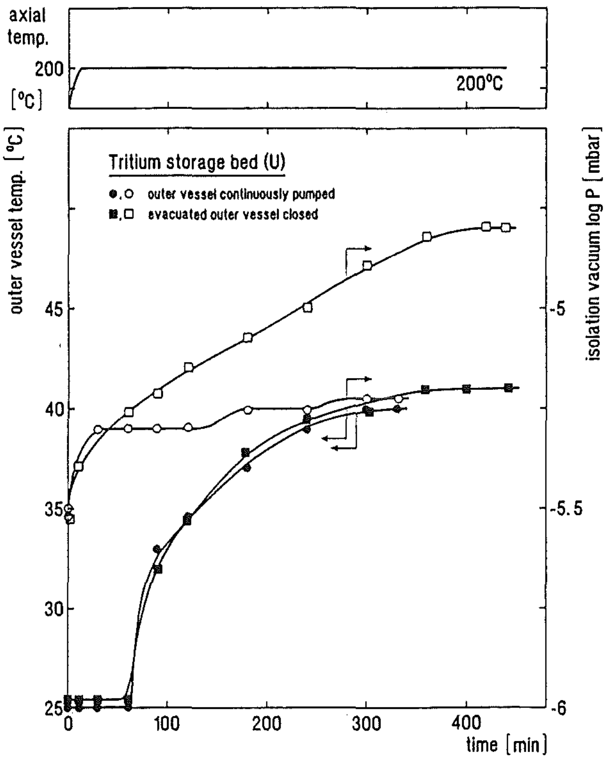

Fig. 1: Heating of tritium storage bed up to 200 °C

In another test the storage vessel was heated up to 490 °C. At this temperature it is possible to recover nearly all the gettered tritium. This high temperature will also be required for the occasional reproportionation of the getter material. As apparent from the data in Fig. 3 axial temperature of 490 °C is reached in approx. 50 min. Even during evacuation of the outer vessel with a turbomolecular pump a pressure increase from 4 x 10^{-6} mbar up to 10^{-3} mbar is observed. Other pumping methods, i.e. ion sputtering pump or a ZrCo getter bed proofed to be equally effective. The reason for the good pumping efficiency of ZrCo is attributed to the fact that the gas liberated during heating of the storage bed was found to

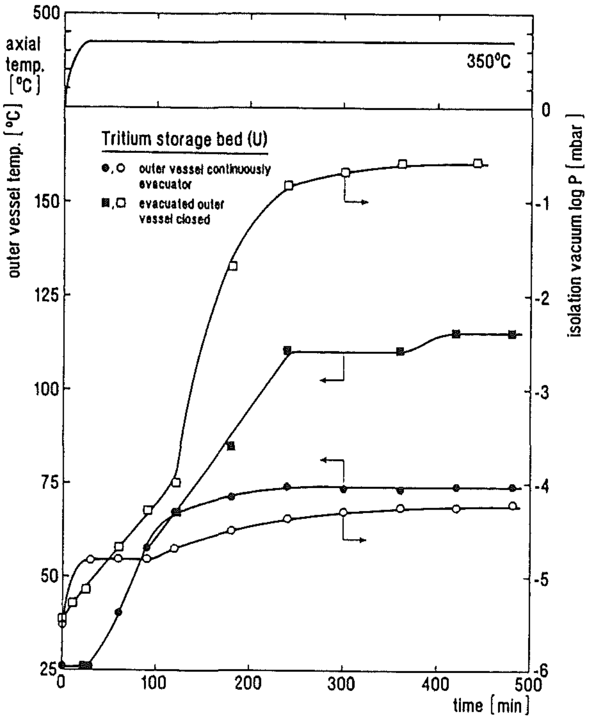

Fig. 2: Heating of tritium storage vessel up to 350 °C

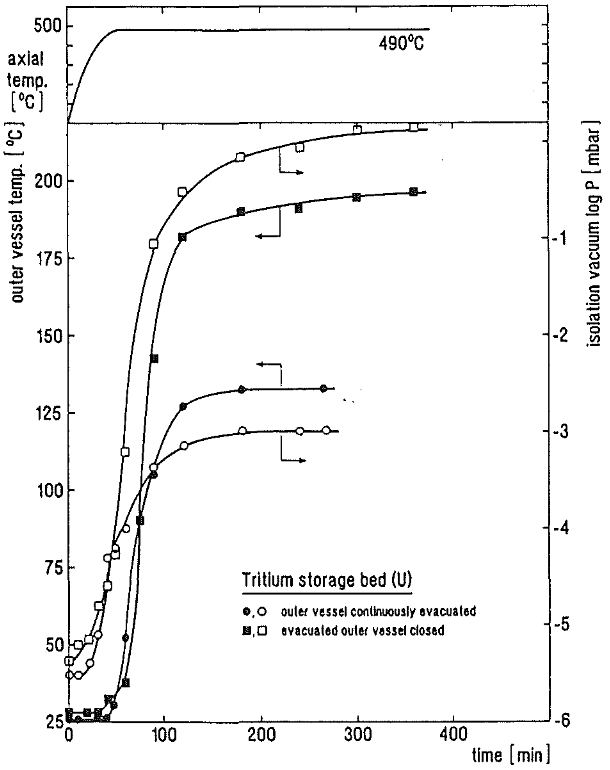

Fig. 3: Heating of tritium storage vessel up to 490 °C

be predominantly hydrogen. Closing the previously evacuated vessel during the heating period causes the pressure in the isolation vessel to increase up to nearly 1 mbar and the outer temperature of the vessel to climb up to almost 200 °C.

A plot of the difference between the core temperature (T_1) to the fourth power minus the outer wall temperature (T_2) to the fourth power vs the electrical power supplied to the getter bed during each of the above described experiments (as well as of others not given in this report) carried out under permanent evacuation of the outer vessel shows that the outer vessel temperature can be attributed solely to radiation heat transfer (see Fig. 4). From these tests it was decided to modify the tritium storage beds to include radiation shields. Because of the small free space between the actual bed and the outer vessel (only 2 mm), new outer vessels had to be constructed to accommodate the radiation shields. The material selected for the radiation shields is molybdenum.

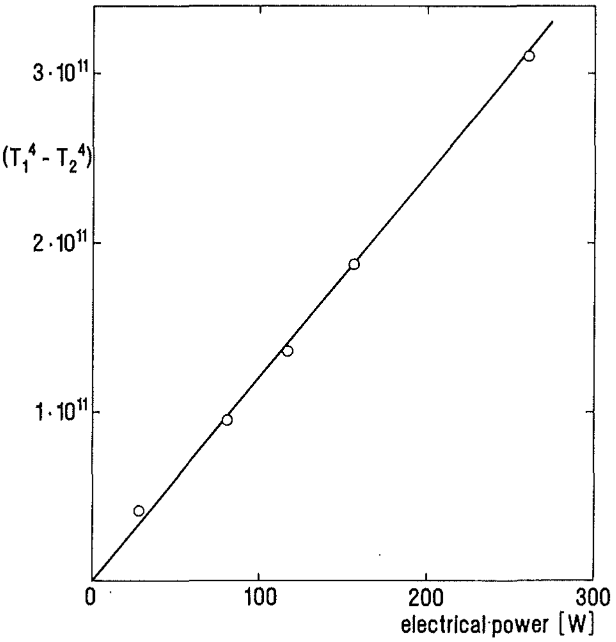

Fig. 4: Outer vessel temperature (T_2) of a tritium storage vessel as a function of supplied electrical power under continuous pumping of the isolation vacuum

Various cooling modes of the getter beds were tested. The cooling gas was circulated in closed loop operation first through a 50 l vessel and then through a copper coil dipped into a 8 °C cold bath. Closed loop operation helps to minimize Tritium release. In all the runs the starting temperature of the getter bed core was 300 °C. From the data given in Fig. 5 it is apparent that air or nitrogen provide a more rapid cooling than helium. The time required to cool the Culham getter bed from 300 °C down to 200 °C using a nitrogen gas stream of 36 [l/min] was found to be 30 min.

Staff:

M. Sirch
R.-D. Penzhorn
A. Perevezentsev (guest scientist)
E. Willin

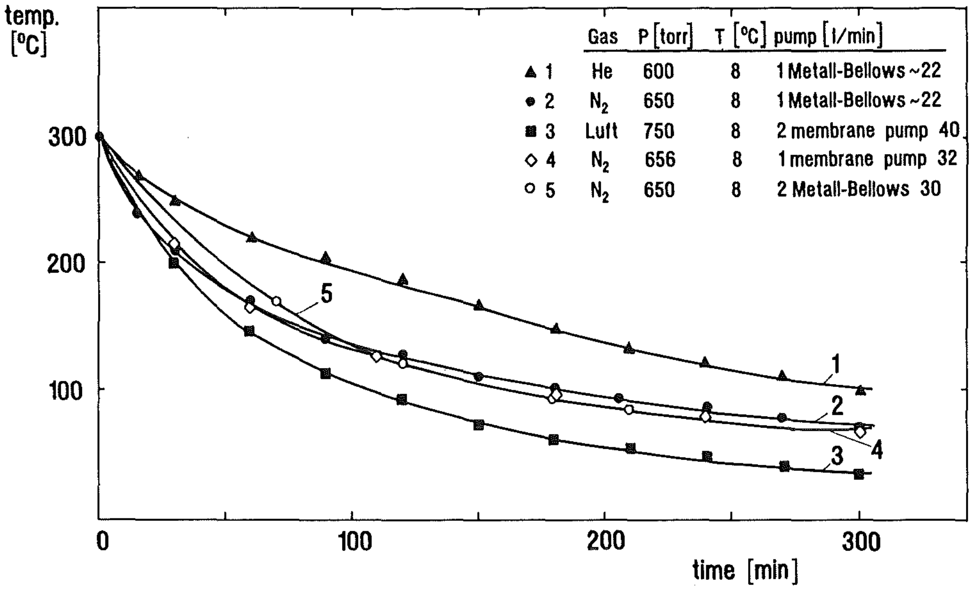

Fig. 5: Tritium storage bed cooling

NDB 2 Neutronics Data Base - Benchmark Experiments

Subtask 2: Shield Penetration Experiments

Neutron and gamma-ray flux densities penetrating the shielding blanket of NET/ITER determine the design limits of fast neutron fluence, atomic displacements and nuclear heating in the superconducting magnets. The calculation tools for $\Phi_n(E)$ and $\Phi_\gamma(E)$ have to be verified in a benchmark with experimental results [1]. From a sensitivity and uncertainty study [2] of the NET-shields it has been concluded that the benchmark must be focussed on Fe. Gaps in the shield as between two adjacent blanket segments are of special importance.

Therefore, a Fe-slab configuration with a plane variable gap has been defined and optimized with respect to both sensitivity to nuclear data uncertainties and influence of the gap in each energy interval. $\Phi_n(E)$ and $\Phi_\gamma(E)$ penetrating the assembly bombarded with 14 MeV neutrons are measured simultaneously with a liquid organic scintillator NE 213 by proton-recoil and Compton-electron spectroscopy. The simultaneous acquisition of the time-of-arrival spectra $\Phi_n(t)$ and $\Phi_\gamma(t)$ allow better resolution of the (n,n')- and (n,n)-processes and background reduction in the $\Phi_\gamma(E)$, respectively. Hydrogen-filled proportional counters shall be used to measure $\Phi_n(E)$ for $0.015 \text{ MeV} \lesssim E < 1 \text{ MeV}$.

The strength of the d-T neutron source is determined by the associated α-particles so that the Φ_n and Φ_γ can be normalized to one source neutron. The neutron generator is operated in pulsed regime for the neutron and gamma time-of-arrival spectroscopy. It has been shown by calculations and measurements, that the main background components can be determined in an additional measurement with a shadow cone in the detector collimator.

The specification and optimization of the benchmark experiment has been described in the First Intermediate Report [3].

Literature:

[1] W. Daenner, ITER Expert meeting on shielding experiments and analysis, Garching (FRG), Febr. 12-14, 1990, ITER-IL-5-0-5.

[2] T. Parish and A. Santamarina, Sensitivity and uncertainty analysis of the NET magnet neutronic design parameters to uncertainties in cross section data, CEA 917/333.

[3] T. Elfruth, J. Hanke, K. Seidel, S. Unholzer: Specification and optimization of the experimental set-up and procedure, 1st Intermediate Report to NDB 2-2. April 1992.

Staff:

T. Elfruth
J. Hanke
K. Seidel
S. Unholzer

Intense Neutron Sources for Materials Research

Critical Basic and Design Problems of a t-H_2O Source

In connection with special fusion materials development programs, the IMF has actively participated in the current international discussions on suitable candidate neutron sources for end-of-life fusion materials testing. A KfK proposal for a high-intensity 14-MeV cutoff neutron source based on the $^1H(t,n)^3He$ reaction (the so-called t-H_2O source) has been recently chosen by the IEA Working Group on Neutron Sources as one of four candidates for a worldwide Intense Fusion Materials Irradiation Facility (IFMIF) to be further developed. In the reporting period, additional neutronic calculations and more detailed investigations on critical feasibility aspects of the water target design were performed.

Concerning neutron calculations, broad-scale estimates of test cell volumes at various given neutron flux levels and of uncollided, space-dependent flux spectra were carried out for a few comparable reference configurations of d-Li and t-H_2O sources. A typical result is shown in Fig. 1 which displays the flux contours for five given "minimum-flux" levels. It can be seen that the fluxes at the same test cell positions are less than a factor of 2 smaller for the t-H_2O than for the d-Li source. The higher flow levels are, however, only achieved on the expense of a correspondingly high fraction of neutrons with energies $14 \leq E_n \leq 50$ MeV which are undesirable.

With regard to the water target design, a few remaining problems raised in the international discussions were investigated in the IRS of KfK. More detailed quantitative calculations were performed, and possible solutions were given for the following target aspects. (1) Erosion rate at the nozzle and momentum transfer down stream. (2) Jet stability at the envisaged beam power deposition in the target. (3) Water jet velocities and pumping power requirements. (4) Water vaporization and ice built up rates on cryogenic pumping surfaces. (5) Neutron production in the vapor cloud.

Literature:

[1] S. Cierjacks, Y. Hino, M. Drosg; Proposal for a high-intensity 14-MeV cutoff neutron source based on the $^1H(t,n)^3He$ reaction; Nucl. Sci. Eng. 106, 183 (1990).

[2] S. Cierjacks, Y. Hino; Additional studies related to the proposal for a novel high intensity 14-MeV cutoff neutron source based on the $^1H(t,n)^3He$ source reaction; Proc. Internat. Panel on 14-MeV Intense Neutron Sources Based on Accelerators for Fusion Materials Study; Eds. A. Miyahara, F.W. Wiffen; Tokyo, Japan, January 14-16, 1991, Nagoya National Institute for Fusion Science Report, NIFS-WS-2, p. 147, 1991.

[3] S. Cierjacks, Y. Hino; Differential flux and spectrum calculations for a novel high-intensity 14-MeV cutoff neutron source based on the $^1H(t,n)^3He$ source reaction; Acta Physica Hungarica 69 (3-4), 285 (1991).

[4] F.H. Coensgen, G.P. Lawrence, S. Cierjacks; Invited poster on "Neutron sources for fusion materials testing"; in Proc. Int. Conf. on Nuclear Data for Science and Technology, p. 395, Jülich, FRG, May 13-17, 1991, Ed. S.M. Qaim, Springer-Verlag Berlin Heidelberg, 1992.

[5] G. Class; Internal Report of the Institut für Reaktorsicherheit, KfK, June 1992.

Staff:

S. Cierjacks
G. Class (IRS)
E. Daum
K. Ehrlich
S. Kelzenberg

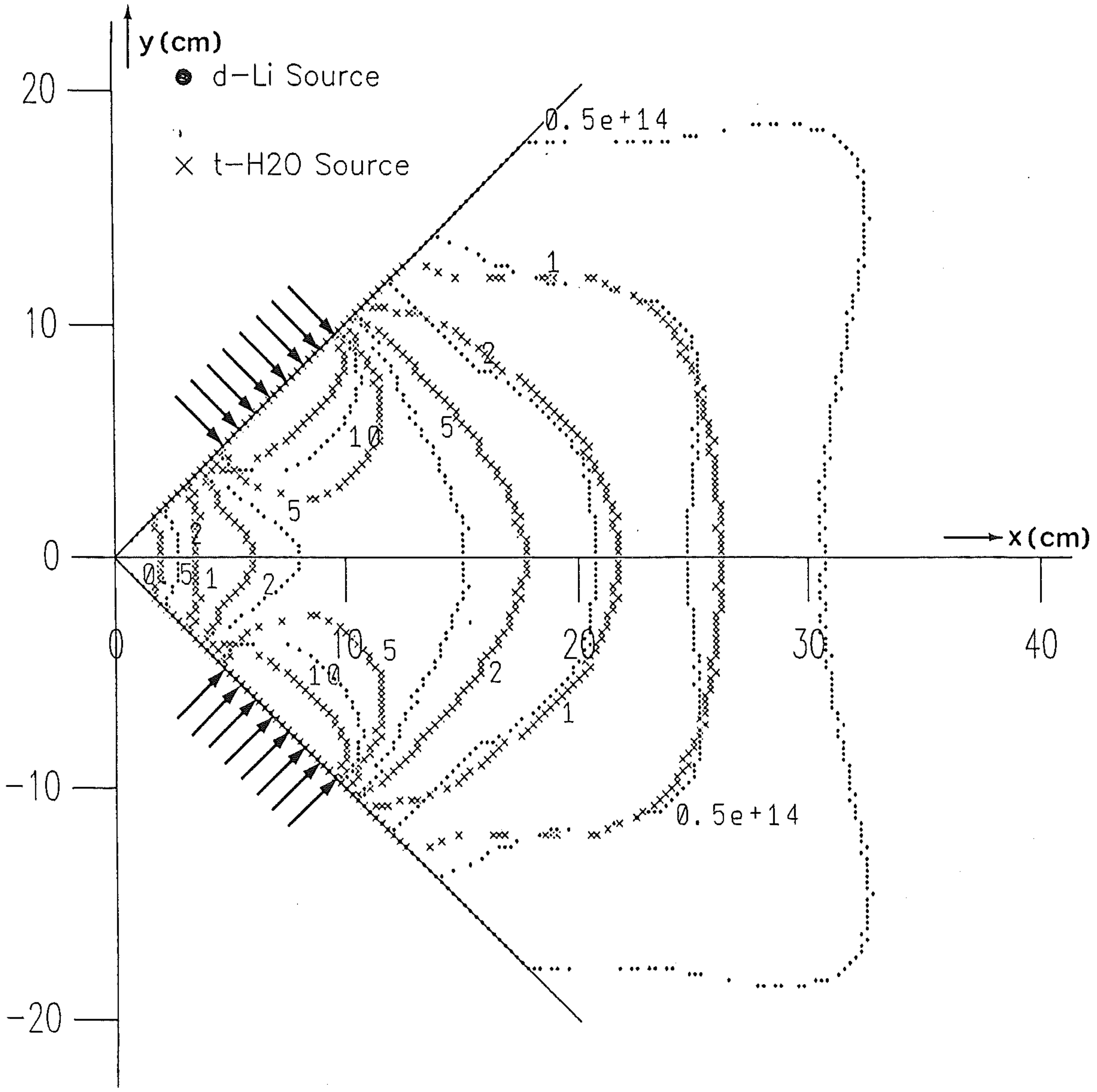

Fig. 1: Comparison of flux contours for an equivalent reference design of a d-Li and a t-H_2O neutron source, respectively. For the reference design a two-beam, two-target configuration, with 8.75 MW beam power for each branch, was chosen. Uncollided minimum neutron fluxes for 5 given flux levels are displayed.
For discussion see text.

Remote Handling / Maintenance

Introduction:

Due to the activation of most components of the NET /ITER basic machine, all operations of inspection, maintenance, connection and disconnection, assembly and disassembly will have to be carried out remotely from the very start of the physics phase. Hands-on or semi-remote maintenance will be possible only in limited areas and for some peripheral components.

The maintenance of the in-vessel components has been identified as a key problem. The preferred solution for NET and ITER is the removal of divertor plates and protective tiles through equatorial ports by an articulated boom or an in-vessel vehicle and of blankets by a blanket handling device from top openings. The equipment for in-vessel maintenance will have to operate under extreme conditions of radiation and temperature. The large variety of operations to be carried out requires versatile and replaceable tools attached to different work units with large lifting capabilities. The high availability targeted by NET will require that in-vessel operations have to be carried out with relatively high speed.

Most of the KfK work concentrates on the development of an in-vessel handling unit (IVHU) with an articulated boom transporter (ABT) and different work units (task RHT 1). This system is primarily needed for the maintenance or replacement of in-vessel components during short term interventions.
The engineering design of the ABT has been completed (phase I of Subtask RHT 1-1).

The Experimental Device for In-Torus Handling EDITH is the prototype of this system (subtask RHT 1-2). It is required to demonstrate that the maintenance of plasma facing components can be carried out with the anticipated reliability and time. It is also needed to optimize the IVHU components and subassemblies and to test different control algorithms.
EDITH has been constructed in full scale, supplemented by a full scale mock-up for divertor plate and protective tiles handling (subtask RHT 1-3) and a manipulator positioning unit (subtask RHT 1-4). The hardening of sensitive IVHU components for NET/ITER typical temperature and radiation levels are being performed in close cooperation with SCK/CEN Mol (subtask RHT 1-5).

Most of the work performed within task RHS 1 of the 1989-91 programme to standardize and qualify basic machine components and to develop remote techniques to assemble and dissassemble these items has been finished, e.g.:

- Electrical connectors	(RHS 1-1),
- Pipe connectors	(RHS 1-2),
- Fluid connectors	(RHS 1-3),
- Welded connectors	(RHS 1-4) and
- Welded vacuum lip seals	(RHS 1-5).

In 1992-94 KfK concentrates its efforts on the development of tools for cryo-connectors (subtask RST 2-1, former subtask RHS 1-6).

Task RHB 1 (RH common subsystems) is new. The objective of this task is to develop different subsystems of common interest and specific applications in various tasks of the remote maintenance program.

Typical subsystems of this type are:

- A 3-D real time kinematic simulator (subtask RHB 1-1) and

- A RH workstation (subtask RHB 1-2).

The work for task RHB 1 is being performed in close cooperation between KfK and JRC Ispra.

RHB 1 RH Common Subsystems

The objective of this new task is to develop a number of subsystems of common interest with specific applications in various tasks of the maintenance programme, in particular those related to the development of prototype equipment.

Typical subsystems of common interest are:

- A 3-D real time kinematic simulator
- A RH workstation.

Subtask 1: Kinematic Simulator

The goal of this subtask is to select a three dimensional kinematic simulation system for the spatial simulation of maintenance devices and of maintenance sequences for ITER/NET in addition to a standard CAD system. As a first step in this subtask the requirements definition document as a basis for system selections and tests is being elaborated.

Subtask 2: Remote Handling Workstation Development

The development of a remote handling workstation for ITER/NET is based on the results of a NET study contract which are documented in [1]. The elaboration of the requirements definition documents for the remote handling workstation is the first step also in this task.

Both subtasks are being performed in close cooperation with JRC Ispra.

Literature:

[1] Leinemann, K.:
NET Remote Workstation. KfK-4785, Oct. 1990.

[2] Kühnapfel, U.:
Graphische Realzeitunterstützung für Fernhandhabungsvorgänge in komplexen Arbeitsumgebungen im Rahmen eines Systems zur Steuerung, Simulation und Off-Line-Programmierung. Diss. TU Karlsruhe 1991.

Staff:

U. Kühnapfel
K. Leinemann

RHS 1 Qualification of Standard Components

In the framework of this task the connecting elements and tools for remote maintenance within the NET/ITER radiation shield were investigated, tested, qualified and standardized.

The data sheets resulting from these activities will constitute the main part of the Remote Handling Manual (R.H.M.).

The following standard components were investigated:

RHS 1.1	Electrical connectors
RHS 1.2	Flange connectors
RHS 1.3	Fluid connectors
RHS 1.4	Welded connections of pipes
RHS 1.5	Welded vacuum lip seals of blanket segments
RHS 1.6	Cryogenic connectors

All subtasks except for subtask RHS 1.6 "cryogenic connectors" were completed at the end of the program period 1989 - 91. A brief summary is given below of the realization and results of these subtasks.

Subtask 1: Electrical Connectors

Under this subtask a range of electrical connectors for standard nuclear use as well as for special application were investigated, tested and qualified.

The results obtained for the electrical connectors for standard nuclear use may be summarized as follows:

(1) For general nuclear use the push-pull type connectors should be chosen as the standard electrical connectors.

(2) Because of the better handling capability and visibility during insertion the elbow version should be preferred whenever possible. The straight-on version should be regarded as a back-up.

(3) As described in the final report [1], the requirements were fulfilled best by the connector family manufactured by LEMOSA.

The handling deficiencies which were found when testing the push-pull type connectors led to a number of modifications. These modifications were extensively discussed and coordinated with the selected manufacturer LEMOSA to provide a basis for integrating the modified designs into series production. An agreement was reached on the future NET/ITER design, and a corresponding order number was fixed.

For the not yet clearly defined electrical connectors for special applications three different high-pin-density connectors available at KfK were tested under R.H. conditions.

The test results, a video which displays the remote handling trials, pictures taken during testing, and proposals for the R.H.M. data sheets were compiled in the form of a final report [2].

Subtask 2: Flange Pipe Connectors

The objective of this subtask was to rationalize a range of flange connectors which are suitable for remote handling.

Following the selection of the JET type as the standard flange, emphasis was placed on the redesign, modification, testing and qualification of the NET/ITER standard UHV flange on the basis of the JET UHV flange design.

General drawings of standard pipe flanges were made for selected diameters in accordance with NET. The data sheet proposals for the standard range of UHV flanges were compiled in the form of a final report [3].

Soft iron material (trade name ARMCO) was tested as a gasket material for liquid-metal pipe connections. In view of the good corrosion resistance and R.H. capability which was revealed during testing, ARMCO can be recommended as a sealing material for Pb-17Li supply lines. The test results of the preliminary trials were compiled in a final report [4].

Subtask 3: Fluid Connectors

This subtask intended to select, rationalize and qualify a range of small-bore fluid connectors suitable for remote handling. In general nuclear use these connectors are applied to couple flexible hoses which may contain water or compressed air.

The investigation and preselection of the different types was followed by qualification tests and the implementation of modifications necessary to improve the connectors' R.H. capability.

The modified-connector test results were discussed with the potential suppliers for future integration of these modifications into R.H. fluid connector manufacturing. These trials were completed. The results were compiled in the form of a final report [5].

Subtask 4: Welded Connections of Pipes (BERT)

The original objective of this subtask was to develop remote handling techniques and tools for welded pipe connections and to verify the assembly and disassembly of T-shaped lip seals (see RHS 1.5) and flanged pipe jumpers for the exchange of supply lines in the upper section of the blankets. These techniques were to be demonstrated in the BERT experimental facility. BERT (Blanket Remote Handling Test Facility) is a full-size mockup of the upper parts of the NET I blanket connections and the blanket supply lines to be connected remotely.

This subtask was reorganized several times on account of fundamental considerations regarding the remote exchange of blanket supply lines. Therefore, work in BERT focused on trials of the remote exchange of the different types of bolted pipe jumpers under general R.H. conditions for NET/ITER.

The results available so far of the trials in BERT are summarized in an interim test report [6].

The pipe cutting and welding tools were tested and qualified in the FEROS test facility.

After the FEROS test facility had been made available for NET/ITER-relevant work the already existing cutting/welding tools, welding source and control system for welded connections of pipes were transferred to FEROS.

The R.H. trials in FEROS focused on the P.O.P. test using

- swarf-free cutting tools for 200 mm OD
- TIG welding tools for 200 mm OD
- pipe-end preparations for 200 mm OD

Since, in the period under review, priority had been given to subtask RHS 1.6 "cryogenic connectors", the existing remote welding and cutting tools were used for verification of the design of the cryogenic connector. The results obtained during these tests provide a preliminary verification of the specific features of cutting and rewelding concentric pipes from outside. (Investigations into bore cutting/rewelding were not part of this subtask.)

The visual remote weld inspection technique was developed and tested in parallel. The design of a quality assurance system based on visual inspection, and the documentation of welding parameters have been completed.

Subtask 5: Welded Vacuum Lip Seals of Blanket Segments

The objective of this subtask was to develop remote handling equipment and procedures for maintaining welded vacuum lip seals, and remote lip weld inspection techniques.

Originally, one planned to demonstrate the method of welding and cutting T-shaped lip seals in the BERT test facility. These lip configurations were realized in the BERT mockup. Bench tests were performed with specific cutting, milling and welding tools.

Since the basic design of the lip seals at the blanket segments was changed significally in agreement with NET, work focused instead on the investigation of different types of updated lip seals and on the conceptual design of modularized welding and cutting tools for two types of vacuum lip seals on the vacuum vessel access ports.

A design proposal for a set of lip welding/cutting tools was elaborated for NET in the form of assembly drawings showing the entire procedures. In agreement with NET Subtask RHS 1.5 is suspended in the 1992-94 program. [7].

Subtask 6: Cryogenic Connectors

This subtask will be continued in the program period 1992-94 as technology task RST 2-1 "Tools for Cryogenic Connectors".

At the end of the program period 1989 - 91 the following status has been reached:

- the general design of the connectors and the tools was agreed among KfK and NET [8],
- the general design of the rigid and flexible connector versions has been completed,
- the manufacturing of two prototype connectors has been started,
- a first set of P.O.P. trials using mockups of the rigid connectors and the existing cutting/welding tools was performed,
- the test results were compiled in a test report [9],
- the general design of the tools and of the auxiliary handling devices has been completed,

The objectives of RST 2-1 "Tools for Cryo-Connectors" in the program period 1992 - 94are as follows:

- design, technical description and preparation of a set of specifications suitable for procurement of the prototype tools for cutting, clamping, alignment and non-destructive examination (NDE) required for the remote disassembly/ assembly of the cryo-connectors,
- technical assistance in the supervision of the procurement of the tools through industrial contracts on the part of NET,
- commissioning of the prototype tools procured,
- performance and acceptance tests at the suppliers workshop and/or on the premises of KfK.

Under the new subtask P.O.P. trials and the design work have been continued. The detailed investigations of the individual working steps during disassembly/ reassembly of the connectors and the preliminary design review which was made with NET in parallel led to modifications of the tools and of the connectors. These experiences have been integrated into the design and have been documented in drawings which are already available.

Work on NDE was started with the aim of assessing the performance and applicability of the different non-destructive examination methods.

The more detailed design of the tools and the investigation of relevant non-destructive examination methods led to modifications of the detailed design of the welds on the cryo-connector. The cryo-connector manufacturing documents were changed and adapted correspondingly.

Moreover, a draft of the technical description of the tools was prepared and was handed over to NET for information along with a set of drawings for documents.

Literature:

[1] Selig, M., et al., Unpublished report of KfK, July 1990.

[2] Selig, M., et al., Unpublished report of KfK, Dec. 1990.

[3] Müller, R., et al., Unpublished report of KfK, Dec. 1991.

[4] Kirchenbauer, U., Selig, M., Unpublished report of KfK, Febr. 1991.

[5] Selig, M., et al., Unpublished report of KfK, Sept. 1991.

[6] Gutzeit H., et al., Unpublished report of KfK, Dec. 1991.

[7] Gumb, L., et al., Unpublished report of KfK, April 1991.

[8] Gumb, L., et al., Unpublished report of KfK, Febr. 1991.

[9] Gumb, L., et al., Unpublished report of KfK, Dec. 1991.

Staff:

R. Gaa
L. Gumb
U. Kirchenbauer
H. Krause
R. Müller
A. Schäf
M. Selig
D. Stern
M. Trettin
R. Ullrich

RHT 1 Articulated Boom Transporter

The aim of the task is to carry out the integral testing of the EDITH prototype articulated boom with representative sub-assemblies and end-effectors, and to demonstrate the feasibility of those in-vessel operations to be performed by the boom [1]. The experience gained will be the basis for the updating of the preliminary design of prototype equipment which will be suitable for the use in NET/ITER. The design, especially of the mechanics and the overall structure, is unchanged from the description published in the semi-annual report 1989 [2]. It is consistent with EDITH.

Subtask 2: EDITH Prototype Articulated Boom

Aim of this subtask is the design, manufacture, testing and follow-up work of an articulated boom transporter (ABT) full scale prototype (EDITH) and a mock-up to perform NET/ITER-typical boom operating procedures and to demonstrate crucial maintenance operations [3].

In continuation of the work performed during the last period of reporting [4] EDITH was delivered and assembled at the Remote Handling Laboratory of KfK (Figure 1). The commissioning of the testbed is ongoing. The control system was implemented and tested. Qualification tests of EDITH were launched.

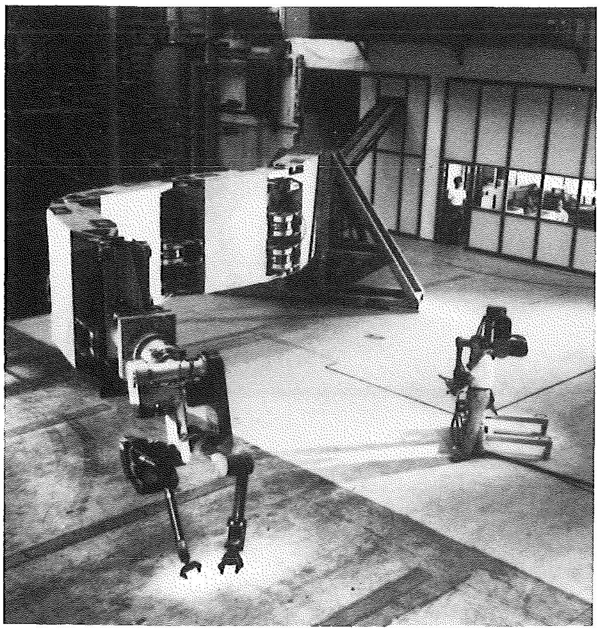

Fig. 1: Testbed EDITH

Mechanics

EDITH is composed of the support structure, four links and an interim manipulator handling unit (MHU) to investigate e.g. armour tile replacement at the first wall.

The links are actuated by coaxial drive units which were delivered by Ansaldo and assembled to the ABT taking into account the deviations of the loaded boom. Their alignment was measured by laser methods. Pretests of the drive units were performed at the supplier. By modifications, mainly of the drive unit casings, the stiffness was increased.

The MHU was fabricated at KfK and assembled to the end-frame of the ABT (Figure 2). It consists of two existing manipulators (one EMSM3 and one EMSM2-B) which are combined by means of an adaptation unit to compensate the kinematical differences of the two arms.

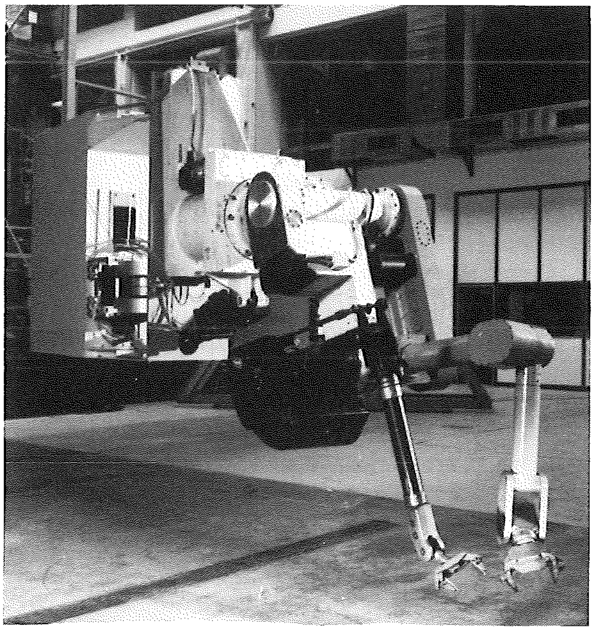

Fig. 2: Interim manipulator handling unit

In order to reach the upper as well as the lower parts of the vacuum vessel an end-effector positioning unit (EEPU) will form in a second stage the connection between the ABT end-frame and the end-effectors like MHU or divertor handling unit. The EEPU was designed by KfK (Figure 3). It consists of the support frame, two extendable slides and one trolley with a work unit interface for the end-effectors. Slides and trolley are electrically actuated via bevel gears and planetary roller spindles. Manufacturer of the EEPU is German Babcock, the delivery time is August 1992.

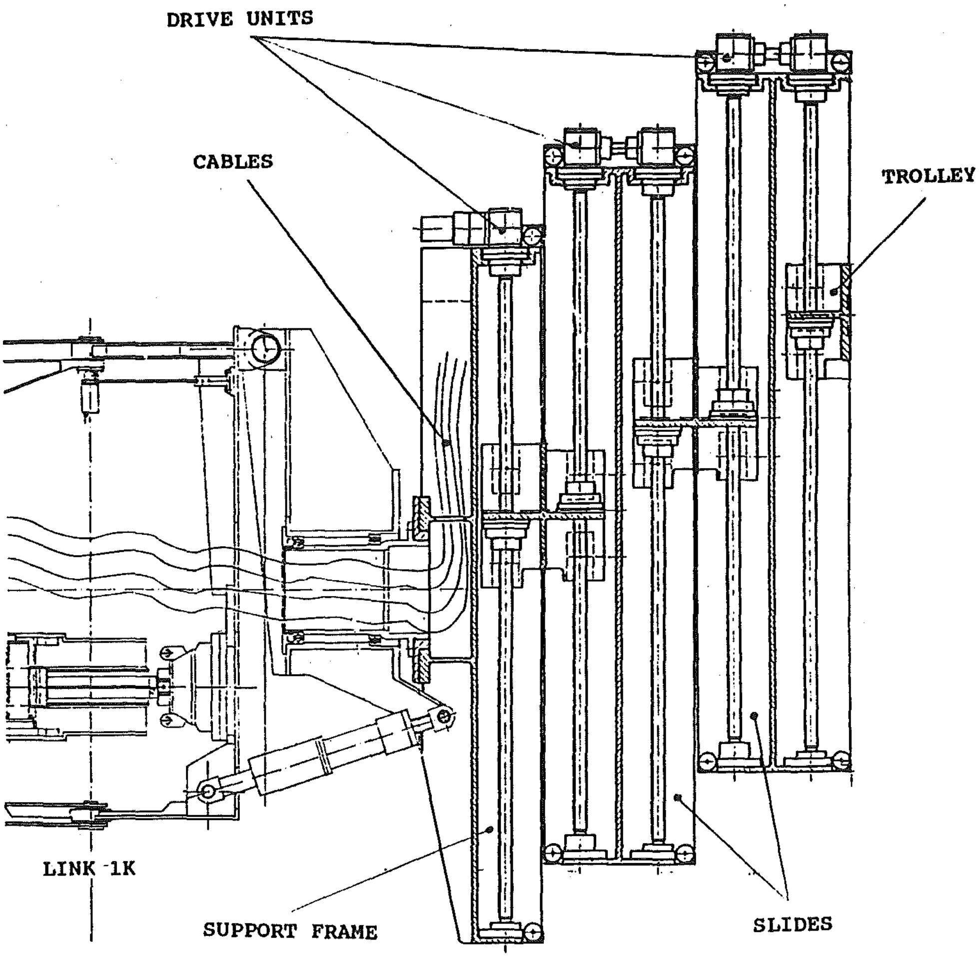

Fig. 3: Endeffector positioning unit

The mock-up [4] simulates one section of the vacuum vessel upper part. It consists of the outer and inner structures, the adaptation pieces for the tiles and divertors and these in-vessel components themselves. The outer and inner structures were fabricated as well as the first wall area with tile dummies. The components were already delivered and the mock-up is under construction. For a later stage it is foreseen to simulate also the lower vacuum vessel part. This will be possible without fabricating additional structure components but only by changing the component arrangement [5].

Control System

The general goal of the RH control system investigation is to define a framework for the RH control system development, validation, test, safe task execution, easy maintainability, and easy integration of new and/or enhanced modules from different sources. The identification of functional modules of the control system and of useful interfaces was of main interest in the general investigation phase. The specific goal in the investigation is to specify the requirements for the Articulated Boom System (ABS)-area control system and to design its functions and architecture. The RH control system is partitioned into RH-area control systems, representing the control system of a set of RH equipment grouped around a major device (e.g. articulated boom system, blanket handling unit). Each RH-area has its own RH-area control system organized as a hierarchy of computers and controllers dedicated to one RH-area. To run a RH-area control system in the operational phase a Remote Handling Workstation (RHWS) is needed. The ABS-area control system integrates the specific control systems of the devices of the ABS-area. The ABT control system is the basic subsystem of the ABS-area control system. Other subsystems of the ABS-area control system are for example the WU control systems and the camera control system.

The EDITH Motion Control System (EMCS) has been placed in the control room system and connected to the servo- and sensor electronics. The EMCS is put to operation with the ABT of EDITH, thus making possible to control EDITH by the EMCS.

The control structure has been modified to a non-central concept with one velocity-controlled motor as master and torque-controlled motors as slaves at each axis. Simulation of EDITH, controlled by a model based control structure with torque interface promises a very good dynamic system behaviour. It will be tested on EDITH in autumn 1992.

After modification of the ABT and construction of the EEPU the control software is being adapted to the new specification.

Remote Handling Workstation

To support the tele-operator as flexible and complete as possible a general purpose remote handling workstation (RHWS) concept was developed and continuously enhanced [6]. The RHWS provides the man-machine interface and operational support functions classified into procedure oriented support, working space oriented support, and device oriented support. This operational support is based on task knowledge represented by procedure models, spatial models, and functional models. These models and the related simulation systems are used for planning, execution, monitoring, training, and recovery (Figure 4). The workstation represents an intelligent, interactive, multi-media handbook guiding the operator through planned procedures and in abnormal situations.

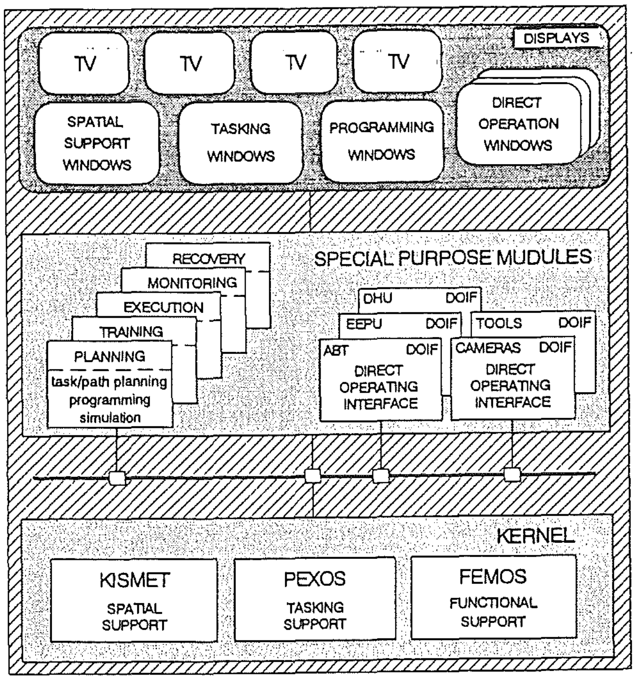

Fig. 4: Functional architecture of the RHWS

The basic subsystem of the RHWS will be a spatial simulation system like KISMET [7] originally developed for the JET-TARM control system and already successfully transferred to various non-fusion applications. The development of the EDITH remote handling workstation as a prototype of the proposed RHWS is going on based on the KISMET system. Two major subsystems are currently being developed: An IRDATA interpreter and a direct operating interface for the EDITH controller (EDITH-DOIF). The IRDATA interpreter is needed for the transfer of off-line taught-in manipulation programs from KISMET to the EDITH controller. The EDITH-DOIF brings the handbox functions on the RHWS and allows for controlling EDITH via the RHWS. This interface may also be used in the simulation mode as a training interface for the operator. The CAMERA-DOIF-software which serves to control the cameras and a TV crossbar switch via the RHWS was completed. The modelling of various EDITH scene details was going on, the models were successfully used for reachability investigations in the context of tile handling (Figure 5). Major KISMET enhancements were: a module for the general solution of the inverse kinematic problem and a bending simulation module for the EDITH model.

At JET a KfK delegate is using KISMET to support selected remote handling experiments with plant mock-ups for the development of remote handling procedures.

The generation of simulation models is the main purpose of the software package ROBOT, which is running in the Bravo3-CAD environment. This package has been augmented by a procedure which automatically extracts the shape information from Bravo3 solid models to ROBOT, such saving many time of editing. As a consequence it has been possible to transfer fusion relevant kinematic models (e.g. of the EDITH facility) to a couple of other CAD, simulation, and robot programming systems via the neutral STEP format (the processors of these tranfers have been developed in the ESPRIT project 5209 NIRO).

Overall Geometry Measurement

For precise geometric modelling, commissioning, and performance testing of large maintenance devices the remote-controlled and CAD-supported surveying system GMS (Geometry Measurement System) - based on triangulation with two or more electronic theodolites - has been developed at KfK. It serves for the determination of the actual geometry of fusion machines. In a first step, a prototype system equipped with only one theodolite has been established to show the feasibility of the sytem design. For a detailed description of the prototype system, refer to [8], [9]. The system has been employed for several surveying tasks, the determination of the permanent deformations and the deflection of the in-vessel handling boom EDITH being the most complex one [10].

By integrating a second electronic theodolite and new software for the adjusted computation of point coordinates into the prototype system, GMS has been extended to an on-line surveying system: Measurements

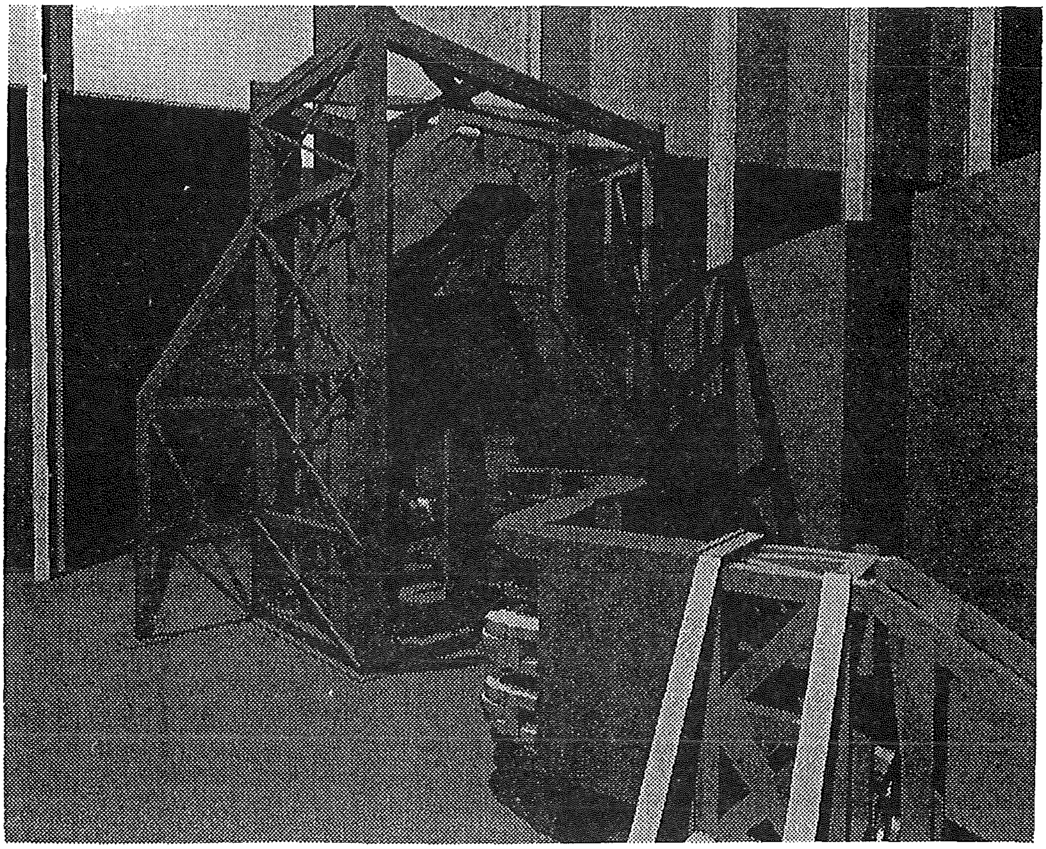

Fig. 5: KISMET simulation of EDITH: The pictures is an example for the enhanced rendering features of KISMET providing more realism

can be checked on-line and coordinates of target points can be computed on-line. These new features will speed up the GMS-surveying process considerably, thus expanding the field of applications.

Stress Analysis and Verification

The optimal design of the articulated boom demanded for an extensive analysis of the mechanical behaviour. This is discussed in detail in [11], together with the comparison of some of the computed deformations with measurements.

Dynamic Simulation

The AMBOSS (ADAMS-Modelled Boom Simulation System) software environment and ABT model have been set up to examine critical remote handling tasks and to optimize control algorithms [12].

This simulation task requires full three-dimensional modelling regarding structural elasticity and non-linear actuator dynamics. The AMBOSS dynamic simulation models the multibody dynamics of the transporter system using a commercial analysis package. Elastic links and a precise dynamic actuator model including backlash and static friction are introduced by applied forces, spring elements and differential equations. The simulation realizes a linear feed-back controller and a developement interface to test advanced control schemes.

Previous works dealed with critical in-vessel handling operations which were especially passing the transporter through the narrow port of the vessel and a disturbance situation during load transfer at the upper divertor. Latest developement of the simulation package concentrates on the examination of possible improvement of the control scheme. Mainly feed-forward algorithms were implemented into the simulation because they do not disturb a stable linear controller.

In Figure 7 performance results of the implemented controllers are compared. The reference task chosen for control optimization is a triangle path of the transporter's end-flange with edges of about 0,2 m length. At each edge motion stops. Figure 6 shows the start position of the in-vessel transporter. The first two curves plotted in Figure 7 belong to linear position controllers. The motor current control (first curve) has obviously the largest position error. The cascaded control scheme with motor servo and overlayed PD-position controller avoids large position errors.

In the next development step the joint torque evaluated in a previous simulation is added to the output of the linear servo controller (third curve). This simple feed-forward

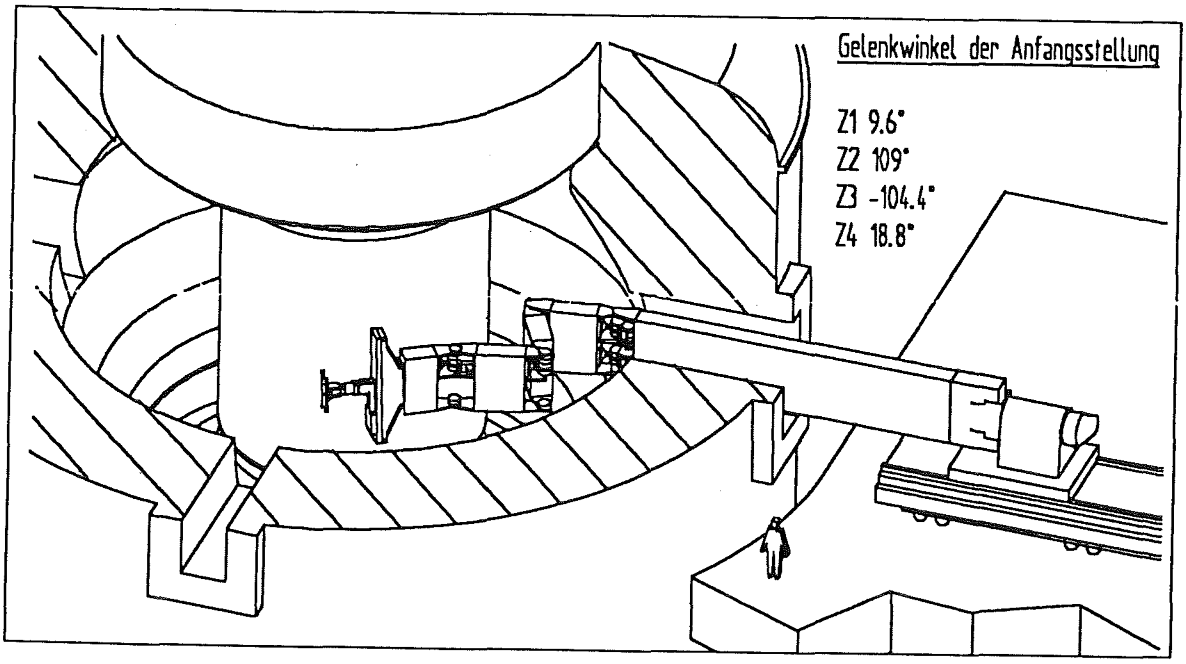

Fig. 6: In-vessel handling unit at start position of triangle path

control is improved by the introduction of an elastic gear model which compensates the expected gear deformation modifying the set point of the servo controller (fourth curve).

The AMBOSS simulation has supported the selection of the linear cascaded controller and points out possible improvements with advanced control schemes.

Verification experiments for the actuator model, the boom model and the whole system have been prepared. They will be carried out on the EDITH prototype device.

Subtask 3: Divertor Plate and Armour Tile Handling (former RHS 3-2)

Objective of this task is the design, production and commissioning of protective tiles and divertor plates handling equipment. The equipment will then be tested in the mock-up of the testbed EDITH.

Protective Tile Handling Devices

In agreement with the NET team two main devices were investigated at KfK which are the tile positioning device (TPD) and the tile detachment device (TDD).

The TPD was designed by KfK and fabricated by industry (Figure 8). It was delivered and the commissioning is ongoing. The TPD consists of the gripper system and the screwing unit. The gripper system is based on a toggle lever system and is actuated by a lifting magnet. In a currentless status the gripper is always closed, an uncontrolled unlocking is impossible. The screw driver unit consists of two screw drivers which are actuated by a common drive unit consisting of an electric motor, a worm gear and spur wheel gears. The torque of the screw drivers is limited by slipping clutches located between the spur wheels and the drivers which are pressed against the tile fastening nuts automatically by springs.

Also the TDD was designed by KfK and discussed with the NET team (Figure 9). A call for tender was launched. The device is composed of the same gripper system as applied at the TPD and the trepan system. The latter one consists of two tubular drilles which are actuated by a common electrical drive via a worm wheel gear and additional spur wheel gears. Their forward feed is performed by the same drive plus spindles. Forward feed and drilling revolutions have therfore a constant ratio.

Divertor Plate Handling Unit (DHU)

The conceptual investigations of the DHU for replacement of divertor plates were continued. According to the NET design, the divertor plates are toroidally segmented. Their supply lines and the fixation of the outer divertor plates are handled from outside the torus. The DHU is composed of the gripper positioning unit and the gripper itself. The positioning unit combines the possibility of longitudinal movement, two tilting movements and rotation. Tasks of the gripper are locking and unlocking of the inner divertor plates,the replacement of the plates and their transfer between their torus position and the transfer unit which enters the torus through additional ports arranged at the torus mid plane.

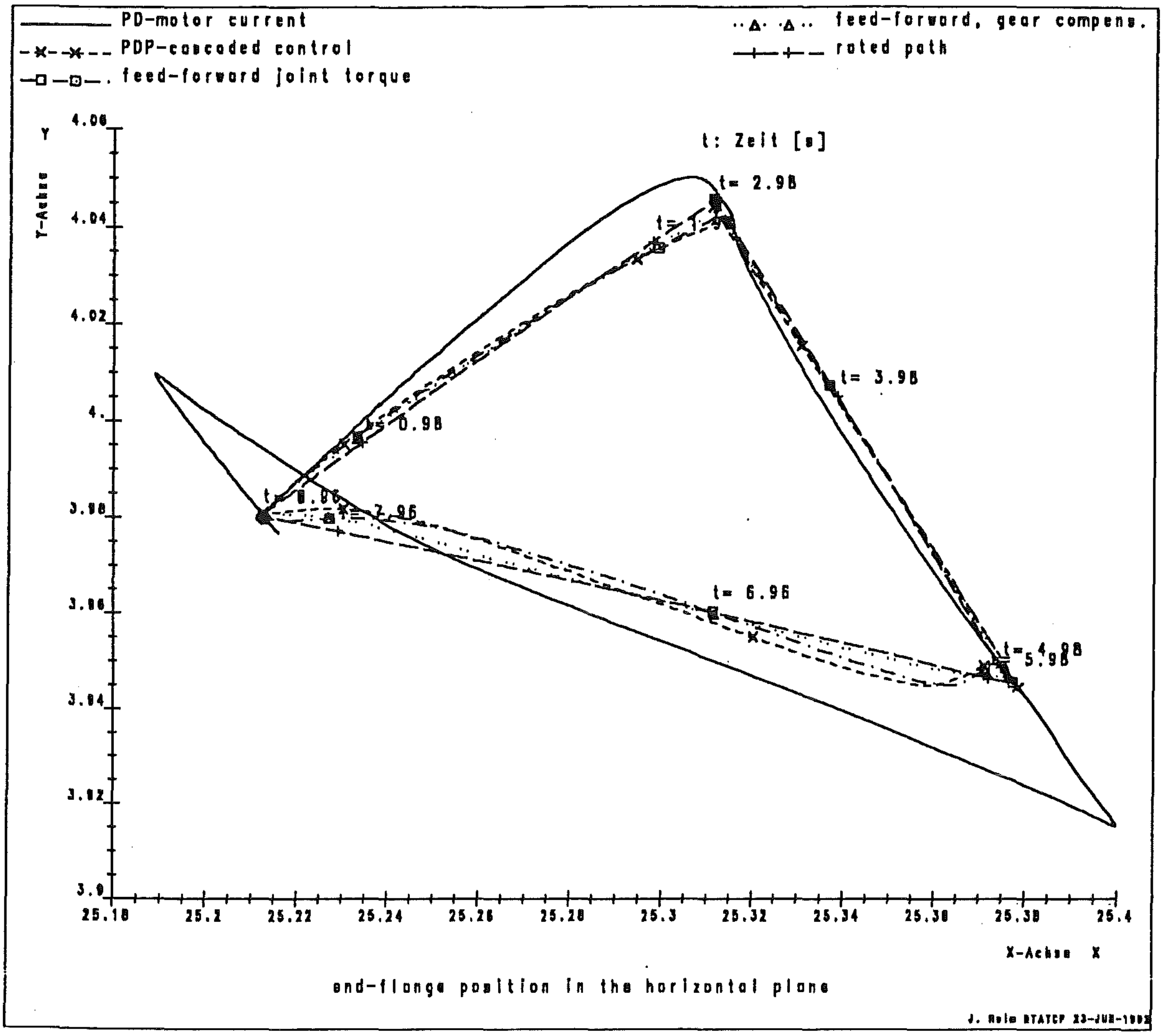

Fig. 7: Comparison of controller Layout for a triangle path

Subtask 4: Manipulator Positioning Unit

To guarantee sufficient maneuverability of the MHU a manipulator positioning unit consisting of an additional link is now under design at KfK. The MHU will be completed by two camera arms equipped with black/white cameras. The fabrication of the camera arms is ongoing.

Subtask 5: Pre- and Post Irradiation Testing of Boom Components (former RHS 2-5 and RHS 2-6)

Components of the NET/ITER Articulated Boom System have to be qualified with respect to reliability, accuracy, radiation and temperature resistance. This is ongoing in collaboration with the suppliers and according to the results of material tests. The material tests include pre-irradiation tests, irradiation tests and post-irradiation tests. Pre- and post-irradiation tests were and will be performed at KfK, the irradiation tests at the BR2 at Mol in collaboration with CEN/SCK Mol. Components to be tested are motors, resolvers, inclinometers, cables and lubricants [13].

Motors, Lubricants, Cables

Following the preliminary irradiation tests of motor base materials and the pre-irradiation tests of modified Maccon and Moog motors in a heating chamber during 1991 [4], first campaigns of irradiation tests were performed up to a total dose of 6,5E6 Gy(Si) and at temperatures of 150 °C. These tests were followed by qualitative post-irradiation investigations. The results are summarized in [14].

Based on the qualitative post-irradiation investigations necessary modifications of the motor components were identified. Failed components were mainly motor resolvers, brakes, cables and, to a certain degree, lubricants. The modifications of the motors are ongoing. This implies

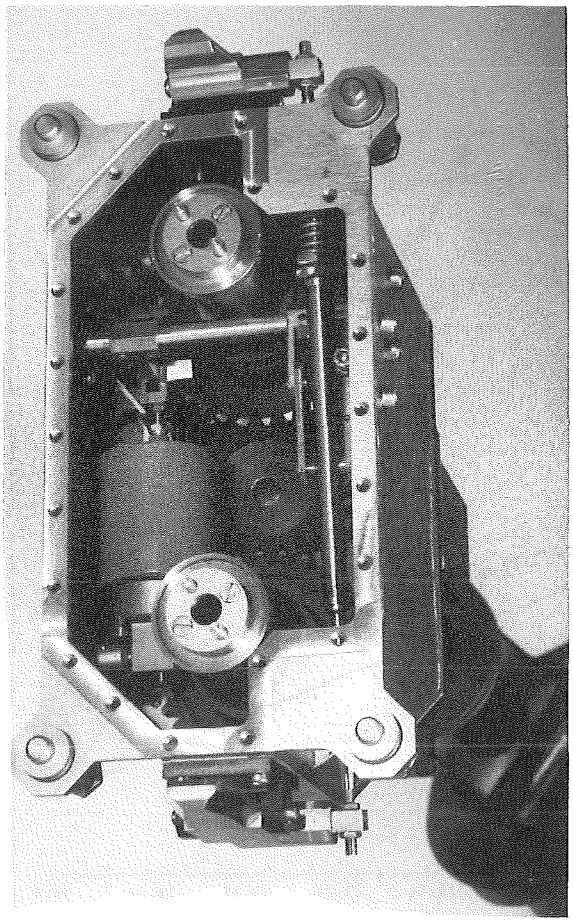

Fig. 8: Tile positioning device

- the application of two alternative resolvers to become more independent from the sub-suppliers,
- minor modifications of the failsafe brakes of the Moog motors and use of the same brake type at the Maccon motors,
- the application of PEEK and Kapton cables instead of RADOX cables,
- and the consequent use of graphite and molybdenum disulfide, respectively, as lubricant.

At the present the modifications of the motors are ongoing. Further irradiation tests with the modified motors will be performed.

Sensors and Electronics

From the evaluation of the irradiation test campaigns in 1991/92 with gamma doses up to 1.2E7 Gy(Si) and moderate ambient temperatures of 50 - 70°C it was clearly shown that only a small number of plastics may be used for sensor applications and electronics. Various specimen of plastics, cable insulators and base materials have been irradiated in the gamma irradiation facility of the BR2 reactor at Mol. Most of the plastics being exposed to up 1,2E7 Gy(Si) must be excluded from an applicability as a consequence of embrittlements and fragmentary surfaces and structures. In this context, the quality decay of nearly all electrical cables with plastic insulations was obvious. ULTRAPEK from BASF and RADOX from SUHNER did operate satisfactorily only under static and non-bending conditions, whilst PEEK and KAPTON from DUPONT turned out nearly unchanged. The total of six gamma irradiation campaigns during the time of review underline the necessity of more irradiation tests with specific plastics to overcome unsolved problems, e.g. the high degree of stiffness for PEEK and KAPTON which rises serious problems for wiring and bending of signal and power supply cables in the area of robotic links and joints. In the frame of EDITH instrumentation single- and multiturn resolvers were pre-tested and mechanically adjusted.

In the meantime, a second generation of modified resolvers containing ULTEM foils and RADOX wiring are now ready to become tested and were calibrated in out-of-pile tests. They will be irradiated during a next irradiation campaign. The schedule is due to the availability of the Gastafiore test facility at the BR2 reactor and depends on the reconstruction progress for the mechanical components of the irradiation test basket for the pneumatic resolver drives and the on-line instrumentation.

Literature:

[1] Suppan, A., et al.:
The NET Articulated Boom: Preliminary Investigations and Justification for a Full Scale Prototype. KfK 4809, Dec. 1990

[2] Kast, G.:
Nuclear Fusion Project - Semi-annual Report of Association KfK/Euratom - April 1989 - September 1989. KFK 4677, EUR 131551 EN, November 1989

[3] Suppan, A., et al.:
EDITH - A Prototypical Boom System for NET/ITER. Proc. 17th SOFT Conference, Rome 1992

[4] Kast, G.:
Nuclear Fusion Project - Annual Report of the Association KfK/Euratom - October 1990 - September 1991. KfK 4944, EUR 14015 EN, October 1991

[5] Kast, G.:
Nuclear Fusion Project - Annual Report of the ion KfK/Euratom - October 1989 - September 1990. KfK 4774, EUR 13151 EN, September 1990

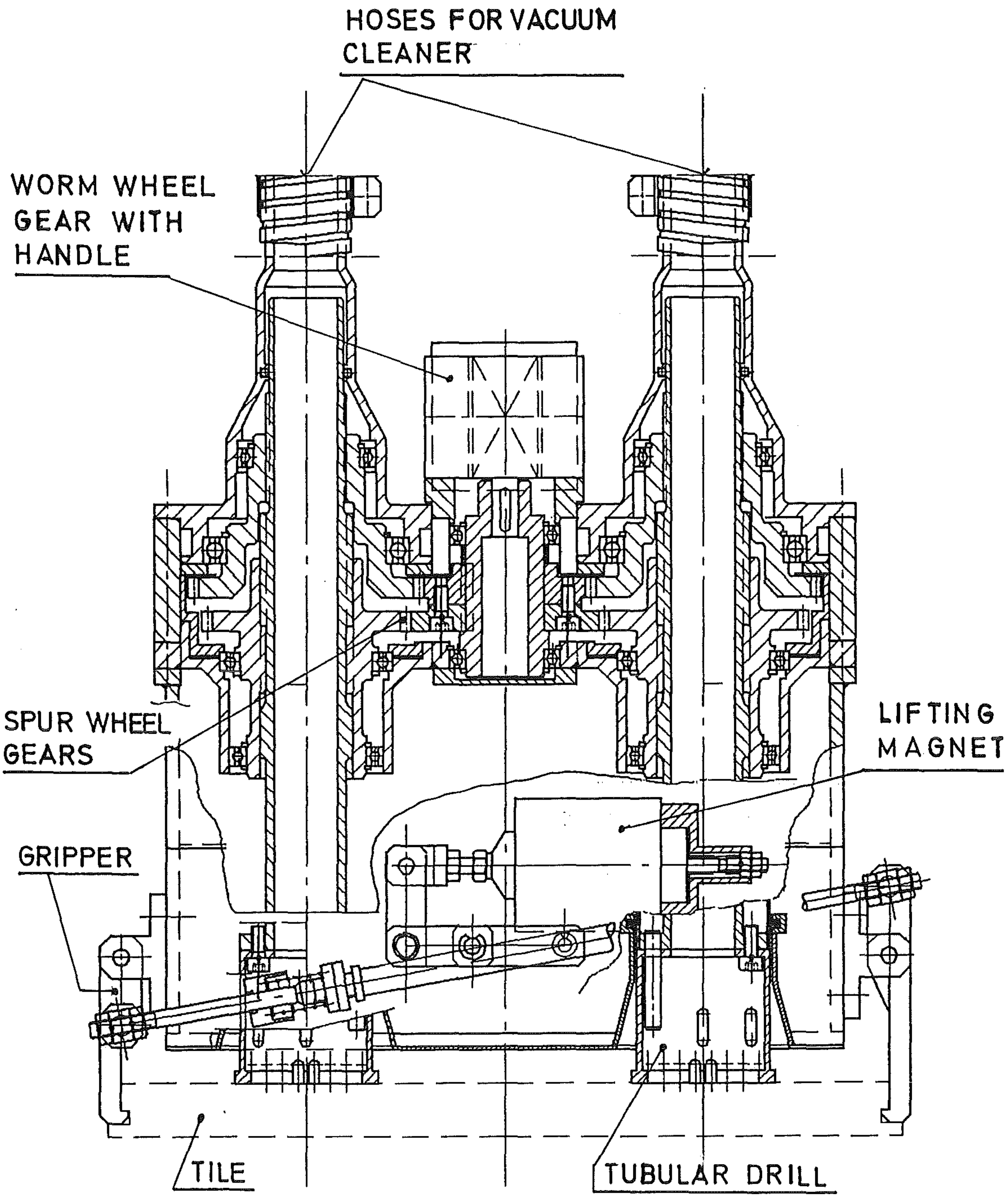

Fig. 9: Tile detachment device

[6] Leinemann, K.:
Teloperator support for fusion plant maintenance: The EDITH remote workstation. Fusion Engineering and Design, 18(1991)517-523

[7] Kuehnapfel, U.:
Graphische Realzeitunterstützung fuer Fernhandhabungsvorgänge in komplexen Arbeitsumgebungen im Rahmen eines Systems zur Steuerung, Simulation und Off-Line-Programmierung. Diss. TU Karlsruhe, 1991.

[8] Koehler, B. :
A High-precision Geometry Measurement System for Large Fusion Reactor Components. IAEA Technical Committee Meeting on Robotics and Remote Maintenance Concepts for Fusion Machines, Karlsruhe, 22.-24.2. 1988

[9] Heeg, R., Koehler, B. :
Unpublished Report of KfK, Nov. 1990.

[10] Dolensky, B., Heeg, R., Koehler, B.:
Unpublished Report of KfK, Maerz 1992.

[11] Krieg, R., Dolensky, B., Raff, S., Wehner, E.:
Festigkeitsauslegung eines Vielgelenkarmes fuer fernbediente Hantierungsarbeiten in der Plasmakammer eines Fusionsreaktors. KfK Nachrichten 24(1992)1,29-40

[12] Reim, J.:
Dynamic simulation of the NET in-vessel handling unit. Fusion Engineering and Design. 18(1991)471-476

[13] Rohrbacher, H.A., Suppan, A.:
Unpublished Report of KfK, March 1991

[14] Suppan, A., Englert, M., Rahn, A.:
Unpublished Report of KfK, in preparation

<u>Staff:</u>

G. Dillmann
B. Dolensky
B. Haferkamp
B. Haist
R. Heeg
W. Hennhoefer
E. Holler
W. E.Hoerl
J. Huebener
H. Knueppel
B. Koehler
W. Koehler
R. Krieg
U. Kuehnapfel
K. Leinemann
W. Link
A. Ludwig
G. Mueller
A. Rahn (KfK-AG Mol)
J. Reim
H.A. Rohrbacher
M. Salaske
E.G. Schlechtendahl
A. Suppan
J. Woll

Safety and Environment

Introduction:

Within the European Fusion Technology Programme 1992-94 the safety analyses for NET/ITER which are being performed in parallel to the design efforts address mainly two different areas:

Safety Assessment Studies

- Operational Safety (SEA 2)
- Reference accident sequences (SEA 3)
- Probabilistic risk studies (SEA 4)

and

Plant Related Studies

- Radioactivity inventories and source terms (SEP 1)
- Environmental impact of tritium and activation products (SEP 2)
- Waste management and decommissioning (SEP 3)

The KfK contributions to this program concentrate on:

- Analyses of reference accident sequences in superconducting magnets (subtask SEA 3-2), and

- Calculation of individual and collective doses to the public for routine and accidental release of tritium and activation products (subtask SEP 2-2).

SEA 3 Reference Accident Sequences

Subtask 2: Management System Safety

Within subtask 3.2 KfK concentrates on RAS-1a (Uncontrolled growing normal conducting zone) and RAS-1b (Low Ohm shorts and arcs on a magnet).

a) Analysis of a growing normal conducting zone with the code system MAGS.

The analysis with the code system MAGS [1] of the shut down of the NET/ITER TF coil system with one shorted coil has been continued as well as the analysis of a spurious uncontrolled quench in a coil.

The results can be summarized as follows [2]:

Quench: Current and magnetic field have a great influence on the quench velocity. The determination of quench velocities, even though it is a common practice, neglects a lot of details and is of use only for very global considerations. While in the high field very high quench velocities have been found, very low ones have been found in the low field region. Nevertheless, it is estimated here that the quench velocities are about 50 m/s, if the initial transient is over. In the case of a spurious quench (case 1) the velocity is initially only 10 m/s, whereas in the case with the shorted coil (case 2) the initial velocity is about 100 m/s.

Quench propagation due to heat conduction between turns and pancakes was observed. A general statement on it's importance, however, is difficult. It certainly is important, if the quench initiation is in a central winding of a pancake, e.g. in the fourth or fifth turn. Then the quench propagation via heat conduction will be more effective than via the He-inlet pipe (see below).

The helium distributing and collecting pipes are important promotors of quench propagation in a coil, since they affect all pancakes of a coil at once. On the other hand they must be designed to cope with the loads during a quench in terms of stresses and temperatures.

Current: While in case 1 the current for the time of the analysis is practically constant, in case two (see Fig.1) the current in the shorted coil (solid line) increases due to induction up to its maximum value of about 60 kA at about 22 seconds. Then the critical current is reached in the high field zone of the coil, and quench is initiated. The growing resistance due to the growth of the normal conducting zone reduces the current with a ramp of about 5 kA per second. The reduction in the other coils, caused by the dump resistances, leads to a linear decrease of it with a ramp of about 0,8 kA per second (broken line).

Voltage: It was found that small normal conducting zones, e.g. in case 1 a quenched zone of 3 m length, lead to a voltage in the order of 4 V. This can be detected reliably by a safety system. Peak voltages observed in case 2 run up to 10 kV for a TF coil. Between individual pancakes voltages run up to 870 V, and between turns in a pancake up to 160V.

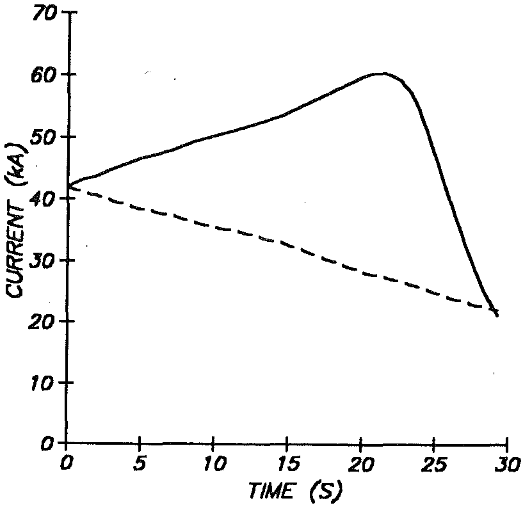

Fig. 1: Currents in TF coil circuit for case 2; upper curve shortened coil, lower curve dumped coil

Temperature: The temperatures in the cable space grow initially at rates of 60 K/s and 120 K/s for cases 1 and 2, respectively. For case 1 a separate, simplified investigation has shown that temperatures will grow until melting and insulation failure is reached. For case 2 (see Fig. 2) 600 K is about the maximum temperature in the coil

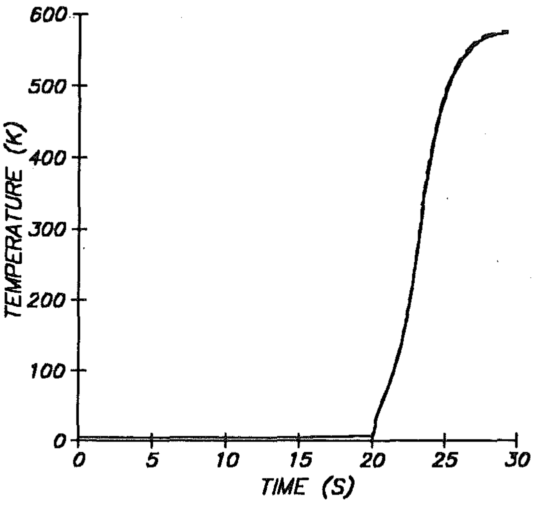

Fig. 2: Peak temperature in cable space for case 2 plotted versus time

The spatial distribution of the temperature shows that there is no hazard in terms of a local heat up of a coil cross section with the potential of a coil unclasp.

A more detailed analysis of the temperature field shows that, while a pancake is not quenched completely, the temperature of its steel jacket can be estimated for zones with a quenched conductor by cable space temperature times 0,6. Similarly, the temperature of the insulation between the pancakes can be estimated by cable space temperature times 0,25.

The circumferential temperature difference of a steel jacket is only 1 K to 3 K, for quenched zones. In zones, where quench propagation due to heat conduction can be expected, the differences may run up to 8 K, showing that a detailed representation is necessary for modelling of this effect. The temperature differences of the steel jacket between adjacent turns are up to 100 K.

Pressure: The pressure in the conductor can reach considerable values. Values beyond 200 bars have been calculated.

b) Analysis of the mechanical behavior of the coil casings under accident conditions.

The work reported in [3] has been continued. The aim was to find critical loadings initiated by electrical faults and to analyse the consequences for the structure. Concerning the actual design this work has been finished.

The electrical faults considered are short circuits or power control malfunctions for both toroidal field coils (TF coils) and poloidal field coils (PF coils).

Typically the electrical faults in the TF coil cause non-axissymmetric force distributions for the TF coil structure and overturning moments and lateral forces for the PF coils. Electrical faults in the PF coils yield high out-of-plane and inplane loadings for the PF coils and high axissymmetric out-of-plane loads for the TF coils.

As a rule the critical electrical faults lead to high induction currents followed by a coil quench. At this state the loading reaches its maximum. Therefore the current at quench is a key value for critical loading, and reliable quench calculation is very important. But detailed quench analyses need a high effort. Therefore the results reported here are based on more simple calculations expected to cause somewhat pessimistic loadings. Detailed quench analyses may be rerun in a next step for the most critical cases.

The principal mechanical behavior and the relevant failure mechanisms of the complex structures have been evaluated using rather simple but transparent models.

Several critical parts have been identified leading to structural failure under fault conditions [4,5,6]. In terms of safety analysis there are two failure categories: tolerable failures where the damage is confined to the magnet system, and severe failures typically being of unstable kind impairing neighbouring radioactivity confining components. The following critical parts are of the latter type where in the actual design a loss of integrity could be initiated:

- Local instability of the central vault in the equatorial plane under radial bending moments due to TF coil faults.
- Loss of torsion rigidity of the central vault under increased torsional loading due to PF coil faults.
- Failure of the coil case bolts and subsequent large unstable lateral displacements at the upper TF coil arches due to increased out of plane loads under PF coil faults.
- Rupture of the solenoid stack structure caused by strong repelling forces due to PF coil faults.
- Rupture of the outer ring coils under excessive hoop stresses due to PF coil faults.
- Rupture of the supportings of the outer ring coils loaded by overturning moments due to TF coil faults.

Having got an overview on the structural behavior the results may be confirmed for the most critical cases using more detailed FEM calculations.

In the next step the consequences of the structural failures on the surrounding radioactivity containing components will be investigated. But this work will depend on details and modifications of the expected new ITER design.

To avoid these failures proposals for an improved design have been made. In the first three cases the failure does not occur due to excessive stresses in the components but is initiated at the interface areas of the composed structure where the clamping is not sufficient. The proper design of such interface connections is of more principal nature and should be investigated in parallel to the designers' work.

Literature:

[1] R.Meyder
KfK Internal Report (May 1992)

[2] G.Bönisch, G.Hailfinger, R.Meyder
Analysis of quench propagation and coupled thermo-hydraulic behavior of coils using the code system MAGS

[3] Contributions to Nuclear Fusion Project Annual Report of the Association KfK/Euratom, October 1991, KfK 4944, Sept. 1991

[4] S.Raff, E.Wehner
KfK Internal Report (July 1990)

[5] S.Raff, E.Wehner, Y.S.Hoang
KfK internal Report (March 1992)

[6] S.Raff, E.Wehner, Y.S.Hoang
KfK Internal Report (August 1992)

Staff:

G. Bönisch
B. Dolensky
G. Hailfinger
Y.S. Hoang
R. Krieg
R. Meyder
S. Raff

SEA 5 Assistance in Preparation of Safety Reports

Subtask 2: Safety Assessment of the NET Magnet Systems

As a contribution to the preliminary safety report for NET a status report on the preliminary safety assessment of the NET magnet systems has been elaborated as of May 1992 [1]. This report is the final report of the task SEA 5.2.

The conclusions drawn in this report are the following ones:

The induced radioactivity in the magnets is small. However, the large amount of stored energy within the coils is considered to be a potential hazard by the possibility to initiate or enhance magnet failures. A still open question to be investigated is whether faults in the magnets may have the consequence that the containment function of an adjacent component is lost. Mechanisms that may lead to a failure are mechanical or thermal electrical impacts or a combination of both.

At KfK a wide spectrum of magnet accidents has been investigated theoretically and experimentally. A short summary of the results is given here.

With respect to safety questions comprehensive experimental investigations on the TESPE torus and corresponding analyses have been performed in order to identify the most relevant faults in TF coil systems. For this part of the safety studies it was assumed that a certain failure has happened and its safety consequences were investigated.

It could be shown that each of the following single events can be taken without safety relevant damage by the magnet system being appropriately designed: Loss of cooling, loss of insulation vacuum and magnetic buckling. Their significance grows in case of simultaneous occurrence of further faults like local damage of electrical insulation outside of the magnets.

However, there are two major faults which had to be studied in more detail due to their safety relevance, namely short-circuits and electrical arcs. Arcs may occur inside or outside of magnets, they may burn in parallel to an inductance or in series. As the environmental conditions (such as magnetic field, various materials as heat sinks, melting and evaporation of materials, gas streams, surface geometry) have a significant influence on the current-voltage characteristics of the arcs, an extensive experimental program was performed. Good reproducibility was found when the environmental conditions were kept. Depending on the conditions values of the burning voltage were found between 20 and 200 V at the currents available in the experiment. This reproducible data basis can be taken for assessing corresponding values by law of similarity. For instance, a 40 kA / 20 mm arc corresponds to a voltage of 100 to 400 V. With these values the current distributions in the system and the energy deposition were calculated.These energy values show clearly the significance of the electrical arcing in the magnet system. Safety relevance can be seen e.g. when a series arc burns to such a length that neighbouring sensitive components are closer than the arcs electrodes, or when a gas stream takes the arc to other components, or when the magnetic field drives the arc, etc..

While the significance of electrical arcing could be demonstrated it should be also made clear that appropriate system design will be capable of handling these questions. However, it is necessary to assist the designer by investigating in more detail the precursors of the named faults, to find more mitigating measures, and have a detailed analysis of the reference accident sequence.

The question of missile generation is under investigation. The status of work is encouraging as the new results obtained so far lead to dramatically lower conversion of magnetic energy to kinetic energy than assumed till now.

To analyse thermal failure events the modular code system MAGS has been developed. MAGS has the capability to describe all essential effects of this events. As sample cases a quench evolving at the operational current as well as the quench of a shorted TF coil during the dump of the TF coil system were investigated. The following results were found:

- Importance of local magnet field on quench velocity

- Importance of helium plena for quench propagation

- No local hot spot during quench

Subject of structural analyses was the evaluation of the consequences of faults in the electric systems on the magnetic loading and the mechanical response of the structures.

According to the different fault locations a systematic study on the spread of the mechanical consequences on the subsystems has been performed. Then a fault scenario for the different circuits with different fault modes (short circuit, erroneous control) has been established containing about 40 fault cases. The transient currents of the circuits coupled inductively have been determined and the magnetical loadings on the coils have been calculated for all cases. The principal mechanical behaviour and the relevant failure mechanisms of the complex structures have been evaluated using simple, transparent models. The results have been confirmed for critical cases by FEM calculations.

Several parts have been identified leading to structural failure under fault loading conditions. In terms of safety analysis there are two failure categories: tolerable failure, where the damage is confined to the magnet system and severe failure, typically being of unstable kind and possibly impairing neighbouring radioactivity confining components. The following critical items are of the latter type where with the actuel design concept a loss of integrity could be initiated:

- Local instability of the central vault in the equatorial plane under radial bending moments due to TF coil faults

- Loss of torsion rigidity of the central vault under increased torsional loading due to PF coil faults

- Failure of the coil case bolts and subsequent large unstable lateral displacements at the upper TF coil arches due to increased out-of-plane loads under PF coil faults

- Rupture of the solenoid stack structure caused by strong repelling forces due to PF coil faults

- Rupture of outer ring coils under excessive hoop stresses due to PF coil faults.

To avoid these failures proposals for an improved design have been made. The failure of the first three items does not occur due to excessive stresses in the components but is initiated at the interface areas of the composed structure. Sometimes theses interfaces are needed for electrical insulation. The proper design of such interface connections is of more principal nature and should be investigated in parallel to the designers work.

For more details about the KfK investigations on magnet safety see the contributions under SEA 3.2.

Concerning further analyses it is recommended to concentrate on those events which have a potential to propagate from the magnet system to adjacent components. The following events are considered to have a potential of failure propagation:

- Uncontrolled growing of a normal conducting zone

- Electric arc outside a coil

- Electric arc inside a coil

- Coil deformation or displacement

- Volume change of cryogenic helium.

Literature:

[1] W. Kramer, R. Meyder, S. Raff, K.P. Jüngst, H. Kronhardt, Preliminary Safety Assessment of the NET Magnet System, KfK 5059, May 1992

Staff:

K.P. Jüngst
W. Kramer
H. Kronhardt
R. Meyder
S. Raff

SEP 2 Environmental Impact of Tritium and Activation Products

Subtask 2: Doses to the Public due to Normal Operation and Accidental Releases

The computer model UFOTRI [1], which dynamically describes the relevant transport processes of tritium in the environment, has been improved by the incorporation of additional submodels. The soil-water model was compared with experimental data of an environmental measurement station of the Meteorological Institute of KfK (IMK) near Karlsruhe. The overall agreement of the model calculations with the measurements is encouraging. Only in the case of rain events the model predictions overestimate the measured daily evapotranspiration rates up to a factor of two.

Two additional nutriment plant species - cereals and potatoes - were introduced in UFOTRI during the preceding working period. By changing the plant model from continuous harvesting to a fixed harvesting time - for potatoes and cereals - the concentration of organically bound tritium (OBT) becomes more important for the dose assessments. To describe the reality in a better way, the transfer of tritium in the plant tissues (HTO) to the organic plant matter was changed. The dominating way to build up organic material is the photosynthesis process. Thus, the translocation of OBT into the seed of winter wheat, the tubers of potatoes and the organic parts of grass and leafy vegetables is now based on a simple photosynthesis model. A net hourly photosynthesis rate is calculated dependent on the actual time within the period from blooming to harvesting, the leaf area index, the incoming photosynthetic active radiation (PAR) and the status of the plant stomata. Together with a weighting factor (no uniform distribution of HTO in the plant) the photosynthesis rate is directly correlated with the transfer rate into the OBT compartment.

Parts of the plant and dose model of UFOTRI were implemented in the Lagrange particle model TRAVELING [2] which has been further developed at KfK/IMK to allow for atmospheric dispersion calculations for accidental tritium releases. If coupled to the flow model KAMM, it will offer the possibility to calculate concentration fields and dose distributions in complex terrain or for non-Gaussian atmospheric dispersion conditions.

Dose calculations were performed for accidental and normal operation releases of tritium and activation products [3].

For accidental releases, the computer codes UFOTRI and COSYMA [4] for assessing the radiological consequences of tritium and activation/fission products, respectively, have been applied for both deterministic and probabilistic calculations. The influence on dose estimates of different release times (2 minutes/1 hour), two release heights (10 m/150 m), two chemical forms of tritium (HT/HTO), and two different model approaches for the deposition velocity of HTO on soil was investigated.

The dose calculations for normal operation effluents were performed using the tritium model of the German regulatory guidelines, parts of the advanced dose assessment model NORMTRI still under development, and the statistical atmospheric dispersion model ISOLA [5]. Accidental and normal operation source terms were defined as follows: 10g (3.7 10^{15} Bq) for accidental tritium releases, 10 Ci/day (3.7 10^{11} Bq/day) for tritium releases during normal operation and unit releases of 10^9 Bq per isotope for accidental releases of activation products and fission products.

After the revision of the NET document [6], preliminary source terms for corrosion products (steel dust AISI-316) from the first wall primary coolant loop and several source terms for tungsten dust have been defined. Additionally, dose assessments (unit releases) for an extended list of fusion relevant isotopes have to be performed. To meet the proposals of the new Requirement Definition Document (extended list of nuclides) a special version of the code system COSYMA is being generated, because it is not worthwhile to change the nuclide list of COSYMA before the relevant nuclides are not definitively fixed. The new code version will contain up to about 300 fusion relevant nuclides, but will consider only the effective dose from cloudshine, groundshine and inhalation pathways. Results of the calculations for different activation product source terms will be presented at the 17th SOFT-conference in Rome in September 1992.

Within the BIOMOVS II (BIOsheric MOdel Validation Study - phase II) study a working group has been established with the aim of testing and validating tritium transfer models. During the second BIOMOVS II Workshop in March 1992 two HTO release scenarios have been defined. The objectives were to evaluate the uncertainties associated with the model predictions, to compare the model results and to identify and analyse the reasons for differences between model predictions lying outside the uncertainty bands. First results calculated with UFOTRI have been transferred to the secretariat. During the 3rd BIOMOVS II Workshop in November 1992, the results of all model predictions will be compared and discussed.

Literature:

[1] Raskob, W.
UFOTRI: Program for Assessing the Off-Site Consequences from Accidental Tritium Releases
KfK-Report 4605, Kernforschungszentrum Karlsruhe, June 1990

[2] Vogel, B., Adrian, G. and Fiedler F.,
The Sandoz Accident-Numerical Simulation of the Transport and Dispersion of the Airborne Releases in: Gräfen, K. and Löbel, J. (eds) Environmental Meteorology, pp 279 - 290 (1988), Kluwer Academic Publishers, Dortrecht, Niederlande

[3] Gulden, W.
Dose Calculations for NET Accidental Releases, S+E Subtask SEP2.2, NI/R/0262/2/A, 29 May 1991

[4] COSYMA: A New Program Package for Accident Consequence Assessments,
A Joint Report by KfK and NRPB
Commission of the European Communities, Report EUR-13028 (1991)

[5] Hübschmann, W. und Raskob, W.
ISOLA V - A FORTRAN 77-Code for the Calculation of the Long-Term Concentration Distribution in the Environment of Nuclear Installations, Report KfK-4606, Kernforschungszentrum Karlsruhe (1990)

[6] Gulden, W.
Requirement Definition Document: Safety and Environment, DRAFT, Doses to the public, environmental impact of tritium and activation products, S+E Subtask SEP 2.2, N/S/0262/1/A, 21 May 1992

Staff:

W. Raskob
I. Hasemann
J. Ehrhardt

Long Term Program for Materials Development

Introduction:

KfK's activities in structural materials development have been continued with an emphasis on characterization of the martensitic steel MANET, investigations into the behaviour after irradiation both by thermal reactor neutrons and p+He beams and contributions to the low-activative materials (LAM) programme.

Some highlights from the reports given below are:

Characterization work on the first heat of MANET has essentially been completed. The strength exceeds requirements in all annealing conditions. The ductile-brittle transition temperature in the standard impact test is 27 °C. The second heat of MANET is being distributed to the European Associations (MANET 1)

In isothermal fatigue the influence both of temperature and strain rate on the number of cycles to failure (N_f) is small for MANET. In thermal fatigue N_f-values are smaller when compared to those under LCF conditions at the maximum temperature of thermal cycling (MANET 3.2).

A first set of measurements has been performed on irradiated (5dpa, different irradiation temperatures) subsize V-notch impact specimens. There is a considerable influence both of original heat treatment and irradiation temperature on the ductile-brittle transition curve. The shift in DBTT is comparable to literature data on other ferritic steels (MANET 3.4).

In the LCF experiments before and after dual-beam irradiation a pronounced influence of hold-times was observed. The additional effect of irradiation was rather small (MANET 5).

Data libraries on materials activation were completed accounting for all kinematically possible sequential reactions. Experimental benchmark testing of critical activation cross sections has started (LAM 2.1).

The characterization of the experimental heat of reduced activation alloy CETA has been completed. Mechanical properties from tensile testing are satisfactory whereas fracture toughness, in particular DBTT, is more favourable than for unmodified MANET (LAM 3).

LAM 2.1 Low-Activation Fusion Materials Development

Nuclear Data Base for Activation Calculations and Integral Data Testing of Critical Cross Sections

Reliable estimates of materials activation in future fusion reactors require the inclusion of all kinematically possible reactions and the allowed permutations of subsequent reaction chains. While one-step neutron-induced reactions have been sufficiently covered in the past, all previous calculations neglected the so-called sequential (x,n) reactions (SxRs), which have been shown to produce often important contributions to the induced radioactivity and/or the related surface γ-dose rates, decay heats and radiotoxicities.

In completion of the total nuclear data base for activation calculations, three new data libraries had been produced during the last two years at KfK. These together with a new computer program PCROSS allow now to treat all kinematically possible SxRs on all stable and radioactive nuclides with $T_{1/2} > 1$ day in the mass range $1 \leq A \leq 209$, except for special cases mainly in the light mass region.

With the existing means of code and library developments, improved activation calculations for important Fe-basis alloys have been performed. A recent result is shown in Fig. 1 which gives the γ-dose rates versus cooling time produced in the first wall of a DEMO fusion reactor. The figure displays the results for the non LA-optimized alloy MANET II and four LA-optimized versions (or candidates) of stainless steel. The new KfK proposal for the LA-alloy OPTIFER is based on the achieved properties for CeTa. It aims at a further improvement of LA properties by replacement of minor constituent elements by similar ones with lower element activation and by strong suppression of critical element impurities (Ag, some rare earth elements, etc.). From present work it seems to be possible to arrive at dose rate levels, practically identical with those of Fe, i.e. the lowest level possible for Fe-basis alloys.

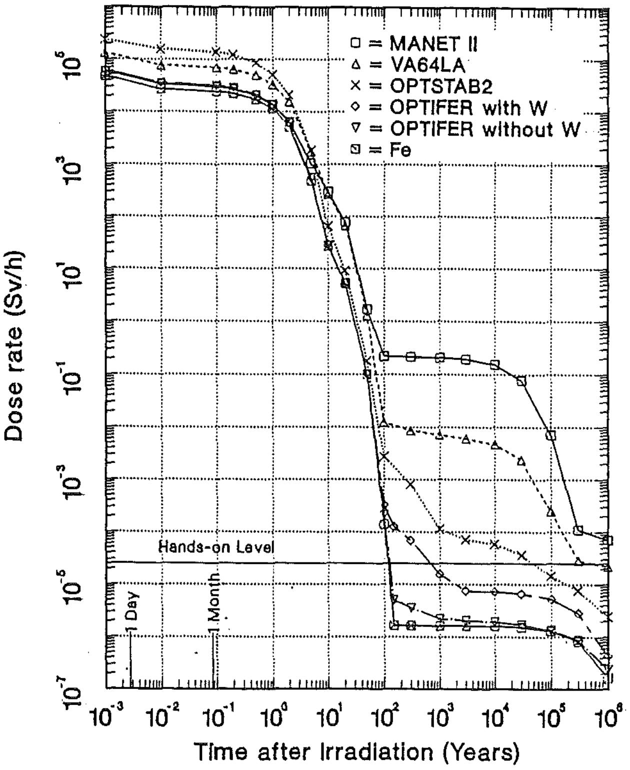

Fig. 1: Comparison of calculated surface γ-dose rates versus time after irradiation. In addition to the non LA-optimized alloy MANET II, four LA-optimized versions (or candidates) of stainless steel are shown. The results refer to neutron irradiation in the first wall of a DEMO fusion reactor. A first wall 14-MeV neutron load of 12.5 MW yr/m^2 was assumed.

In addition to library and code developments integral data testing experiments for critical activation cross sections have been carried out at the Karlsruhe Isochronous Cyclotron (KIZ). In addition to a first experimental proof for the occurrence of sequential (x,n) reactions, important (n,x) reactions on ^{51}V have been determined experimentally. Data evaluation for these measurements is in progress. In the last year the following improvements of the data testing facility have been finalized: (1) Replacement of the Cu by a thick Be neutron target. (2) Replacement of the very old Ge(Li) detector by a new pure Ge γ-ray detector device. (3) Installation of a new Si(Li) detector system for weak X-ray measurements from radionuclides decaying by electron capture only.

Literature:

[1] S. Cierjacks; Nuclear data needs for low-activation fusion materials development; Fus. Engrg. Design 13, 229 (1990).

[2] S. Cierjacks, K. Ehrlich; Invited paper on "Nuclear data for fusion materials research"; in Proc. Int. Conf. on Nuclear Data for Science and Technology, p. 259, Jülich, FRG, May 13-17, 1991, Ed. S.M. Qaim, Springer-Verlag Berlin Heidelberg, 1992.

[3] S. Cierjacks, P. Oblozinsky, S. Kelzenberg, B. Rzehorz; Development of a novel algorithm and production of new nuclear data libraries for the treatment of sequential (x,n) reactions in fusion materials activation calculations; submitted to Fusion Technology (1990).

[4] S. Cierjacks, P. Oblozinsky, B. Rzehorz; Nuclear data libraries for the treatment of sequential (x,n) reactions in fusion materials activation calculations; Kernforschungszentrum Karlsruhe Report, KfK-4867, Juli 1991.

[5] S. Ravndal, P. Oblozinsky, S. Kelzenberg, S. Cierjacks; User manual for the KfK Code PCROSS; Kernforschungszentrum Karlsruhe Report, KfK-4873, August 1991.

[6] S. Ravndal, P. Oblozinsky, S. Kelzenberg, S. Cierjacks; Reference manual for the KfK Code PCROSS; Kernforschungszentrum Karlsruhe Report, KfK-4956, December 1991.

[7] P. Oblozinsky, S. Cierjacks, S. Kelzenberg, B. Rzehorz; Production of new nuclear data libraries for low-activation materials development from statistical/preequilibrium model calculations; OECD/NEA Topical Conf. on Nuclear Data for Fusion Reactor Technology, Karlsruhe, FRG, October 23, 1991; Proc. to be published.

[8] P. Oblozinsky, S. Cierjacks, S. Ravndal, S. Kelzenberg; A novel algorithm for the treatment of sequential (x,n) reactions in standard activation calculations; OECD/NEA Topical Conf. on Nuclear Data for Fusion Reactor Technology, Karlsruhe, FRG, October 23, 1991; Proc. to be published.

[9] S. Kelzenberg, S. Cierjacks, P. Oblozinsky, J. Kaneko; Integral data testing of critical activation cross sections for fusion materials development at the Karlsruhe Isochronous Cyclotron. OECD/NEA Topical Conf. on Nuclear Data for Fusion Reactor Technology, Karlsruhe, FRG, October 23, 1991; Proc. to be published.

[10] K. Anderko, L. Schäfer, M. Schirra, S. Cierjacks, K. Ehrlich; Low activation martensitic steels, KfK-Program 89-91, Progress-report and new proposals; Presented at the LAM-Martensitic Steels Meeting, Garching, FRG, February 25, 1992.

Staff:

S. Cierjacks
E. Daum
K. Ehrlich
S. Kelzenberg
P. Oblozinsky

LAM 3.2 Development of Low Activation Martensitic Steel

Structural material in the region of the first wall and the blanket is activated by neutron exposure during reactor operation. This may cause problems when such components must be repaired or stored in a repository. For this reason, the Nb, Mo and Ni alloying constituents, with high susceptibility to activation in CETA-grade steel, were replaced by W, Ta, and Ce, which are elements less prone to being activated. The last of the mechanical properties to be discussed in this paper is creep-rupture strength. It is shown in Fig.1 as a function of a time-temperature parameter for three different conditions of material treatment. The highest creep-rupture strength is achieved by applying the lowest tempering temperature (T = 600°C). It is approximately comparable to that of MANET-I-grade steel.

Staff:

L. Schäfer
M. Schirra

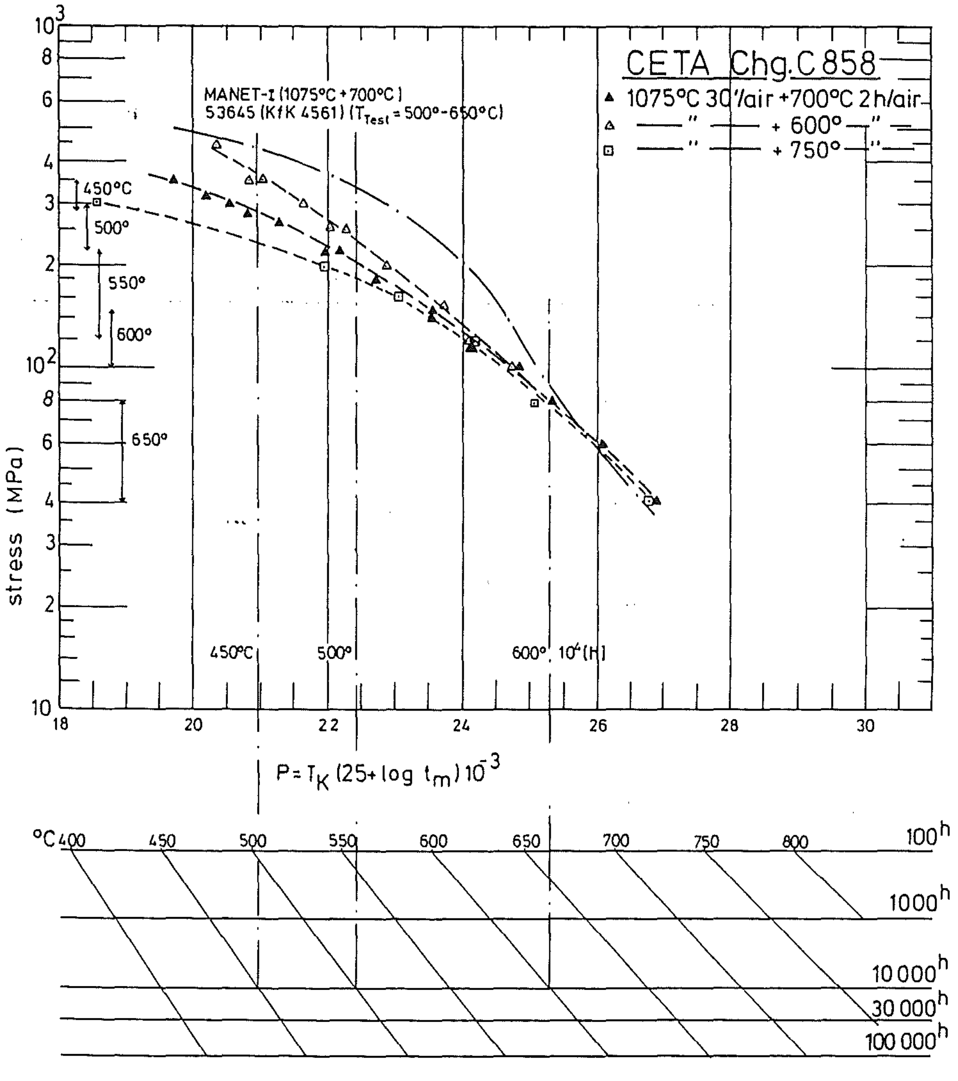

Fig. 1: Stress rupture strength of the steel CETA in dependency of a time-temperature parameter

MANET 1.1 Characterization and Optimization of MANET - II Steel

For application as structural materials of the first wall and of blanket structures, ferritic steel grades constitute a good alternative to austenitic steel grades because of their more advantageous thermal characteristics and irradiation properties. The first type of steel developed for this purpose, MANET-I, has meanwhile been studied in sufficient depth [1]-[3], and the stocks of materials have been used up. Consequently, an improved second version, MANET-II, was produced which so far has been examined for its metallurgical properties and, in part, also its mechanical characteristics. Its hardenability (or increase in hardness) is good above an austenitizing temperature of T = 900 °C, and no coarse grain occurs up to T = 1125 °C; T = 1075 °C therefore was retained as the hardening temperature. The tempering temperature producing the highest decrease of hardness and the maximum expected increase in toughness is T = 750 °C (2 h). In view of the notch impact properties, it was retained as well. Consequently, the standard quenching and tempering treatment of MANET-II-type steel is identical with that applied to MANET-I-type steel.

Among the mechanical properties, only the tensile ones have so far been examined completely [4], [5]. Figures 1 and 2 show the tensile properties plotted as a function of the main parameter, the test temperature. They are in line with the preliminary requirements established by reactor designers. However, ultimate elongation at T = 300 to 350 °C still needs to be slightly improve.

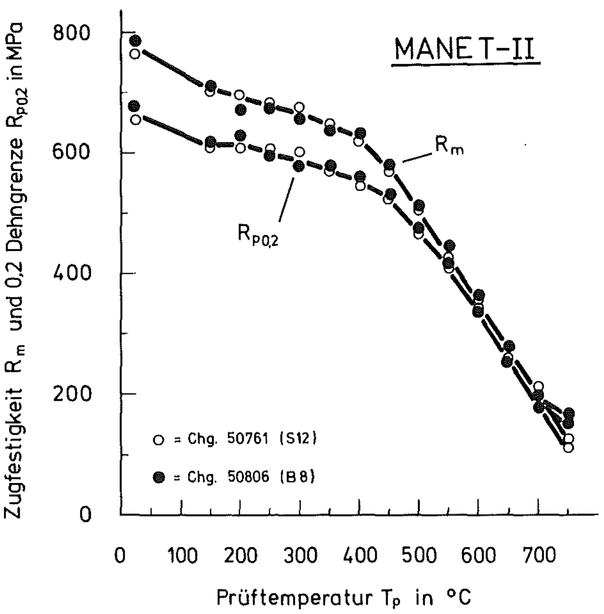

Fig. 1: Ultimate tensile strength and yield strength of MANET-II-Type Steel in dependency of the test temperature.

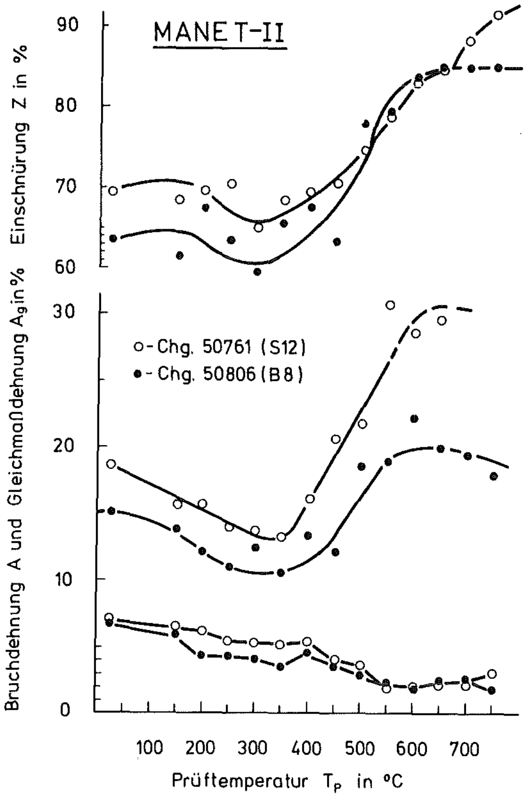

Fig. 2: Total elongation, uniform elongation and reduction of area of MANET-II-type steel in dependency of the test temperature.

Literature:

[1] M .Schirra et al.:
KfK-Bericht 4561 (1989)

[2] L.O. Schäfer, W. Meyer:
Unpublished Report of KfK (8/1991)

[3] G. Balzer, S. Müller:
Unpublished Report of KfK (4/1989)

[4] M. Schirra:
(Febr. 1991)

[5] L.O. Schäfer, H. Kempe:
Unpublished Report of KfK (2/1992)

Staff:

H. Kempe
L. Schäfer
M. Schirra

MANET 3.2 Pre- and Post-Irradiation Fatigue Properties

Thermal cycling of large components is a serious problem for the designer. The structure considered in the present case is the first wall of a fusion reactor. Its surface, in the actual design concept, will be subjected to radiation heating from the plasma facing side which may lead to severe thermal stresses. Due to the discontinuous operational mode, thermal cycling will generate oscillating temperature gradients. These, depending on the loading conditions, will cause elastic or elasto-plastic reversed deformation, giving rise to thermal fatigue which at present is considered as the most detrimental lifetime phenomenon for the structure considered. The investigations of MANET 3.2 are devoted to this problem.

The studies to be reported within MANET 3.2 are:

- The influence of temperature and hold-times in tension upon isothermal low-cycle fatigue behaviour of MANET 1 at 450 °C and 550 °C and a strain rate of 3 x 10^{-3}/s on S-GRIM specimens.
- Thermal fatigue on H-GRIM specimens from MANET 1 with a ΔT between 400 and 500 K with hold times of 100s at T_{max} of T_{min} or both.
- Microstructural examinations of thermally cycled MANET 1 specimens with hold-times.
- The thermomechanical test facility is in operation now.

1. Isothermal Fatigue of MANET 1

In Fig. 1 results of low cycle fatigue tests with hold-times in tension phase of the cycle are plotted for two temperatures (450 and 550 °C) and two strain ranges (0.6 and 1.0 %). For all tests the strain rate was 3 · 10^{-3}/s. The two lower curves for $\Delta\varepsilon_t$ = 1 % (open circles and closed triangels) show only a slight reduction of the number of cycles to fracture N_f with increasing hold-time. For a strain range of 6.0 % (open triangels and closed circles) a similar behaviour can be observed. The small reduction of the N_f-values causes essentially longer test times i.e. tests with hold-times ≥ 10 minutes could not be performed in all cases.

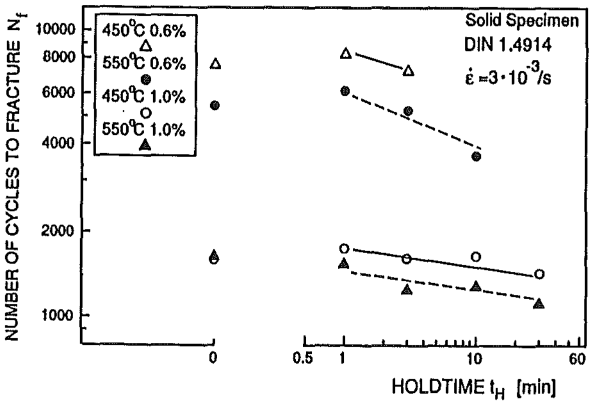

Fig. 1: Number of cycles to fracture vs. hold-time in tension as function of strain range and temperature for S-GRIM specimens of MANET-1

First results with hold-times in compression indicate that for this loading type the N_f-values will be reduced substantially more as compared to tension hold-time tests. This is in contrast to results of tests on austenitic materials. Hold-time tests on AISI type 304 have shown that under comparable conditions the most damaging loading type is that with tension dwell-times as a result of creep damage which occurs during stress relaxation phase of the cycle.

2. Thermal fatigue of MANET-1

2.1 Tests with hold-times

The thermal fatigue tests with hold-times were performed on H-GRIM specimens. The essential feature of the method is to convert any longitudinal thermal elongation of the specimen into elastic or inelastic deformation. The cyclic thermal stress in the sample is generated by cycling between T_L (the low temperature) and T_H (the high temperature). This has been accomplished by allowing the rigid clamped specimen to serve as its own heater by passing a current through it. The tests were performed under different thermal cyclic conditions of $\Delta T = T_H \cdot T_L$ with a constant T_L =473 K. Variable values of T_H were selected in the 873 - 973 K range. The temperature rate was kept constant equal to 5.8 K/s for all thermal conditions. Constant temperature hold periods of 100 s were imposed at T_H, hold time at high temperature (HTH), at T_L, hold time at low temperature (HTL), or at both (HTHL).

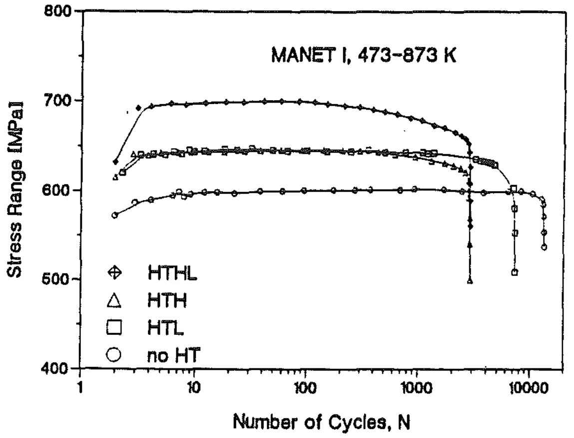

Fig. 2: Stress range Δσ versus number of cycles for tests with a temperature change of 473 - 873 K and different hold time conditions

To study the influence, that temperature hold periods have on mechanical behaviour and microstructural changes of the material, tests were performed with temperature hold times at HTL, at HTH and at HTHL of the cycle. In Fig. 2 the stress range response during tests of samples fatigued with temperature change of 473-873 K for the above temperature hold conditions is compared to a test without hold time (no HT). As it can be seen, tests with hold times represent higher stress ranges than tests without hold times.

All temperature hold-time conditions influence the mechanical behaviour of the sample reducing the number of cycles to failure N_f, as it is shown in Fig. 3, where N_f is plotted versus the high temperature of the cycle by leading to a pronounced softening which is almost not observed in the no HT condition. It is also evident from Fig. 2 that even though the HTH and HTL tests show during the first two hundred cycles similar mechanical behaviour, the HTH condition is more damaging because it accelerates the softening processes occurring during fatigue deformation.

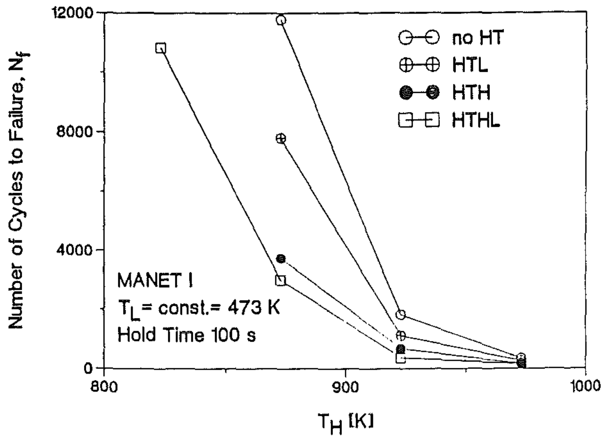

Fig. 3: Number of cycles to failure versus the high temperature T_H of thermal cycle in the indicated combination

From Fig. 2 it is evident that thermal fatigued MANET 1 also shows a continuous softening that is preceded by a stability period whose duration will depend on the temperature change and type of temperature hold period applied. Further it can be determined that a higher temperature change (i.e. a. higher stress range) and the application of a temperature hold period will always produce an accelerated softening process that leads to shorter life times.

2.2 Microstructural observations

After the specimens had been tested they were examined by transmission electron microscopy. Shells were cut from the tubular specimens to ensure that the observed region would have been the same for all failed samples.

The microstructure observed in Fig. 4 corresponding to a sample thermal fatigued up to failure with a temperature change of 473 - 873 K, shows that an intermediate structure of expanded laths - coming from the original lath structure whose geometry is preserved - with a lower density of dislocations, coexists together with a subgrain structure. Similarly comparing the microstructure of samples fatigued up to failure with and without hold time with the same temperature change (473 - 873 K) one observes also a transition from a mixed structure of expanded lath and subgrains (Fig. 4) to a full subgrain structure (Fig. 5) for the two extreme conditions, no HT and HTHL, respectively.

Fig. 4: Coexistence of an expanded lath structure and subgrain structure observed for $\Delta\tau$ = 473-873 K and no HT at N_f = 14296 cycles.

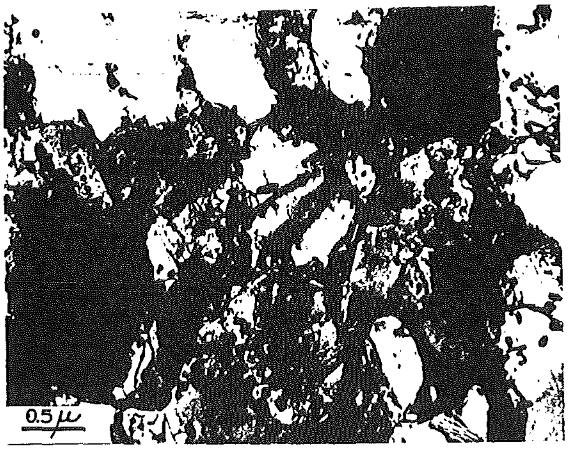

Fig. 5: Equiaxed subgrain structure formed after N_f = 2952 cycles with a temperature change of 473 - 873 K and HTHL condition.

A statistical analysis was performed from micrographs obtained by tests up to failure to analyse the evolution from the lath to the subgrain structure. In thermal fatigued MANET 1 the original lath structure will evolve to a subgrain structure. The cells in this last substructure will also become larger during the test. How fast the subgrain structure will be obtained and how large the final mean size of the cells will be, depends on the temperature change and the temperature where the hold periods are applied. The proposed substructural evolution begins with a lath structure that transforms first to small cells allocated near the boundaries of prior austenite grains. The amount of this small cells will increase inside the grains and some of these will become larger during the test.

2.3 Thermomechanical test facility

The test rig consists of an ohmic heating device, a thermally as well as electrically from the sample insulated load frame of an INSTRON material testing device and a digital control an data acquisition system, synchronizing the temperature and strain controlling signals.

First, zero strain control, reference experiments with a temperature change of 473 - 923 K show in Fig. 6 a strong load increase at the start of the experiment compared to thermal fatigue. The cyclic softening is similar as well as the number of cycles to failure.

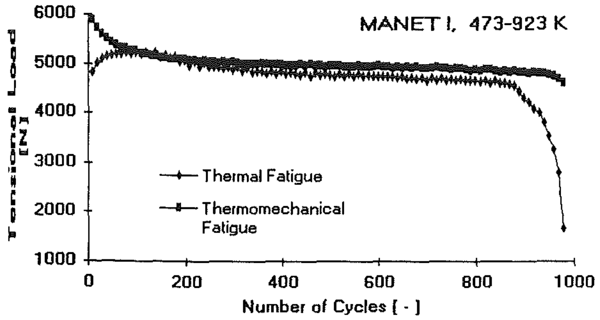

Fig. 6: Tensional load vs. number of cycles under thermal and thermomechanical fatigue.

Literature:

[1] W. Scheibe and R. Schmitt:
Isothermal Fatigue of Martensitic Steel MANET 1. Workshop on Fatigue of Fusion Reactor Candidate Materials Vevey, CH, Oct. 18.-20.1991.

[2] C. Petersen, A.F. Armas and I. Alvarez-Armas:
Thermal Fatigue on Martensitic Steels. Workshop on Fatigue of Fusion Reactor Candidate Materials, Vevey, Ch, Oct. 18.-20.1991

[3] A.F. Armas, I. Alvarez-Armas and C. Petersen:
Thermal Fatigue Behaviour and Dislocation Substructures of 316-Type Austenitic Stainless Steels. 5th Internat. Conf. on Fusion Reactor Materials (ICFRM-5), Clearwater, Fla., Nov. 17.-22.1991.

[4] I. Alvarez-Armas, A.F. Armas and C. Petersen: Dislocation Substructures Developed in Martensitic Steels under Thermal Fatige. 5th Internat. Conf. on Fusion Reactor Materials (ICFRM-5), Clearwater, Fla., Nov. 17.-22.1991.

[5] A.F. Armas, I. Alvarez-Armas and C. Petersen:
Thermal Fatigue Behaviour of Austenitic and Martensitic Stainless Steel. 3rd Internat. Conf. on Low Cycle Fatigue an Elasto-Plastic Behaviour of Materials, Berlin, FRG, Sept. 7.-11.1992.

Staff:

W. Baumgärtner
C. Petersen
D. Rodrian
W. Scheibe
R. Schmitt
H. Schneider
W. Schweiger
(I. Alvarez-Armas)
(A.F. Armas)
(F. Wolter)

MANET 3.4 Pre- and Post-Irradiation Fracture Toughness

Instrumented impact testing with KLST V-notch specimens has been used for evaluating toughness changes caused by variations in structure, and by irradiation embrittlement.

The aims of the investigation program are to establish the influence of the initial microstructure and the effects of the irradiation-induced microstructural changes on the impact properties of the 12% Cr steel, MANET-I:

1. To determine the values of the ductile-to-brittle transition temperature (DBTT) and the upper-shelf energy (USE) of the MANET-I steel.
2. To establish the effects of initial microstructure and irradiation on DBTT and USE.
3. To determine the stress intensity factor, K_{Id}, and the relative fracture toughness, J_{Ic}, of unirradiated and irradiated MANET-I steel.
4. To determine the irradiation-induced changes of the dynamic stress intensity factor and the relative fracture toughness.
5. To establish the relationship between dynamic fracture toughness (K_{Id}) of the material in the irradiated condition and the energy (U) involved in fracture during impact testing.

The obtained experimental results and the experiments to be carried out within the SIENA project will enable to study in more detail the effects of irradiation temperature, neutron dose, and initial structure on the fracture toughness properties and on the dynamic load behaviour of MANET-I steel. Special attention is paid to the related recording aspects associated with the determination of the true dynamic load and energy.

The temperature dependence of the total impact energy leading to fracture and DBTT will be discussed in the following. The temperature above which low energy (brittle) fracture does not occur is named the transition temperature. It can be determined in various ways, e.g. as the temperature at which the fracture surface exhibits a specified value of a shiny, crystalline faceted, appearance. This temperature is commonly called fracture appearance transition temperature or $FATT_n$ where "n" is the percentage of shear fracture. $FATT_{50}$ has most frequently been specified. However, FATT depends on the geometry of the specimen. Comparative studies have to be carried out with specimens of equivalent geometries. $FATT_{50}$ has been chosen to determine the transition temperature of the unirradiated and the irradiated material, in order to establish the effect of the irradiation-inducded evolution of microstructure on DBTT.

Studies [1] concerning the effect of irradiation temperature on the impact properties of the 12% Cr steel MANET-I are under way. The experimental results available up to now for the MANET-I material as examined in the reference condition before and after irradiation to 5 dpa at 300, 400, and 475°C are summarized in Fig. 1. The results show that the accumulation of irradiation-induced defects leads to the

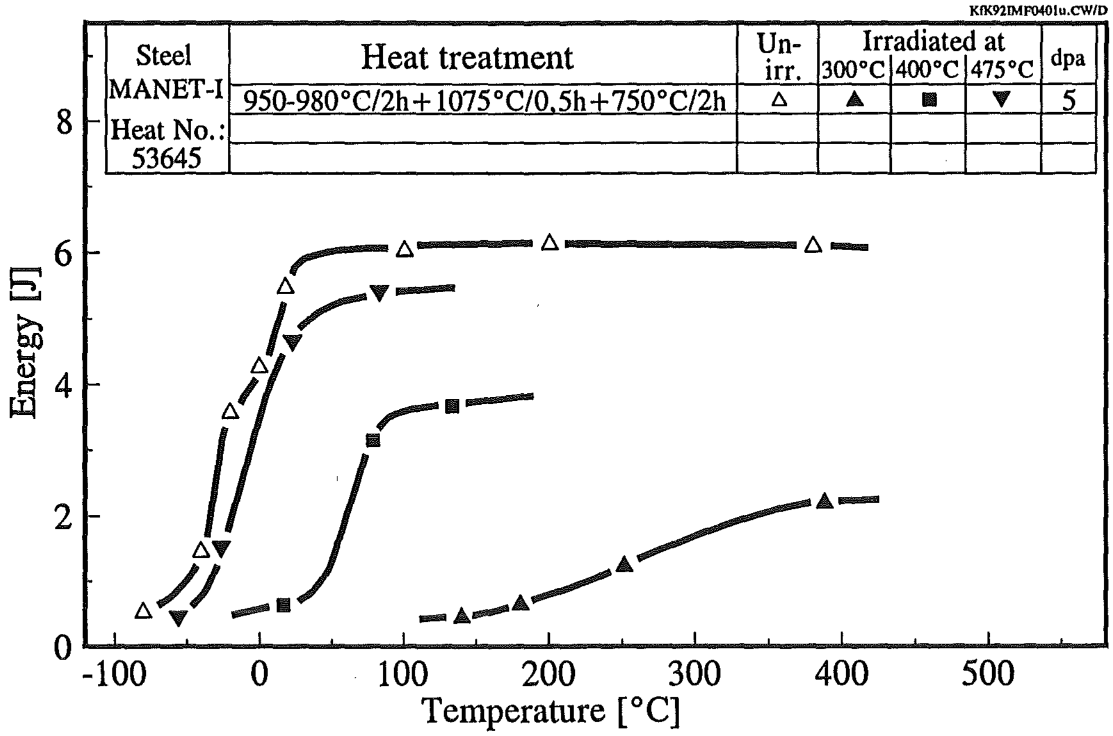

Fig. 1: Effects of irradiation temperature on the impact properties of MANET-I steel

observed DBTT shifts, and that the reductions of USE clearly depend on the irradiation temperature.

The degradation of the impact properties following irradiation at 475°C is very small. However, the effect intensifies dramatically as the irradiation temperature drops below approximately 400°C. These findings are consistent with experimental data obtained for irradiated 12% Cr steels [1, 2]. The DBTT of the material increases with decreasing irradiation temperature from approximately -10°C for T_{irr} = 475°C, to 45°C for T_{irr} = 400°C, and jumps to ca. 245°C for T_{irr} = 300°C.

Conclusions

1. The instrumented V-notch test has been shown to be a powerful tool in testing material under dynamic loading conditions and gives additional information about the load and energy as a function of time.

2. The DBTT-shift depends upon the irradiation temperature and the initial microstructure.

3. The degradation of USE depends likewise upon the irradiation temperature and the initial microstructure.

4. The irradiation-induced degradation of impact properties can be recovered by a suitable heat treatment.

Literature:

[1] C. Wassilew, B. Dafferner, M. Rieth, and A. Kräutter: "Effect of Neutron Irradiation on the Dynamic Fracture Toughness Behaviour of the 12%Cr Steel Manet-I Investigated Using Subsize V-Notch Specimens", ICFRM-5, Fifth International Conference on Fusion Reactor Materials, Clearwater, Florida, USA, Nov. 17-22, 1991, Proceedings to appear

[2] W.R. Corwin and A.M. Hougland, ASTM STP 888, W.R. Corwin and G.E. Lucas, Eds., American Society for Testing and Materials, Philadelphia, 1986, pp. 325-338

[3] E 813-87 - Standard Test Method for J_{Ic}, A Measure of Fracture Toughness, Annual Book of ASTM Standards, Part 10, 1983, American Society of Testing and Materials, Philadelphia

Staff:

B. Dafferner
A. Kräutter
O. Romer
M. Rieth
C. Wassilew

MAT 5 Ion-Beam Irradiation Fatigue and Creep Fatigue Tests

The Dual Beam Facility of KfK, where alpha-particles (≤ 104 MeV) and protons (≤ 40 MeV) are focussed onto a target, was developed as a research tool for materials within the European Fusion Technology Programme. This high energy Dual Beam Technique allows the simulation of fusion neutrons by the systematic variation of hydrogen, helium and damage production in thick metal and ceramic specimens as well as the simulation of Tokamak relevant thermal and mechanical loadings in proposed plasma-facing materials.

The effect of irradiation on mechanical properties is studied in the vast majority by means of postirradiation experiments. This means that the irradiation induced microstructure is fully developed before the mechanical test is started. However, realistic fusion conditions with simultaneous irradiation and fatigue loading can lead to an inherently different material response. Therefore, we have focussed the experimental activities on "in-beam" fatigue tests.

1. Development of in-beam fatigue experiments

Fully instrumented in-beam push-pull fatigue tests on macroscopic specimens as they are envisaged here are of special complexity, because they combine simultaneously the high energy irradiation facility with the fatigue test technology.

Fig. 1 shows a schematic view of the in-beam fatigue experiments. The irradiation of a fatigue specimen can be performed in a vacuum chamber using simultaneously the alpha-particle beam to get a homogeneous He-implantation profile and a proton beam, penetrating the specimens to adjust the damage level. Because the currents of both beams can be chosen independently it is possible to vary the helium production rate without changing the damage rate. The temperature is measured with four tiny thermocouples welded at different parts of the gauge length and controlled by the flow rate of the helium gas inside the hollow fatigue specimen. An additional heating system by induction coils (Fig. 2) prevents temperature gradients in the gauge volume and maintains the temperature in unirradiated control experiments. Fig. 2 also shows an extensiometer clamped at the ends of the gauge length. With a modern universal testing machine various static and dynamic loadings in terms of stresses and strains like push-pull fatigue or creep fatigue can be applied during irradiation. Fig. 3 shows a front view of the Dual Beam Facility with the two beam lines (right), the beam diagnostic chamber (middle), and the universal testing machine (left) with the integrated vacuum chamber.

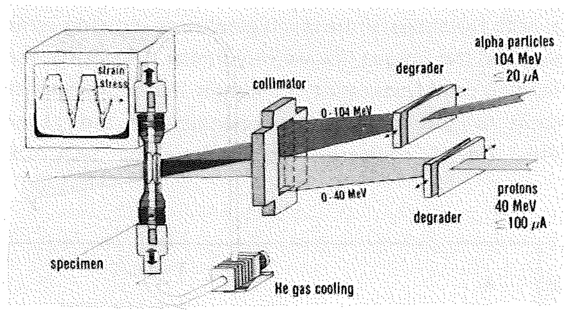

Fig. 1: Schematic view of the in-beam fatigue experiments

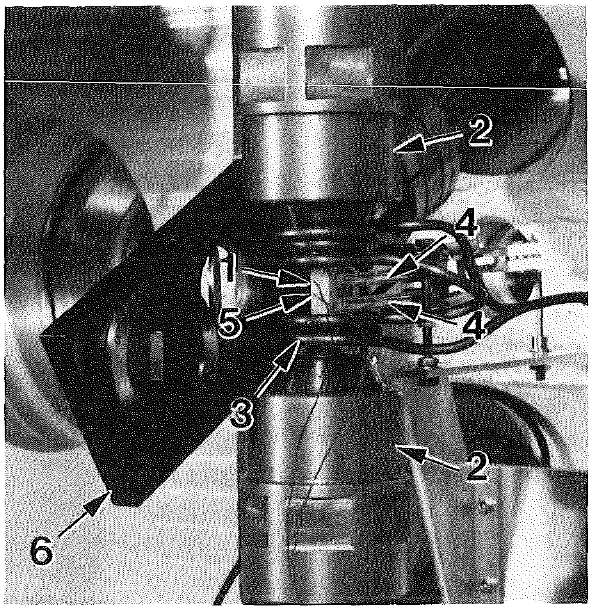

Fig. 2: Interior of the vacuum chamber with the fatigue specimens (1), the pulling rods (2), the HF heating system (3), the extensiometer (4), the tiny thermocouples (5), and the beam collimator (6)

The main features of the high energy Dual Beam Facility are:

specimen temperature:	80 - 850°C
proton range in steel:	2.9 mm
particle range in steel:	1.4 mm
He-dose/damage ratios:	(10-400) appm He/dpa
damage rates:	(1-500) x10^{-7} dpa/s
fatigue modes:	- stress or strain controlled - with/without hold periods - beam cycling experiments - thermal fatigue

It is worth to notice, that in contrast to many other accelerator based irradiations relatively low, but fusion relevant He-production and damage rates can be adjusted at this Dual Beam Facility.

2. The in-beam fatigue specimen

Requirements on push-pull fatigue testing for material characterisation experiments include

- specimen thickness within the gauge volume less than range of projectiles
- well defined stress and strain states

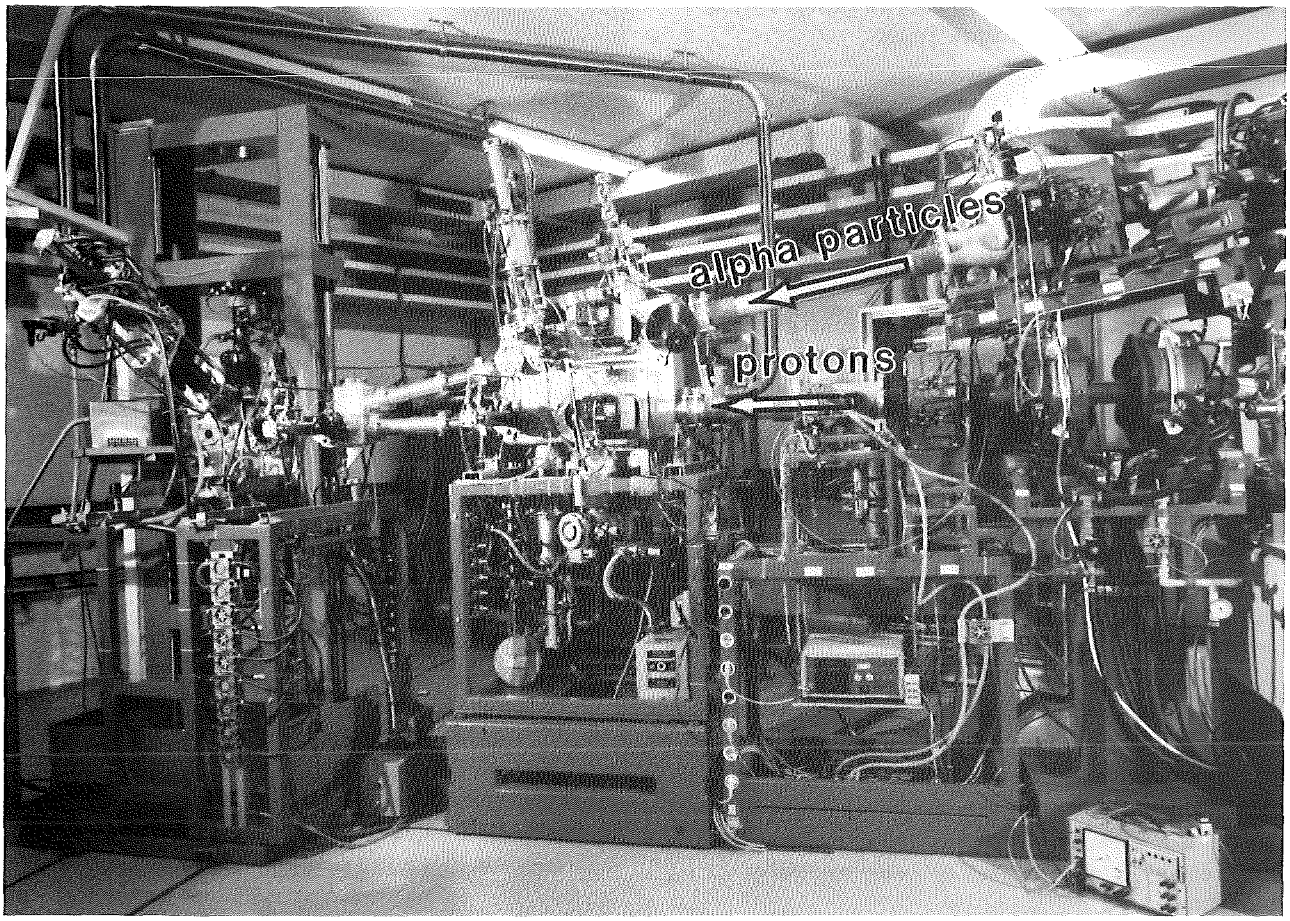

Fig. 3: Front view of the Dual Beam facility. The integrated universal testing machine allows in-beam fatigue experiments

- structural stability during fatigue experiments
- reproducible results with a small amount of scatter in the number of cycles to failure N_f.

To meet all these requirements a hollow specimen with a square cross section was developed and optimized by FE-calculations. This H-QUADR specimen has a constant wall thickness of 0.40 mm, a gauge width of 7.00 mm an a gauge length of 10.0 mm. In Fig. 4 the fatigue characteristics of that specimen are compared with those of a hollow cylindrical specimen (H-ZYL) with the same wall thickness and gauge length. Both the shape of the strain amplitude showing cyclic softening and the fatigue life are very similar. Obviously, the same loading conditions result in the same material response in suitable fatigue specimens, independent of the gauge geometry. Fig. 5 compares the lifetimes of S-QUADR specimens and solid S-GRIM specimens (KfK report 4944, 1991, p. 91) at 450°C in strain controlled isothermal fatigue

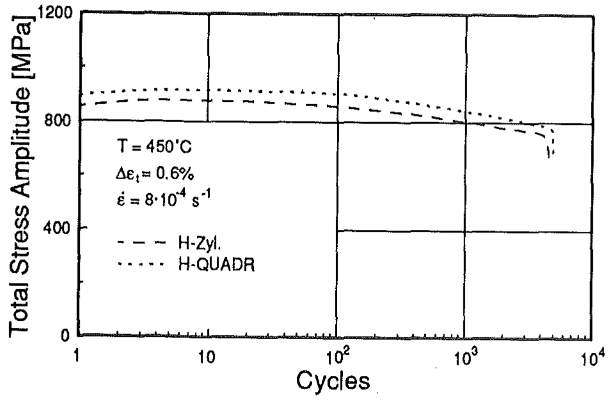

Fig. 4: Different gauge geometries of MANET specimens showing the same fatigue behaviour

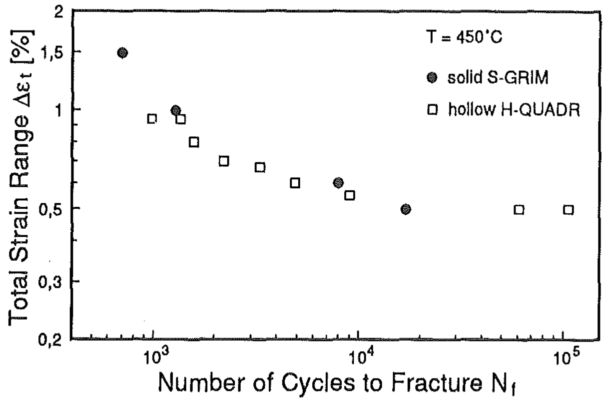

Fig. 5: Total strain range vs. number of cycles to fracture. Comparison between H-QUADR specimens used in in-beam fatigue tests and conventional S-GRIM specimens

experiments (R=-1). It can be concluded that within a broad strain range the lifetimes of H-QUADR specimens are in reasonable agreement with solid fatigue specimens even at elevated temperatures. Only at low strain levels the lifetime of H-QUADR specimens is systematicly higher. Altogether the comparison of H-QUADR-specimens with more conventional specimen geometries confirms the general consensus of the present fatigue experiments, that within a broad range the measured fatigue properties of H-QUADR specimens can be regarded as material specific.

3. The first in-beam fatigue experiments

Meanwhile the first strain controlled isothermal in-beam fatigue tests have been performed on specimens made of the martensitic European reference steel MANET I with the following loading conditions:

Temperature	450°C
Environment specimen outside	vacuum (< 10^{-3} mbar)
Environment specimen inside	purified He-gas
Inner surface heat flux	(0.7-1.0) MW/m^2
Damage production rate	(2-3)x10^{-6} dpa/s
Helium production rate	(6-8)x10^{-4} appm He/s
Fatigue mode	continuous cycling (R=-1)
strain rate $\Delta\varepsilon_t$	8x10^{-4}/s

The results on the first in-beam fatigue experiment are given in Fig. 6 together with two out-of beam control tests. In the unirradiated reference specimens the total stress amplitude continuously decreases with increasing number of cycles, a characteristic feature of ferritic/martensitic steels. After the most extended fatigue crack propagated through the wall, the helium gas inside the specimen escaped into the vacuum defining easily the number of cycles to failure N_f. Under in-beam conditions a fatigue life of 42000 cycles, a helium concentration of 400 appm and a damage dose of nearly 2 dpa have been reached during the six days of continuous operation. This number of cycles to failure is not significantly below the 60900 or 106000 cycles reached in the two unirradiated reference tests. The observed N_f-reduction can be understood by the slope of the stress amplitude (solid line in Fig. 6) which deviates more and more from the unirradiated ones above about 3000 cycles. Because the stress amplitude is strongly connected with microstructural changes, the observed deviation can be directly related to irradiation induced hardening. This hardening accelerates crack propagation and consequently reduces fatigue life.

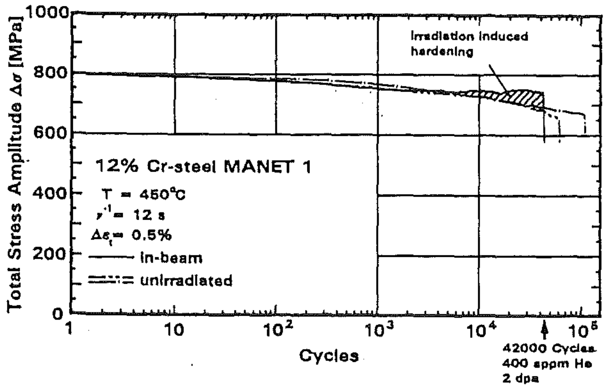

Fig. 6: Comparison between the first in-beam fatigue experiment and two out-of-beam control tests. Note, that the effect of irradiation on stress

Presently the design parameters for ITER require a total number of 20000-50000 pulses, and during the technology phase some hundred appm helium will be accumulated in plasma facing structural components. It should be emphasized that the MANET I meets the required fatigue life even under the above in-beam conditions. This experiment also has shown, that at 450°C the selected total strain amplitude of 0.5% should be regarded as upper load limit in ITER fusion devices.

Several other in-beam experiments performed at 450°C with total strain amplitudes between 0.7 and 1.2% showed lifetimes very similar to reference tests. This was expected because at higher loads fatigue life is smaller than the time to build up irradiation induced defects which are large enough to affect strength properties.

Literature:

[1] A. Möslang, S. Cierjacks and R. Lindau; "Test of fusion reactor materials with cyclotrons and presentation of the Karlsruhe Dual Beam Facility", in 12th Int. Conf. on cyclotrons and their applications, p. 545; Eds. B. Martin and K. Ziegler, World Scientific, London (1991)

[2] R. Lindau and A. Möslang; "Behaviour in fatigue relaxation of a creep resistant 12% Cr-steel after helium implantation"; ICFRM-5, Clearwater, Nov. 1991, to be published in J. Nucl. Mater. 1992

[3] K.K. Bae, K. Ehrlich, and A. Möslang; Tensile behaviour and microstructure of the helium and hydrogen implanted 12% Cr-steel MANET; ICFRM-5, Clearwater, Nov. 1991; to be published in J. Nucl. Mater. 1992

[4] D. Preininger; patent 4101220.8 (1991) on "Verfahren zur Duktilitätsverbesserung von 9-12% Cr-Stählen"

[5] A. Möslang, and D. Kaletta; patent DE-PS 37 05 295 (Nov. 1991) on "Einrichtung zur tiefenabhängigen Implantation von Teilchen in ein Target"

[6] A. Möslang, S. Baumgärtner, G. Bürkle, R. Lindau, G. Przykutta, and K. Ehrlich; "In-situ fatigue experiments at the Karlsruhe Dual Beam Facility: Capabilities and first results"; 17. SOFT-Conference, Rome, Sept. 1992

Staff:

S. Baumgärtner
G. Bürkle
R. Lindau
A. Möslang
D. Preininger
G. Przykutta

Test Blanket Development

Introduction:

Within the European Fusion Technology Program blanket development is divided in work for the NET/ITER basic machine and work for the test blankets. In agreement with the NET-Team and after establishing two European working groups KfK has concentrated its efforts on the development of test blankets for NET/ITER. By test blankets we understand blankets for the next step towards a commercial power station, so called DEMO relevant blankets. In the DEMO-reactor, the potential of a fusion machine to produce electricity shall be tested for the first time. Consequently the test blankets have to be designed for DEMO relevance in terms of breeding rate, temperatures and pressure. Structural materials, maintainability, reliability and safety have to satisfy the more stringent requirements of power production in comparison with driver or shielding blankets for the NET/ITER basic machine. The boundary conditions mentioned above cannot be satisfied full scale and at the same time in the test positions available in NET/ITER. Therefore the definition of test objects and the testing program is one of the main objectives of KfK besides the proof of DEMO relevance of the KfK blanket design alternatives.

The European Test Blanket Development Groups mentioned above deal with two development lines, one with solid breeder helium cooled, the other with liquid metal breeder and either liquid metal (selfcooled) or water cooled blankets. Both KfK developed designs, the selfcooled lithium-lead blanket and the helium cooled, breeder out of tube, canister blanket are accepted alternatives within the European test blanket development program - see BS-DE and BL-DE tasks. A part of the work defined by the partners - KfK, CEA, ENEA and JRC Ispra - consists of common work, relevant to all blanket designs, whereas the design work itself remains independent for the time being. It is foreseen to reduce the number of blanket alternatives to two in 1994/95, one solid breeder and one liquid metal breeder design, which will than be tested in NET/ITER.

The Solid Breeder Blanket Tasks (BS)

Solid breeder design, already mentioned above (DE-D-1), includes besides the design work proper, also small scale thermomechanical and fabricability tests. The KfK solid breeder material program has concentrated, in agreement with the European partners, on lithium orthosilicate. The program tasks include preparation, characterization, irradiation and postirradiation examination as well as measurement of the physical, chemical and mechanical properties. Of special interest are the in and out of pile tritium release studies, performed at KfK and within the common breeder development program in several European reactors. The KfK breeder program is described in tasks BR-D-1 through D-8. The main non nuclear testing facility to prove the feasibility of KfK's solid breeder design will be the helium loop HEBLO, in which elements as well as canister sections may be tested - see NN-D-1.

The Liquid Metal Blanket Tasks (BL)

Design activities (DE-D-1) concentrate on a solution featuring an inboard / outboard blanket without beryllium as a neutron multiplier. The liquid metal breeder blankets are so far the only blanket alternatives, including solid breeder blankets which allow a sufficiently high tritium breeding rate, not using beryllium.

Of great importance to the development of the selfcooled blanket is the knowhow and the data base of magneto-hydrodynamic behaviour of liquid metal flow aquired in theoretical and experimental studies of task MH-D-1. The test facility MEKKA and the cooperation with Argonne National Laboratory play a central role in MHD development.

In addition to design and MHD activities KfK studies the physico-chemical behaviour, task PC-D-1, especially corrosion of structural materials in the lithium lead eutectic (Pb-17Li) and the behaviour of impurities (Polonium) including methods of clean-up. Newly taken up in the development of electrically insulating coatings. Task EX-D-1 describes tritium removal and recovery by permeation and cold trapping. The sodium-potassium loop WAWIK and the Pb-17Li loop TRITEX are the main testbeds for the experimental studies.

The BL CO activities are dedicated to the development of crucial components like the electrically insulating flow channel inserts and ancillary loop components (steam generator, pumps).

BS DE-D 1 Solid Breeder Test Blanket Design

The first months of the reporting period were taken by the writing up of the Status Report of the Reference Design of the BOT Helium Cooled Sold Breeder Blanket [1, 2]. This design is based on the use of beryllium plates which are brazed on to the helium cooling tubes (Fig. 1). This solution offers the advantage that the beryllium acts as a permeation barrier against tritium losses to the helium coolant system. However, data on the swelling of beryllium under irradiation at high temperatures are very uncertain. On the base of the most pessimistic data the peak beryllium swelling might be too high for this design. Therefore during the reporting period the work concentrated on an alternative design , which should cope with large swelling. Fig. 1 shows the new design as compared to the old one. The beryllium is in form of 2 mm diameter pebbles, which fill up 60 % of the bed space. Between the large Be-pebbles there are 0.1 - 0.2 mm pebbles which take up 20 % of the space. Of the small pebbles 75 % are of Li_4SiO_4 and 25 % of beryllium. The use of beryllium in pebble form offers the advantage that the pebble bed can accomodate increases of pebble volume without formation of gaps between the bed and the coolant tubes, and that a volume increase produces an enlargement of the contact surfaces of the highly conducting Be-pebbles. Thus the thermal conductivity of the bed increases, the bed temperature decreases and the volume swelling is reduced.

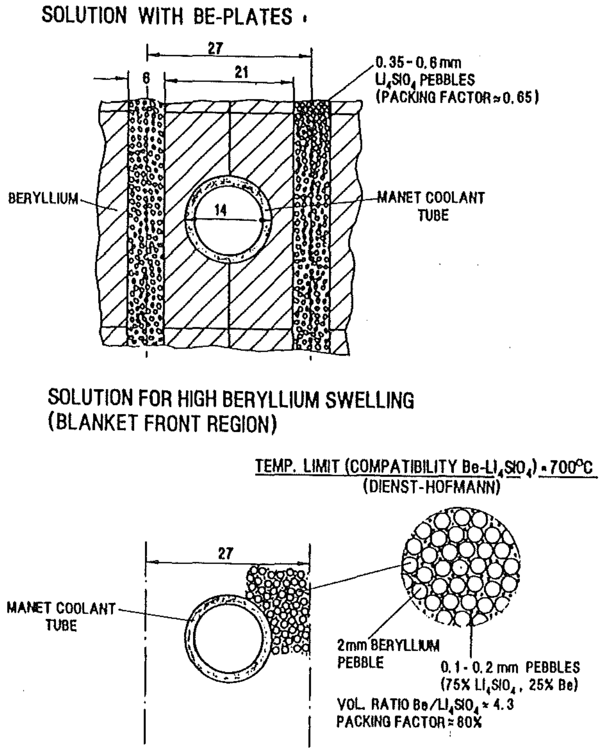

Fig. 1: DEMO-relevant Solid Breeder Blanket. Comparison of the breeder region for the solution with beryllium plates and with beryllium pebbles.

The chosen pebble bed arrangement ensures a high thermal conductivity of the bed, due to the high packing factor and to the fact that contact between the high conducting metallic pebbles is maintained. This is particularly important, as the maximum temperature in the bed is limited to 700 °C, which is the recommended compatibility limit beryllium - Li_4SiO_4 [3]. Information on the thermal conductivity of the mixed bed was obtained by measurements performed in an experimental device at KfK. The mixed bed of Be and Li_4SiO_4 pebbles was simulated with a bed of 2 mm Aluminum pebbles and 0.1 - 0.2 mm Li_4SiO_4 pebbles in helium [4]. The experimental data obtained could be extrapolated to the case of the actual Be / Li_4SiO_4 mixed bed and were used to calculate the temperature in the blanket.

So far the design work concentrated on the outbaord blanket. Fig. 2 shows an isometric view of a segment of the outboard blanket. This looks quite similar to the blanket segment of the previous solution with the beryllium plates [2]. However, there are, inside the box, some important differences. In the present solution the outboard segment is divided in 11 elements (Fig. 2). In each element there are 7 stiffening plates placed in radial-toroidal planes. The mixed bed Be/Li_4SiO_4 is placed in the front region of the blanket, the back being occupied by a bed of Li_4SiO_4 pebbles in the range

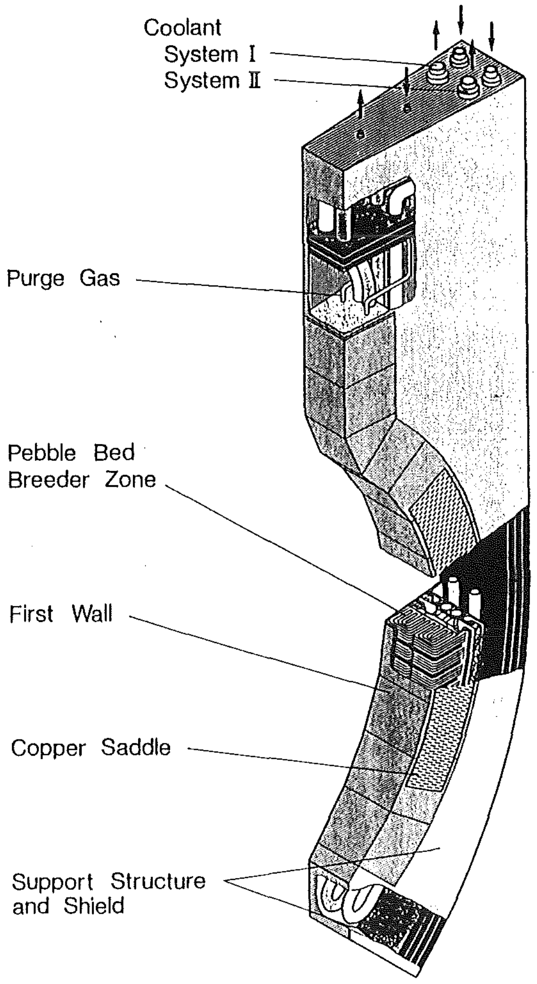

Fig. 2: Isometric view of the central segment of the outboard blanket for the beryllium pebble solution

0.2 - 0.6 mm diameter, without beryllium (Fig. 3). Both beds are cooled by two independent high pressure helium cooling systems running in coils placed in radial-toroidal planes (Fig. 3). Due to the presence of the stiffening plates, the segment box is strong enough to withstand the full helium coolant pressure of 8 MPa. This increases the reliability of the blanket which can operate with failed cooling tubes. Furthermore the design has been considerably simplified and the number of welds in the box has been minimized.

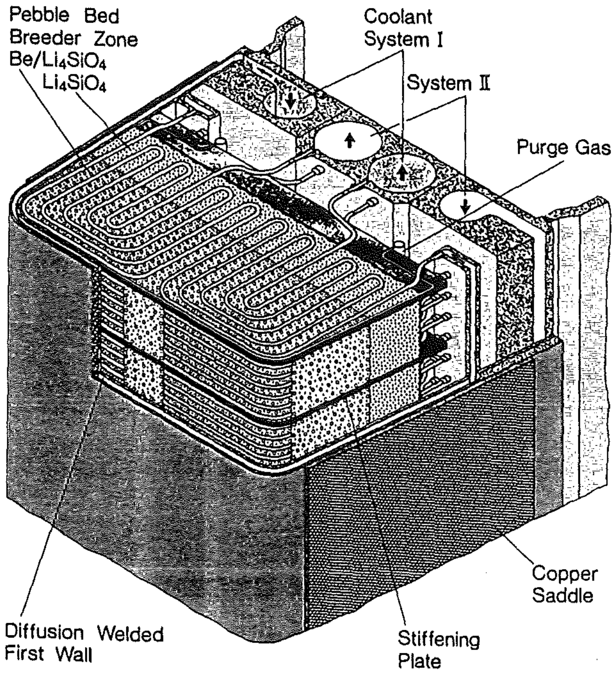

Fig. 3: Isometric view of a portion of the central segment of the outboard blanket for the beryllium-pebble solution

Fig. 4 shows the schematization of the blanket used for the neutronphysics calculations. It can be seen that in the blanket portions behind the divertor and in the upper part of the outboard segment there is no beryllium, but only Li_4SiO_4 in form of 0.2 - 0.6 mm pebbles.

Fig. 5 showsshows the results of the temperature calculations for the blanket front region of the highest rated position (outboard blanket, equatorial plane).

Table 1 the main results of the calculations performed so far. The maximum temperature in the mixed Be-Li_4SiO_4 pebble bed is below the compatibility limit between beryllium and lithiumorthosilicate of 700 °C [3]. The tritium breeding ratio is about the same as in the solution with beryllium plates, while the peak burn-up in Li_4SiO_4 is lower. More information on the new design will be presented at the SOFT-conference [5].

The electromagnetic forces and stresses caused by a major disruption (linear decay of the plasma current from 20 MA to zero in 20 ms) in the box of an outboard blanket segment were calculated with the computer program CARKFK. Due account was taken of the effects of the vacuum vessel and of the saddle loop. The presence of the magnetic steel MANET as structural material has been roughly estimated. The static calculations performed so far show that the stresses remain within the elasticity limits [6]. First calculations accounting for the magnetic properties of MANET on the outboard blanket segment have been performed with an integral method [7]. The calculations confirm the assumptions used in Ref. [6]. The computer programme CARKFK has been tested against experiments performed in ASDEX-Upgrade. The agreement between experiment and calculation is excellent [8].

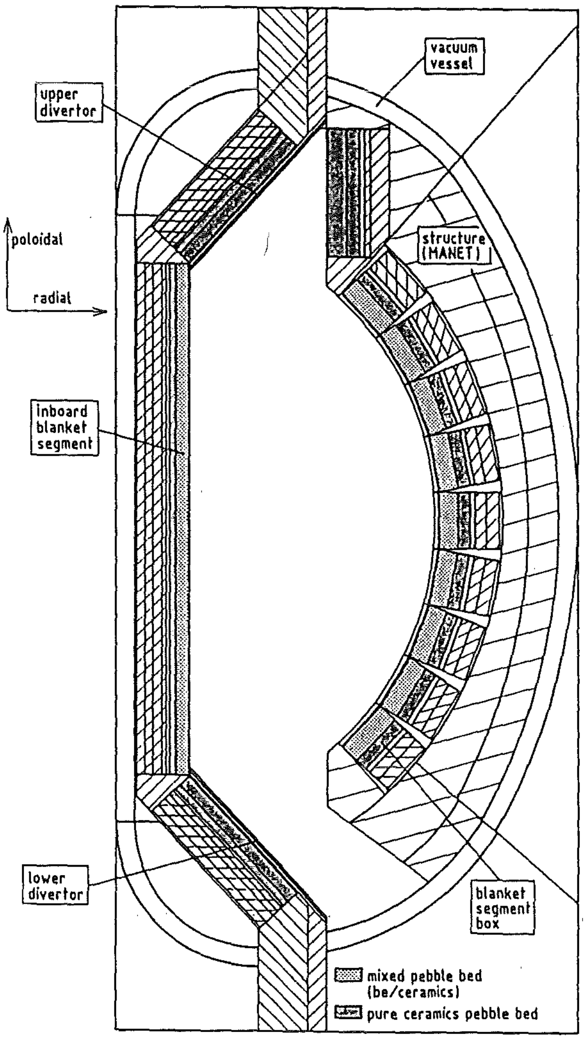

Fig. 4: Radial-poloidal cross section of the torus showing the geometrical model used for the Monte-Carlo neutronic calculations for the beryllium pebble blanket

During the reporting time the fracture loads of the reference orthosilicate pebbles (Li_4SiO_4 + 2.2 % SiO_2 manufactured by the melting process and annealed by 1030 °C for five minutes) were measured before and after an heating period of 56 days at 800 °C in IMF III. The fracture loads were practically unaffected by the heating at 800 °C. Also the thermal cycle tests performed on the reference pebbles in the diameter range 0.35 - 0.6 mm after the heating test at 800 °C gave satisfactory results. The broken fraction was 1.8 % and the

Table 1: Main characteristic of BOT Helium Cooled Solid Breeder Blanket for the DEMO reactor. Solution with Beryllium Pebbles.

Breeding and multiplying material:
near-plasma region: mixed Be-Li_4SiO_4 pebble bed with 2 mm Be-pebbles (total amount 114 tonnes), 0.1 - 0.2 mm Be pebbles (10.7 tonnes) and 0.1 - 0.2 mm Li_4SiO_4 pebbles with 25 % Li^6 enrichment (37.1 tonnes)
back region: bed of 0.2 - 0.6 mm Li_4SiO_4 pebbles with 60 % Li^6 enrichment (191.8 tonnes)
Total blanket power: 2500 MW (+ 300 MW in the divertors)
Coolant temperature: inlet = 250 °C, outlet = 450 °C
Coolant helium pressure: 8 MPa outboard, 10 MPa inboard
First wall max. steel temp.: 535 °C
Max. temp. in beryllium pebbles: 680 °C
Mixed bed temp.: Min = 380 °C, Max. = 680 °C
Real tridimensional tritium breeding ratio (assuming ten 3 x 1 m ports on outbaord blanket): 1.08
Tritium production rate: 370 g/d
Peak burn-ups in Li_4SiO_4 (referred to total lithium): 6.5 % (22 dpa) in near plasma region (mixed bed), 1.5 % in back region (Li_4SiO_4 bed).
Peak fluence in MANET: 70 dpa
Peak fluence in beryllium: 2.47 x 10^{22} n/cm^2 (E > 1 MeV), 17000 appm He

minimum size of the broken particles was 20 - 30 µm. By flowing with helium in the downward direction the pebble bed placed on a steel net with a mesh of 0.1 mm, it could be shown that no particle is carried out through the net for helium velocities typical of the blanket purge flow system. The same result was obtained for beds with broken fractions up to 10 % [9].

Literature:

[1] M. Dalle Donne et al., "Status Report. KfK Contribution to the Development of Demo-relevant Test Blankets for NET / ITER. Part 2: BOT Helium Cooled Solid Breeder Blanket. Vol. 1: Summary", KfK 4928, October 1991.

[2] M. Dalle Donne et al., "Status Report. KfK Contribution to the Development of Demo-relevant Test Blankets for NET / ITER. Part 2: BOT Helium Cooled Solid Breeder Blanket, Vol. 2: Detailed Version", KfK 4929, October 1991.

[3] P. Hoffmann and W. Dienst, "Chemical Interactions of Beryllium with Lithium-Based Oxides and Stainless Steel", J. Nucl. Mat. 171 (1990) 203 - 214.

[4] M. Dalle Donne, A. Goraieb and G. Sordon, "Measurements of the Effective Thermal Conductivity of a Bed of Li_4SiO_4 Pebbles of 0.35 - 0.6 mm Diameter and of a Mixed Bed of Li_4SiO_4 and Aluminum Pebbles", 5th Int. Conf. on Fusion Reactor Materials (ICFRM-5), Clearwater, Fla, November 17 - 22, 1991.

[5] M. Dalle Donne, E. Bojarsky, U. Fischer, A. Goraieb, P. Norajitra, G. Reimann, H. Reiser, G. Sordon, "Conceptual Design of a Helium Cooled Solid Breeder Blanket Based on the Use of a Mixed Bed of Beryllium and Li_4SiO_4 Pebbles", 17th SOFT, Rome, Sept. 14 - 18, 1992.

[6] L.V. Boccaccini, "Calculation of the Electromagnetic Forces and Stresses Caused by a Plasma Disruption in the Karlsruhe Solid Breeder Blanket for the DEMO Reactor", 17th SOFT, Rome, Sept. 14 - 18, 1992.

[7] P. Ruatto, "First Calculations of the Electromagnetic Forces Caused by a Disruption in a Solid Breeder Blanket with a

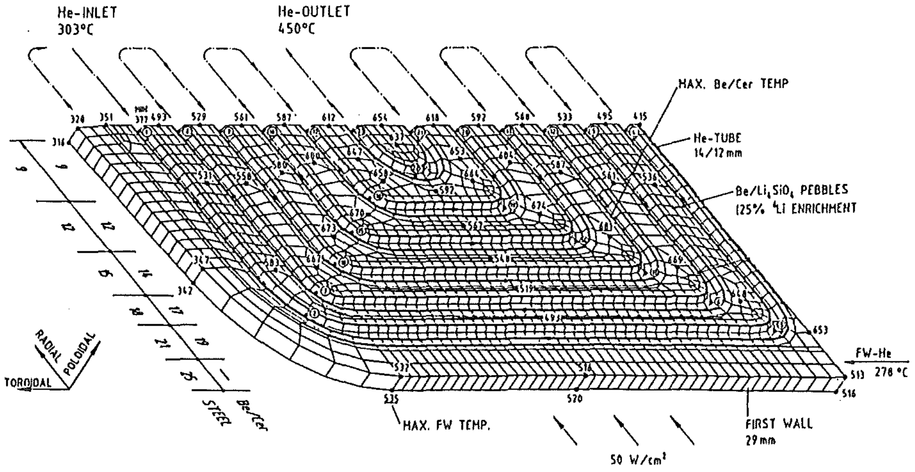

Fig. 5: Isometric view of a radial-toroidal slice of the front region of the blanket with beryllium pebbles showing the results of the temperature calculations

Ferromagnetic Structural Material", 17th SOFT, Rome, Sept. 14 - 18, 1992.

[8] L. Bottura, R. Albanese, L. Boccaccini, R. Fresa, I. Gernhardt, O. Gruber, R. Martone, W. Wokye, "Eddy Current Codes Validation against Electromagnetic Transients in ASDEX-Upgrade", 17th SOFT, Rome, Sept. 14 - 18. 1992.

[9] V. Schauer, M. Dalle Donne, R. Huber, B. Schmitt, G. Schumacher, H. Werle, "Mechanical Properties and Dehydration of Li_4SiO_4 Pebbles", 17th SOFT, Rome, Sept. 14 - 18 1992

Staff:

L. Boccacini
E. Bojarsky
M. Dalle Donne
U. Fischer
A. Goraieb
R. Huber
P. Norajitra
G. Reimann
H. Reiser
P. Ruatto
F. Scaffidi-Argentina
B. Schmitt
G. Schumacher
G. Sordon

BS BR-D 1 Preparation of Ceramic Breeder Materials

The preparation of lithium containing monosilicates, especially Li_4SiO_4, and metazirconate, Li_2ZrO_3, are under development to be used as breeder materials within the European Fusion Program. The development was concentrated on a long-time annealing test to obtain more information on the structural behaviour of the breeder materials under elevated temperatures.

The out-of-pile long-time test was carried-out with a variety of specimens of Li_4SiO_4 and Li_2ZrO_3, as pointed out in Table 1. The sintered materials were prepared by powder metallurgical methods as already previously described. The molten pebbles were fabricated by SCHOTT company.

Material	shape of material	
Li_4SiO_4	sintered pellets, sintered pebbles, molten pebbles,	8 x 8 mm 0.5 mm Ø 0.5 mm Ø
Li_2ZrO_3	sintered pellets,	8 x 8 mm

Table 1: Materials for long-time annealing test

The breeder materials were annealed in a tube furnace at a temperature of 800 °C under flowing He-0.1% H_2 for up to 273 days. Specimens for characterization were taken out of the furncace after every two to three weeks. The results of the characterization work are reviewed in the following chapter.

Literature:

[1] H. Wedemeyer, H. Werle, E. Günther:
Influence of Grain-Size and Carbonate Impurities on the Tritium Release from Lithium Orthosilicate, 5th Intern. Conf. on Fusion Reactor Materials (ICFRM-5), Nov. 1991, Clearwater, Florida, J. Nucl. Mater. (in press)

[2] M. Dalle Donne, E. Günther, G. Schumacher, G. Sordon, D. Vollath:
Research and Development Work for the Lithium Orthosilicate Pebbles for the Karlsruhe Ceramic Breeder Blanket, J. Nucl. Mater. 197-181 (1991) 796-799.

[3] K.R. Kummerer, H.-J. Ritzhaupt-Kleissl:
Comparative Irradiation of Different Lithium Ceramics, J. Nucl. Mater. 197-181 (1991) 831-834.

Staff:

E. Günther
J. Heger
U. Maciejewski
H. Wedemeyer

BS BR-D 2 Characterization of Ceramic Breeder Materials

Little is known about the long-time behaviour of lithium ceramic materials at elevated temperature. Therefore a long-term annealing study with sintered and molten lithium orthosilicate (Li_4SiO_4) and sintered samples of lithium metazirconate (Li_2ZrO_3) was performed at 800 °C. Experiment durations with pebbles and pellets varied from 14 to 273 days. The aim of this study was to observe possible changes in microstructure, chemical composition and mechanical behaviour.

The samples were characterized with respect to phase analysis by x-ray diffraction, fracture load and microstructure by optical and scanning electron microscopy. The lithium content was measured by atomic absorption spectrometry (AAS), silicon and zirconium by x-ray fluorescence spectrometry (RFA).

Due to lithium losses during preparation some amount of lithium metasilicate (Li_2SiO_3) was observed in all Li_4SiO_4 samples by x-ray diffraction with the exception of the initial material of the molten pebbles. In almost all lithium metazirconate samples zirconia was found as a foreign phase. However no significant increase of foreign phases with increasing annealing time was detected and no clear decrease in lithium content was determined by chemical analysis.

During annealing the grain size of the samples increased from about 10 to 20 µm and from less than 10 to 15 µm in lithium orthosilicate and metazirconate, respectively. The grain boundaries in the sintered orthosilicate samples and the cracks in the molten pebbles were broadened. The foreign phases, Li_2SiO_3 and ZrO_2, resp., were mostly present at grain boundaries. No significant increase in the amount of these phases was observed by microscopy, too.

In order to determine changes in the mechanical behaviour, the fracture loads of 10 single pebbles were measured after different annealing times (Fig. 1). The relatively large standard deviations of the orthosilicate data are due to hollow spheres and cracks in the molten material and to the non-spherical form of the sintered pebbles. There is a decrease in fracture load within the first 40-60 days, especially for the molten pebbles with a decrease from about 14 to 5 N. After longer annealing times the fracture load remains constant; for both orthosilicate variants fracture loads of 4-5 N were measured. Additionally some of the molten Li_4SiO_4 pebbles were preheated at 1030 °C to reduce thermal stress and then annealed at 800 °C up to 56 days. The values of fracture load of these samples are about 4 N, without changes by annealing. Because of the lower density of about 77 %TD, the fracture load of the untreated metazirconate pebbles is only about 3 N and decreases to 1.5 N after longer annealing times.

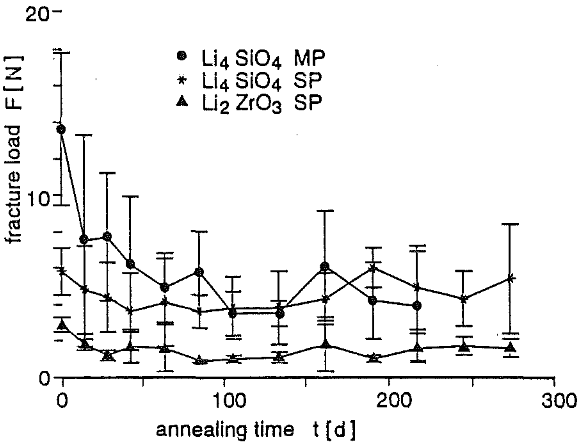

Fig. 1: Measured fracture loads as a function of the annealing time for sintered and molten Li_4SiO_4 pebbles (SP and MP, resp.) and sintered Li_2ZrO_3 pebbles (SP).

These results should be compared and verified by a long-time irradiation experiment.

Literature:

[1] H. Wedemeyer, E. Günther, R. Knitter: Thermisches Langzeitverhalten lithiumhaltiger Fusionskeramiken; Jahrestagung Kerntechnik, Karlsruhe, 5.-7.5.1992

Staff:

R. Hanselmann
R. Knitter
W. Laub
C. Odemer

BS-BR-D 3 Irradiation Testing and Post Irradiation Examination

Post Irradiation Examination

1. COMPLIMENT

The solid breeder concept requires ceramic compounds with high lithium content, good tritium extraction characteristic at moderate temperatures, mechanical integrity, minor swelling and chemical compatibility to the containment. Measurement and comparison of the properties of various breeding ceramics irradiated in closed capsules at different temperatures and neutron fluences are carried out in the Fusion Ceramics Laboratory (FKL). For the European COMPLIMENT experiment [1,2] Comparison of Lithium Materials Damage Effects by Fast Neutrons and ^{6}Li(n,α)T Reactions): Li_2O, $LiAlO_2$, Li_2ZrO_3, Li_2SiO_3, Li_4SiO_4 samples were irradiated at (400 - 450) °C and (650 - 700) °C at the reactors HFR-Petten and OSIRIS-Saclay, respectively. After irradiation the sample rods were transfered to the FKL at KfK. Post irradiation examination (PIE) of the samples (pellet & pebbles) ist now nearly finished. Tab. 1 shows the test maxtrix with the breeding materials of different European partners. The UKAEA and the CEN-Mol have cancelled the further post irradiation examinations. The samples of the CEA an ENEA have been dismantled and partly shipped back into their laboratories. The table shows the status of the pellet columns after dismantling. By this report we present some PIE results of the KfK pebbles irradiated at blanket relevant temperatures:

ELIMA 2	DELICE 03
MS 173	MS 175
SS 113	SS 115

As can be seen (Tab. 1) the KfK samples consisted of two sorts of Li-orthosilicate. After tritium extraction at 850 °C the material came into the metallography for preparation and microscopic examination. Figs. 1 - 2 show the, polished cross sections of pebbles of the two fabrication routes. The sintered spheres (SS 113, SS 115) show a fraction of broken particles between 50 - 70 % (Tab. 1). In comparison the molten spheres (MS 173) irradiated in the HFR are not fractured but darkly coloured. The kernels of the same batch (MS 175) irradiated in OSIRIS are partly (50 %) broken. The irradiation conditions with respect to the different fluences are presented in Fig. 7.

Figs. 3 - 6 show some results from the Scanning Electron Microscope (SEM). The molted pebbles have a smooth surface. The broken "necks" are the result of the tempering step (1024 °C) which was applied to enhance the mechanical stability of the product before irradiation. The sintered spheres or "granules" have a very porous surface. In fact of the small quantities a granulometry could not be made. An estimate performed with the SEM shows that the fractured particles have a size from 10 - 100 μm. The mode of fracture is for both cases intercristalline.

Table 1: Comparative Irradiation Experiment COMPLIMENT Identification of Sample Rods

European Partners	ELIMA 2 / HFR-Petten		DELICE 03 / OSIRIS-Saclay		Sum of samples
	Matrix I 400 - 450 °C	Matrix II 650 - 700 °C	Matrix III 400 - 450 °C	Matrix IV 650 - 700 °C	
CEA, Saclay	$LiAlO_2$ 78 %*) P 139**) $LiAlO_2$ 78 % P 140 □ $LiAlO_2$ 62 % P 141 d $LiAlO_2$ 84 % P 142 i	$LiAlO_2$ 78 % P 143 i $LiAlO_2$ 78 % P 144 □ $LiAlO_2$ 62 % P 145 □ $LiAlO_2$ 84 % P 146 i	$LiAlO_2$ 78 % P 147 □ $LiAlO_2$ 78 % P 148 □ $LiAlO_2$ 62 % P 149 □ $LiAlO_2$ 84 % P 150 d	$LiAlO_2$ 78 % P 151 i $LiAlO_2$ 78 % P 152 □ $LiAlO_2$ 62 % P 153 □ $LiAlO_2$ 84 % P 154 i	16
ENEA, Cassacia	$LiAlO_2$ 80 % P 117 i $LiAlO_2$ 80 % P 118 i $LiAlO_2$ 80 % P 119 i	$LiAlO_2$ 80 % P 120 i $LiAlO_2$ 80 % P 121 □ $LiAlO_2$ 80 % P 122 i	$LiAlO_2$ 80 % P 155 i $LiAlO_2$ 80 % P 156 i $LiAlO_2$ 80 % P 157 i	$LiAlO_2$ 80 % P 158 i $LiAlO_2$ 80 % P 159 i $LiAlO_2$ 80 % P 160 i	12
UKAEA, Springfield	Li_2O 83 % P 131 i Li_2O 79 % P 132 □ Li_2ZrO_3 80 % P 123 i Li_2ZrO_3 80 % P 124 i	Li_2O 80 % P 133 i Li_2O 82 % P 134 □ Li_2ZrO_3 80 % P 125 □ Li_2ZrO_3 80 % P 126 i	Li_2O 79 % P 135 □ Li_2O 81 % P 136 □ Li_2ZrO_3 80 % P 127 □ Li_2ZrO_3 80 % P 128 i	Li_2O 82 % P 137 d Li_2O 82 % P 138 □ Li_2ZrO_3 80 % P 129 □ Li_2ZrO_3 80 % P 130 i	8 8
CEN, Mol	Li_2SiO_3 82 % P 161 i Li_2SiO_3 82% P 163 □ Li_2SiO_3 75% P 165 □	Li_2SiO_3 82 % P 162 □ Li_2SiO_3 75% P 166 □ Li_2ZrO_3 80% P 164 i	Li_2SiO_3 82 % P 167 d Li_2SiO_3 82% P 169 □ Li_2SiO_3 75% P 171 □	Li_2SiO_3 82 % P 168 □ Li_2SiO_3 75% P 172 □ Li_2ZrO_3 80% P 170 □	10 2
KfK, Karlsruhe	Li_4SiO_4 98 % MS 173 i Li_4SiO_4 85 % SS 113 50% Li_4SiO_4 90 % P 109 i Li_2SiO_3 90 % P 101 i	Li_4SiO_4 98 % MS 174 i Li_4SiO_4 85 % SS 114 i Li_4SiO_4 90 % P 110 i Li_2SiO_3 90 % P 102 i	Li_4SiO_4 98 % MS 175 50% Li_4SiO_4 85 % SS 115 70% Li_4SiO_4 90 % P 111 d Li_2SiO_3 90 % P 103 i	Li_4SiO_4 98 % MS 176 i Li_4SiO_4 85 % SS 116 i Li_4SiO_4 90 % P 112 d Li_2SiO_3 90 % P 104 i	4 4 4 4
Sum	18	18	18	18	72

*) % Theoretical Density
**) KfK Rod Number

P = Sintered Pellets
MS = Molten Spheres
SS = Sintered Spheres

□ = not dismantled
i ,= intact
d = defect
% .= percentage of broken pebbels

Literature:

[1] H.E. Häfner et al. in Fusion Technology Programme, Semi Annual Report Oct. 89 - Sept. 90 and Sept. 90 - Oct. 91

[2] K.R. Kummerer and H.J. Ritzhaupt-Kleissl in J. Nucl. Mat. 179-181 (1991) 831-834

Staff:

T. Eberle
R. Hanselmann
E. Kaiser
D. Knebel
R. Pejsa
O. Romer
D. Schild
H. Steiner
P. Weimar
F. Weiser
R. Zerull
H. Ziegler
L. Dörr

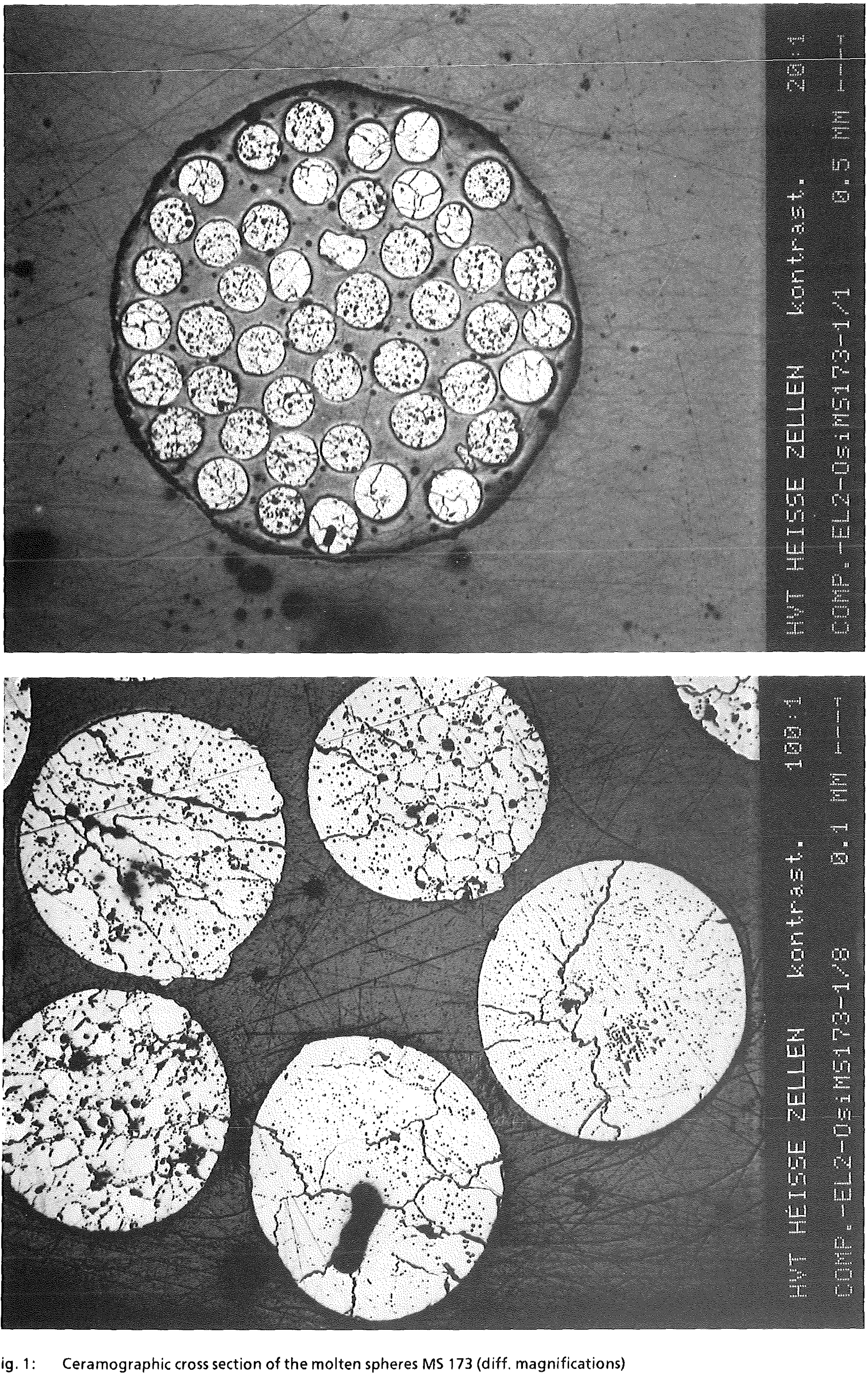

Fig. 1: Ceramographic cross section of the molten spheres MS 173 (diff. magnifications)

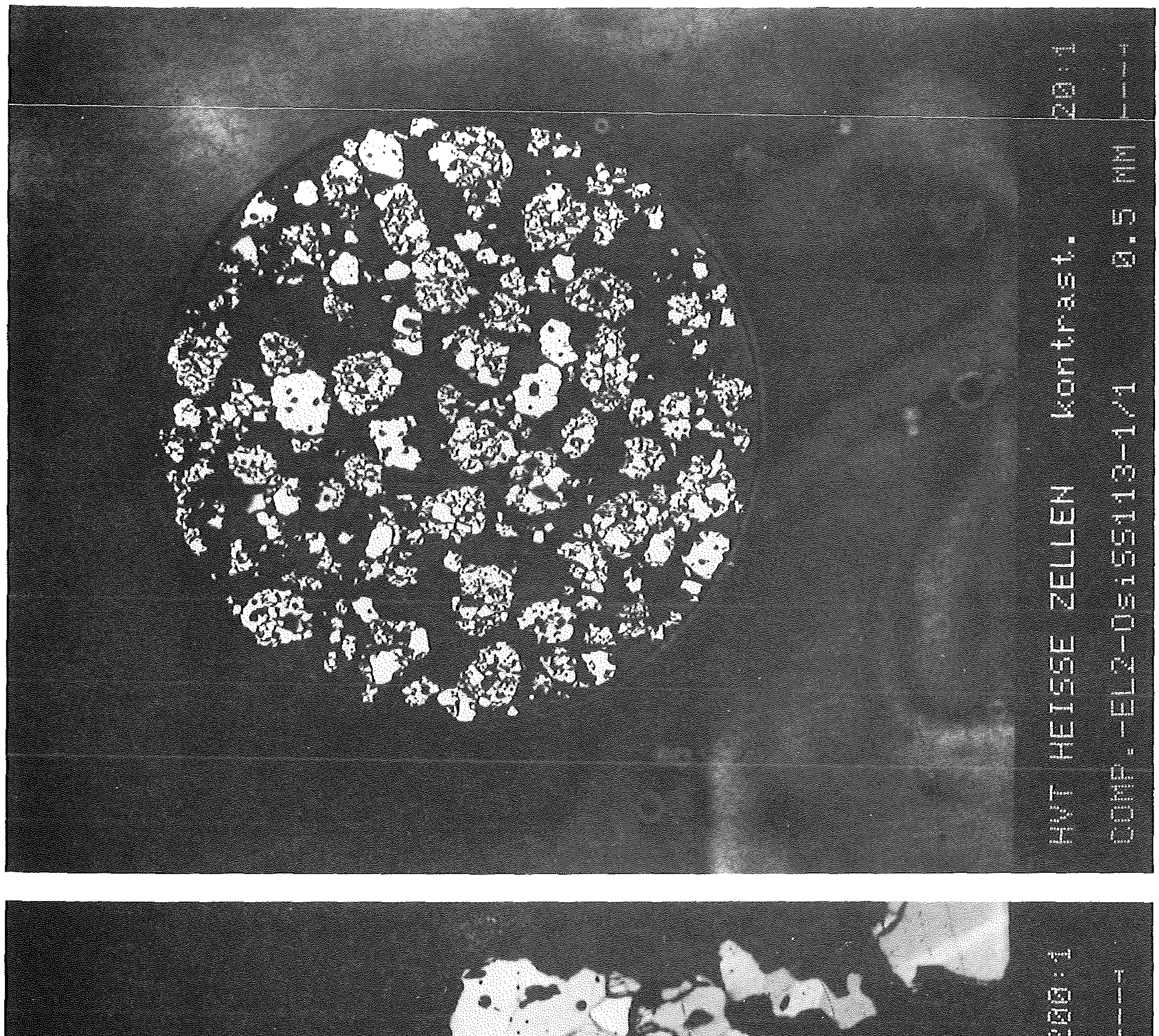

Fig. 2: Ceramographic cross section of the sintered speres SS 113 (diff. magnifications)

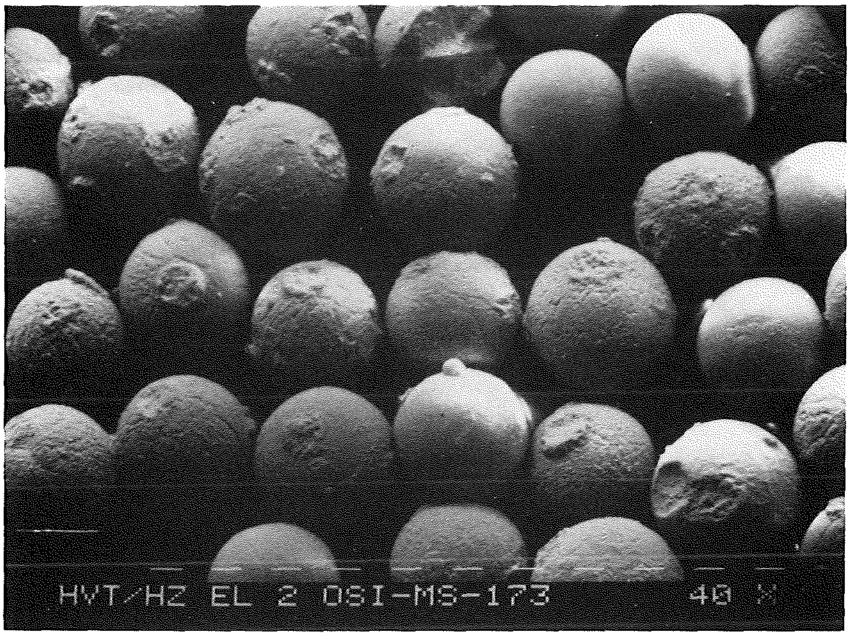

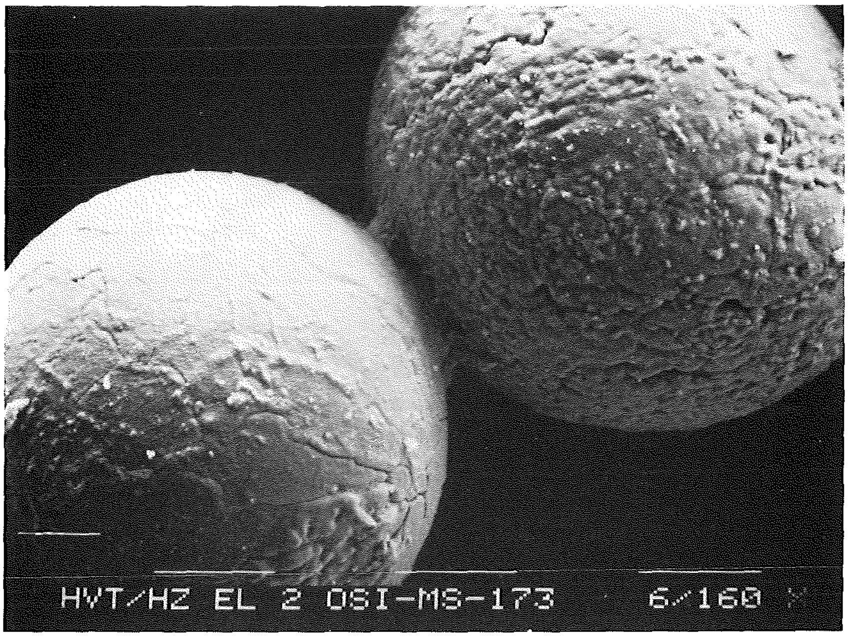

Fig. 3: Scanning Electron Microscope (SEM): surface structure of the molten spheres MS 173 (necks are the result of the tempering procedure)

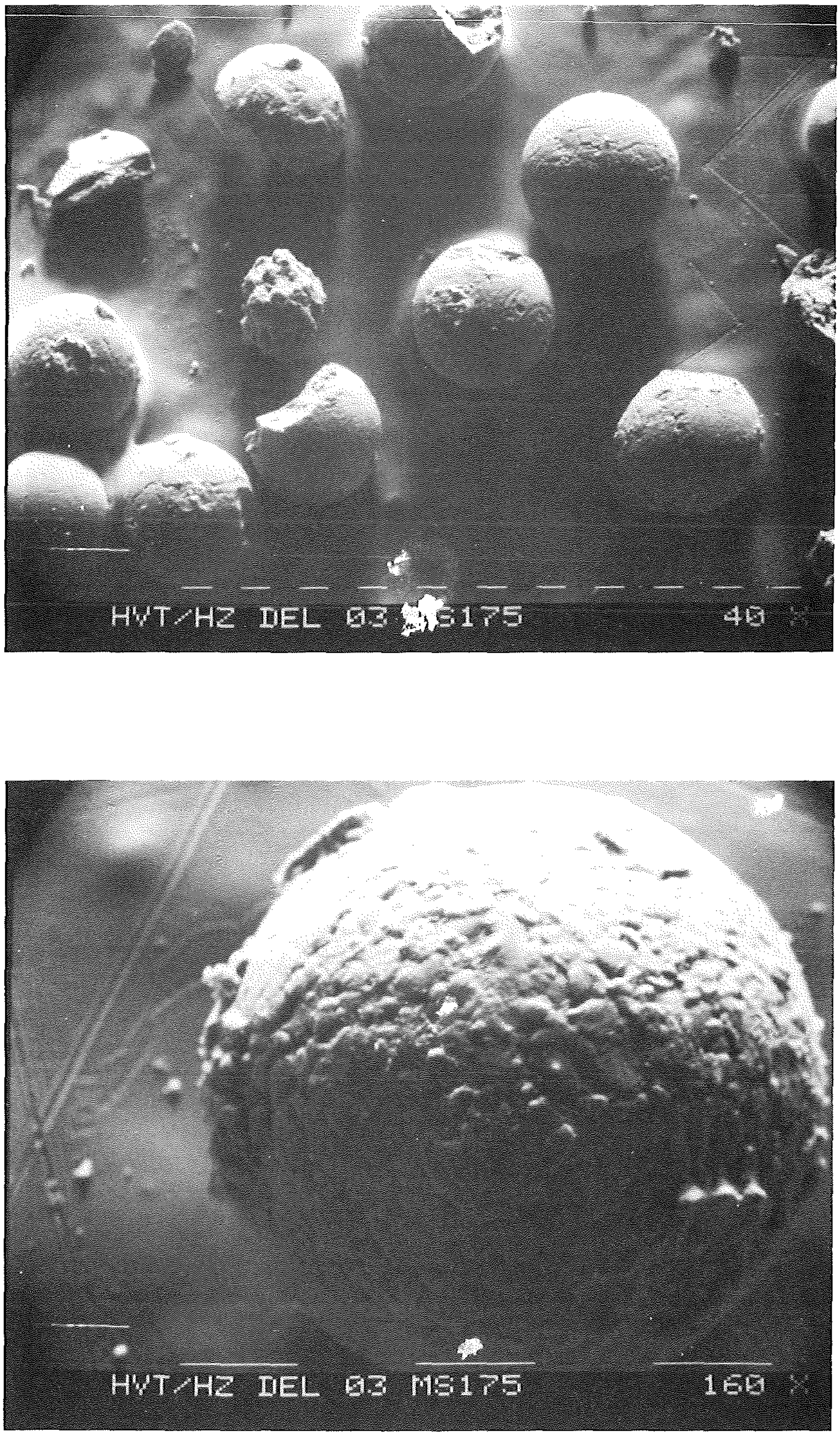

Fig. 4: Scanning Electron Microscope (SEM) surface structure of the molten spheres MS 175 (necks are the result of the tempering procedure)

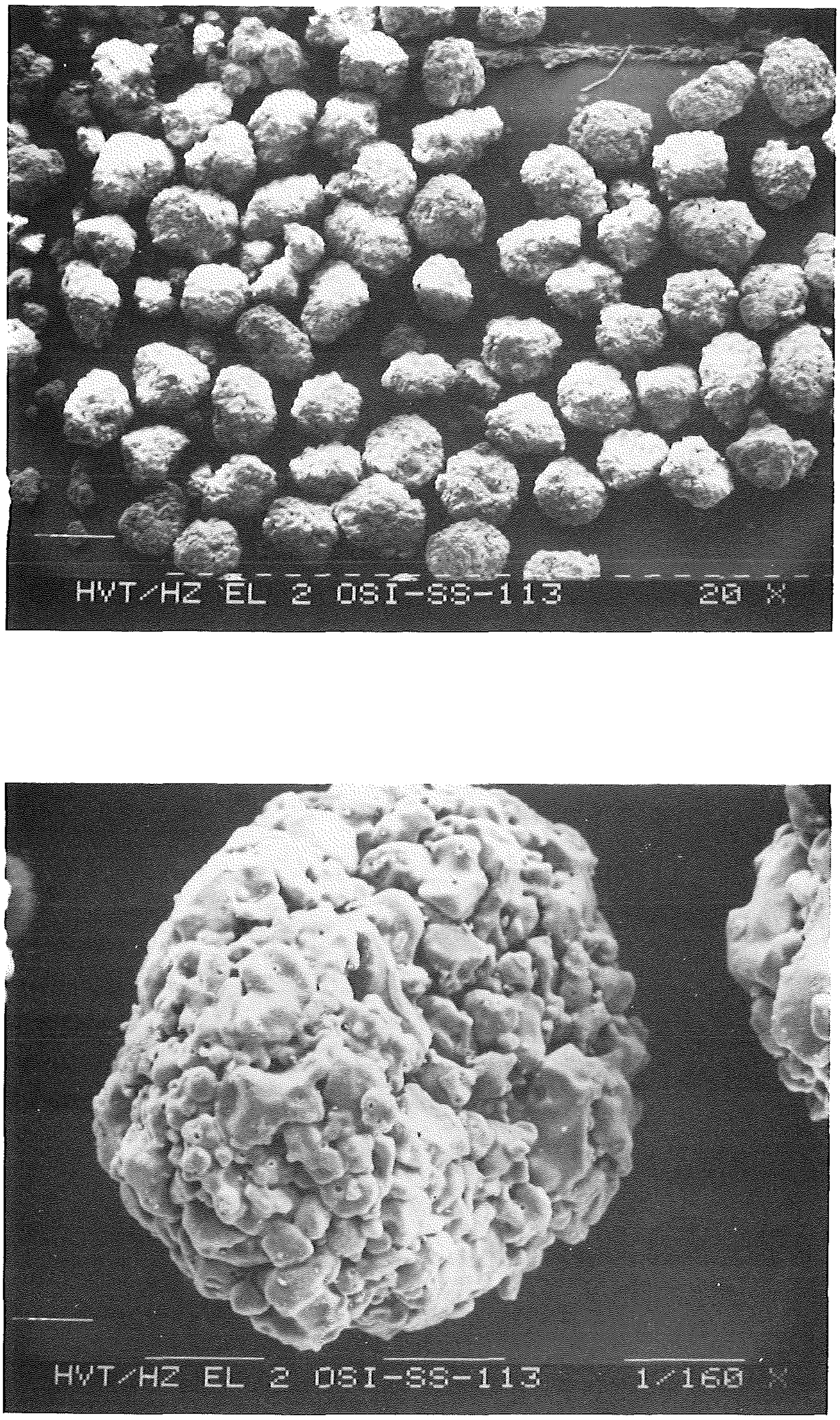

Fig. 5: SEM image of the sintered spheres SS 113

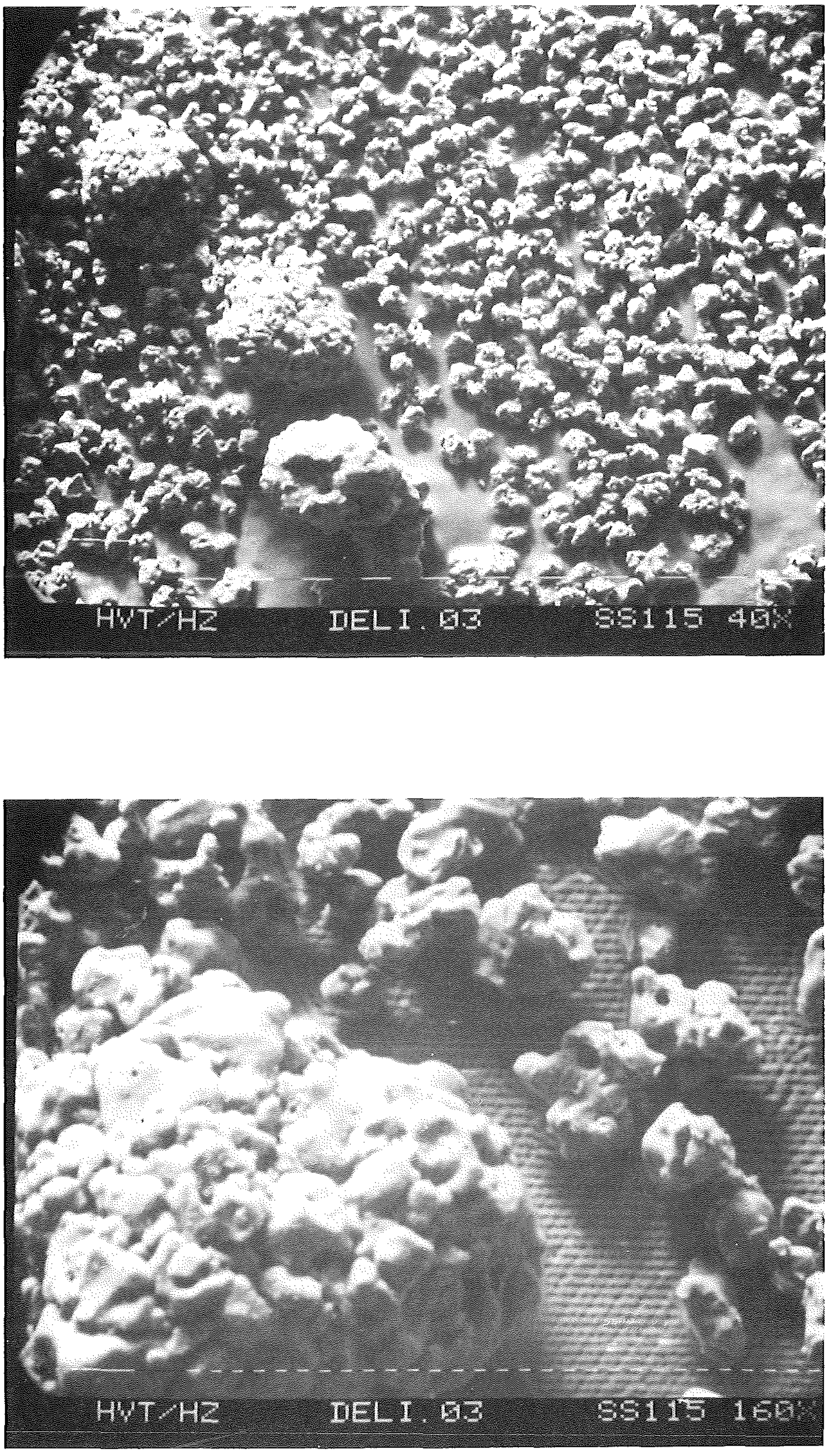

Fig. 6: SEM image of the sintered spheres SS 115 (see the large fraction of broken pebbles)

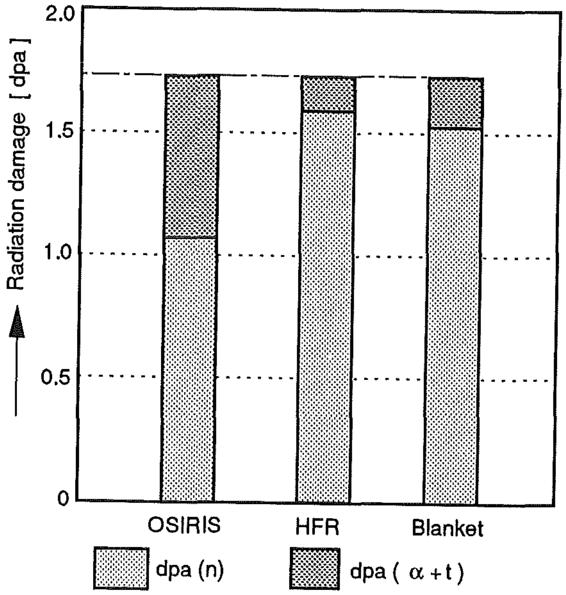

OSIRIS-Position 64: 7.5% ^{6}Li, 75 FPD
HFR-Position F2 with Cd: 7.5% ^{6}Li, 175 FPD
Blanket-Position at 1 MW/m^2: 60 % ^{6}Li, 75 FPD

Fig. 7: Comparison of radiation damage & damage by (α+t)-reaction in the reactors OSIRIS and HFR-Petten

2. SIBELIUS

One of the objectives of the experiment SIBELIUS, performed from April to October 1990 in the SILOE reactor at Grenoble, was to assess the compatibility of the neutron multiplier material beryllium with ceramic breeder materials and with steels under neutron irradiation.

Reaction couples of beryllium discs with Li_2O or Li_4SiO_4 pellets and with 316L or 1.4914 steel discs were investigated after 1690 h irradiation at 550 °C. Cross-sections parallel to the disc and pellet axes were prepared for the microscopic observation of chemical reaction zones on the couple interfaces, mostly in polished condition.

Concerning the couple Be/316L (17.4 % Cr, 12.3 % Ni) the steel showed a reaction product layer of 2 - 3 μm thickness and precipitates to a depth of about 15 μm which probably consist of BeNi [1]. The Be surface appeared roughened to a maximum depth of 3 - 4 μm. The Be/1.4914 (10.6 % Cr, martensitic-ferritic) reaction showed an even smaller extent. These results agree with those of former laboratory annealing tests [1], and no additional irradiation influence could be detected, in accordance with expectation.

The same is true for the observation that no detectable chemical reaction occurred at the interface of the Be/Li_2O and Be/Li_4SiO_4 couples, except a minor roughening of the Be surface. But there was a marked change in the Be microstructure that is certainly irradiation-induced. Rather large pores (2 - 15 μm diameter) had formed in a 40 μm zone under the Be surface (Fig. 8). The pore diameters and also the pore volume fraction appeared considerably larger with Li_2O than with Li_4SiO_4. Similar pore formation has been observed in CEA investigations on Be/Li_2ZrO_3 and $LiAlO_2$ [2].

There are good arguments to assume that this pore formation is caused by the triton bombardment from the breeder material and that the pores are filled with tritium. The Li-burnup (1.5 to 2 %), the 2.7 MeV-triton penetration depth (about 40 μm in Be), and literature data of the diffusion coefficient and the solubility of tritium in beryllium seem to fit this assumption.

Literature:

[1] P. Hofmann, W. Dienst, Chemical interactions of beryllium with lithium-based oxides and stainless steel, J. Nucl. Mater. 171 (1990) 203

[2] N. Roux, J.J. Abassin, M. Briec, D. Cruz, T. Flament, I. Schuster, Compatibility behavior of beryllium with $LiAlO_2$ and Li_2ZrO_3 ceramics, with 316L and 1.4914 steels in SIBELIUS, Fifth Int. Conf. on Fusion Reactor Materials, Nov. 17-22, 1991, Clearwater, Florida, to appear in J. Nucl. Mater.

Staff:

W. Dienst
P. Hofmann
E. Kaiser
D. Schild
F. Weiser

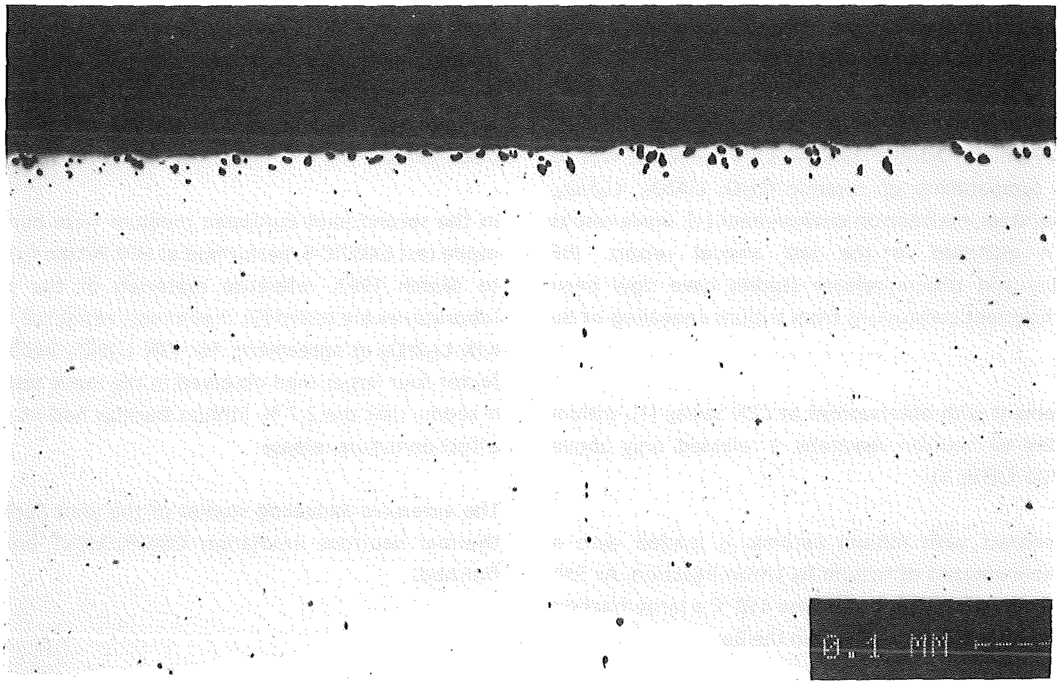

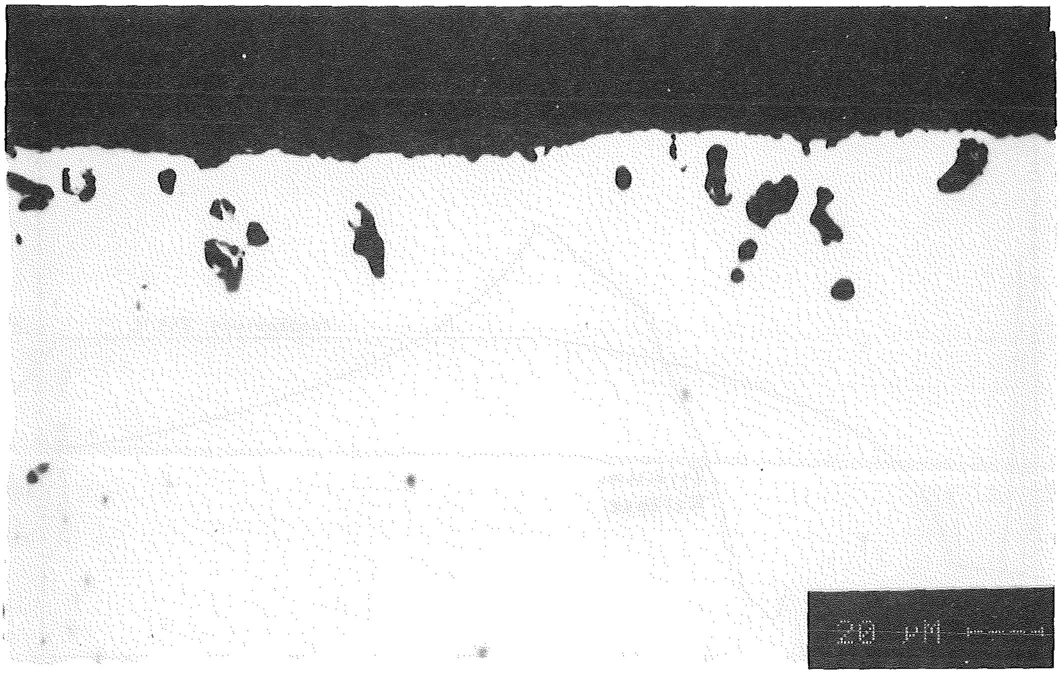

Fig. 8: Pore zone in beryllium near the surface having been in contact with Li_2O under neutron irradiation

BS BR-D 4 Tritium Release

In assessing the performance of ceramic breeders, tritium release is an important aspect. KfK concentrates on lithium orthosilicate and metazirconate. Purged inpile and out-of-pile annealing tests are performed.

The primary objective of the purged inpile test SIBELIUS, performed April to October 1990 at CEN Grenoble, was to study the compatibility of ceramic (Li_2O, $LiAlO_2$, Li_4SiO_4, Li_2ZrO_3) /Be/ steel in a neutron environment [1]. Inpile results have been discussed in the last annual report. PIE compatibility and tritium release studies have now been finished. Important conclusions from tritium annealing of Be are:

- In agreement with observations at CEN Saclay [1], tritium generated by neutron reactions is released only above about 700 °C (Fig. 1)

- Be in contact with lithium ceramic is loaded with a remarkable amount of tritium by triton injection. At 550 °C only a minor fraction, but below 450 °C a large fraction of the injected tritium stays within the Be.

In the CORELLI inpile test, performed May to July 1991 in Grenoble, orthosilicate pellets with different grain sizes (7 and 80 µ) were tested by KfK [2]. Erroneously, the inpile data have been misinterpreted in [2] and the last annual report. After a careful check of the irradiation documentation at CEN Grenoble, we have to conclude that inpile tritium release from the large (80 µ) grains is faster than from the small (7 µ) grains. This result is in contradiction with annealing tests and with observations at other laboratories. Therefore the samples will be sent to KfK for PIE to solve this severe discrepancy.

In the second joint European medium term burnup (2.7 %) inpile test EXOTIC-6, performed at HFR Petten from May 1991 to March 1992, reference materials of the participating laboratories are tested [3]. Preliminary residence times are for KfK Li_2ZrO_3 in agreement, for KfK Li_4SiO_4 pebbles about a factor four larger than observed in the inpile test TRIDEX [4]. It seems that the 2.7 % lithium burnup had no detrimental effect on tritium release.

The extensive annealing studies of the joint European fast / thermal neutrons irradiation COMPLIMENT are essentially finished.

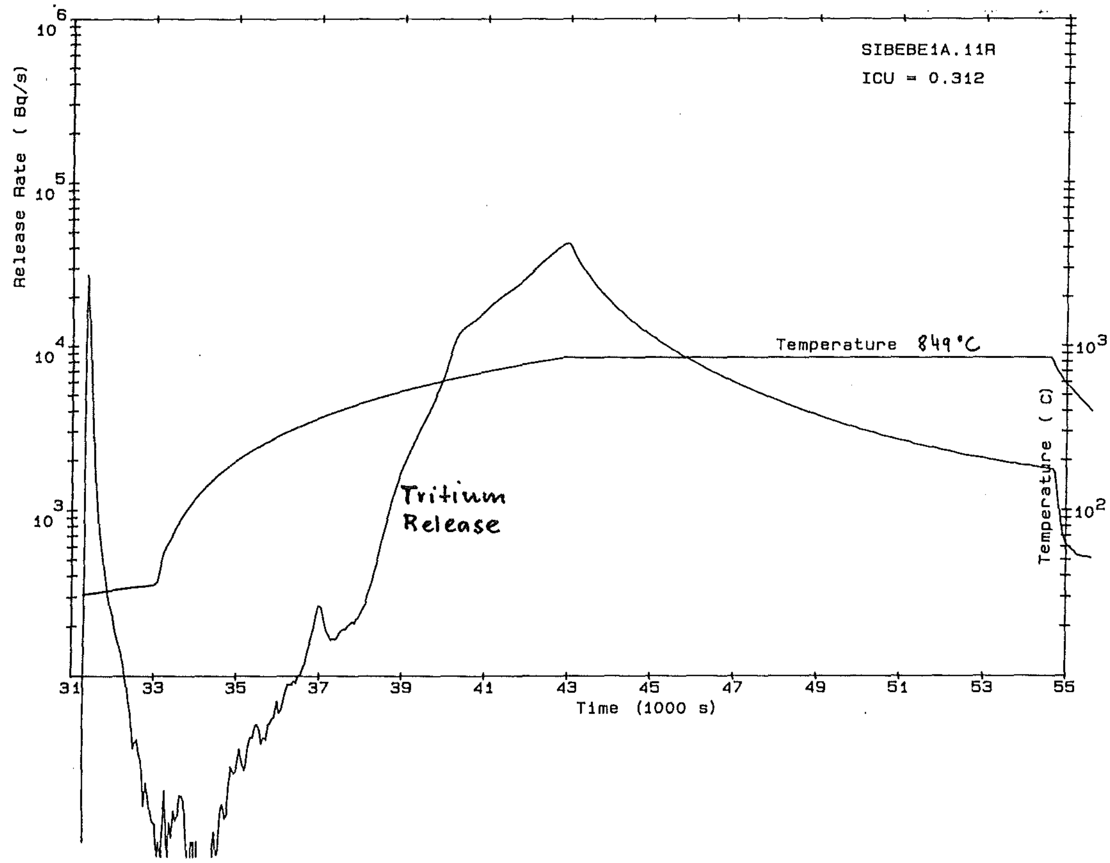

Fig. 1: Tritium Release from Beryllium during heating with 5°C/min (purge gas He+0.1 vol % H_2)

Literature:

[1] N. Roux et al., "Compatibility Behaviour of Beryllium with $LiAlO_2$ and Li_2ZrO_3 Ceramics, with 316 L and 1.4914 Steels in SIBELIUS", ICFRM-5, Clearwater, 1991.

[2] H. Wedemeyer, H. Werle, E. Günther, "Influence of Grain-Size and Carbonate Impurities on the Tritium Release from Lithium Orthosilicate", ICFRM-5, Clearwater, 1991.

[3] R. Conrad et al., "Irradiation Progress Report No. 8, Cycle 92.02, EXOTIC-6", Technical Memorandum HFR/92/3839, JRC Petten, March 1992.

[4] W. Krug et al., "Inpile Tritium Release from Ceramic Breeder Materials in TRIDEX Experiments 1 to 6", Fusion Eng. Design 17 (1991) 65.

Staff:

W. Breitung
T. Eberle
J. Lebkücher
M. Möschke
H. Werle

BS BR-D 8 Solubility of Molecular Hydrogen in Lithium Orthosilicate

The solubility of hydrogen in ceramic materials proposed for tritium breeding in a fusion reactor is one of the properties that need to be investigated for an estimation of the tritium inventory in a blanket. Previous investigations have concentrated on the measurement of the solubility of hydrogen in Li_2O and in Li_2SiO_3. In this report first results on the solubility of hydrogen in Li_4SiO_4 are published.

Hydrogen solubility measurements in lithium orthosilicate were performed at constant temperature and various pressures employing a volumetric technique. Briefly, tablets of the lithium ceramic material were placed in an alumina vessel containing an alumina insert above the sample and, after extended conditioning of the sample at high temperature under vacuum, exposed for periods of up to a week to a constant pressure of hydrogen at a temperature of 580 °C. After equilibration the ceramic vessel was cooled down to room temperature and the supernatant gas pumped-off. While usually the pumping period was limited to only a few minutes it was found that long periods of pumping, e.g. 1 hour at room temperature, did not alter the results. To determine the dissolved gas the sample was first heated to 580 °C and after equilibration the liberated gas determined volumetrically at room temperature. This procedure was repeated three consecutive times, the amount of liberated gas decreasing each time. The solubility was calculated from the cumulative gas release. Identical experiments carried out with the empty alumina vessel demonstrated that only a minimal blank correction was necessary. This is substantiated by a comparison of the number of atoms dissolved in the alumina vessel (held at 580°C), in the stainless steel inlet tube (reaching up to 120 °C) and in the 0.3 moles Li_4SiO_4 after a period of one week (see Fig. 1). From the calculated solubilities it is apparent that the solubility of hydrogen in the alumina vessel is approx. five orders of magnitude lower than that in the lithium ceramic. While in comparison to the lithium ceramic the contribution from the stainless steel tubing located immediately above the ceramic vessel is more important, practically no correction to the measured values is needed.

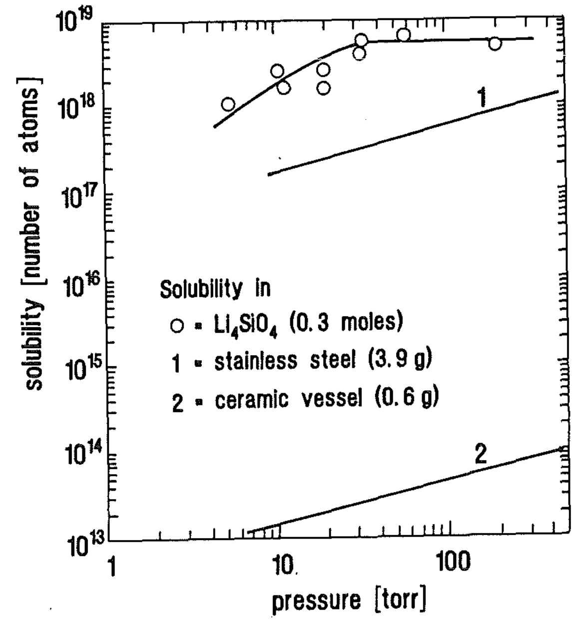

Fig. 1: Measured solubility of hydrogen (not corrected for blank) in lithium orthosilicate and calculated solubility of hydrogen in the alumina vessel as well as in the stainless steel tubing above the vessel

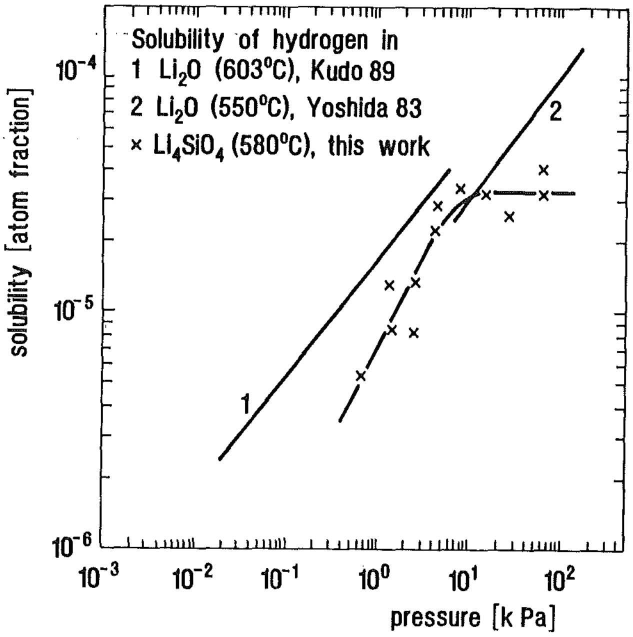

Fig. 2: Solubility of hydrogen in Li_2O and in Li_4SiO_4

Results on the solubility of hydrogen in Li_4SiO_4 at 580 °C are given in Fig. 2 together with results from the literature on Li_2O. The experimental data for Li_4SiO_4 indicate that the solubility follows a Langmuir type behaviour, suggesting molecular rather than atomic solubility. This is in line with an experiment in which Li_4SiO_4 was first exposed to molecular hydrogen at 580 °C for a period of one week and then, after pumping-off the supernatant gas, an analysis of the released gas was carried out with an omegatron. A measurable pressure increase was only observed after the sample had been heated up to 523 K. The analysis showed that the liberated gas consists predominantely of molecular hydrogen with very little water. The latter would have been expected in the case of an atomic dissolution. From thermodynamic considerations it was concluded that at the temperature in question a reaction between water and stainless steel to yield hydrogen was not very likely.

From the results obtained it can be concluded that the solubility of hydrogen in Li_4SiO_4 is not higher than that in Li_2O and therefore very low ($n_H/n_{Li4SiO4} = 1 \times 10^{-6}$) at the hydrogen partial pressures proposed for the blanket sweep gas (100 Pa).

Staff:

S. Anthonysamy (guest scientist)
U. Engelmann
Dr. M. Glugla
W. Jung
Dr. R.-D. Penzhorn
K.H. Simon

BS NN-D 1 Helium Blanket Test Loop

A Helium Blanket Test Loop (HEBLO) was built in order to be able to perform thermomechanical tests on components of gas-cooled blankets. The helium flow rate in HEBLO is 330 g/s at 80 bar operating pressure. Assembly work of the test loop is completed and a functional test was made. The recirculating compressor equipped with gas bearings was put into service during that test and all control and safety functions were programmed and tested. All the tests carried out until this day have been successful.

Operation of the test facility is expected to start in autumn 1992 after some additional work such as providing the thermal insulation, etc. has been done.

For the initial phase two test objects are available:

- Wall elements made of steel with cooling tubes brazed onto them (Fig. 1).
  Several types of braze were used. The wall element surfaces facing the cooling tubes are equipped with electric heaters. The tubes are passed by helium at approximately 50 °C. Temperature cycles similar to those in actual operation will be generated by variation of the heating power and of the coolant gas throughput. The tests will be carried out in the main loop of the helium blanket test loop.

- A cooling pipe coil (Fig. 2) with parts made of beryllium brazed onto it in an arrangement resulting from the external shape of a plane rectangular beryllium plate 200x264x21 mm in size.
  The temperature transients in the plate and hence the thermal stresses are generated by abrupt variation of the coolant gas temperature. A special Temperature Cycle Test Facility is available for these tests which is connected with the HEBLO main loop. It is possible to generate in that facility temperature cycles between about 260 °C and 440 °C.

Staff:

E. Bojarsky
M. Dalle Donne
H. Deckers
H. Lehning
D. Piel
H. Reiser

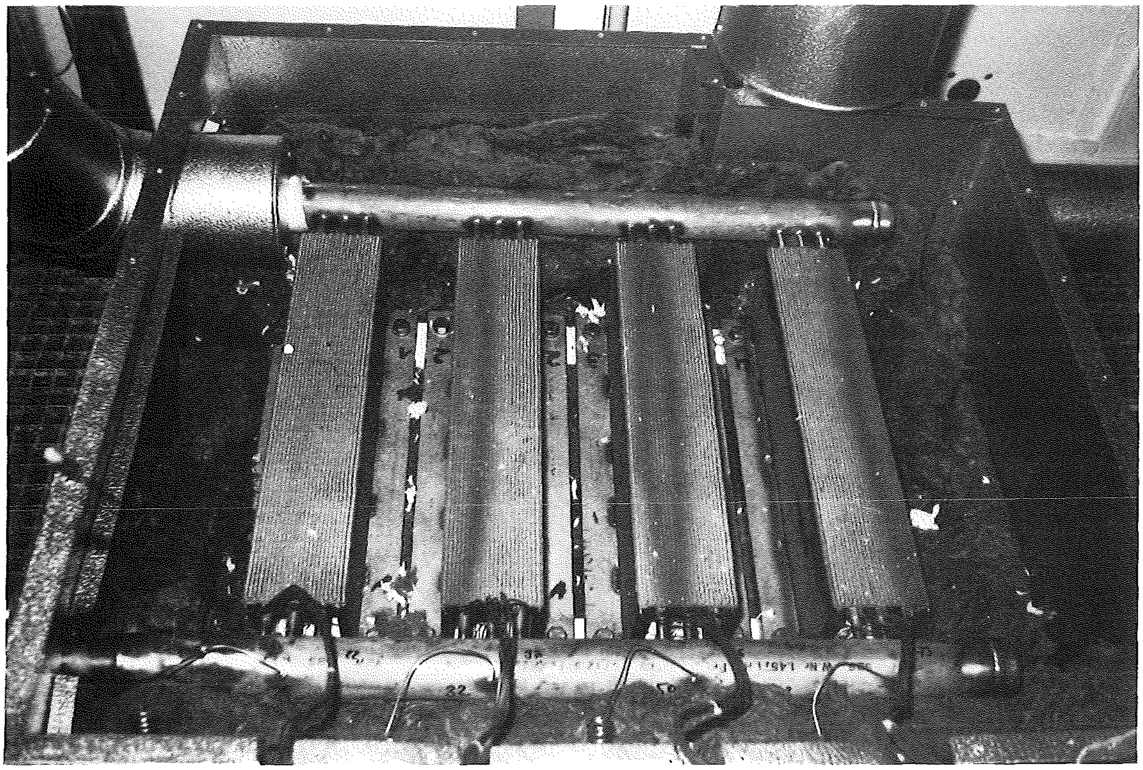

Fig. 1: Electrically heated wall elements with cooling tubes brazed onto them.

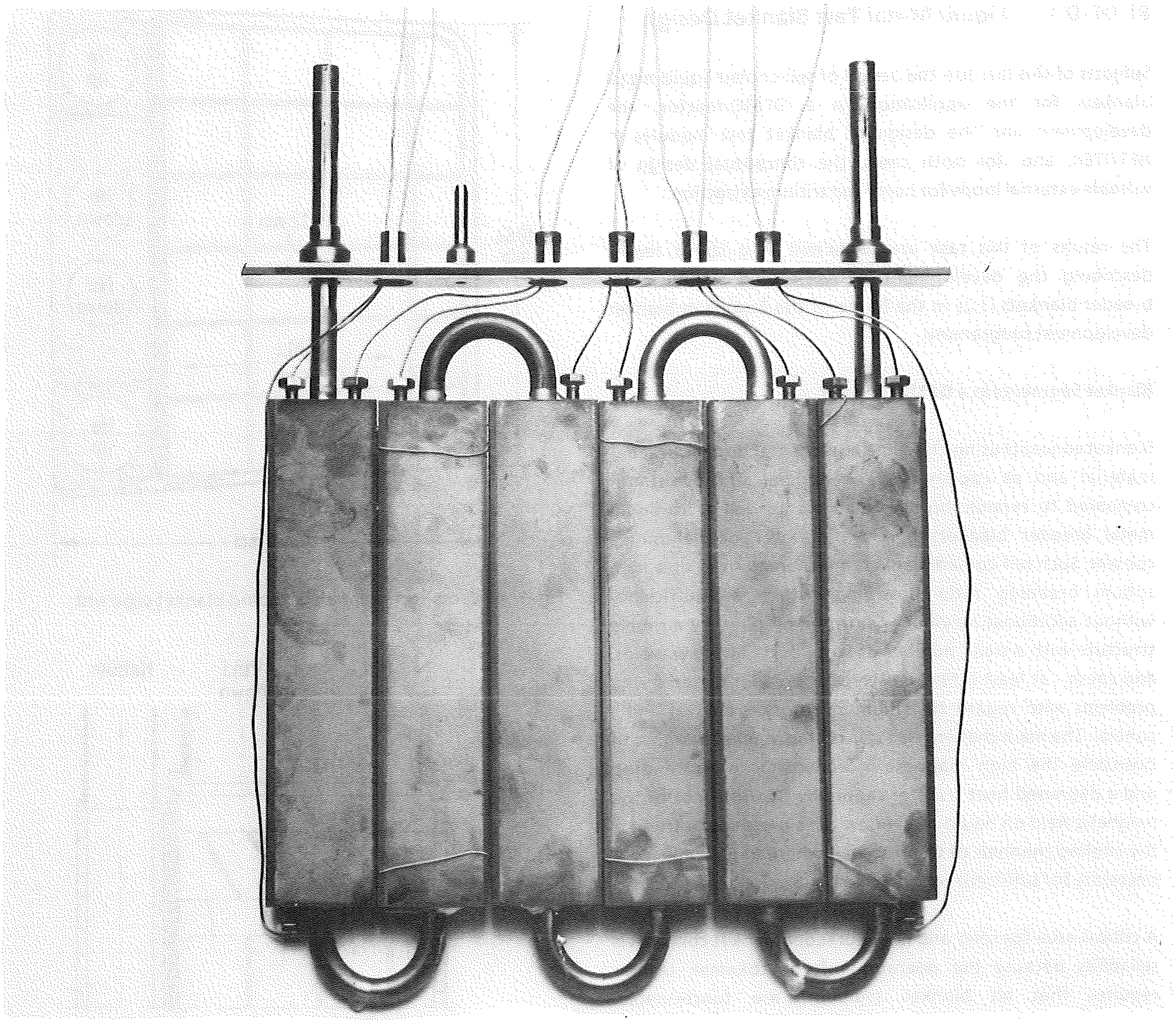

Fig. 2: Beryllium parts brazed onto a cooling pipe coil for temperature transient tests

BL DE-D 1 Liquid Metal Test Blanket Design

Subjects of this task are the design of self-cooled liquid metal blankets for the application in a DEMO-reactor, the development and the design of blanket test modules in NET/ITER, and, for both cases, the conceptual design of suitable external loops for heat- and tritium extraction.

The results of this task are contained in a status report describing the development of self-cooled liquid metal breeder blankets [1,2] in the frame of the European blanket development programme.

Blanket Segments in a DEMO-Reactor

Blanket concepts using the same liquid metal both as breeder material and as coolant have a number of advantages compared to ceramic breeder blankets as well as to liquid metal breeder blankets employing water or helium as coolant. Such self-cooled blankets are characterized by a high tritium breeding ratio providing tritium self-sufficiency without additional beryllium neutron multiplier, by a simple structure with a small number of large ducts and few welds, and cause - at least if Pb-17Li serves as breeder material - no problems with regard to tritium-inventory, -removal and -control. The main challenge of self-cooled blanket design is to overcome the high magneto-hydrodynamic pressure drop and a degraded heat transfer caused by the influence of the magnetic field on liquid metal flow. This is especially true for the cooling channels of the first wall where a high velocity is necessary for sufficient cooling.

A critical issue for solid and liquid breeder blanket concepts is reliability because the operation of the tokamak reactor requires that all blanket segments are functionable. Malfunction of one segment requires an exchange and causes a long downtime of the machine and has to have, therefore, a very low probability. The desire to improve cooling of the first wall and the reliability of blanket segments have led to a novel design employing helium as coolant for the first wall and using Pb-17Li as breeder and coolant for the bulk structure. This concept was briefly described in the previous annual report [3]. The design work on this concept has been continued.

Fig. 1 shows a horizontal cross section of an outboard blanket segment, Fig. 2 the vertical cross sections of the upper and lower end. The FW box is assembled by welding together U-shaped sections containing the helium cooling channels. The welds between two of these sections and between a section and the helium manifold are shown in Fig. 3. This figure indicates that double welds are used with a leak detection gap between, resulting in a real double containment of the liquid metal. Fig. 4 shows the principle of the helium flow in the first wall. There are multiple passes (4 to 8) of the total flow through the first wall cooling channels, resulting in high velocities together with a tolerable pressure drop and, for the reason of a stiff FW box, relatively large channels. The following goals are reached with the dual coolant concept:

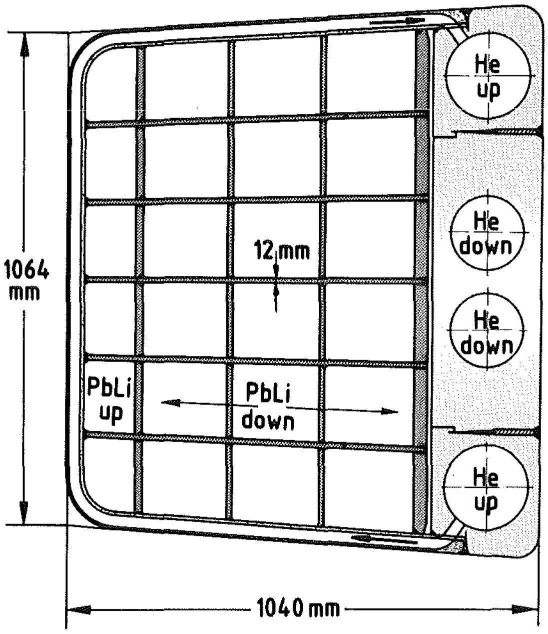

Fig. 1: Cross-section of an outboard blanket segment

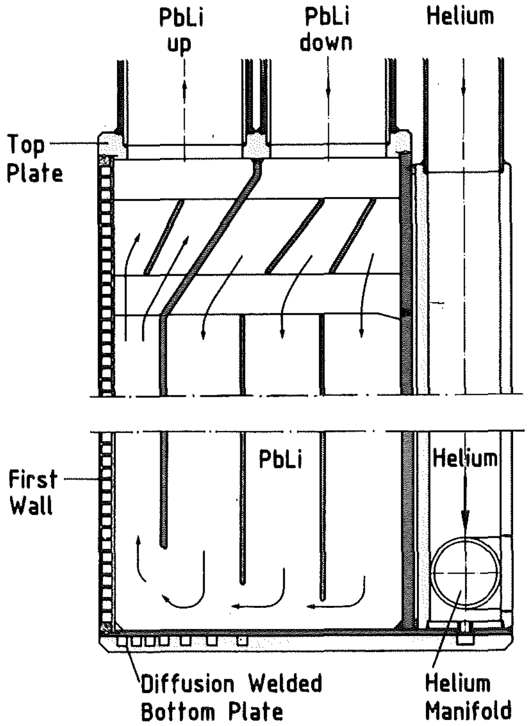

Fig. 2: Upper and lower end of the blanket segment

- Recently developed MHD-tools sufficient for analysing the liquid metal flow due to the simple flow channel geometry of the proposed concept.

- MHD pressure drop and heat transfer properties well within acceptable engineering limits.

- Improved safety and reliability due to leak tolerant design, real double containment of the liquid metal, redundant

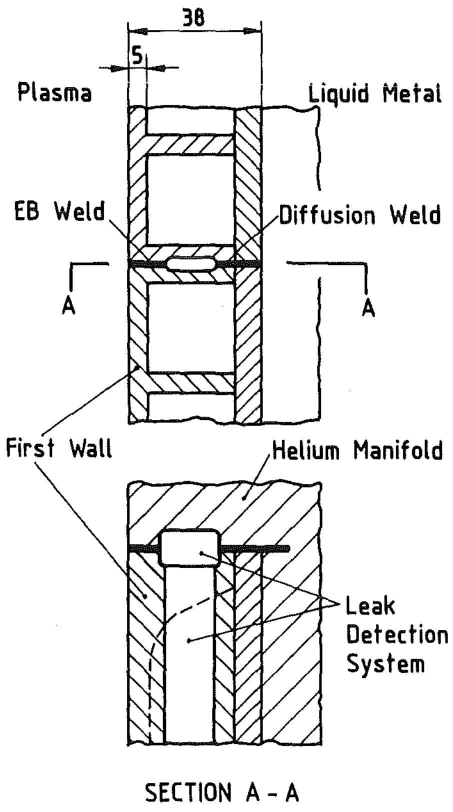

Fig. 3: Double welds and leak detection system of the FW-box

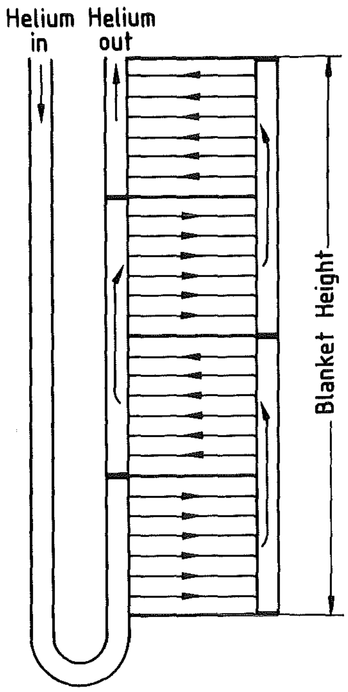

Fig. 4: Principle of the helium flow in the FW-box

and diverse cooling systems (liquid metal, helium), requiring no additional system for after heat removal.

- Helium cooling system can be used for preheating the blanket and to keep the breeder material liquid under all circumstances (guard heating).

The main results of the analysis in the fields of neutronics and thermo-hydraulics are listed in Table 1.

DEMO-reactor specification		
Average neutron wall load	2.2 MW/m²	
Average surface heat flux	0.4 MW/m²	
Maximum surface heat flux	0.5 MW/m²	
Temperature limits		
Structural material (MANET)	550 °C	
Interface Pb-17Li/MANET	450 °C	
Selected coolant conditions		
Liquid metal inlet temperature	275 °C	
Liquid metal outlet temperature	425 °C	
Helium pressure		80 bar
Helium inlet temperature	250 °C	
Helium outlet temperature	350 °C	
Results of the analysis		
Total tritium breeding ratio (including the effect of 10 horizontal ports for plasma heating etc.)	1.15	
Power to be removed from one outboard segment		
- He-Cooling of FW		7 MW
- LM-Cooling of breeding zone	23 MW	
Helium flow rate		13.2 kg/s
Maximum helium velocity	50 m/s	
Helium pressure drop	1.1 bar	
LM flow rate		815 kg/s
Maximum LM velocity	1.1 m/s	

Tab. 1: Main parameter of the dual coolant concept

Literature:

[1] S. Malang, J. Reimann, H. Sebening (comp.): Status report. DEMO relevant Test Blankets for NET/ITER, Part 1: Self-cooled Liquid Metal Breeder Blanket, KfK 4907, October 1991, Volume 1: Summary

[2] H. John, S. Malang, H. Sebening (comp.): Status report. DEMO relevant Test Blankets for NET/ITER, Part 1: Self-cooled Liquid Metal Breeder Blanket, KfK 4908, October 1991, Volume 2: Detailed Version

[3] G. Kast (comp.): Nuclear Fusion Project, Annual Report of the Association KfK/Euratom, October 1990 - September 1991, KfK 4944 (Oct. 91).

Staff:

E. Bojarsky
H. Deckers
U. Fischer
H. John
S. Malang
P. Norajitra
H. Reiser

BL PC-D 2 Active and Inactive Impurities and Clean-up of Molten Pb-17Li

As in any liquid metal system also in a molten Pb-17Li blanket impurities may cause safety and operational problems. The aim of this work is to characterize the different kinds of impurities, to study their transport behavior in the blanket, and to find methods for the removal from the liquid metal. Special attention has to be given to the behavior of lithium during purification processes.

1. Behavior of Lithium

A partial separation of Li and Pb was observed during the production of Pb-17Li (1). In one test we heated static Pb-17Li in a thermal gradient (room temperature to 750°C) for 950 hours. We found a small area with less than 0.04 wt.% Li in the low temperature range, and correspondingly 0.85 wt.% at the high temperature part. It is not clear if there may be also a depletion of Li in the cold trap of a loop. In the cold trap of the facility TRITEX a small amount of material was found with such low Li-concentration; however deposits with up to 4 wt.% Li were also found.

2. Behavior of Po-210 and Bismuth

Po-210 is formed by activation of bismuth impurities: However even if Bi free LM is used, Po-210 will be formed after an extended operation time of the reactor because of the build-up of bismuth from lead.

Inspite of the high vapor pressure of the element polonium, the evaporation rate from the eutectic is small (2). Lead polonide is formed, with a low chemical activity of Po.

Experiments are under way to measure the solubility of Bi in Pb-17Li. Preliminary tests gave a value of about 500 ppm at 350°C. An intermetallic compound Li_3Bi is formed, reducing the solubility and chemical activity considerably.

3. Pb-17Li loop TRITEX

TRITEX is a pumped Pb-17Li loop from ferritic steel. It was operated in run number V for 3100 hours. During this run the temperature in the cold trap was kept between 250 and 260°C, while the temperature in the main loop was usually at 450°C. Phase V was finished when the loop was blocked - probably by deposited particles in the magnetic trap. Investigations of the deposits are under way.

For the next operation phase a new cold trap, magnetic trap and test section are under construction.

Literature:

[1] A. Overs et.al., LIMET-4, Avignon, Oct. 17-21, 1988

[2] H. Feuerstein et.al., ICFRM-5, Clearwater, Nov. 17-22, 1991

Staff:

J. Beyer
H. Feuerstein
L. Hörner
S. Horn
G. Kieser
J. Oschinski

BL EI-D 1 Electrical Insulation and Coatings

In order to reduce the magneto-hydro-dynamic pressure drop the duct walls of the liquid metal (Pb-17Li) breeder blanket must be electrically insulated. Two methods are developed:

- use of so called Flow Channel Inserts (FCI) consistent of an insulating ceramic layer sandwiched between two thin protecting metal sheeths and
- the direct coating of the dust wall by insulating materials

Development of electrical insulations includes choice of materials, manufacturing methods, thermomechanical and compatibility tests and the assessment of irradiation behaviour. (Subtask BLEI-D-1 includes former subtasks BLPC-D-1 and BLCO-D-1).

1. Flow Channel Inserts

Flow Channel inserts (FCI), a laminated element (steel-ceramic-steel), shall be fitted loosely into the coolant ducts of liquid metal cooled blanket. They avoid elektrical short circuits through the steel structure of the blanket. The electrical potential is induced in flow channels arranged perpendicular to the magnetic field.

Work on development of fabrication methods for flow channel inserts has been continued. With two of the methods investigated FCI could be fabricated having high mechanical strength.

The fabrication method being favoured utilizes the following procedure: A metal basic sheet (martensitic steel) is plasma sprayed with a sublayer of Fe13Cr, then with an aluminium-titanate-layer (>200 μm), and with a top layer of Fe13Cr. On this coated sheet a top sheet (martensitic steel) coated by plasmaspraying on one side with Fe13Cr is diffusion welded to the first sheet. The diffusion welding takes place between the two Fe13Cr-layers. The diffusion welding conditions are 1250 °C, 120 MPa, 30 minutes. The FCI-specimens have a tensile strength $\sigma = 28.4 \pm 8$ MPa. A tensile strength of less than 20 MPa is sufficient to withstand the mechanical load in a blanket (thermal stresses).

The second fabrication method applies coating of the martensitic basic steel sheet with Ti(C, N) and Al_2O_3 by chemical vapour deposition. The thickness of the coating is 10-15 μm. On this coated steel a top sheet (martensitic steel) is diffusion welded. Interlayers of copper, nickel, Fe13Cr were used. With copper high tensile strength was achieved ($\sigma_t = 33.8$ and 38.9 MPa, respectively). FCI with nickel showed a tensile strength of $\sigma_t = 9.2$, 17.8, 18.8 MPa, respectively. With Fe13Cr $\sigma_t = 8.0$, 10.2, 11.6 MPa were achieved. It is assumed to reach with nickel and Fe13Cr a higher strength with an additional metallic top layer on the ceramic. On a larger number of specimens - coated by chemical vapour deposition - the top sheets were brazed using silver-base alloys. These specimens had high tensile strength; $\sigma_t = 37.8 \pm 4.3$ MPa. The brazed version had in some cases penetration of the ceramic layer by brazing material. It is assumed to be able to avoid this in future by better control of the brazing process.

FCI have to insulate an electric tension less than 1 V. Investigations carried out by [1] show, that the combined attack of ionizing radiation, temperature (450 °C), and electrical potential converts the isolation material Al_2O_3 into a conductor. A production of metallic aluminium by the combined attack is assumed. With the present knowledge we aspect that our FCI with insulation produced by chemical vapour deposition might fail (insulation layer amounts only 10 μm). The first version with plasmasprayed ceramic (200 μm) perhaps may withstand the combined load.

Irradiation tests are required before further improvements are carried out to optimize the mechanical strength.

Literature:

[1] E.R. Hodgson:
Radiation-enhanced electrical breakdown in fusion insulators. J. Nucl. Mat. 179-181(1991), p. 383-386.

Staff:

V. Casal
M. Gegenheimer

2. Insulating Coatings

The corrosion tests in the PICOLO loop at 450 °C and 0.3 m/s were extended to aluminized specimens of the austenitic steel 316 L(N) furnished by CEA. The tests have now reached more than 5000 hours. The material losses were evaluated on the basis of diameter measurements. As is shown in Fig. 1, the

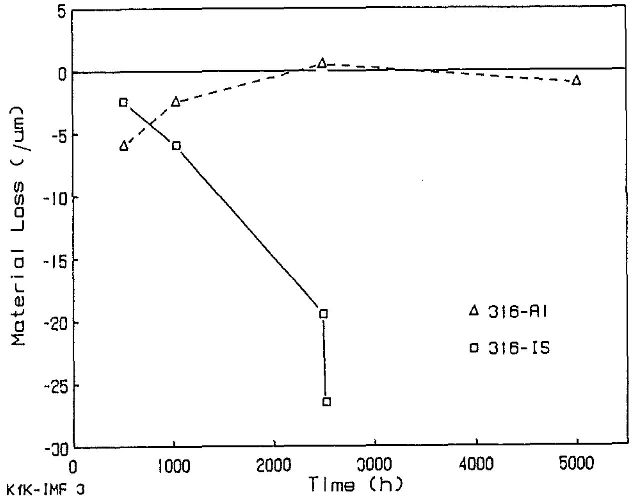

Fig. 1: Mass losses of cylindrical specimens of steel 316 L(N) with and without aluminized surfaces in corrosion tests in the PICOLO loop at 450 °C.

diameter losses of the unprotected steel 316 L(N) were considerable in 2500 hours, while the diameter changes of the aluminized specimens were nearly zero.

Metallographic examinations have shown that there were no corrosion effects upon the aluminized layers, while the unprotected surfaces of the steel showed regions with relatively deep losses of material. The local effects exceed the losses which are indicated on the figure. The aluminized surfaces which were not initially oxidized lost their insulating properties during the exposure to the flowing liquid metal.

First attempts to apply the "HOT-DIP ALUMINIZING" in pure molten Al to produce Al containing surface layers on MANET steel and steel 316 L(N) gave promising results. Layers of aluminium and iron aluminide were formed on both the materials. The formation of oxide layers as electrically insulating components of the surfaces was started to be investigated. The physico-chemical work on the oxygen potentials in Pb-17Li and the capacity of the eutectic alloy to dissolve metallic components of the materials was documented [1,2].

The effect of radioactive irradiation upon the resistivity of alumina was studied in the literature [3]. The recently discovered effect of "radiation induced electrical degradation" (RIED), based on experimental results of E.R. Hodgson and G. P. Pells indicates that the resistivity of ceramic materials suffer a breakdown of orders of magnitude, if an electrical field is present during the irradiation. It has to be concluded that experimental work has to be performed in order to see, if the irradiation of the candidate coating in an electrical field causes a breakdown of resistivity below the level required for the suppression of MHD effects. Such irradiation tests have to be extended to reach doses which may produce 70 dpa's in the material.

Literature:

[1] N.P. Bhat, H.U. Borgstedt, "Oxygen in the liquid metal fusion reactor blanket and its possible influence on the compatibility with materials", Fusion Technology 21 (1992) 52-59.

[2] H.U. Borgstedt, H. Feuerstein, "The solubility of metals in Pb-17Li liquid alloy", 5th Internat. Conf. on Fusion Reactor Materials, Clearwater, Fa. USA, Nov. 17-22, 1991, J. Nucl. Mater.

[3] H. John, unpublished report of KfK

Staff:

Ch. Adelhelm
H.U. Borgstedt
G. Frees
H. Glasbrenner
H. John
P. Judex
D. Linder
E. Nold
Z. Peric
G. Streib
S. Winkler

BL EX-D 1 Tritium Extraction by Permeation and Cold Trapping

The selected tritium removal technique for the self-cooled Pb-17Li blanket with an intermediate NaK loop consists of tritum permeation into the NaK and precipitation as tritide in a cold trap. For tritium recovery, the tritide is decomposed by heating up the cold trap and the tritum gas is pumped off.

In the experiments in the WAWIK facility hydrogen (protium) is used to simulate tritium. Sufficient knowledge was achieved on the kinetics of hydrogen recovery; present work, therefore, concentrates on the investigation of kinetics of hydrogen precipitation.

In the experiments with a cold trap consisting of a mesh packed cylinder it proved that the circumferential temperatures were not constant for constant radii and axial positions. The fact was overcome by insertion of a concentrical cylinder and only using wire meshes in the annular gap. Another advantage of this cold trap was that higher liquid metal velocities within the cold trap could be realized.

Three sets of experiments were performed where the inlet and outlet temperatures were kept constant and the liquid metal flow rate was varied. Each experiment started with a "fresh" cold trap (regenerated cold trap), loading the cold trap for five hours, characteristic for anticipated blanket conditions.

Fig. 1 shows a comparison between measured and calculated outlet concentrations for the end of the loading period. The calculations were performed with a two-dimensional model assuming diffusion controlled mass transfer [1]. The measured values are even lower than the calculated ones which indicates that the integration of the molecules in the hydride crystal is not the limiting step. The differences between the two values could be due to a higher mass transfer coefficient or the increase of effective surface available for precipitation due to the growing crystals. Future work will concentrate on these topics.

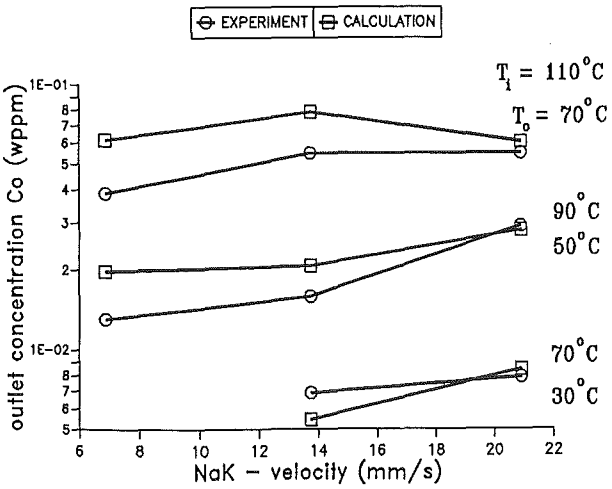

Fig. 1: Cold trap outlet concentration as a function of NaK velocity: Comparison between theory and experiment

Literature:

[1] Reimann, J. Kirchner, R., Pfeff, M., and Rackel, D., „Tritium removal from NaK-cold traps: First results on hydride precipitation kinetics", Fourth Top. Meet. Tritium Techn. Albuquerque, USA, Sept. 29 - Oct. 4, (1991), to be published in Fusion Technology.

Staff:

R. Kirchner
M. Pfeff
D. Rackel
J. Reimann

BL MH-D 1 Liquid Metal MHD

In designing a self-cooled liquid metal blanket based on the poloidal-toroidal flow concept, the magnitude of the MHD pressure drop and the character of the velocity distribution in the first wall coolant channels, that result from3-dimensional MHD effects associated with the required right angle bends in the coolant flow, represent important design issues. To address these issues and to verify the relevant models used in the design, MHD experiments were conducted in order to get basic information about pressure drop and velocity distribution in the cooling channels of the reference concept and to validate numerical codes developed at KfK to describe MHD-flow in complex geometries.

The joint ANL/KfK single channel toroidal-radial-toroidal bend experiment TRT1

The experiment was conducted by Argonne National Laboratory (ANL) and Kernforschungszentrum Karlsruhe (KfK). The test article was designed and built at ANL, and the experiments were performed at KfK's MEKKA facility using a 3.6 Tesla superconducting solenoid magnet and a eutectic sodium potassium alloy working fluid.

In the experiments, detailed voltage and pressure distributions on the duct walls and voltage distributions within the liquid metal were measured under a variety of Hartmann numbers and interaction parameters and for different orientation of the magnetic field. A comparison of the measured potential and pressure distribution on the duct walls with the results of numerical calculations indicate that the codes developed by ANL and KfK on the base of the Core Flow Approximation are capable to describe the MHD flow in rather complex geometries in a wide range. Deviations found are confined to the immediate vicinity of the right angle corner.

In Fig. 1 the results of the pressure loss measurements are summarized. The figure shows that, for fusion blanket conditions, the 3-dimensional pressure drop in the radial-toroidal bend of an electrically separated single channel is small compared with the pressure drop of the radial flow.

The voltage distribution measurements within the liquid metal aimed to investigate velocity distributions indicate an even stronger depression of the velocity profile near the first wall than predicted (see Fig. 2).

However analytical considerations show that the unfavourable velocity distribution can be improved by properly shaping the electric conductivity of the walls so that most of the flow is concentrated at the first wall in a very thin high-velocity layer. This improves heat transfer from the first wall.

Multichannel U-bend experiments

In electrically coupled multichannel ducts with a U-bend geometry magnetohydrodynamic effects are expected to cause strong uneven distributions of flow rates Qi and pressure drops Δpi in the individual channels. A U-bend geometry is part of the KfK self-cooled Pb-17 Li blanket design (radial-toroidal-radial channels), however, inserts are proposed which isolate electrically the radial channels (not the toroidal ones).

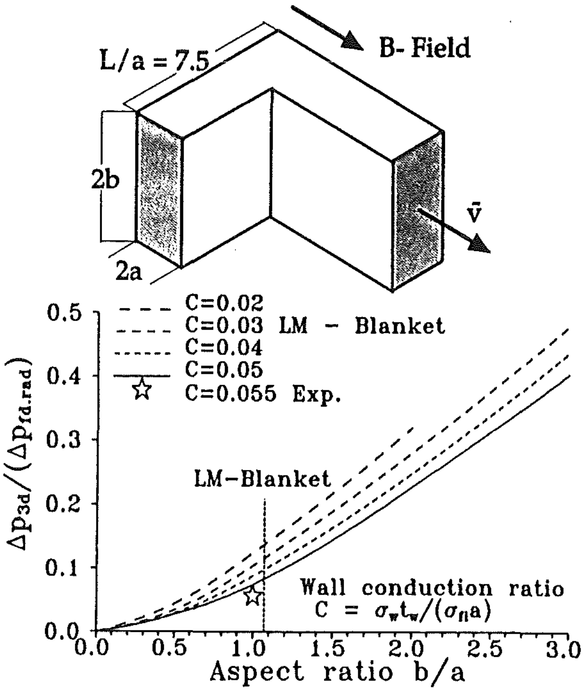

Fig. 1: Fraction of the 3D-MHD-pressure drop in the right angle radial-toroidal bend

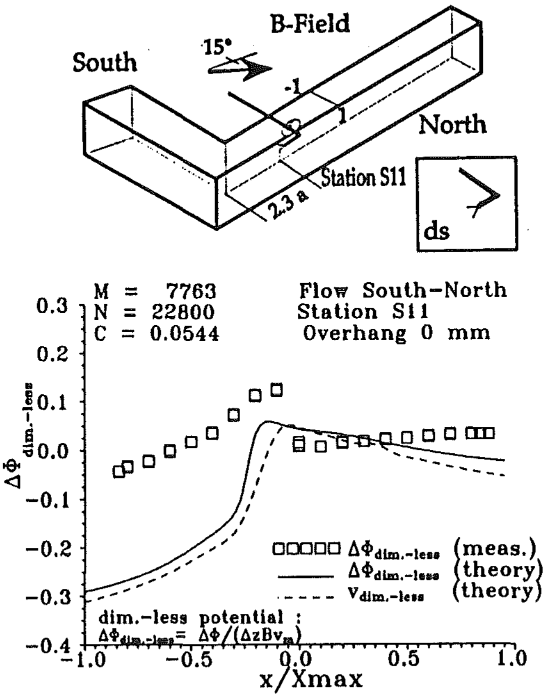

Fig. 2: Measured and predicted potential differences along a traverse in the Midplane of the toroidal branch

This multichannel effect (MCE) may cause large pressure drops, corresponding experiments and theoretical work are required.

Two types of experiments were planned:

Screening tests to obtain basic information of the influence of the main parameters, especially different configurations of the channel geometries. These experiments were performed in the MAGDA facility of the Latvian Academy of Sciences (LAS) in Riga, using InGaSn as liquid metal.

Code verification experiments which require a more elaborated test section manufacturing and instrumentation. These experiments will be performed in the MEKKA facility.

Screening tests

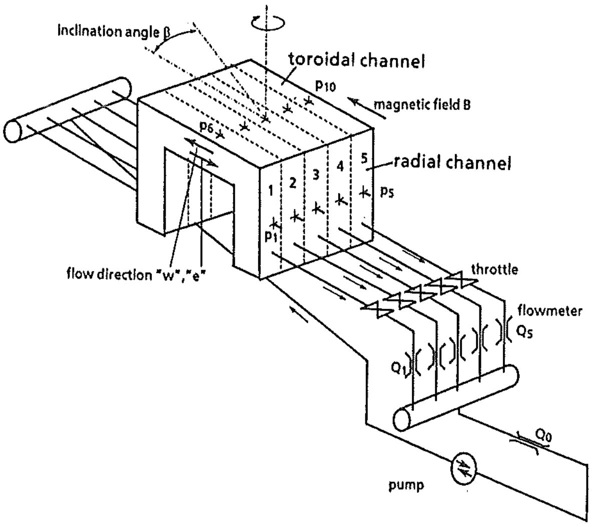

Fig. 3: Schematic set-up of test section

Figure 3 shows schematically the test loop. The test section consisted of up to 5 channels. These channels were either electrically coupled by using stainless steel inserts as dividing walls and either non conducting outside walls (Geometry I) or thin conducting outside walls (Geometry II). Channel Geometry III was characterized by conducting outside walls but electrically separated radial channels. This geometry corresponds to the reference blanket design.

The experiments were performed by varying the total flow rate and magnetic field strength (Hartmann number between 0 and 1600; interaction parameter between 0 and 10000) with keeping constant either the pressure drop Δpi or the flow rate Qi of the individual channels.

Fig. 4 shows results for Δpi$\simeq$const. For Geometries I and II the flow rates through the outer channels is considerably larger than those in the inner channels. For Geometry III this effect is not observed.

Fig. 5 contains results for Qi=const. For Geometries I and II, the normalized pressure drop increases with increasing number total channels, k, and is largest for the middle channel. Again, this tendency is not observed for Geometry III. Here, the pressure drop of the individual channel is comparable to the pressure drop of a single channel. Therefore, the use of flow channel inserts which decouple electrically the radial channels up to the first wall is very effective in order to reduce the multichannel pressure drop.

Code verification experiments

The laser beam welded manufacturing of the test section has been finished, other components are in the final stage of manufacturing. The installation of the test section is foreseen in the third quarter of 1992.

Code development

To analyze MHD flow in ducts two kinds of codes are developed the "core flow solution" and the "full solution"

- The core flow solution which considers inviscid and inertialess MHD-flow was improved for more general complex geometries. This method was used to calculate the flow structure, pressure drop and electric potential for the 3D-MHD-flow in the 90° bend of the ANL-KfK-experiment. A comparison of experimental and theoretical results shows good agreement for pressures (see Fig. 6) and potentials at high interaction parameters.

- The full solution is developed in order to describe the complete flow behavior including inertia and viscosity. Special techniques allow calculation in a bigger range of Reynolds numbers. As an example the velocity distribution in a right angle bend for given inlet and outlet conditions is shown in Fig. 7.

Literature:

[1] Barleon, L., Bühler, L., Mack, K.J., Stieglitz, R., "Liquid Metal Flow through a Right Angle Bend in a Strong Magnetic Field", 10th Top. Meeting on Technology of Fusion Energy, Boston, June 7-12, 1992.

[2] Barleon, L., Bühler, L., Mack, K.J., Stieglietz, R., Picologlou, B.F., Hua, T.Q., Reed, C.B., "Investigations of Liquid Metal Flow through a Right Angle Bend under Fusion Relevant Conditions", 17th Symp. on Fusion Technology, Rome, Sept. 14-18, 1992.

[3] Reimann, J., Molokov, S., Platnieks, I., Platacis, E., "MHD Flow in Multichannel U-bends: Screening Experiments and Theoretical Analysis", 17th Symposium on Fusion Technology, Roma, Italy, September 14-18, 1992.

[4] Bühler, L., "Additional Pressure Drop at Junctions of Flow Channel Inserts in Ducts of Self-cooled Fusion Reactor Blankets", 17th Symp. on Fusion Technology, Rome, Sept. 14-18, 1992.

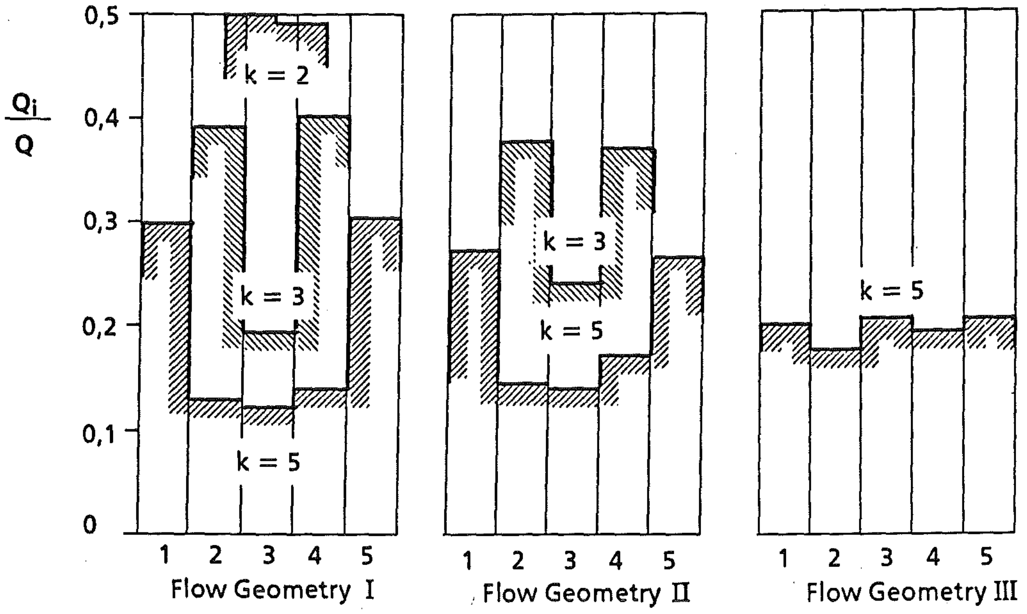

Fig. 4: Flow rate distribution for the high Hartmann Numbers and Interaction Parameters (M ≈ 1600, 1700 < N < 2500)

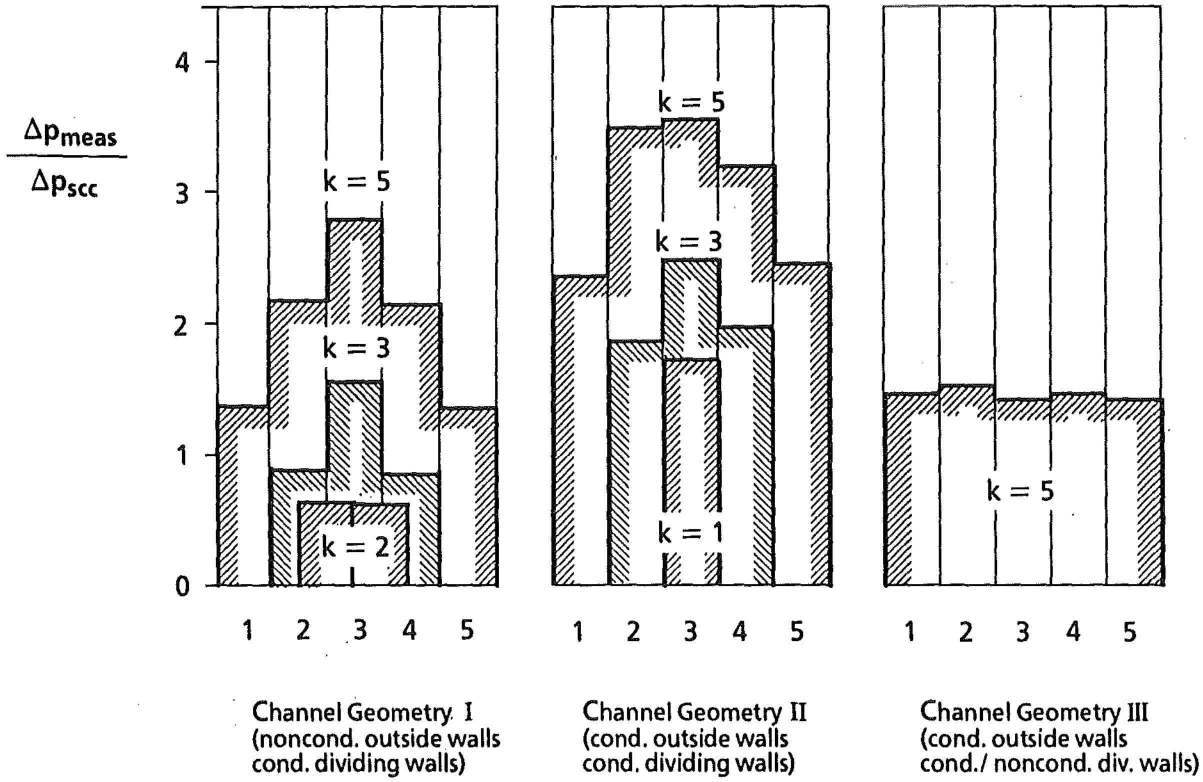

Fig. 5: Pressure drop distributions for high Hartmann Numbers and Interaction Parameters (M ≈ 1600, 1760 < N < 2800)

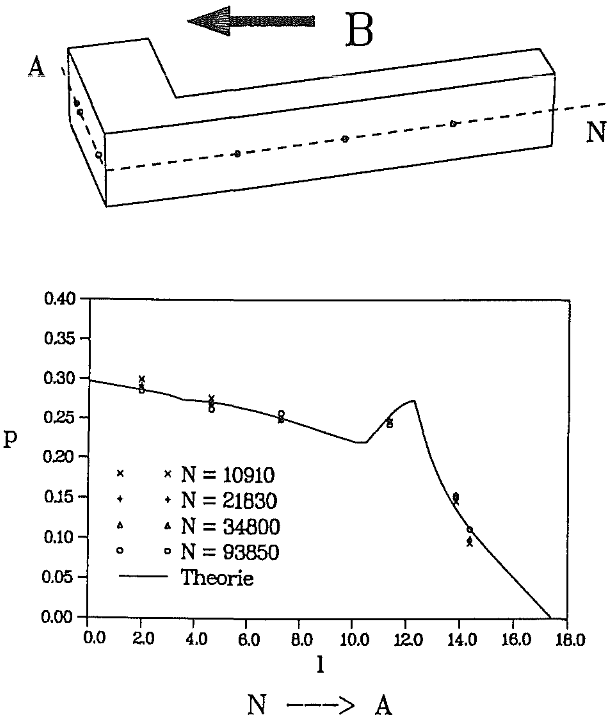

Fig. 6: Comparison of calculated and measured MHD-pressures of a right anlge bend

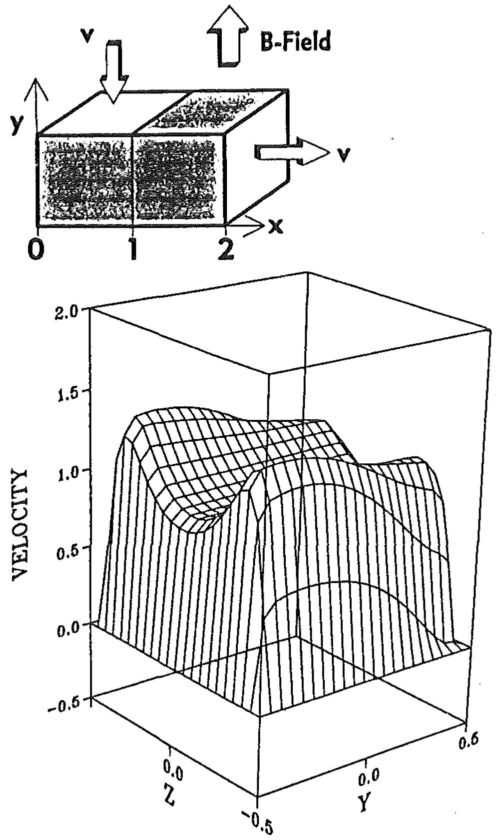

Fig. 7: Velocity distribution in a right angle bend for prescribed inlet and outlet conditions M = 100, N = 100.

Staff:

L. Barleon

L. Bühler

E. Höschele

H. Kreuzinger

L. Lenhart

O.A. Lielausis

K.J. Mack

S. Molokov

J. Reimann

R. Stieglitz

R. Vollmer

BL SA-D 1 Reliability Assessment

Main point of the contribution was the reliability of the blanket cooling system. The reliability of the blanket cooling system will be expressed by the system availability. The availability in the previous case can be strongly influenced by the arrangement of the circuit components in the cooling system. Improvements in the individual component availability are problematic because of the prototype character of the components and of the insufficient operating experience.

Bypassing this problem of uncertainty in data is possible by delegation of component functions in case of component failures to other components or systems, e.g. by the principle of redundancy. But the degree of redundancy is restricted by the requirement of a strict electrical separation of the blanket sectors or segments, respectively. It is not possible to answer all this questions sufficiently at the present time, therefore the availability of the cooling system is determined as a function of different lay-out variations.

The failure probability of Steam Generators (SG's) influences the system availability considerably. On the basis of adequate operating experience with SG's in liquid sodium-water systems a reference failure rate of

$$3.0 @ 10^{-6}/h$$

for a unit of 35 MW is assumed. From the data base a dependancy on unit size may not be deduced but it is suggested to take account of it.

Five different lay-out configurations are considered. An availability spectrum varying between 70 to >99 % will be achieved by use of the identical individual components and only by different degrees of redundancy in the lay out. The problem of spatial arrangement of components was not considered. On the one hand an improvement of the individual component reliability, and this is especially important in case of the SG's, seems to be problematic because of the operating experience with comparable components which show the data assumed for analysis are not pessimistic, that means not over estimated. On the other hand one should have in mind, the components are of prototype character and therefore should tend more to the pessimistic direction.

The variations in the design concept lead to acceptable design solutions concerning the availability. Which solution finally will be used, can't be answered definitely yet. This question depends on the space situation for the arrangement of the components but also on the requirements given by physics.

Concerning the availability of heat sink, behind the SG's, problems are not expected, because of the operating experiences in the commercial fission reactor technology.

Staff:

H. Schnauder

BL SA-D 2 Electromagnetic Forces

The FORTRAN program CARADI couples the 3D eddy current program CARIDDI and the finite element code ADINA. These tools allow to compute the electromagnetic loading and the mechanical response of the blanket during a plasma disruption, which is described by a linear decay of the plasma current of 20 MA within 20 ms. This decay induces eddy currents and strong forces in the blanket.

The computations based on a rather realistic model of the blanket including the internal flow channels having a sloping position predict maximum von-Mises stresses of 285 MPa in the side walls (compare Fig. 1). Due to the rigid fixing of the back, the top and the bottom of the blanket the eddy current damping effects are negligible.

It should be noted that for these computations the plasma center was positioned at a radius of 5.7 m, which is in fact a little bit too close to the blanket. This leads to less realisitc eddy current and force disruptions. Computations with a

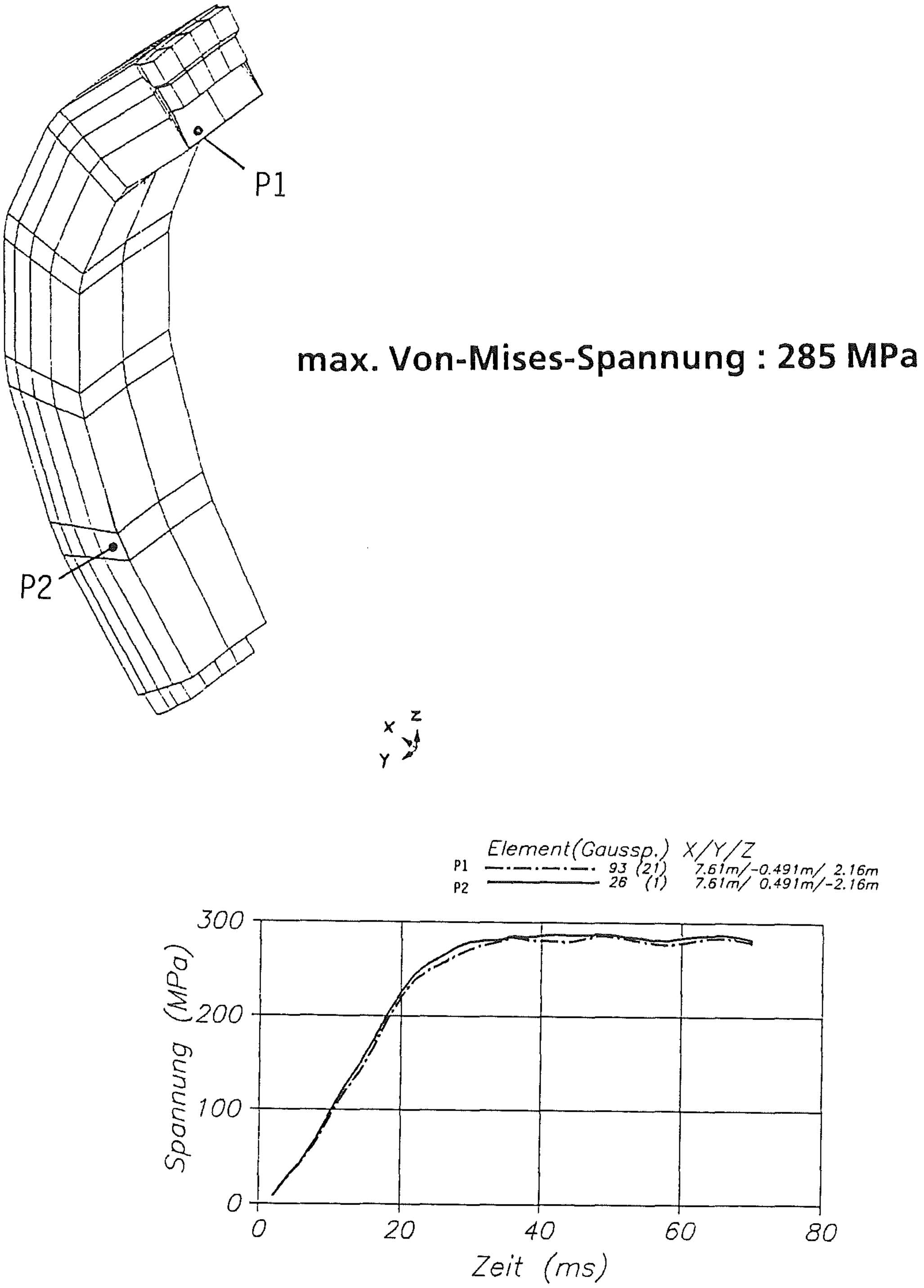

Fig. 1: Location and time characteristic of the maximum von Mises stresses

more realistic plasma position have to be accomplished. In spite of the sloping position of the internal flow channels the results of the electromagnetic and structural analysis reveal certain symmetries. So a smaller model using two symmetry planes has been developed. Of course, this model neglects the bevel (sloping position) of the flow channels. A comparison of the results obtained by employing the different models is on the way.

For stiff structures damping was found to be of little importance to the maximum stresses. However, variations of the mechanical boundary conditions to reduce the maximum stresses in the blanket are intended.

It is still necessary to clarify the influence of the fluid motion on the damping of the structural motion. Therefore, a detail analysis of a poloidal flow channel should be conducted. At the moment even small models using symmetries are too complex to resolve the fluid regions of the blanket sufficiently. Therefore, the detailed analysis will consider only one channel. It is expected that the damped fluid deflection lowers the resulting stresses in the structure.

Staff:

T. Jordan
R. Krieg

BL CO-D 2 Liquid Metal Loop Components and Testing

A study presently performed in cooperation with Siemens (Interatom) is investigating the safety aspects of the DEMO steam generator (SG).

The SG, which transfers the heat from the cooling fluid Pb-17Li to the water steam system and the bred tritium to the NaK system has a double-walled tube bundle with water in the inner tubes Pb-17Li around the outer tubes and NaK in the small gaps between the walls of the concentric tubes [1].

The amount and the velocity of a leakage propagation by a NaK water reaction in case of a water leakage into the NaK system was still an open question. Especially in the region of the NaK collection chambers a wastage propagation seems to be possible and was a crucial point for the planned ancillary loops.

An important design improvement was the arrangement of wastage protection tubes which covers the water tubes in the region of the NaK collection chambers. This supplement is described and illustrated in the last annual report.

The study, which is nearly finished, was made on the basis of experiments performed by Interatom and other experimentators, to investigate the nature of a Na-water reaction and the progress of wastage.

The study shows that the improved SG is not a safety risk and that in case of a water leakage to the NaK system a rapid wastage propagation is incredible so that enough time remains to isolate the failing component.

Further experimental effort during the conceptual phase for DEMO is therefore not necessary.

Literature:

[1] H. John, S. Malang, H. Sebening (comp.) Status Report, DEMO-relevant Test Blankets for NET/ITER, Part 1: Self-cooled Liquid Metal Breeder Blanket, KfK 4908, December 1991.

Staff:

H. John
S. Malang

Development of ECRH Power Sources

Introduction

The programme aims at developing advanced high-power millimeter-wave gyrotrons to supply current plasma experiments at the Max-Planck-Institut für Plasmaphysik (IPP Garching) and the planned ITER device with electron cyclotron wave (ECW) systems for various applications. The frequency of 140 GHz corresponds to the second harmonic of the electron cyclotron resonance in the confining magnetic field of the modular stellerator Wendelstein W7-AS and of ASDEX Upgrade (B = 2.5 T). In addition this frequency is a reference frequency for ECRH sources development for ITER with the goal 1-2 MW unit power in continuous wave (CW) operation. ECRH development is the subject of cooperation between KfK Karlsruhe (power generation and millimeter-wave diagnostics), IPF University of Stuttgart (millimeter-wave transmission and diagnostics) and IPP Garching (plasma experiments). Gyrotron design and prototype testing is the specific task of KfK, whereas fabrication of tube components and complete gyrotron tubes is done by industry. The experiments at IPP Garching on Wendelstein 7-AS present an intermediate goal for the development in terms of pulse length and output power requirements.

140 GHz ECRH Experiments on Wendelstein 7-AS

As a first step a $TE_{0,3}$ tube with a pulse length of 400 ms and an output power of up to 120 kW was constructed, tested [1] and successfully used for plasma heating and plasma diagnostics of neutral beam sustained, high density plasmas in the W7-AS stellerator at IPP Garching [2,3]. The use of the gyrotron for electron heat pulse propagation experiments requires the possibility of modulating the output power during a single pulse. By changing the modulation voltage by a few kV we were able to switch the output power on and off. Modulation frequencies up to 3 kHz have been achieved. A pulse length of 1s and power of 100 kW were obtained in pulses with on/off modulation (duty factor 50 %).

The experiments were performed with perpendicular launch in X-mode polarization at the second harmonic of the electron cyclotron frequency. The cut-off density for this mode is $1.2 \cdot 10^{20}$ m^{-3}. The power deposition and electron heating near the cut-off density was investigated by adding the 140 GHz beam to an NBI sustained target plasma with a slow density ramp. The density ramp was adjusted to meet both the 70 GHz and the 140 GHz cut-off density during a sufficiently long pulse of a discharge. A microwave pulse train consisting of a 50 ms, 70 GHz pulse in O-mode polarization (130 kW) and a successive 80 ms, 140 GHz pulse in X-mode polarization (65 kW) was launched at different time intervals during the discharge from shot to shot. The electron temperature response to ECRH was measured by Electron Cyclotron Emission (ECE) and Soft X Ray (SX) diagnostics with high spatial and time resolution. The line integrated density (top), the central electron temperature (middle) and the microwave power (bottom) are shown in Fig. 1 as a function of time for the case when the density is well above the 70 GHz cut-off, but still below the 140 GHz density. No central electron temperature increase is observed during the 70 GHz pulse interval. This observation is confirmed by SX measurements.

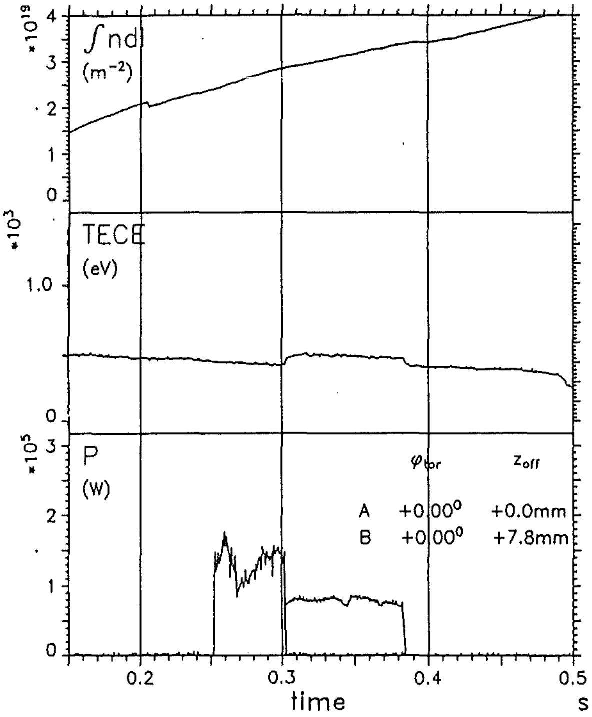

Fig. 1: Line integrated density $\int n_e \, dl$ (top), central electron temperature T_{ece} (middle) and microwave input power P (bottom) as a function of time for a NBI sustained discharge with a density ramp. The microwave pulse train consists of a 70 GHz pulse and a successive 140 GHz pulse.

These measurements indicate the propagation of the 140 GHz microwaves towards the plasma centre and central power deposition at densities well above the 70 GHz cut-off as expected from ray tracing calculations. This behaviour remains valid up to a density of $n_e = 1.1 \cdot 10^{20}$ m^{-3} (close to the 140 GHz cut-off), above which no temperature increase by the 140 GHz pulse was observed.

Both the power deposition profile and the electron heat diffusivity can be derived from the measurement of the phase shift and amplitude decay of an electron temperature modulation generated by a 100 % amplitude modulation of the incident microwave beam (heat pulse propagation analysis). This method was applied for the first time to a NBI-heated target plasma with a density well above the 70 GHz cut-off.

An example for on- and off-axis power deposition of the power-modulated microwave beam at 140 GHz, which is added to a discharge maintained with 0.35 MW of on-axis 70 GHz ECRH is shown in Fig. 2. The 140 GHz power deposition was shifted shot by shot from the plasma centre towards the plasma boundary (by moveable launching mirrors). The time delay of the electron temperature modulation at different

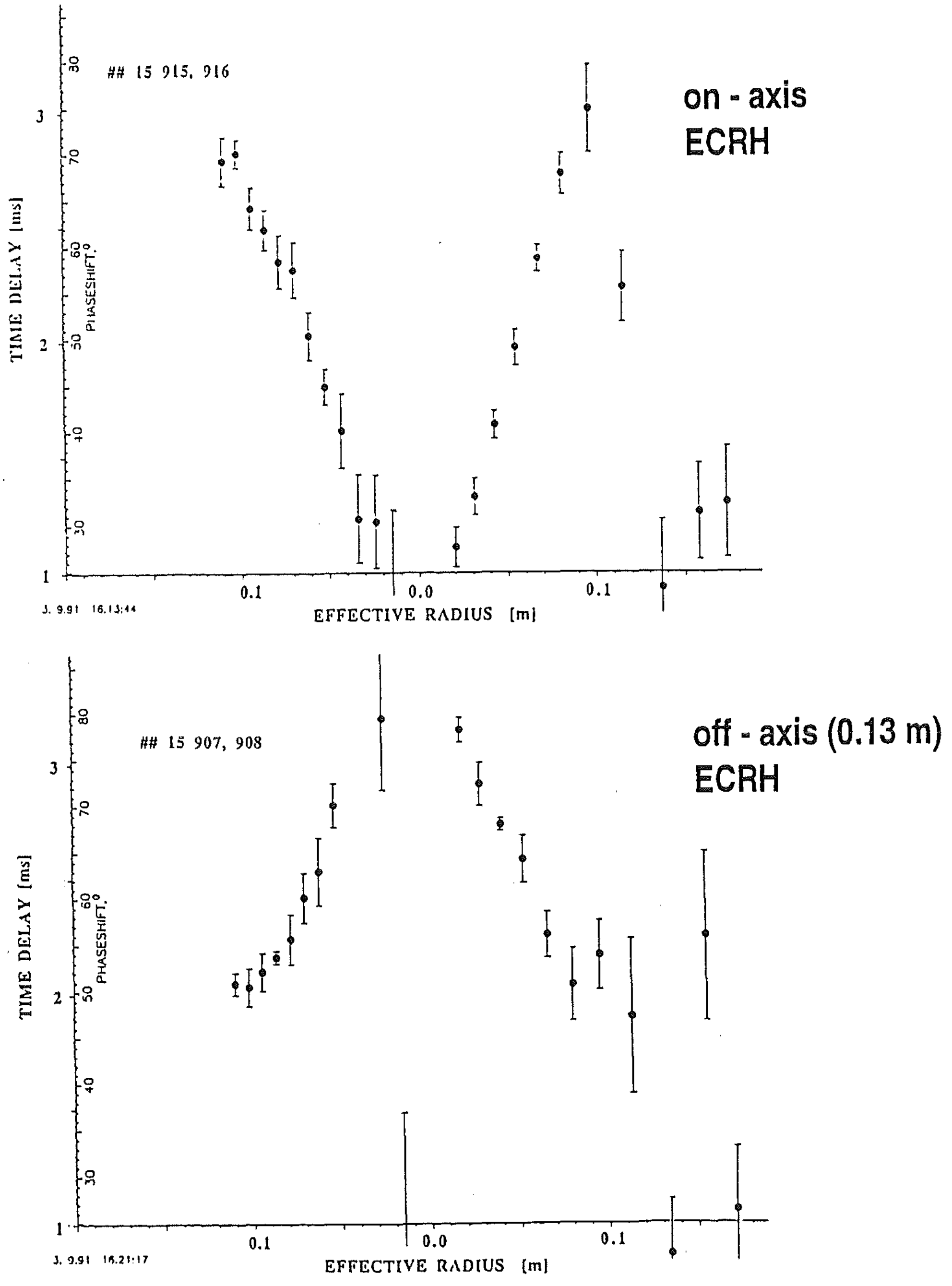

Fig. 2: Time delay of the electron temperature modulation with respect to the driving 140 GHz microwave power modulated as a function of the effective plasma radius.The time delay is shown for on-axis power deposition (top) and off-axis power deposition of the modulated 140 GHz microwave beam at an effective plasma radius of 0.13 m (bottom). The plasma boundary is at 0.17 m.

radial channels detected by ECE-diagnostics with respect to the power modulation is plotted as a function of the effective plasma radius. Two extreme cases are shown: central power deposition (top) and power deposition close to the plasma edge Fig. 2 (bottom), respectively. The heat wave propagates radially outward with central power deposition, whereas for edge deposition an inward propagation is observed.

These experiments indicate a narrow and well localized power deposition even at the moderate temperatures of $T_e = 0.9$ keV in the outer plasma region, which is in agreement with ray tracing calculations for the given plasma parameters. This confirms the experimental results on wave absorption. Further results of measurements on W7-AS are given elsewhere [2,3].

Experiments with a Russian 140 GHz, 0,5 MW, 0.5 s Gyrotron

As a part of the Russian-German scientific and technological collaboration in the field of nuclear fusion research, a recently developed Russian high-power 140 GHz gyrotron with 0.5 MW, 0.5 s pulse length (alternatively: 0.9 MW, 0.3 s) was delivered to IPP Garching together with a superconducting magnet in autumn 1991. The limitations on the pulse duration are due to the microwave output window design.

This representative of a new generation of gyrotrons provides a number of attractive features:

- a built-in quasi-optical mode transducer converts the $TE_{22,6}$ cavity mode into a linearly polarized Gaussian output beam, which can be fed directly to the transmission line.
- the quasi-optical mode converter separates the microwave beam (horizontal output) from the electron beam and serves as an isolator for reflections from the output window.
- no control anode is implemented in this gyrotron, which allows for a substantial simplification of the high-voltage power supply. Output power control is provided by modulation of the beam voltage. A power swing from 150 to 550 kW was measured by changing the beam voltage, from 60 to 70 kV. Power modulation with frequencies of up to 200 Hz is possible.These results confirm the easy power handling of the tube without a control anode. No change of the cavity working mode was observed.

The robust construction of the tube allowed for full-performance operation (0.5 MW, 0.5 s) within a few days; reliable operation at a duty cycle of 0.002 (typical W7-AS requirement for normal machine operation) was achieved

The KfK gyrotron diagnostics system employing a frequency time-interval analyzer allows instantaneous frequency measurements during a single pulse [4]. The measurements show a very stable single mode operation of the Russian tube.

Involved in this collaboration are the Institute of Applied Physics in Nizhny Novgorod, the Kurchatov Institute in Moscow, the Russian manufacturer of the tube (SALUT), IPP Garching, IPF Stuttgart and KfK Karlsruhe.

High Power Gyrotron Development

Since 1990 KfK has designed, built, and is now testing a gyrotron which operates in the $TE_{10,4}$ mode with an output power of 500 kW, and at a frequency of 140 GHz [5-13]. The RF-power is coupled out conventionally with an axial window. This phase of the programme aims to demonstrate the capabilities of the asymmetric volume mode (AVM) approach in generating high power levels. One of the critical factors in the design of a high power gyrotron is the minimization of Ohmic losses in the resonator walls. This is the reason for using a highly overmoded cavity in spite of the problems associated with mode competition [1]. Higher efficiencies and more stable operation can be achieved if the working mode is chosen to be as isolated as possible from possible competing modes. One reason for choosing the $TE_{10,4}$ mode, in addition to the possibility of using our present magnet for first experiments, is its rather good isolation from nearby possible competitors that couple strongly to the beam. This requires also good beam quality and careful choice of beam radius. Some of the design parameters are summarized in Table 1. The realistic maximum Ohmic losses at 500 kW output power are approximately 3 kW/cm^2. The choice of geometry is a compromise between reasonably low minimum currents (permitting operation at 400-500 kW, and requiring moderately high Q), and low maximum wall losses (which requires low Q). The rather high magnetic compression ratio is chosen in order to keep the gun diameter below 100 mm. As a consequence, the maximum emitter current density is around 6 A/cm^2. The cathode angle was chosen to permit operation over a wide current range without any significant change of other beam parameters. It will also be possible to investigate the influence of space charge effects (mainly voltage depression) since with a modular device the resonator can be exchanged for a $TE_{10,p}$ mode with $p > 4$ using the same gun.

beam current (A)	25	cavity radius (mm)	8.11
beam voltage (kV)	80	cavity length (mm)	11.0
anode voltage (kV)	24.5	quality factor	590
beam radius (mm)	3.65	magnetic field (T)	5.53
beam thickness(mm)	0.53	magnetic compress.	29.5
voltage depression	5.6%	cathode radius (mm)	19.8
cavity $v_\perp/v_z$	1.5-1.7	cathode angle (deg)	26.6

Table 1: 500 kW, 140 GHz gyrotron parameters ($TE_{10,4}$ mode)

Experimental Results

The operating mode can be identified by measuring the frequency of the output signal. A new contiguous filterbank receiver with a spectral resolution of 100 MHz [4] is used for this purpose. Instantaneous frequency measurement during a single pulse is achieved using a time-frequency analyzer. Mode purity is measured with a wave number spectrometer and power measurements are made using an octanol-filled ballistic calorimeter. First measurements without ultimate parameter optimization have given output powers up to 0.42 MW at short pulse length. The measured frequencies of the working mode and possible competing modes for this first $TE_{10,4}$ gyrotron agree very well with the calculated values. The principal competing mode in the example of Fig. 3 is the $TE_{8,5}$ but the working mode is well isolated.

The mode purity, of the rotating $TE_{10,4}$ mode (with respect to the $TE_{10,3}$, $TE_{10,5}$, $TM_{10,3}$ and $TM_{10,4}$ modes) was better than 98 %. The electronic efficiency at the maximum achieved output power of about 425 kW was 28 %.

The design value $U_{mod}=24.5$ kV was not achievable due to increasing leakage current to the modulation anode. Therefore the experiment was carried out at lower modulation anode voltage. Numerical simulations using a pitch angle $\alpha=v_\perp/v_z=1.1$ and a maximum velocity spread $\Delta v_{\perp max} = (v_o-v_\perp)/v_\perp=0.3$ are in agreement with this experimental efficiency and show the influence of a non ideal electron beam.

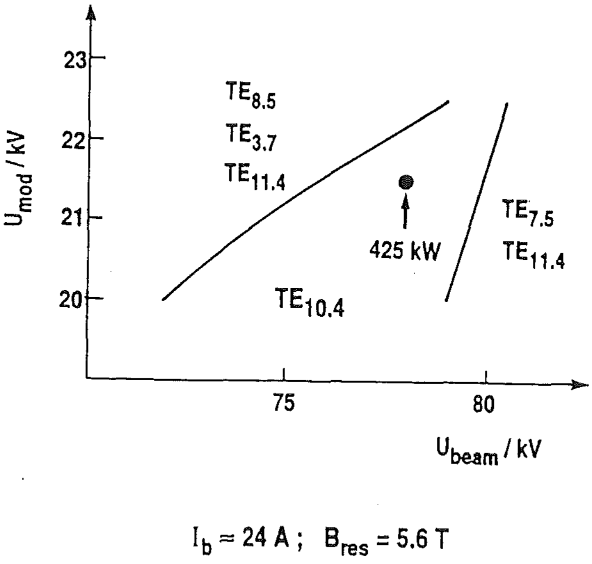

Fig. 3: Oscillation mode map of the $TE_{10,4}$ mode

An output power of 0.52 MW at short pulse lengths (up to 1 ms) could be achieved after a careful realignment and optimization of the magnetic field profile [14]. Each one of the 6 magnets was adjusted individually in order to give maximum output power. The principal competing modes, $TE_{7,5}$ and $TE_{8,5}$, were suppressed, but a small impurity of the $TE_{11,4}$-mode at a frequency of 147.53 GHz could not be avoided if the modulation voltage was higher than 22.4 kV. Fig. 4 shows the output power as a function of beam current. Oscillations without this admixture in the $TE_{10,4}$-mode were observed when $U_{mod} \leq 22.4$ kV. The optimized magnetic field strength was 5.52 T.

To improve mode purity and efficiency and to reduce mode competition between $TE_{10,4}$ and $TE_{11,4}$ a second cavity with curved transitions between its segments [15] and with a higher Q-value (Q = 1100, optimized for $\alpha = 1.1$) together with a single-disk quartz window with lower reflection for parasitic modes will be investigated.

Future Development

The next version of the KfK gyrotron will be installed in a new magnet (with larger inner bore hole) and will use a built in quasi-optical mode transducing antenna which converts the rotating $TE_{10,4}$ mode to a free space Gaussian beam [16], and a radial window, in order to separate the mm-wave output and the electron beam (Fig. 5). The influence of the quasi-optical converter on the beam field interaction in the resonator and the behavior of the converter under hot test conditions will be investigated. It will then be possible to extend the pulse length up to 0.2 s. In order to achieve an output power of 1 MW, CW or long pulse, from a single tube, a still higher order AVM mode is required, in order to reduce the Ohmic losses in the resonator walls to acceptable levels (<3 kW/cm²). As a result of extensive theoretical studies, the $TE_{22,6}$ mode has been selected as the most promising candidate [7]. The components for this gyrotron tube, including a cryogenically cooled single-disc sapphire window, are being designed.

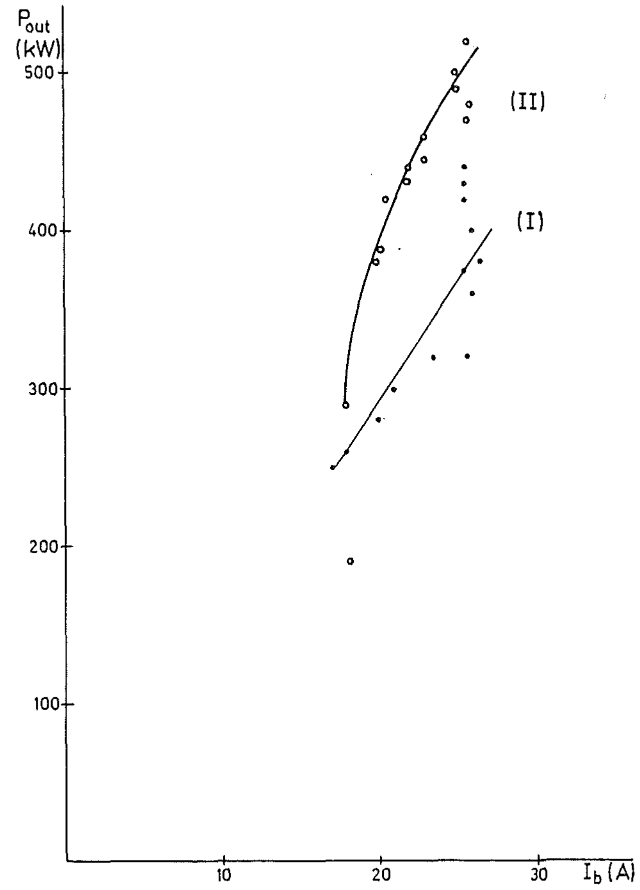

Fig. 4: Output power of the $TE_{10,4}$-mode as a function of beam current. (I) $TE_{10,4}$, only: gun anode voltage = 22.4 kV, beam voltage = 83 kV. (II) $TE_{10,4}$ and $TE_{11,4}$: gun anode voltage = 23.2 kV, beam voltage = 84.5 kV. Magnetic field 5.52 T

Literature:

[1] Borie, E., G. Gantenbein, B. Jödicke, G. Dammertz, T. Geist, G. Hochschild, M. Kuntze, H.-U. Nickel, B. Piosczyk, M. Thumm: Mode competition using TE03 gyrotron cavities, Int. J. Electronics, 1992, Vol. 72, Nr. 5 and 6, 687-720.

[2] Erckmann, V., U. Gasparino, L. Gionnone, H.J. Hartfuß, H. Maaßberg, M. Tutter, W VII-AS Team, W. Kasparek, G.A. Müller, P.G. Schüller, G. Dammertz, G. Gantenbein, T. Geist, M. Kuntze, H.-U. Nickel, B. Piosczyk, M. Thumm: ECRH-experiments with a 140 and 70 GHz at the WVII-AS stellerator, Proc. Course and Workshop on High Power Microwave Generation and Applications, Int. School of Plasma Physics, Varenna,

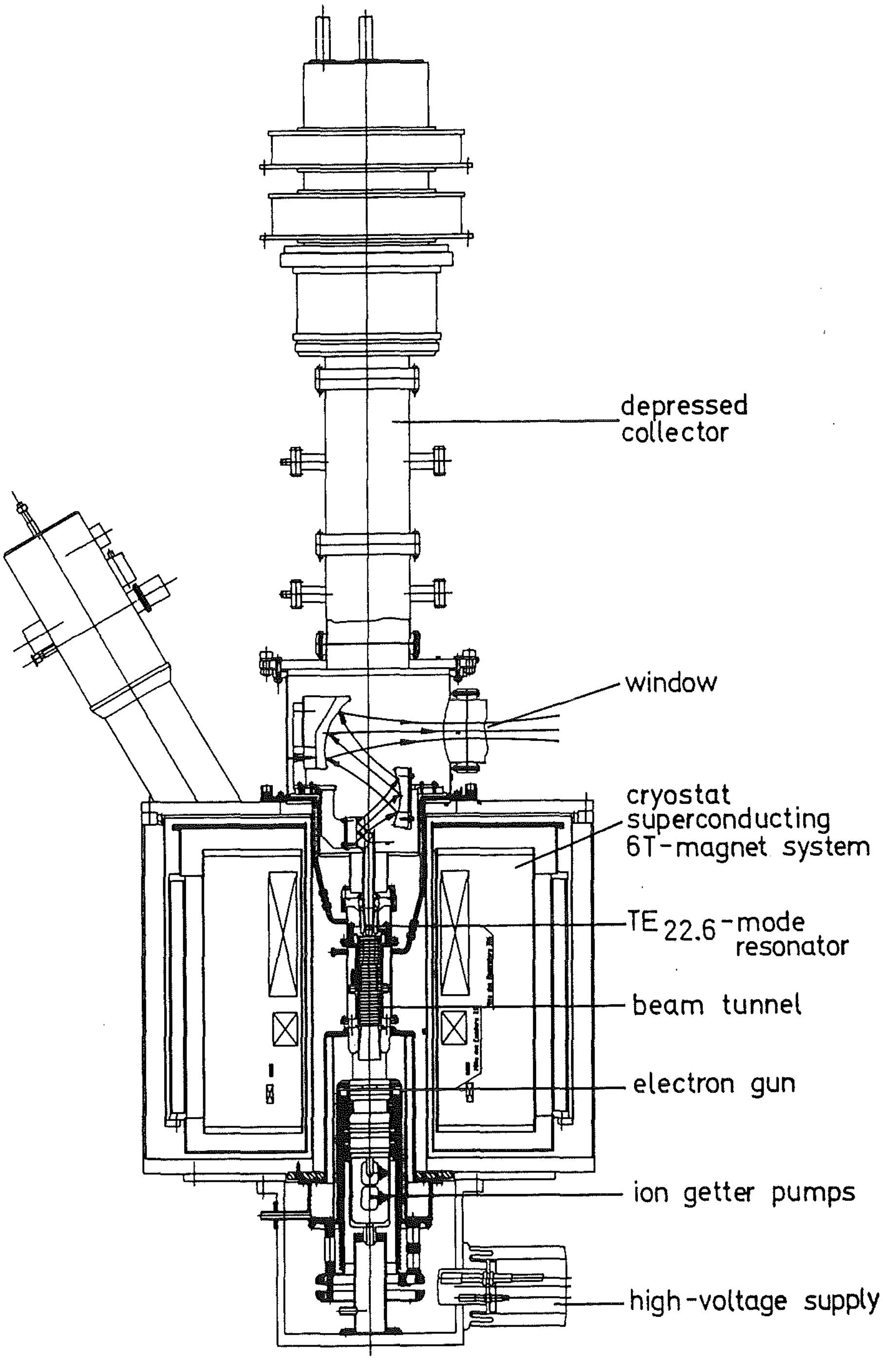

Fig. 5: Schematic layout of an advanced AVM gyrotron with quasi-optical converter

Italy, 1991, eds. D. Akulina, E. Sidoni and C. Wharton, Editrice Compositori Bologna, 1992, pp. 511-518.

[3] Erckmann, V., W7-AS Team, IPF ECRH Group, G. Dammertz, G. Gantenbein, T. Geist, M. Kuntze, H.-U. Nickel, B. Pioszcyk, M. Thumm , IAP Gyrotron Group, KIAE ECRH Group: Recent results with ECRH and ECCD at 70 and 140 GHz on W7-AS, Proc. 4th Russian-German Meeting on ECRH and Gyrotrons, Nizhny Novgorod, 1992, pp. 301-326.

[4] Geist, T., M. Thumm, W. Wiesbeck: Contiguous filterbank receiver for a pulsed 140 GHz Gyrotron, Conf. Digest, 16th Int. Conf. on Infrared and Millimeter Waves, Lausanne, 1991, Proc. SPIE, Vol 1576, pp. 274-275.

[5] Gantenbein, G., E. Borie, G. Dammertz, O. Dumbrajs, T. Geist, M. Kuntze, A. Möbius, H.-U. Nickel, B. Pioszcyk, M. Thumm: Design of a high-power 140 GHz gyrotron oscillator operating in an asymmetric volume mode,

Proc. 3rd Joint USSR-FRG Meeting on ECRH and Gyrotrons, Karlsruhe, 1991, pp. 15-33.

[6] Borie, E., G. Dammertz, O. Dumbrajs, G. Gantenbein, T. Geist, M. Kuntze, A. Möbius, H.-U. Nickel, B. Piosczyk, M. Thumm: 140 GHz gyrotron development for plasma heating, Conf. Digest, 16th Int. Conf. on Infrared and Millimeter Waves, Lausanne, 1991, Proc., SPIE 1576, pp. 260-263 (Invited Paper).

[7] Gantenbein, G., E. Borie, A. Möbius, B. Piosczyk, M. Thumm: Design of a high-power 140 GHz gyrotron oscillator operating in an asymmetric volume mode at KfK, Conf. Digest, 16th Int. Conf. on Infrared and Millimeter Waves, Lausanne, 1991, Proc., SPIE 1576, pp. 264-265.

[8] Borie, E., G. Dammertz, O. Dumbrajs, G. Gantenbein, T. Geist, M. Kuntze, A. Möbius, H.-U. Nickel, B. Pioscyk, M. Thumm: 140 GHz gyrotron development for EC wave applications, Course and Workshop on High Power Generation and Applications, International School of Plasma Physics, Varenna, Italy, 1991, eds. D. Akulina, E. Sindoni and C. Wharton, Editrice Compositori Bologna, 1992, pp. 557-564.

[9] Thumm, M., E. Borie, G. Dammertz, O. Dumbrajs, G. Gantenbein, T. Geist, M. Kuntze, A. Möbius, H.-U. Nickel, B. Pioszcyk: Development of high power 140 GHz gyrotrons for fusion plasma applications, Proc. IEE Colloquium on New Developments and Applications of Microwave Tubes, London, 1992, pp. 25-27.

[10] Baumgärtner, H., E. Borie, H. Budig, G. Dammertz, O. Dumbrajs, G. Gantenbein, P, Grundel, A. Hornung, M. Kuntze, R. Lehm, A. Möbius, N. Münch, H.-U. Nickel, B. Piosczyk, G. Redemann, M. Thumm, R. Vincon: The 140 GHz TE10,4 gyrotron at KfK, present status and near future prospects, Proc. 4th Russian-German Meeting on ECRH and Gyrotrons, Nizhny Novgorod, 1992, pp. 67-89.

[11] Dumbrajs, O., G. Gantenbein, M. Thumm: Optimization of high order volume mode cavities with respect to mode conversation and mode competition. Proc. 4th Russian-German Meeting on ECRH and Gyrotrons, Nizhny Novgorod, 1992, pp. 103-131.

[12] Thumm, M.: Current status and prospects of gyrotron development, ITG Fachbericht 120, Vacuumelectronics and Display, Garmisch-Partenkirchen, VDE Verlag, 1992, pp.63-85.

[13] Piosczyk, B., E. Borie, G. Dammertz, O. Dumbrajs, G. Gantenbein, T. Geist, M. Kuntze, A. Möbius, H.-U. Nickel, M. Thumm: Entwicklung von 140 GHz Gyrotrons hoher Leistung am KfK , ITG-Fachbericht 120, Vacuumelectronics and Displays, Garmisch-Partenkirchen, VDE Verlag, 1992, pp. 87-92.

[14] Piosczyk, B., E. Borie, G. Dammertz, O. Dumbrajs, E. Gantenbein, T. Geist, M. Kuntze, A. Möbius, H.-U. Nickel, M. Thumm: Development of High Power 140 GHz Gyrotrons at KfK, SOFT, Rom, Sept. 1992, contributed paper Z38.

[15] Dumbrajs, O., M. Thumm, J. Pretterebener, D. Wagner: A cavity with reduced mode conversation for gyrotrons, Int. J. Infrared and Millimeter Waves, Vol 13, 825-840 (1992).

[16] Möbius, A., J. Pretterebner: Avoidance of edge diffraction effects of WGM-fed quasi-optical antennas by feed waveguide deformation, Conf. Digest 16th Int. Conf. on Infrared and Millimeter Waves, Lausanne, 1991, Proc. SPIE, Vol. 1576, 531-532

Staff:

W. Baumgärtner
E. Borie
H. Budig
G. Dammertz
O. Dumbrajs (TU Hamburg-Harburg) bis 31.2.92
U. Feißt
G. Gantenbein
T. Geist (Uni Karlsruhe) bis 31.1.92
P. Grundel
A. Hornung
M. Kuntze
R. Lehm
N. Münch
H.-U. Nickel (ab 1.2.92 Uni Karlsruhe)
B. Piosczyk
G. Redemann
M. Thumm
R. Vincon

High Power Windows

The failure behaviour of ceramic windows for gyrotron tubes is governed by the inert strength and in the presence of subcritical crack growth by the parameters of the crack growth power law. A number of ceramic materials has been investigated (Table 2).

	Material	Manufacturer	Reference
I	Al_2O_3 99.7%		[1]
II	Al_2O_3 99.99%	CERATEN, Madrid	
III	Al_2O_3 +5%ZrO_2	CERATEN, Madrid	
IV	Al_2O_3 +10%ZrO_2	Desmarquest	
V	AlN		[1]
VI	sapphire	Crystal Systems	

Table 2: Materials investigated

The inert bending strength σc - responsible for spontaneous failure - can be described in most cases by a 2-parametric Weibull distribution.

$$F(\sigma_c) = 1 - \exp\left[-\left(\frac{\sigma_c}{\sigma_0}\right)^m\right]$$

where F denotes the cumulative density function and m, σ0 are the Weibull parameters. For the materials listed in Table 2 it was found:

Material	σ_0 (MPa)	m	K_{Ic} (MPa$\sqrt{m}$)
I	420	10.1	4.5
II	410	6	
III	560	≃8	
IV	577	8.5	
V	310	15.3	3.2
VI	470	4	

Table 3: Strength data

In the range of linear-elastic material behaviour the crack growth rate v of subcritical crack growth is a function of the stress intensity factor KI which usually can be described by a power law:

$$v = \frac{da}{dt} = A^* (K_I / K_{IC})^n$$

A* and n are parameters which depend on the material and the environment. KIC is the fracture toughness.

Material	lg(A^*),(A^* in m/s)	n
I	-3.8	33
II	-4.5	45
III	-5.2	≃32
IV	-7.4	14
V	-3.8	135

Table 4: Subcritical crack growth data

Figure 6 shows the subcritical crack growth rate v in dependence of the stress intensity factor KI.

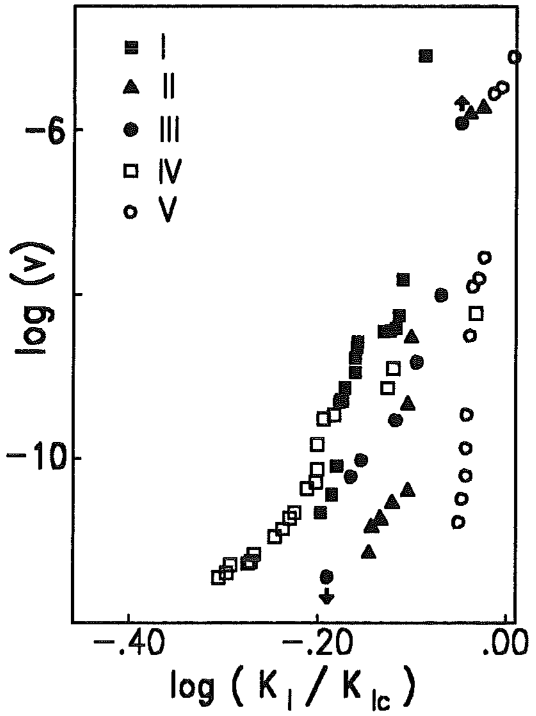

Fig. 6: Comparison of subcritical crack growth data.

Literature:

[1] T. Fett, D. Munz:
Lifetime evaluation of ceramic windows in microwave heating tubes for fusion reactors, J. Nucl. Mater. 171 (1990), 172-179.

Staff:

T. Fett

One of the ways of plasma heating in nuclear fusion reactors consists in microwave feed from gyrotrons. Reliable windows have to be developed to separate the ultra-high vacuum of the gyrotron and the plasma space, resp., from the waveguides. Transmission powers on the order of 1 MW in permanent operation are the present goal of development work.

KfK is working on a window concept with an edge cooled single disk. The present design is based on a circular disk, 140 mm in diameter and about 2 mm in thickness, with a waveguide diameter of about 90 mm. The material used for the window is monocrystalline Al_2O_3 (sapphire), which offers favorable properties at low temperatures, above all in terms of energy absorption (loss tangent) and thermal conductivity. The energy absorbed in the window is removed by boiling liquid nitrogen at atmospheric pressure in an annulus around the edge of the disk.

The design computations have already been described in the preceding annual report. It has appeared that the loss tangent plays a crucial role as regards the transmittance of the window [1].

But also the heat removal from the edge of the disk through bubble boiling in the open LN2-pool plays an important part. The heat transfer coefficients achievable depend on the heat flow density, and transition from bubble boiling to film boiling must be avoided. The test device shown in Fig. 7 has been set up in order to study these problems, but also to test the concept of the window as a whole.

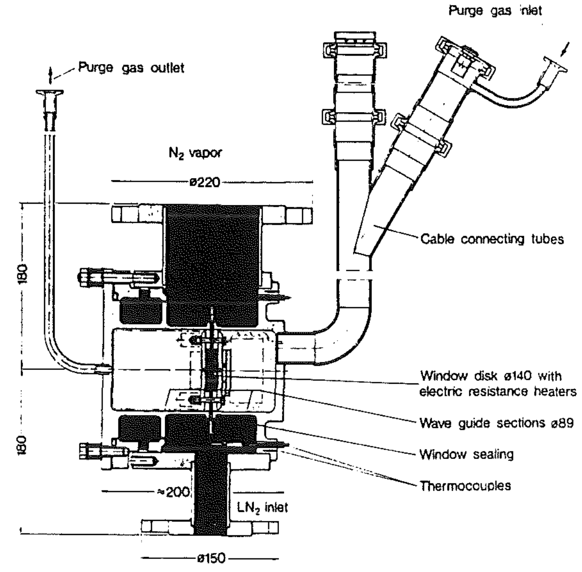

Fig. 7: Window test device

The figure shows the window disk tightly pressed into a section of the waveguide. On each side of the disk one small electrical heating plate of 1 kW heating power has been fixed. The edge of the window where the heat supplied has to be removed protrudes into an annulus of the housing which during operation is flooded with liquid nitrogen. When the heater is connected, the heat is removed from the surface of the edge of the window by bubble boiling. The annulus has been given a design allowing the vapor bubbles to rise unhindered while the liquid nitrogen from the surrounding tank on the bottom flows upwards as an unimpeded flow. The electrical lines (heater connections and thermocouples) run out of the housing in a pipe provided laterally which is closed on top by tight plug-in connections. The interior of the test device can be flushed from the connected line and maintained at a slight overpressure.

First, a number of tests were performed on an electrically heated window, which had been simulated by copper material and equipped with a sufficient number of thermocouples in order to verify the computation model. Good agreement has been found to exist between the measured and the calculated temperature distributions in the copper disk [2]. Fig. 8 shows the arrangement of the thermocouples and the temperature distribution in the copper disk for heating powers of 100 up to 1000 W. The tests have also shown that for the given geometry up to 1300 W can be removed by bubble boiling from the edge of the disk into liquid nitrogen, and this applies even in permanent operation. Only at higher powers critical heat flux densities and instable boiling conditions are reached. Consequently, no limits are imposed on the window design by cooling.

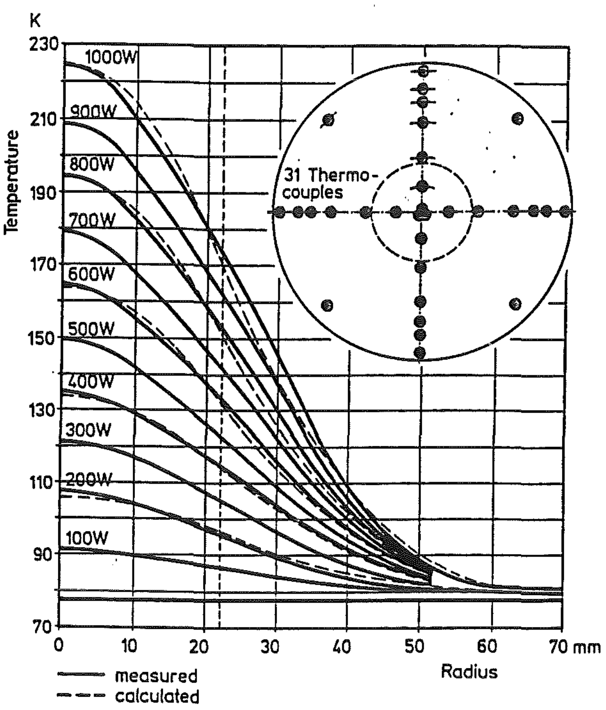

Fig. 8: Radial temperature distribution in a cupper simulator disk

Some tests involving electrical heating have already been performed with a sapphire disk. Fig. 9 shows the arrangement of the thermocouples as well as the temperatures prevailing in the center of the disk and on its edge as a function of the power absorbed. Due to the thermal stresses in the sapphire disk, the power is limited to approx. 450 W. Some discrepancies between the measured and the calculated central temperatures have been observed in the tests on the sapphire disk. The reason might be that the assumed distribution of thermal conductivity in the sapphire is not quite the same as in reality. Therefore, the measurement of the thermal conductivity of the sapphire material used is of special importance to future work.

Literature:

[1] P. Norajitra, E. Bojarsky, H. Reiser, H.E. Häfner
Cryo-cooled High-power Window for High-frequency Plasma Heating
KfK-Bericht 4930, September 1991.

[2] H.E. Häfner, K. Heckert, K. Philipp, R. Vouriot unpublished report.

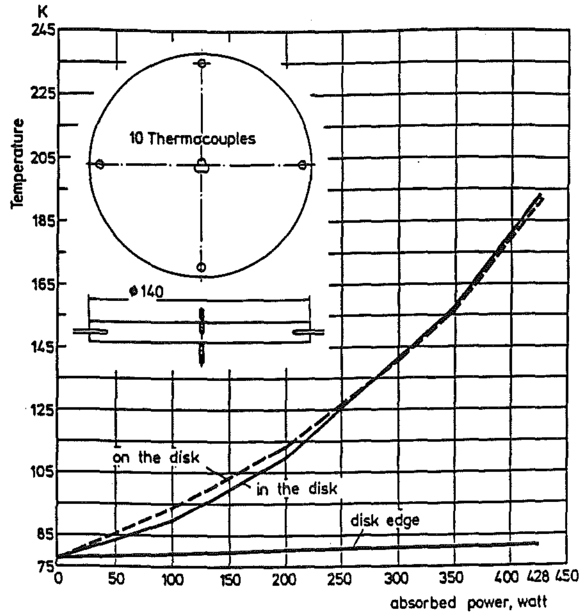

Fig. 9: Temperature of the sapphire disk as a function of absorbed power

Staff:

E. Bojarsky
H.E. Häfner
K. Heckert
A. Hofmann
H.-U. Nickel
P. Norajitra
N. Münch
K. Philipp
H. Reiser
R. Vouriot

The development of cryogenically cooled windows has been continued. The program aims to meet the ITER specifications with 1 MW transmission of 140 GHz continuous wave power. The concept favoured by KfK is an edge-cooled single-disk sapphire window. The investigations done so far have shown that there is still the possibility to reach the aim with the most simple technique of cooling with LN_2. But to be prepared for having more safety margin, future investigations will also be extended to temperatures lower than 77 K.

Sapphire disks with 140 mm diameter, the same size as it will be required for ITER windows, have been purchased. They have been used for various investigations such as

a) modelling of LN_2 operation (IMF III),

b) measurements of dielectric parameters (IMF I),

c) studying of fracture and fatigue (IMF II),

d) development of bakeable sapphire/metal joints. (Metallizing and welding is in progress in collaboration with Philips GmbH.)

Moreover we have implemented such disks in the design of a pulsed gyrotron window (140 GHz, 500 kW, > 1 s). This window can alternatively be cooled with water, with LN_2 (77 K) or with liquid Ne (≈ 30 K).

The transmission characteristics as a function of frequency are studied by computer models [1] and by experiments in a special test set-up (Fig. 10). This low-power set-up allows the measurement of window reflection and transmission as a function of frequency in a wide frequency range (e. g. 120 - 150 GHz). The system has been built-up by upgrading an existing set-up with two Gaussian beam antennas and two focussing mirrors. The Gaussian beam components have been designed especially to allow measurements with ITER relevant beam parameters. This set-up is also used for the development of broadband windows which are necessary for future frequency tunable ECRH-sources. Respective investigations have been started.

Literature:

[1] Nickel, H.-U.; Thumm, M.; 1991, Plane transverse waveguide windows - Survey of formulas for reflection, transmission and absorption, 16th Int. Conf. on Infrared and Millimeter Waves, Lausanne, Switzerland, Conference Digest, SPIE Vol. 1576, 444-445.

[2] Nickel, H.-U.; Halbritter, J.; 1991, Surface melting at ceramic windows due to high-power millimeter waves, 16th Int. Conf. on Infrared and Millimeter Waves, Lausanne, Switzerland, Conference Digest, SPIE Vol. 1576, 456-457.

[3] Heidinger, R.; Hofmann, A.; Nickel, H.-U.; Norajitra, P.; 1991, The impact of neutron irradiation on the performance of cryogenically cooled windows for electron cyclotron resonance heating, Fusion Engineering and Design, 18, 337-340.

Staff:

A. Hofmann
N. Münch
H.-U. Nickel (Uni Karlsruhe)
G. Redemann

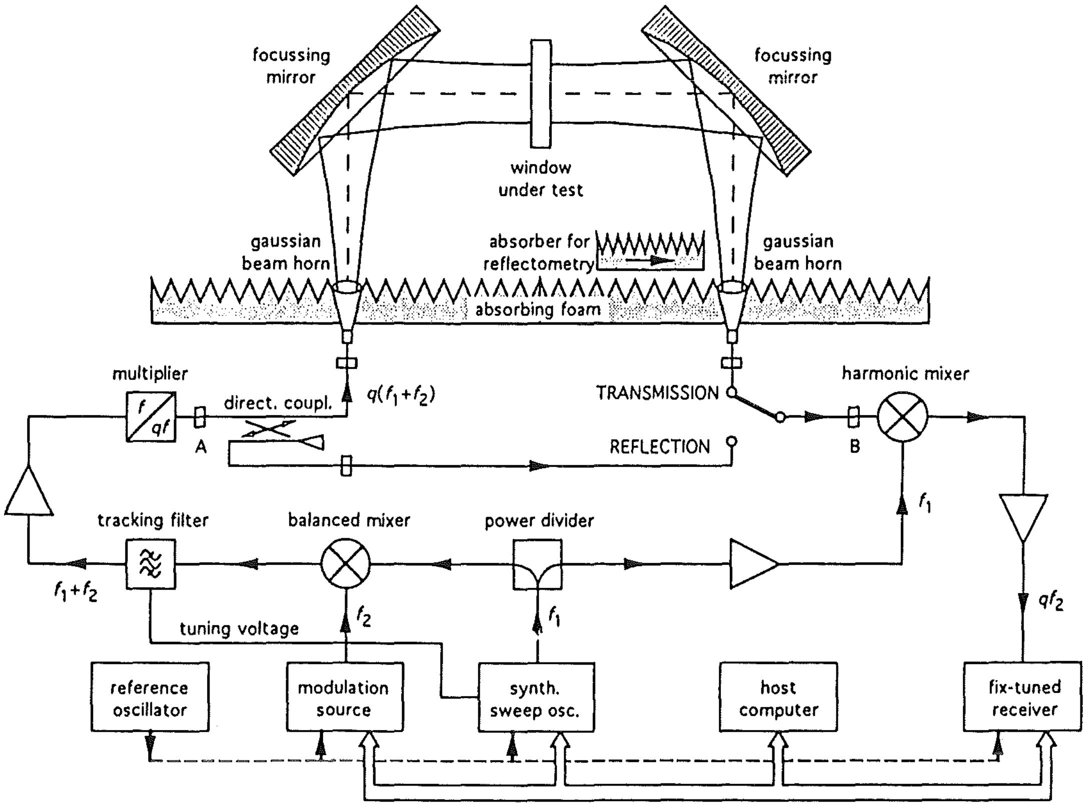

Fig. 10: Set-up for swept-frequency measuring of reflection and transmission of a fundamental Gaussian beam in windows.

Studies for NET

Introduction:

By granting study contracts to KfK, NET draws upon special expertise available in the laboratory. In contrast to the technology tasks which extend over a longer period of time and consist in most cases of experimental work, study contracts are agreed on short notice and are of limited duration. In the term span the KfK has spent approximate two manyears for this kind of arrangements. Subjects scatter widely according to the need arising from the design activity for NET/ITER.

Simulations on Jacket Material Failure by Crack Growth at 4 K for the NET-Superconductors

In close accordance with recent 2-dimensional fatigue crack growth rate (FCGR) measurements of standard 316 LN plate material [1] further cyclic investigations were performed with the aim to simulate a jacket material failure on an original superconductor conduit piece. For this purpose NET supplied a ~ 1500 mm long ready manufactured U-section. The materials condition was in this context cold drawn. Due to the fact of limited wall thickness of the section (~ 5 mm) the recently used specimen configuration [1] with threaded ends (M 10 x 1.5) couldn't be taken for this cyclic measurements. A new pin loaded flat specimen configuration was designed and pretested to its ultimate shape. After establishing the new specimen configuration with a test area of 4 x 7 mm^2 cross section, 15 specimens were prepared from the delivered jacket to be tested at 12 K in the previously described [1] cryogenic test facility. During these series of investigations an improvement towards the crack monitoring were made by installing a CCD-video screen system. The monitoring of the crack propagation on the mirror polished specimen allowed thus to measure small crack lengths with a magnification of 50 - 70 x (resolution < 20 µm). With this improved measurements technique it was possible to obtain FCGR values of $< 10^{-7}$ mm/cycles.

The necessary stress intensity factor (SIF) calculation along the penetrated crack front were performed according to the Newman/Raju expression given in [2,3]. For the reason of checking the crack depth and to visualize the crack front (circular or elliptical) marker loads were applied at distinct crack lengths successfully. The best marking result could be obtained by changing the R-ratio from 0.1 to 0.7. Fig. 1 shows one of the cyclic loaded specimen after its fracture with the distinct marks of the crack front. So far these measurements show that the penetrated crack deviates from the semi-circular crack front shape after ~ 1 mm crack growth in either direction a (a=crack depth) and c (c=crack length on the surface). This means after 1/4 of the nominal specimen thickness the crack penetrates with a different aspect ratio than 1. With several tests the depth "a" was measured to be ~ 1.95 mm at the last point of interest on the surface where c=2.5 mm long. With the use of an empirical gained linear equation the value of "a" could be calculated between 1 mm ≥ c ≥ 2.5 mm in any position. By inserting this linear equation in the Newman/Raju relation, we were able thus to calculate exactly the SIF for a measured c-value on the surface. All dc/dN values were calculated within these investigations after positioning the initiated crack at c=0.5 mm and cycling of the specimen up to c=2.5 mm. Fig. 2 gives the FCGR response of the jacket material for R=0.1 and R=0.7. Comparing these results with the recently determined dc/dN vs. ΔK of the 316 LN plate material show that the original jacket materials FCGR is ~ a factor of 3 higher than the standard 316 LN material. This finding is attributed to the different microstructures of both materials. The fractured surface of the jacket materials microstructure shows a much finer grain structure than the coarse grained 316 LN plate material.

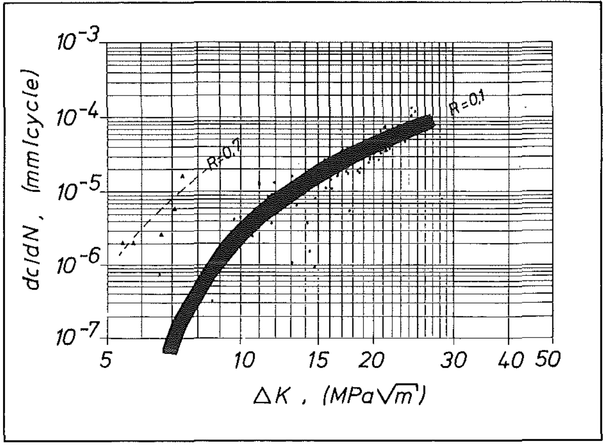

Fig. 2: Fatigue crack growth rate (da/dN) vs. stress intensity factors range (ΔK) of 316 LN cold drawn material at 12 K for two load ratios R = 0.1 and R = 0.7.

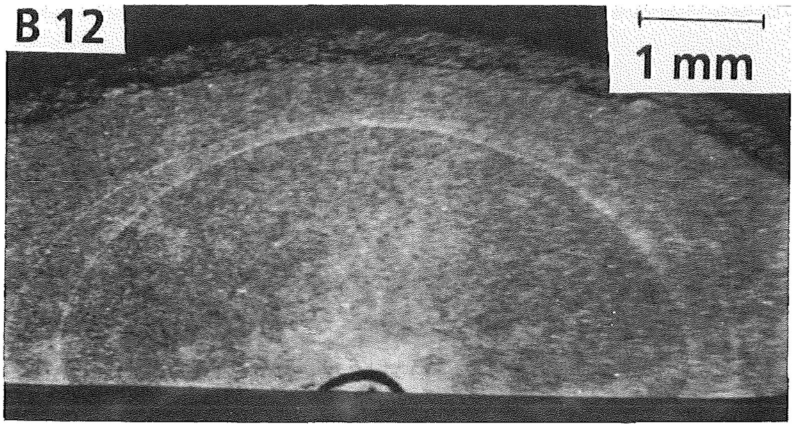

Fig. 1: Fractured surface of the fatigue loaded 316 LN cold drawn material with semi circular and semi elliptical markers

Eight specimens out of the 15 were used to determine the necessary cycle number for a given crack propagation (from c=0.5 mm to c=2.5 mm) at a constant peak stress in the non cracked cross section. To control the constant peak stress the peak loads are calculated according to the simple relation, where the growing of the semi-circular or semi-elliptical crack area was steadily substracted from the nominal test sectional area (7 x 4 mm). According to the calculated plot one was able to decrease the load stepwise by measuring the crack length c at various positions. This procedure seemed to be more reliable than any other method such as the on line measuring of the specimen displacement via high resolution transducers. The resolution in latter case was worse as compared to the technique used with the aid of the calculation.

Fig. 3 gives the results of the peak constant stress vs. cycle number N relation in log-log scale. As shown the required cycle number for a certain crack advance (in this case from c=0.5 mm to c=2.5 mm) can be predicted according to the plotted linear (in log-log scale) relationship. Two of the specimens out of the last batch (8 specimen) were tested with a triangular load time history instead of the sinusoidal mode at R=0.1. No significant difference in the FCGR rate could be observed between the two load time histories. In addition, two specimens (B-16 and B-17) were both loaded with an alternating triangular constant peak stress of 400/500 MPa loadtime history at R=0.1. The necessary cycle number for the crack propagation from c=0.5 mm to c=2.5 mm was approximately 90000 cycle. This measured cycle number is in good agreement with the determined plot of Fig. 3. The two points of these tests yield a peak stress value of ~ 450 MPa, which is the mean of the alternating stress.

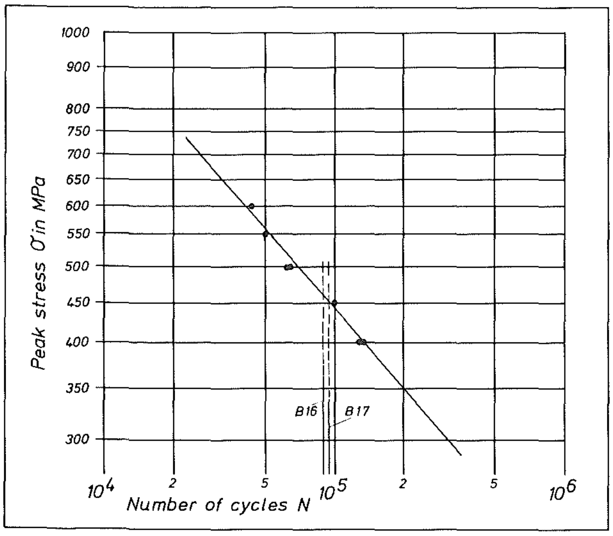

Fig. 3: Peak constant stress (σ) vs. cycle number (N) for crack propagation between c = 0.5 mm to c = 2.5 mm in log-log scale at 12 K (R = 0.1).

Literature:

[1] A. Nyilas, J. Zhang, B. Obst, and A. Ulbricht: Fatigue and Fatigue Crack Growth Properties of 316 LN and Incoloy 908 below 10 K
Adv. in Cry. Eng. Materials Vol. 38, 1991, p. 133-140

[2] J.C. Newmann and I.S. Raju: Analysis of surface crack in finite plates under tension or bending load.
NASA STP 1578, 1979

[3] J.C. Newmann: A Review and Assessment of the Stress-Intensity Factors for Surface Cracks, ASTM STP 687, 21979 pp. 16-42

Staff:

A. Nyilas
H. P. Raber

Specification of Vacuum System Prototypes

For the procurement of prototype components of the plasma exhaust pumping system, the following technical specifications have been defined:

- turbomolecular pump 18 000 l/s

- electrostatic precipitator ND 2000

- gate valve ND 1500

Technical assessments have been delivered for two feasibility studies carried out by industry with regard to divisible gate valves ND 1500 which can be repaired in a remote-controlled manner.

With this information supplied to the NET-Team the contract was concluded.

Staff:

H. Illbruck
D. Perinic

Crack Growth of the NET First Wall

The first wall (FW) of a fusion machine of the next generation (ITER/NET) is subjected to high heat fluxes that change cyclically. A periodically changing inhomogeneous temperature fields is induced in the component. The integrated FW as part of a whole blanket box is prevented from free expansion and bending in both, toroidal and poloidal direction. Therefore, global and local thermal stresses are applied, which are periodically changing, too, due to the thermally pulsed operation.

As some 50,000 cycles of operation are planned for the machine, fatigue of the FW has to be considered. The dominant failure mechanism of the component will most probably be some fracture/fatigue mechanism. On one hand side, there will be fatigue growth of existing cracks under repeated load. These flaws may be generated during the fabrication processes ,during machining or as defects of welds. On the other hand side, the FW is subjected to severe loadings under off-normal conditions (plasma disruptions, run-away-electrons). During these events new cracks can be initiated, that further will propagate as fatigue cracks. Failure of the component has to be defined at least, if any crack penetrating the wall under stable crack growth reaches the plasma facing surface of the FW. Due to the high vacuum conditions requested in the plasma chamber any leak can't be tolerated.

Problems of fatigue/fracture interaction have been studied. Within a first part of the contract methods know from linear elastic fracture mechanics have been applied to fatigue growth of (existing) cracks.

The investigations performed include a thermal and mechanical analysis of the first wall and fracture mechanical analysis of the following:

- different crack location,
- different length and shape of starter cracks,
- comparison of results gathered under slightly modified assumptions on loading or boundary conditions.

Fig. 1 shows a schematical view of the FW. Depending on the initial flaw size two locations (denominated by A and B) have been identified as most critical with respect to fatigue crack extension. Due to uncertainties in the operational conditions different mechanical boundary conditions and different surface heat fluxes have been applied. Fig. 2 summarizes the lifetime predicted under the assumption of various starter cracks and under different conditions. In order to reach 50,000 of full power cycles, cracks of 0.5 mm in depth have to be safely detected within a non-destructive evaluation procedure before operation.

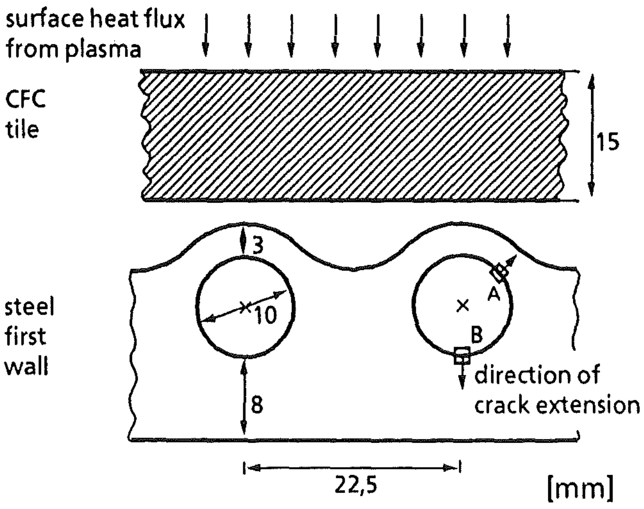

Fig.1: Sketch of FW geometry.

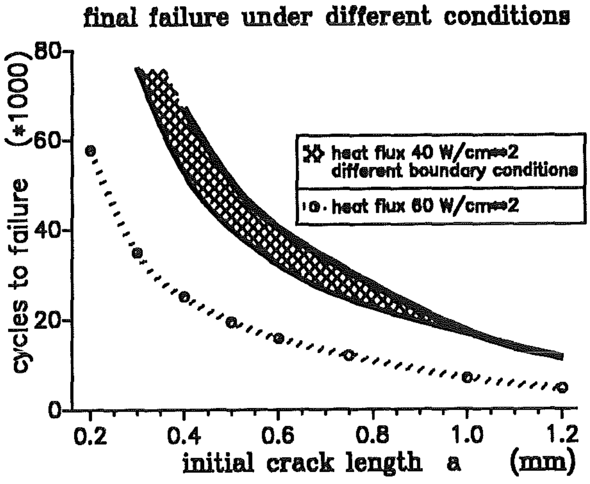

Fig. 2: Final failure of FW under different conditions.

Staff:

E. Diegele
G. Schweinfurther

Appendix I: Allocation of Tasks

Task No.	Title	KfK Departments
Plasma Facing Components		
PSM 3	Low Cycle Fatigue of 316 and Welds	IMF II
PSM 8	High Emissivity Coatings on 316L	IMF II
PPM 0	Development and Characterization of Graphites and CFCs including Neutron Irradiation Effects	IMF I, IMF II
PPM 3	Off-Normal High Heat Loads	INR
PPM 4	Material Characterization and Irradiation Effects in Ceramic Insulators	IMF I
PDT 1	First Wall Mock-up and Tests	IMF II, IATF
PDT 2	Divertor Mock-up and Tests	IRS
Superconducting Magnets		
MCON	Full-Size 40 kA Conductor	ITP
MTOS	TOSKA Upgrading for Model Coil Testing	ITP, HIT
MBAC	High Field Operation of NBTI at 1.8 K	ITP, HIT
Vacuum and Fuel Cycle		
TPV 1	Mechanical Vacuum Components	HIT
TPV 2	Cryogenic Vacuum Components	HIT
TEP 1	Cryosorption	IRCH
TEP 2	Permeation and Catalytic Cracking	IRCH
TEP 3	Tritium Storage and Transportation	IRCH
Nuclear Engineering / Basic Blanket		
NDB 2	Neutronics Data Base - Benchmark Experiments	TU Dresden
--------	Intense Neutron Sources for Materials Research	IMF I, IRS
Remote Handling / Maintenance		
RHB 1	RH Common Subsystems	IRS
RHS 1	Qualification of Standard Components	HIT
RHT 1	Articulated Boom Transporter	HIT, IRS

Safety and Environment

SEA 3	Reference Accident Sequences	IRS
SEA 5	Assistance in Preparation of Safety Reports	IRS, ITP
SEP 2	Environmental Impact of Tritium and Activation Products	INR

Long Term Program for Materials Development

LAM 2.1	Low-Activation Fusion Materials Development	IMF II
LAM 3.2	Development of Low Activation Martensitic Steel	IMF I, IMF II
MANET 1.1	Characterization and Optimization of MANET - II Steel	IMF I, IMF II
MANET 3.2	Pre- and Post-Irradiation Fatigue Properties	IMF II
MANET 3.4	Pre- and Post-Irradiation Fracture Toughness	IMF II, HVT/HZ
MAT 5	Ion-Beam Irradiation Fatigue and Creep Fatigue Tests	IMF I

Test Blanket Development

BS - Solid Breeder Test Blankets

BS DE-D 1	Solid Breeder Test Blanket Design	IMF III, INR
BS BR-D 1	Preparation of Ceramic Breeder Materials	IMF III
BS BR-D 2	Characterization of Ceramic Breeder Materials	IMF III
BS-BR-D 3	Irradiation Testing and Post Irradiation Examination	IMF I, IMF III, HVT/HZ
BS BR-D 4	Tritium Release	INR, HVT/HZ
BS BR-D 8	Solubility of Molecular Hydrogen in Lithium Orthosilicate	IRCH
BS NN-D 1	Helium Blanket Test Loop	IMF III, INR

BL - Liquid Metal Test Blankets

BL DE-D 1	Liquid Metal Test Blanket Design	IMF III, INR, IATF
BL PC-D 2	Active and Inactive Impurities and Clean-up of Molten Pb-17Li	HIT
BL EI-D 1	Electrical Insulation and Coatings	IMF I, IMF III
BL EX-D 1	Tritium Extraction by Permeation and Cold Trapping	IATF
BL MH-D 1	Liquid Metal MHD	IATF
BL SA-D 1	Reliability Assessment	IRS
BL SA-D 2	Electromagnetic Forces	IRS
BL CO-D 2	Liquid Metal Loop Components and Testing	IATF

Development of ECRH Power Sources

ITP, IMF II

Appendix II: Table of NET Contracts

Theme	Contract No.	Working Period
Simulations on Jacket Material Failure by Crack Growth at 4 K for the NET-Superconductors	447-91-2/FU-D/NET	8/91 - 1/92
Specification of Vacuum System Prototypes	426/90-7/FU-D/NET	8/90 - 12/91
Crack Growth of the NET First Wall	ERB 5000 CT 9100 72 NET	11/91 - 10/92

Appendix III: KfK Departments Contributing to the Fusion Project

Kernforschungszentrum Karlsruhe GmbH Telephone (07247) 82-1
Postfach 3640 Telex 17 724 716
D-7500 Karlsruhe 1 Telefax/Telecopies (0) 07247/825070
Federal Republic of Germany

KfK Department	KfK Institut/Abteilung	Director	Ext.
Institute for Materials Research	Institut für Material- und Festkörperforschung (IMF)	I. Prof. Dr.K.-H. Zum Gahr II. Prof. Dr. D. Munz III. DI. E. Bojarsky (acting)	3897 4815 2583
Institute for Neutron Physics and Reactor Engineering	Institut für Neutronenphysik und Reaktortechnik (INR)	Prof. Dr. G. Keßler	2440
Institute for Applied Thermo- and Fluiddynamic	Institut für Angewandte Thermo- und Fluiddynamik (IATF)	Prof. Dr. U. Müller	3450
Institute for Radiochemistry	Institut für Radiochemie (IRCH)	Prof. Dr. H.J. Ache	3200
Institute for Reactor Safety	Institut für Reaktorsicherheit (IRS)	DI. W. Kramer (acting)	2949
Central Engineering Department	Hauptabteilung Ingenieurtechnik (HIT)	Dr. H. Rininsland	3000
Institute for Technical Physics	Institut für Technische Physik (ITP)	Prof. Dr. P. Komarek	3500
Central Experimental Engineering Department	Hauptabteilung Versuchstechnik (HVT)	Dr. Schubert	3114
- Hot Cells	- Heiße Zellen	DI. Enderlein	3650
- Tritum Laboratory Karlsruhe	- Tritiumlabor Karlsruhe	DP. Jourdan	2514
Remote Handling Laboratory	Handhabungstechnik-Labor (HT)	DI. Müller-Dietsche	2942
Central Safety Department	Hauptabteilung Sicherheit (HS)	DP. W. Koelzer	2660
Institute for Meteorology and Climate Research	Institut für Meteorologie und Klimaforschung (IMK)	Prof. Dr. F. Fiedler	2093
Institute for Nuclear and Atomic Physics of the Technical University Dresden		Prof. Dr. K. Seidel	035101/8982

Appendix IV: Fusion Project Management Staff

Head of the Research Unit	Dr. J. E. Vetter	ext. 5460
Secretariat:	Fr. I. Sickinger	ext. 5461
	Fr. I. Pleli	ext. 5466
	Fr. M. Zimmer	ext. 5466
Project Budgets, Administration, Documentation	BW G. Kast	ext. 5462
Studies, NET / ITER Contacts	Dr. J.E. Vetter	ext. 5460
Blanket Development and Test Facilities	DI H. Sebening	ext. 5464
Superconducting Magnets, Development of Gyrotrons and Transmission Components	DI H. Knuth	ext. 5468
Tritium Technology Structural Materials	Dr. H.D. Röhrig	ext. 5463
Safety and Environmental Impact, Remote Handling	DI A. Fiege	ext. 5465

Address:
Kernforschungszentrum Karlsruhe GmbH
Nuclear Fusion Project Management

Post Office Box 3640, D-7500 Karlsruhe / Germany

Telephone No: 07247-82- Extensions ....

Telefax No: 07247 - 82 - 5467

Telex No: 17 724 716